

Abstract

Thin-film 3D Resonators for Superconducting Quantum Circuits

Lev Viktorovich Krayzman

2022

Quantum computing has garnered a lot of attention due to the belief that it would be able to solve certain kinds of problems which are intractable to classical computers. One of the leading candidate platforms for quantum computing is superconducting circuits. Within this platform, there are two main methods of storing quantum information: Josephson-junction based artificial atoms and harmonic oscillators. The large Hilbert space of the bosonic excitations of a harmonic oscillator allows for redundant storage of quantum information. Quantum error correction in a single mode using bosonic codes has been demonstrated beyond break-even. However, devices with more than a handful of oscillators have not yet been demonstrated. One of the main challenges in scaling up devices is oscillator design. Currently, coaxial stub cavities machined from high-purity aluminium are most commonly used. Fully-lithographic micromachined cavities have previously been demonstrated, but had short lifetimes due to loss in the seams. In this thesis, I describe a way to fabricate and measure ultra-high-quality microwave seams using indium bump-bonding. I then discuss the application of this to micromachined cavities, improving their lifetime hundredfold and exceeding that of stub cavities. I also demonstrate suspended coaxial resonators, which have a demountable centre conductor. They are easier to make than micromachined cavities and can slightly exceed stub cavities' lifetime without the use of high-purity aluminium. Finally, I discuss recent work on ways of measuring the losses of different materials or interfaces using multimode resonators, and the comparison of this to traditional materials studies methods.

Thin-film 3D Resonators for Superconducting Quantum Circuits

A Dissertation
Presented to the Faculty of the Graduate School
of
Yale University
in Candidacy for the Degree of
Doctor of Philosophy

by
Lev Viktorovich Krayzman

Dissertation Director: Professor Robert J. Schoelkopf

December 2022

Copyright © 2022 by Lev Viktorovich Krayzman

All rights reserved.

Contents

| | |
|--|-----------|
| Acknowledgments | xv |
| 1 Introduction | 1 |
| 1.1 Thesis overview | 5 |
| 2 Superconducting Microwave Resonators for Storage of Quantum Information | 9 |
| 2.1 Platform selection | 10 |
| 2.1.1 Bosonic encodings in harmonic oscillators | 11 |
| 2.1.2 Superconducting microwave cavities | 12 |
| 2.1.3 Planar-patterned vs. 3D resonators | 15 |
| 2.2 Losses in superconducting microwave resonators | 18 |
| 2.2.1 The Participation Ratio Model | 18 |
| 2.2.2 Coupling | 20 |
| 2.2.3 Bulk Dielectric Loss | 23 |
| 2.2.4 Surface Dielectric Loss | 25 |
| 2.2.5 Conductor Loss | 31 |
| 2.2.6 Seam Loss | 34 |
| 2.2.7 Beyond the Participation Ratio Model | 38 |
| 2.3 Variations in Temperature | 39 |
| 2.3.1 Conductor Loss | 41 |
| 2.4 Designs of superconducting microwave resonators | 49 |

| | | |
|----------|--|-----------|
| 2.4.1 | Requirements and Wish List for a Good Resonator | 49 |
| 2.5 | Measuring the Properties of a Resonator | 50 |
| 2.5.1 | Frequency-domain | 50 |
| 2.5.2 | Time-domain | 58 |
| 3 | Micromachined Cavities and High-quality Superconducting Mi- | |
| | crowave Seams | |
| | | 61 |
| 3.1 | Micromachined Cavities | 62 |
| 3.2 | Ultra-low-loss Microwave Seams with Indium Bump Bonding | 64 |
| 3.2.1 | Measuring Seam Quality | 65 |
| 3.3 | Micromachined Cavity Fabrication | 74 |
| 3.3.1 | Fabrication of the Cavity Itself | 74 |
| 3.3.2 | Bonding Process | 76 |
| 3.3.3 | Coupling to a Micromachined Cavity | 77 |
| 3.4 | Micromachined Cavity Measurements | 78 |
| 3.5 | Micromachined Cavity Outlook | 87 |
| 4 | Suspended Coaxial Resonators | |
| | | 88 |
| 4.1 | Suspended Rod Resonators | 89 |
| 4.1.1 | Plastic Clamp, Rod Considerations | 90 |
| 4.1.2 | Single-piece Clips | 93 |
| 4.1.3 | Two-piece Clips | 101 |
| 4.2 | Suspended stripline Resonators | 106 |
| 4.2.1 | Suspended stripline Centre Conductor | 107 |
| 4.2.2 | Suspended stripline Seam Package | 110 |
| 4.2.3 | Suspended stripline Seamless Package | 113 |
| 4.3 | Suspended Coaxial Resonators Outlook | 122 |

| | |
|---|------------|
| 5 Materials Studies for and Using Superconducting Microwave Resonators | 125 |
| 5.1 Multimode Resonators as a Materials Loss Characterisation Platform | 126 |
| 5.1.1 Basic Principle | 126 |
| 5.1.2 Ellipsoidal Cavity | 129 |
| 5.2 Materials Characterisation Using Traditional Methods | 136 |
| 5.2.1 In-house Measurements | 137 |
| 5.2.2 TEM | 139 |
| 5.2.3 X-ray | 149 |
| 5.3 Outlook | 157 |
| 6 Conclusion and Outlook | 159 |
| 6.1 Future of Resonators | 161 |
| 6.2 Future for Materials | 162 |
| Appendices | 165 |
| A Fabrication details | 166 |
| A.1 Basic processes | 166 |
| A.1.1 Cleaning or preparing the wafer | 166 |
| A.1.2 Lithography | 169 |
| A.1.3 Indium evaporation | 173 |
| A.1.4 Electron-beam lithography | 174 |
| A.1.5 Aluminium evaporation | 175 |
| A.1.6 Liftoff | 175 |
| A.1.7 Chip or wafer bonding | 177 |
| A.2 Specific fabrication processes | 178 |
| A.2.1 Interrupted stripline resonators | 180 |
| A.2.2 Micromachined cavity | 181 |

| | | |
|----------|--|------------|
| A.2.3 | Transmons | 182 |
| A.3 | Cracking Sapphire with the E-beam Writer | 183 |
| A.4 | High-Purity Aluminium Etching | 185 |
| B | Electromagnetic simulations | 187 |
| B.1 | Meshing | 187 |
| B.2 | Couplings, participations | 189 |
| B.3 | Fields calculator | 190 |
| B.4 | Potpourri | 191 |
| C | De-Gaussing Magnetic Shielding | 192 |
| D | Mattis-Bardeen Fitting Code | 195 |
| E | Useful Tables | 197 |
| E.1 | Material Properties | 197 |
| E.2 | Participations | 199 |

List of Figures

| | | |
|-----|--|----|
| 1.1 | This thesis in context of the broad field | 6 |
| 2.1 | Planar microwave resonators | 16 |
| 2.2 | Coupling to planar and 3-D microwave resonators | 22 |
| 2.3 | Sample temperature dependence of a resonator | 40 |
| 2.4 | Complex conductivity compared to approximations. | 43 |
| 2.5 | Scaled superconducting gap vs. scaled temperature | 46 |
| 2.6 | Sample surface impedance for thick film in local limit | 48 |

| | | |
|------|--|-----|
| 2.7 | Microwave resonator measurement setups | 52 |
| 2.8 | Sample reflection measurement | 54 |
| 3.1 | A diagram of the crosssection of a micromachined cavity | 62 |
| 3.2 | A diagram of the TE101 mode of a rectangular cavity | 63 |
| 3.3 | An image of a disassembled micromachined cavity | 64 |
| 3.4 | Interrupted stripline for g_{seam} measurement | 67 |
| 3.5 | Micrograph of a bonded interrupted stripline | 68 |
| 3.6 | Seam loss of indium bump bonded devices | 71 |
| 3.7 | The fabrication process of a micromachined cavity | 77 |
| 3.8 | A diagram of the coupler for a micromachined cavity | 78 |
| 3.9 | Measurements of a micromachined cavity | 80 |
| 3.10 | Micromachined cavity results | 82 |
| 3.11 | Micromachined cavity power and temperature sweeps | 84 |
| 3.12 | Mattis-Bardeen fits for a micromachined cavity | 85 |
| 4.1 | Tiling of stub cavities vs. suspended coaxial resonators | 90 |
| 4.2 | Quarter-wavelength vs. half-wavelength coaxial resonators | 91 |
| 4.3 | Rod resonators with a one-piece clip | 94 |
| 4.4 | Rod resonator with a seam | 95 |
| 4.5 | Measurements of rod resonators in Al 6061 package | 97 |
| 4.6 | Power dependence of suspended Al wire Q | 98 |
| 4.7 | Measurements of rod resonators with various centrepin materials in a 5N Al package | 99 |
| 4.8 | Shaking mode of a suspended rod on a VNA | 100 |
| 4.9 | Temperature sweep of a suspended Ta rod in an Al package | 102 |
| 4.10 | CAD drawings of a rod suspended with two-piece clips | 103 |
| 4.11 | Inventor model of stress in clips | 104 |

| | | |
|------|--|-----|
| 4.12 | Suspended stripline centre conductor | 106 |
| 4.13 | Sidewalls of Laser-cut Chips | 108 |
| 4.14 | Metallisation of a suspended stripline | 109 |
| 4.15 | Suspended stripline in a seam package | 110 |
| 4.16 | Seamless suspended stripline package | 114 |
| 4.17 | Wiring diagram for suspended stripline | 117 |
| 4.18 | T_1 measurements of a suspended stripline resonator | 118 |
| 4.19 | T_2 measurement of a suspended stripline resonator | 119 |
| 4.20 | Transmon T1 jumping with pulse tube | 121 |
| | | |
| 5.1 | Design and mode structure of an ellipsoidal cavity | 129 |
| 5.2 | Ellipsoidal cavity mode diagram | 130 |
| 5.3 | Extracted losses for ellipsoidal cavities | 131 |
| 5.4 | Sensitivity plots for an ellipsoidal cavity | 132 |
| 5.5 | Ellipsoidal cavities with different surfaces | 133 |
| 5.6 | Predicted vs. measured Q for ellipsoidal cavities | 134 |
| 5.7 | Shroud around lifted-off e-beam metal features | 139 |
| 5.8 | Etched 5N5 Al surface TEM | 142 |
| 5.9 | Unetched 5N5 Al surface TEM | 143 |
| 5.10 | TEM of 100 μm into etched and unetched 5N5 Al | 144 |
| 5.11 | HAADF and EELS of a copper inclusion | 145 |
| 5.12 | TEM and EDX of surface oxide layer in etched and unetched 5N5 Al | 146 |
| 5.13 | TEM and EELS of grain boundary and cracks in Al | 148 |
| 5.14 | XPS survey of the 5N5 Al coupons | 150 |
| 5.15 | XPS of the 5N5 Al coupons, Ni and Fe focus | 151 |
| 5.16 | XPS of the 5N5 Al coupons, Al 2S and 2P focus | 152 |
| 5.17 | XRR of thin sapphire wafer | 154 |
| 5.18 | XRR of thin sapphire wafer, solvent cleaned | 155 |

| | | |
|------|---|-----|
| 5.19 | XRR of thin sapphire wafer, solvent cleaned | 156 |
| A.1 | Alignment mark | 171 |
| A.2 | Transmon e-beam pattern | 183 |
| A.3 | Optical image of crack in the sapphire | 185 |
| A.4 | SEM of crack in the sapphire | 186 |
| B.1 | Issues with using a curved mesh | 189 |
| C.1 | The setup used for de-Gaussing magnetic shielding | 193 |
| C.2 | Diagram of loss due to flux vortices | 194 |

List of Tables

| | | |
|-----|---|-----|
| 3.1 | Mattis-Bardeen fit results for a micromachined cavity | 86 |
| 4.1 | Participations for seam package for suspended stripline resonator . . . | 111 |
| 4.2 | Measurements of suspended striplines in seam packages | 112 |
| 4.3 | Measurement results for suspended striplines in seamless package . . | 120 |
| 5.1 | Ellipsoidal cavity measurement results | 135 |
| 5.2 | Ellipsometry of Al | 138 |
| 5.3 | XRR fit results for sapphire wafers | 157 |
| A.1 | Standard wafer cleaning process | 167 |
| A.2 | RCA clean for silicon | 168 |
| A.3 | Piranha organic clean | 169 |
| A.4 | Spinning resist | 170 |

| | | |
|------|---|-----|
| A.5 | Exposure | 171 |
| A.6 | Development of photoresist | 172 |
| A.7 | Development of e-beam resist | 173 |
| A.8 | Indium evaporation | 174 |
| A.9 | Electron beam lithography | 175 |
| A.10 | Thick liftoff | 176 |
| A.11 | Thin liftoff | 177 |
| A.12 | Chip bonding | 178 |
| A.13 | Interrupted stripline resonator fab | 180 |
| A.14 | Interrupted stripline resonator fab | 181 |
| A.15 | Transmon fab | 182 |
| A.16 | Relative doses for transmon | 184 |
| E.1 | Superconductor properties | 198 |
| E.2 | Table of participations | 199 |

Acronyms

AFM atomic force microscopy. 156

AWG arbitrary waveform generator. 58

BCS Bardeen-Cooper-Schrieffer theory of superconductivity. 41, 44, 45

BNL Brookhaven National Laboratory. 126, 137, 139, 149, 153, 154

BOE buffered oxide etch. 74, 108, 167, 168, 181

CAD computer-aided design. 94, 103, 109

CPW coplanar waveguide. 15, 16, 21, 22, 30, 83, 160

cQED circuit quantum electrodynamics. 115, 116

DI de-ionised. 166–169, 172, 173, 181, 182, 186

EDX energy-dispersive x-ray spectroscopy. 138, 140–147

EELS electron energy loss spectroscopy. 146–148

FIB focussed ion beam. 139, 140, 142, 143

FPGA field-programmable gate array. 58, 59, 115

HAADF high-angle annular dark-field. 140, 144, 145

HEMT high-electron-mobility transistor. 79

IPA isopropanol. 74, 172, 173, 176, 177, 181, 182

JJ Josephson junction. 2, 4, 12

MA metal-air. 26, 27, 98, 128

MMIQC multilayer microwave integrated quantum circuits. 61–64, 87

MS metal-substrate. 26, 128

NMP 1-methyl-2-pyrrolidone. 74, 149, 167, 176, 177, 180–182

OFHC oxygen-free high thermal conductivity (copper). 133

PCB printed circuit board. 15, 17, 76, 87

PECVD plasma-assisted chemical vapour deposition. 74

PSSA poly(styrene sulfonic acid). 172–175, 182, 184

RIE reactive ion etch. 74

SA substrate-air. 26, 107, 128, 138

SEM scanning electron microscopy. 64, 67, 76, 108, 137–139, 156, 183

SMA SubMiniature version A. 50, 77

SNR signal-noise ratio. 116

SPA SNAIL parametric amplifier. 116

TEM transmission electron microscopy. 39, 126, 139–144, 146–149, 163

TLS two-level system. 10, 29–31, 39, 40, 83–86, 97, 137, 196

VNA vector network analyser. 50, 51, 57, 59, 97, 99, 100, 112

WGMR whispering-gallery mode resonator. 17

XPS x-ray photoelectron spectroscopy. 149–152

XRD x-ray diffraction. 126

XRR x-ray reflectivity. 153–157

Glossary

EDM Electrical discharge machining. EDM removes metal via electrical discharge through a dielectric fluid (i.e. sparks). [113](#), [123](#), [161](#)

EFG Edge-defined film-fed growth: a growing mechanism for boules of sapphire. [107](#)

HEMEX Sapphire wafers grown by the heat-exchanger method (HEM) that are then screened for good optical properties. [107](#)

HMDS Hexamethyldisilazane. Promotes adhesion to Si wafers. [169](#), [170](#), [180](#), [181](#)

PTFE Polytetrafluoroethylene (Teflon is a trade name for this), a dielectric. [89](#), [91–94](#), [99](#), [101](#), [104](#), [105](#), [115](#), [120](#), [121](#), [167–169](#), [176](#), [185](#)

RCA clean A standard cleaning procedure for silicon wafers, developed at the Radio Corporation of America. [108](#), [167](#), [168](#)

RPM Rabi population measurement. A way to measure the excited state population of a transmon that corrects for readout inefficiency. [121](#)

SNAP Selective number-dependent arbitrary phase gate. A universal way to generate gates on a resonator using a transmon. SNAP requires only displacements on the resonator, alternating with selective rotations on the transmon. See [Heeres et al., 2015, Krastanov et al., 2015]. [116](#), [118](#), [119](#)

Acknowledgments

This Ph.D. would not have been possible without a large group of people providing me with instruction, advice, and support. I shall enumerate some of these people, although I note in advance that it is not possible to include every single person due to their sheer number and apologise to anyone who was left out. I must also thank the U.S. taxpayers for funding some of this research¹.

ROB SCHOELKOPF has served as my advisor for the entirety of my graduate education, and has taught me a large amount of what I now know about science. This spans from big-picture ideas of what to think about when designing an experiment to details such as dilution fridge operation and SMA cable management. I very much appreciate his lessons about and insistence on communicating results clearly, as well as emphasis on the safety and well-being of his group. I am always amazed at his ability to work on so many different projects while remembering the details and long-term goals of each. MICHEL DEVORET's unique way of thinking as well as in-depth knowledge of both physics and its history ensures that you will learn a lot of new things in any conversation with him. He is very attentive to detail, and will ensure that what you are saying is correct. I appreciate his constant desire to really understand the physics of what is going on, both in terms of looking for classical

1. The research in this thesis was sponsored by the Army Research Office (ARO), and was accomplished under Grant Numbers W911-14-1-0011 and W911-18-1-0212. The views and conclusions contained in this document are those of the author and should not be interpreted as representing the official policies, either expressed or implied, of the ARO or the U.S. Government. The U.S. Government is authorized to reproduce and distribute reprints for Government purpose notwithstanding any copyright notation herein.

analogues of the system, and in really thinking through the consequences of proposed explanations. Although I interacted less with LEONID GLAZMAN and HONG TANG, I have appreciated their input in seminars, as well as their feedback and advice on this thesis. Thanks to MICHAEL HATRIDGE as well for taking the time to read and comment on my thesis. I must also thank LUIGI FRUNZIO, who is always available to help out with equipment, provide advice on experiments or life in general, or tell an anecdote. Luigi is a veritable treasure trove of scientific information, including past results and references to papers. His omnipresent touch ensures that the lab keeps running, and his good humour always brightens the mood of everyone around him.

Over the years, I have worked particularly closely with some graduate students and postdocs. TERESA BRECHT was my graduate mentor for the first two years of graduate school. She taught me not only the physics and fab, but also what it means to get a Ph.D. I am grateful for her guidance, starting off without which would have been a drastically more difficult task. CHAN U LEI and I worked together for many years – most of my graduate education. It is difficult to summarise all that I have learned from him; most of this dissertation involves work that we did together. I admire his persistence and dedication to getting things to work. I have also spent a number of years working with SUHAS GANJAM. I am inspired by his optimism and willingness to try new ideas, which have resulted a number of new projects, which I’m sure the group will be working on for some time to come. I have had the pleasure of working with JAMES TEOH on the suspended rod project. He has also been generous with his time, explaining a lot about both the theory and the practical side of qubit measurement to me. I have briefly worked with YANHAO WANG and ARCHAN BANERJEE, and I am confident that they will find new exciting directions in materials or devices.

I have also benefited from interactions with many others. CHRIS AXLINE taught me how to do simulations in HFSS; I have also learned that most the time when I

have an idea, he has already tried it several years ago. I have had many interesting conversations with KEVIN CHOU, LUKE BURKHART, PHIL REINHOLD, SERGE ROSENBLUM, SAL ELDER, JACOB CURTIS, JAYA VENKATRAMAN, ANIKET MAITI, VIJAY JAIN, ARPIT DUA, and IOANNIS TSIOUTSIOS, both about science, and about life. I have spent some time working with ALEX READ and BEN CHAPMAN on resonator studies and learned a lot from the experience. CHRIS WANG joined the group at almost the same time as I did and helped make the experience easier for me. YAO LU, ALEC EICKBUSCH, and NAT COTTET, and especially YANNI DAHMANI have spent a lot of time teaching me how to measure a qubit in general, and helping me with my measurements in particular; PATRICK WINTEL joined me on this journey. VICTOR ALBERT convinced me to play with him at the Rock-n-Roll Physics Sing-along at the APS March Meeting for several years. I also thank ZHIXIN WANG for putting up with me for two years. I have additionally learned a lot about materials science from our BNL collaborators ASHLEY HEAD, KIM KISSLINGER, SOOYEON HWANG, and in particular IGNACE JARRIGE, who organised the collaboration.

A large number of staff have worked to ensure that the group is able to keep doing its work. On the administrative side, TERRI EVANGELISTE, NUCH GRAVES, GISELLE MAILLET, MARIA RAO, and ALEX BOZZI, as well as STEPHANIE HESSING, FLORIAN CARLE, and RACQUEL MILLER at YQI. In the cleanroom, MIKE POWER, CHRIS TILLINGHAST, JIM AGRESTA, YONG SUN, KELLY WOODS, and SEAN RINEHART, as well as MIKE ROOKS at YINQE. I would also like to thank NICO, CHLOE, CONNIE, KATHRYN, JEN, and TIM for keeping me company, and also ANDREW for sharing his music selection. Finally, I would like to thank my parents, VICTOR and IRINA for raising me, moving me to a safe place, and always supporting me, my brother EUGENE for his advice and for always being willing to help me out, and my grandmother, МАРИЮ ЛЬВОВНУ ШОЛОХОВИЧ, for teaching me about chemistry and for her eternal kindness. Эта диссертация посвящается её памяти.

CHAPTER 1

Introduction

During the course of this Ph.D., quantum computing has grown from a still relatively-niche area that never quite fit within condensed matter physics, to a rapidly-expanding discipline of its own. On the academic side, the growth is visible in the dramatic increase in the number of academic research groups studying the subject. This has been recognised by the APS (the Division of Quantum Information was officially established in 2017), and nurtured by generous funding from governments around the world. On the industry side, the number of both start-ups and established companies pursuing quantum computing has also exploded, most recently including the listing of Ion Q and Rigetti on the NYSE. Although public interest has already existed for some time (one of my high school projects was about quantum computing – we were convinced trapped ions were the way to go), it has seen a resurgence with the announcement of IBM Q System One and the achievement of quantum supremacy by Google [Arute et al., 2019] in 2019.

Nevertheless, the field is still very much in the early stages of development, at least on the experimental side. It is as of now unclear which (if any) of the currently-existing

platforms for quantum computation will prove to be successful. Current contenders include trapped ions, superconductors, colour centres, linear optics, semiconductors, anyons, neutral atoms, mechanics, electrons on helium; the list is continuing to grow. My Ph.D. has focussed on the superconducting platform, which is the one that will be described in this thesis.

Superconducting quantum computing is so named due its usage of superconducting circuits for the storage and manipulation of quantum information. The first experiments which hinted at the possibility of superconducting qubits were ones which demonstrated macroscopic quantum tunnelling in **Josephson junctions (JJ's)** [Devoret et al., 1984, Martinis et al., 1985, Devoret et al., 1985]. In order for electrical circuits to be quantum, they require very low temperatures such that thermal occupation of the states is low: $k_B T \ll \hbar\omega$, which for relevant frequencies on the order of GHz gives temperature in the 10's of mK. Additionally, the excitations need to be on the level of single photons. The first superconducting qubit was demonstrated some time later [Nakamura et al., 1999].

Today, there are two main branches within the superconducting quantum computing platform: in one, information is stored in effectively-two-level systems (generally transmons, to be described in more detail later, although there are other proposals, such as the fluxonium [Manucharyan et al., 2009], 0- π [Kitaev, 2006, Brooks et al., 2013, Gyenis et al., 2021], etc.), with the redundancy necessary for error correction being envisioned via cleverly distributing the information between large numbers of physical devices. There are a number of encoding schemes used, with toric/surface codes being popular. In the other branch, information is instead stored in harmonic oscillators, with the redundancy achieved by exploiting the large Hilbert space of the oscillator. As of the writing of this thesis, it is again unclear which, if either, branch will prove to be successful, although there is considerably more effort in and attention to the first.

Common arguments about which is better centre around the performance and requirements of the codes (with error correction beyond the break-even point [Ofek* & Petrenko* et al., 2016] and logical manifold stabilisation allowing for steady-state error correction [Campagne-Ibarcq*, Eickbusch*, Touzard*, et al., 2020] being demonstrated only in bosonic codes at this time)¹, as well as the scalability of the hardware (with devices with over 100 transmons being claimed [Chow et al., 2021] and devices with tens of qubits being published [Arute et al., 2019]). There are additional considerations over what exactly is the correct metric to compare the performance of different quantum computers. I shall not attempt to address these issues in this thesis, but instead focus on the platform studied in my group, namely bosonic codes in harmonic oscillators in the form of superconducting microwave circuits.

There are two main circuit elements necessary for the creation and controlled modification of quantum states in such a system (of course, there are many more necessary in practice, but we neglect those for now). The first is naturally the harmonic oscillator itself, which in our platform is embodied by a superconducting microwave resonator. This element stores the quantum information in the quantum states of its electromagnetic field, with the particular encoding depending on which bosonic code is used. However, the harmonic oscillator is a linear device (the energy is linear in the number of photons in the mode), meaning that it can only be prepared in a thermal state or driven to a coherent state, which is not enough for quantum computation (see e.g. [Braunstein and van Loock, 2005] Sec. VI). The second element therefore needs to be non-linear. Transmons, or transmon-like elements are common for this purpose, as they are anharmonic oscillators. For quantum computation, it is important to improve the qualities of both elements, depending on which aspect one is focussing.

1. In this thesis, multiple authors who are stated to have contributed equally to a paper will be marked by an asterisk.

Over the past two decades, the lifetimes of the nonlinear elements have improved by orders of magnitude. This was possible due to the fact that these devices are relatively new in principle, being described [Shnirman et al., 1997] and realised [Bouchiat et al., 1998, Nakamura et al., 1999] only in the late 1990's, leaving a lot of room for improvement, although similar devices using Josephson junctions for quantum effects have been made in the late 1980's [Clarke et al., 1988]. There have been concerns about losses from the **JJ** being a limiting factor for these elements, however, evidence suggests the contrary, see e.g. [Kim et al., 2011, Pop et al., 2014].

The situation is somewhat different with microwave resonators. They were developed in the early 20th century for radar applications, with on-chip devices becoming available a few decades later. By the late 1960's, superconducting microwave cavities at several-GHz frequencies with Q factors in the tens of billions had been developed for usage in accelerators [Turneaure and Weissman, 1968, Turneaure, 1972]. However, these amazing Q's are only found at high temperatures (around 1.2 K) and extremely high powers (equivalent number of photons with double-digits orders of magnitude), whereas in order to perform quantum operations, we need to operate at temperatures in the tens of mK and powers equivalent to around a single photon circulating. While there has recently been some work on applying these cavities to superconducting quantum computing [Romanenko et al., 2020], there is a drastic decrease in quality in the regime described above; additionally, the crucial coupling to a non-linear element has not yet been demonstrated.

Let us now briefly summarise the history of microwave resonators in superconducting quantum computation. At the time when the transmon was introduced [Koch et al., 2007, Schreier et al., 2008], it was coupled to a resonator in the form of a coplanar waveguide transmission line (hence the name). Several years later, the transmon was housed in a 3D cavity machined from aluminium, which not only provided a resonance to be used as a readout mode, but also protected the transmon from decoherence due

to the external environment [Paik et al., 2011]. Around the same time, microwave resonators were used as a memory for storage of quantum information [Mariantoni et al., 2011]. For the 3D cavity, assembling a system with several parts while maintaining coherence proved to be a challenge, which was solved by clever design of the coaxial stub cavity [Reagor et al., 2016, Axline et al., 2016]. This new design enabled systems to incorporate several cavities and control elements while maintaining coherence, and is the most common fully-3D resonator used for superconducting quantum computation to this day. Around the same time, 3D cavities micromachined into a silicon chip were used as a quantum memory made with more scalable lithographic fabrication, compared to traditional machining [Brecht et al., 2015].

This is the point at which the work in this thesis begins. The work included here has advanced the quality of micromachined cavities to above what is achieved in coaxial stub cavities [Lei* & Krayzman* et al., 2020], provided a more scalable resonator design which combines bulk-machined and thin-film materials, and started the process of more serious analysis of materials used for superconducting quantum circuits.

1.1 Thesis overview

Whereas a thesis written several years ago would surely start with an explanation of what quantum computing is, this hardly seems necessary now, given the recent popularisation of the subject. Most readers have likely already encountered the concept. I shall therefore avoid describing quantum computing in general and refer the interested reader to the classic textbook [Nielsen and Chuang, 2000].

The next section would undoubtedly describe circuit quantum electrodynamics (cQED), toward the realisations of which most of the research in this thesis was performed. cQED is the field studying interactions of microwave photons (or excitations

of the electromagnetic field, to be more precise) with superconducting circuits; it is the microwave version of cavity QED, with superconducting resonators acting as cavities, and Josephson junctions (JJ) providing the nonlinearity necessary to provide photon interactions [Blais et al., 2004, Wallraff et al., 2004]. With over a decade having passed since the publication of both of the eponymous theses [Schuster, 2007, Bishop, 2010], I shall once again mostly refer the reader to existing literature, such as the recently-published review article [Blais et al., 2021] for an introduction to the subject.

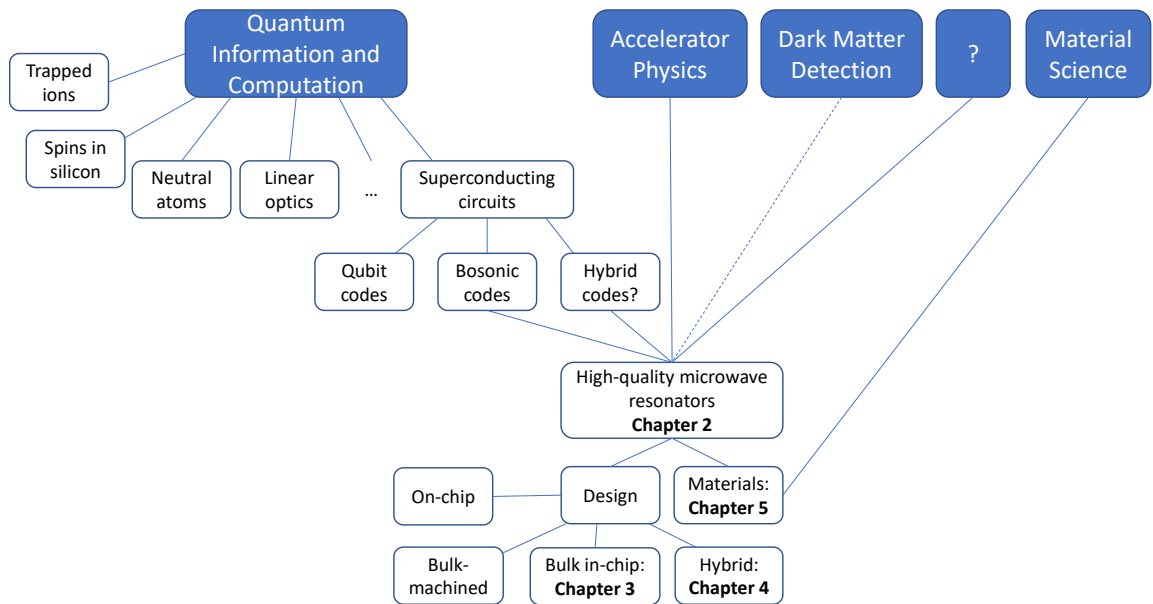


Figure 1.1: The chapters of this thesis in context of the broad fields of physics.

Having extensively informed the reader about what I will *not* be writing, I now turn to an overview of the chapters of this thesis. In chapter 2, I explain why superconducting microwave resonators are an important medium for storing quantum information, and what requirements they must fulfil in order to serve well in this role. I also describe their electrical properties, modelling of their loss channels, and their temperature dependence. Finally, I provide a brief overview of different designs of superconducting microwave resonators, and some additional applications.

In order to build a practical quantum computer, we will need a large number of resonators. Currently, devices with up to four addressable cavities have been demon-

strated [Chou et al., 2018, Zhou et al., 2022]. It is therefore crucial for the resonator design to be scalable to larger systems. In chapter 3, I discuss a candidate resonator, the micromachined cavity. Due to its design constraints, this cavity is very sensitive to seam loss. I next cover indium bump bonding: a technology for making ultra-low-loss microwave seams, and present a way to measure the resulting seam quality. I then discuss the fabrication of the cavity itself. I finally present measurements of the micromachined cavity incorporating indium bump bonded seams. The seams are sufficiently good to not limit our cavity quality, and the cavity is several times longer-lived than currently-used bulk aluminium cavities.

Although the micromachined cavity has a long lifetime and a clear path to mass-production, it is relatively labour-intensive to make in a research setting. In chapter 4, I present a new, easier to produce design concept for a long-lived microwave cavity, the suspended-centrepin coaxial superconducting resonator. I explain the advantages of suspending the centrepin, and describe several designs which achieve the goal in different ways. I present results from measured suspended rod and suspended lasercut chip resonators.

Aside from developing new designs, the other way to improve the quality of our resonators is by using better materials and process techniques. One outstanding challenge is to be able to measure, rather than place bounds on, the quality of the materials. In chapter 5, I describe several methods for extracting the loss properties of the materials used in our systems via specially-constructed multimode microwave resonators. Although many groups have studied the microwave losses in cQED, the microscopic mechanisms behind them are still largely unknown. I additionally present early work on using crystallographic and microscopic structure as well as chemical analysis performed by colleagues at Brookhaven National Laboratory (BNL) to attempt to understand the causes of our losses.

Finally, in chapter 6, I summarise what has been learned during this Ph.D. I

discuss possible ways to build upon the work described in the earlier sections, and highlight some remaining open questions.

CHAPTER 2

Superconducting Microwave Resonators for Storage of Quantum Information

The career of a young theoretical physicist consists of treating the harmonic oscillator in ever-increasing levels of abstraction.

Attributed to Sidney Coleman

In this chapter, we discuss the usage of superconducting microwave resonators for the storage of quantum information. At their heart, they are, of course, just (quantum) harmonic oscillators. However, as young experimental physicists, we shall take an approach opposite to the one supposedly espoused by Sidney Coleman, and rather than treat increasingly-complicated problems as harmonic oscillators, we shall examine a real resonator, and study the ever-increasing number of ways it differs from the ideal, lossless harmonic oscillator.

☞ A note on terminology.

In electrical engineering, a distinction is sometimes maintained between “resonator” and “oscillator”. A resonator is an element which has a strong frequency response near a particular frequency dubbed the “resonant frequency”. An oscillator is a circuit which produces output at a particular frequency on its own; an oscillator can typically include a resonator, as well as some closed-loop amplification or power source. For us, a resonator will generally refer to the physical object, and an oscillator to the physical model, although we shall not always maintain a distinction in favour of using the more common term.

This chapter therefore starts with a discussion of why we want to use harmonic oscillators, and the particular physical implementation of choice, the 3D superconducting microwave resonator, for quantum information storage: section 2.1. I then discuss the loss mechanisms present in real implementations of these resonators, including [two-level system \(TLS\)](#) and seam loss in section 2.2. The next section 2.3 covers what variations are expected in temperature, primarily due to conductor loss (Mattis-Bardeen model). Next, I cover the considerations in designing a superconducting microwave resonator in section 2.4. I conclude with a description of how we actually measure the electrical properties of the aforementioned resonators in section 2.5.

2.1 Platform selection

As mentioned in the introduction, there are many flavours of quantum computing platforms, and even a number of options within superconducting quantum computing. In this section, I discuss the various reasons for which one might choose the particular architecture on which I worked, namely 3D superconducting microwave resonators.

2.1.1 Bosonic encodings in harmonic oscillators

Harmonic oscillators are an attractive candidate, regardless of physical implementation, due to fundamental properties of how quantum information can be stored in them. The types of codes used for this are called bosonic codes since the excitations they use obey Bose-Einstein statistics. Bosonic codes achieve the redundancy necessary for error detection/correction by taking advantage of the large Hilbert space of the harmonic oscillator, allowing a logical qubit to be encoded in one physical device. This provides hardware efficiency compared to surface codes, which generally require a single logical qubit to be distributed across many physical artificial atoms in order to achieve error correction. This relative simplicity has enabled quantum error correction beyond the break-even point [Ofek* & Petrenko* et al., 2016] (without stabilisation), [de Neeve et al., 2022] (using post-selection), and [Campagne-Ibarcq*, Eickbusch*, Touzard*, et al., 2020], while surface codes are not at this point yet [Chen et al., 2021, Krinner et al., 2022].

Additionally, harmonic oscillators nominally have only one error channel – photon loss \hat{a} (and photon gain \hat{a}^\dagger if the resonator is insufficiently cold). This is indeed the dominant error channel for the physical oscillators used, although in practice, dephasing can be inherited from the nonlinear control element or other parts of the system. The particular details of the noise model for a given system allow one to choose a bosonic code which will offer better protection in the given case; there exist a number of codes for different situations. I note that superconducting resonators are not the only bosonic systems used for quantum information storage: for example, motional states of trapped ions [Flühmann et al., 2019] and phonons in mechanical resonators [Chu et al., 2017, Arrangoiz-Arriola et al., 2019] are being developed as well. More in-depth discussion of this aspect of the choice to use harmonic oscillators is outside the scope of this thesis; I refer the interested reader to several recent reviews of the subject [Albert et al., 2018, Joshi et al., 2021].

2.1.2 Superconducting microwave cavities

A note on the limits on frequency.

Although we have the freedom to design a resonator with a frequency within a very large range, some are more amenable to storing and processing quantum information. On one end, the minimum frequency is set by readily-achievable temperatures, since we want to have very low population outside the ground state without driving the system. Dilution refrigerators offer the ability to maintain a relatively large payload at 10 mK indefinitely. This sets the frequency via

$$k_{\text{B}}T \ll hf,$$

which gives a linear frequency $f \gg 200\text{ MHz}$. Note that if we implement active cooling protocols, we could achieve ground state in lower-frequency resonators, e.g. mechanical drums [Teufel et al., 2011].

The upper limit is less well-defined. One factor is the existence of a lossless non-linear element (the [JJ](#)) which can be made to operate at GHz frequencies, up to around 50 GHz. Another is that there exists a large amount of equipment and tools which function up to around 10-20 GHz due to a long history of applications in radar, radio communications, microwave-frequency electronics, etc. An example cutoff is the upper range of the original SMA connector, 12 GHz, although there are now connectors for higher frequencies. These are not fundamental limits: in fact, one may abandon the superconducting platform and move all the way up to the optical domain in frequency. (This does create difficulties with nonlinear interactions, unless one uses a quantum computing scheme that does not require them [Knill et al., 2001]).

Let us now discuss the advantages arising from our particular physical implementation of harmonic oscillators: superconducting microwave cavities. A commonly brought-up reason is that superconducting resonators can have longer lifetimes than superconducting artificial atoms such as transmons (this is true for 3D resonators, see the next section). However, the comparison of lifetimes is actually quite a non-trivial task, with several complications. First, we must address the question of what do we actually mean by lifetime? For an isolated cavity with only one loss channel \hat{a} , this is simply the timescale T_1 over which the energy stored in the cavity decays by a factor of $1/e$. Note that higher Fock states decay faster than lower Fock states, which means the effective physical decay rate depends on the average number of photons \bar{n} in the

code (which forces the codewords for $|0\rangle$ and $|1\rangle$ to have the same \bar{n} , and provides part of the overhead of some bosonic codes).

For a harmonic oscillator coupled to other systems or for a non-linear resonator, there is an additional time scale T_ϕ over which phase information in a coherent superposition is lost (assuming no energy decay); this is referred to as the pure dephasing time. When the energy decay is accounted for as well, we obtain the total dephasing time T_2 given by

$$\frac{1}{T_2} = \frac{1}{2T_1} + \frac{1}{T_\phi}$$

Here, the 2 on the T_1 comes from the fact that T_2 and T_ϕ are amplitude decay terms, while T_1 is an energy decay term. Although a detailed treatment of the sources of these errors is outside the scope of this dissertation, the salient point is that there are different quantities which can be called a lifetime. Depending on what task one is interested in performing, either of these, or some combination thereof, can be the relevant time scale. Typically, superconducting resonators have a very long T_ϕ ($T_2 \approx 2T_1$), whereas the artificial atoms used have varying regimes depending on the type: transmons frequently have appreciable dephasing, so $T_1 \approx T_2$, recent fluxonium results are similar [Nguyen et al., 2019], while other types of qubits have $T_2 \ll 2T_1$, e.g. the $0-\pi$. Returning to the claim, it is currently broadly-speaking true that superconducting 3D resonators have longer lifetimes than the artificial atoms, with resonators routinely achieving coherences on the millisecond scale [Reagor et al., 2016, Lei* & Krayzman* et al., 2020], while the best transmons and fluxonia are currently in the several-hundred microseconds for both T_1 and T_2 [Place et al., 2020, Wang et al., 2022, Nguyen et al., 2019], and the recent $0-\pi$ has T_1 of around 1.6 ms and T_2 on the order of 10 μ s [Gyenis et al., 2021]. I note that these lifetimes are still improving and fundamental limits have likely not been reached. Planar superconducting resonators tend to have lifetimes comparable to the artificial atoms, see e.g. [Altoé*, Banerjee*, Berk*, Hajr* et al., 2022].

 Note:

There is another complication with comparing lifetimes: the potential frequency difference. It is intuitively true that a 1 Hz resonator with a lifetime of 1 s is somehow less impressive than a 1 GHz resonator with the same lifetime. For this purpose, the quality factor Q is defined:

$$Q \equiv \frac{f}{\Delta f} = \frac{\omega}{\Delta\omega} = \omega\tau \quad (2.1)$$

for Δf being the full width at half maximum or bandwidth and τ being the time constant of energy decay of the resonator. An alternative definition is

$$Q \equiv 2\pi \times \frac{\text{total energy in oscillator}}{\text{energy lost in one cycle}} = \omega \frac{E_{\text{tot}}}{P_{\text{diss}}} \quad (2.2)$$

with E_{tot} being the total energy in the oscillator (remembering to account for both electric and magnetic energy in the case of an electromagnetic oscillator) and P_{diss} being the power dissipating from the oscillator. Q can be defined for any oscillator or resonance, such as a musical instrument, a shock absorber, or a filter. See e.g. [Collin, 2001] Section 7.1 for a discussion (note that his $\Delta\omega$ is half of ours).

It is too early to declare victory for cavities, however. Another crucial factor that must be considered is the length of the operations which we wish to perform on the stored information, which generally scales inversely with coupling strengths. Consider the following example: a hypothetical new resonator has very low internal losses and is very strongly isolated from the environment and thus has a lifetime of 1 s. However, due to its strong isolation, the gates or measurements we want to perform on it would take 5 s, meaning the information stored in the resonator would be long gone before the operation is complete. Clearly, such a device would not be particularly useful for our applications, even though its lifetime exceeds current devices' by orders of magnitude. This highlights the fact that what really matters is not the lifetime itself, but the ratio of operation time to the lifetime.

Since there are, in general, many different types of operations one may want to perform, there is no catch-all formula for the operation time as a function of system parameters. In general, for harmonic oscillators which are controlled by a dispersive

interaction of strength χ to a non-linear element, the operation time will be related to $1/\chi$. For non-linear oscillators with anharmonicity α , the operation time is generally related to $1/\alpha$. For a typical resonator with T_1 of 1 ms and $\chi/(2\pi)$ of 1 MHz, the ratio is 1000; for a typical transmon with T_1 of 100 μ s and $\alpha/(2\pi)$ of 200 MHz, the ratio is 20000 (keeping in mind that there may be different prefactors). Indeed, for single-qubit gate fidelities, transmons currently outperform cavity resonators. The situation is more complicated with two-qubit gates, where there is not yet a clear comparison. I once again note that all of the above is very much a rapidly developing area of research and it is far too early to draw any conclusions. For an example of recent development in speeding up cavity gates compared $1/\chi$, see [[Eickbusch et al., 2022](#)].

2.1.3 Planar-patterned vs. 3D resonators

Finally, we discuss the different ways conductive microwave resonators can be physically implemented (there are also other options, e.g. dielectric resonators, which I shall not discuss here). Broadly, these fall into two categories: devices patterned on a plane, and multi-layer or bulk 3D devices. Planar-patterned resonators (often called “planar” or “2D”) refers to structures which can be made with a thin film on some surface (e.g. a [printed circuit board \(PCB\)](#)), and potentially one or more ground planes. Common examples include [coplanar waveguide \(CPW\)](#), microstrip, stripline, and lumped-element resonators. Note that the term “planar” is better thought as describing the manufacture process or physical structure of the resonator rather than its electromagnetic fields, which live in the full three spacial dimensions provided by our world. Fig. 2.1 shows several examples of such resonators.

3D resonators, on the other hand, occupy sizeable amounts of space in all three dimensions, or may be patterned on multiple separate layers. These are most commonly formed from one or several bulk pieces of superconductor (although as we

show in this thesis, a thin film of superconductor on e.g. a dielectric also works, and can in fact be better). Most often, a cavity is machined into the superconductor. The resonant modes of the cavity can then be used to store quantum information. Common shapes currently used in the field include rectangular cavities and coaxial stub cavities, although there are a number of other variants, e.g. the TESLA cavity originally developed for accelerators [Romanenko et al., 2020].

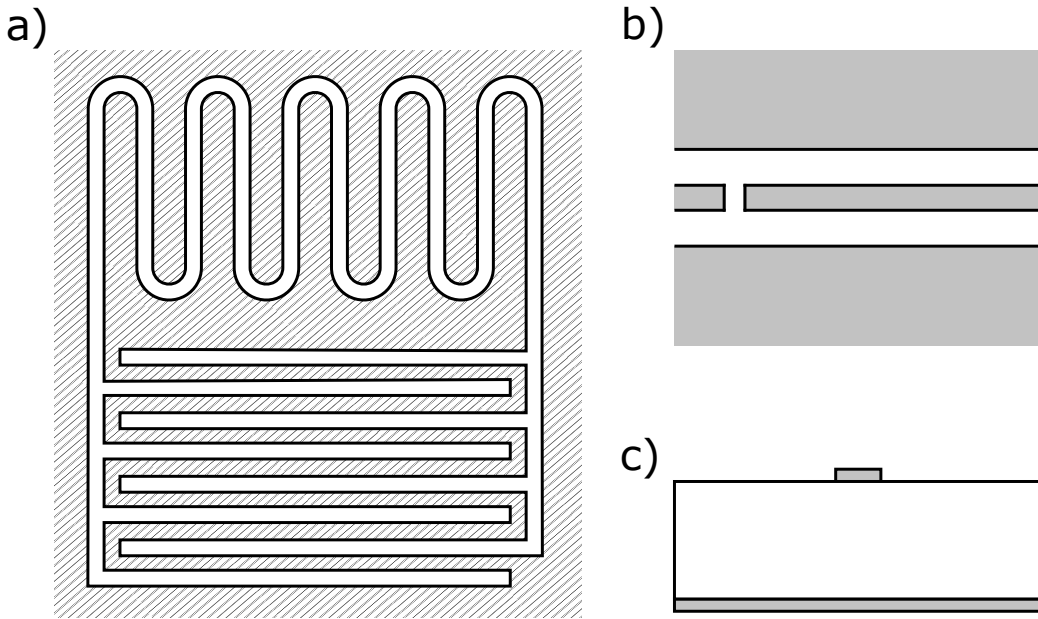


Figure 2.1: Several types of planar microwave resonators used in superconducting quantum computing. a) Top view of a lumped-element resonator. The top half is a meander inductor, the bottom half – an interdigitated capacitor. For an example of such a device, see [Geerlings et al., 2012]. b) Top view of a CPW resonator, with grey representing metallisation on the white substrate. The centre conductor together with the ground planes forms a transmission line; the ends can be left open or shorted to the ground plane (not shown). An example of capacitive coupling is shown to a transmission line on the left side of the image. For an example, see [Göppel et al., 2008]. c) Side view of a microstrip resonator, with grey representing metallisation on the white substrate. Unlike b), the ground plane is formed on the opposite site of the substrate, so most of the electric field lines run through it. For an example, see [Sandberg et al., 2013].

Multilayer 3D resonators are sometimes described as “2.5D” due to the fact that one of their dimensions is much smaller than the other two; however, their mode

structure is really three-dimensional. These include the [whispering-gallery mode resonator \(WGMR\)](#) [Minev et al., 2016], the micromachined cavity [Brecht et al., 2017], as well as other designs featuring indium bump-bonding. A feature commonly shared between these resonators is their production from two bonded chips.

Each type of resonator has its own advantages and disadvantages. Planar-patterned resonators tend to be easier to produce, since they can be made using standard [PCB](#) methods or on a crystalline substrate with lithography. Lithography is relatively easy to scale up to large numbers of devices, as it is already very well-developed for the traditional electronics industry. It also provides for very high precision (sub-micron, if necessary) and allows the use of high-quality thin film superconductors. They can have smaller distances between elements, which allow for stronger couplings as well. However, this also poses a challenge: they store a relatively large amount of energy in lossy surfaces (see section [2.2.4](#)) as well as in the substrate, which causes their lifetimes to be relatively low. Finally, a planar-patterned resonator cannot contain its 3D fields, resulting in a predisposition to cross-talk and other unwanted couplings.

3D resonators, on the other hand, are generally traditionally machined (e.g. milled) out of bulk metals, which is often a less-precise and more difficult-to-scale method of manufacture with resources available to a university laboratory. As we have found, the quality of a bulk metal surface after machining can also more difficult to control than of a deposited thin film, although the details of why this is the case are not yet understood. However, their dimensions are larger, resulting in most of the field being stored in vacuum and lower participations in lossy interfaces, resulting in much longer lifetimes. Additionally, the fully-3D nature allows the fields to be completely enclosed in superconductor, preventing any unwanted interactions with external modes. Since current devices are not limited by the physical size or ease of production of the resonators, the advantages offered by 3D resonators outweigh any scalability challenges. As the field advances, it becomes increasingly more important to re-examine these

aspects. Therefore, in chapters 3 and 4, I discuss hybrid resonator designs which aim to combine advantages of thin film/lithographic fabrication with 3D encapsulation of the fields.

Meanwhile, in the rest of the section, I shall describe the causes of losses, effects of thermal quasiparticles, design strategies, and measurements of superconducting microwave resonators.

2.2 Losses in superconducting microwave resonators

There are a number of channels through which energy can be lost from a superconducting resonator. We start this section by discussing the participation ratio model, which is currently used to analyse losses in existing devices, and predict losses in new designs. We then discuss the specific channels known to be relevant for our devices. We conclude with a brief discussion of going outside the participation ratio regime, and possible approaches there.

2.2.1 The Participation Ratio Model

The basic idea of this model is quite straightforward: essentially, the total loss rate of energy P_{tot} in a resonator is just the sum of the power losses in the different loss channels l :

$$P_{\text{tot}} = \sum_l P_l$$

In this case, a channel refers to a single type of loss, generally associated with a particular material, e.g. a lossy dielectric. For a given resonant mode at angular frequency ω and with energy E_{tot} , we can then write

$$\frac{1}{Q_{\text{tot}}} = \frac{P_{\text{tot}}}{\omega E_{\text{tot}}} = \sum_l \frac{P_l}{\omega E_{\text{tot}}}$$

We then separate out radiative losses, including coupling to the generally- $50\ \Omega$ transmission line:

$$\frac{1}{Q_{\text{tot}}} = \frac{1}{Q_c} + \frac{1}{Q_{\text{rad}}} + \sum_l \frac{P_l}{\omega E_{\text{tot}}}$$

We then rewrite the loss of each channel as a ratio of two dimensionless numbers: p_l and q_l . p_l is called the participation in the loss channel, which is what gives the participation model its name, and is the fraction of the total electromagnetic energy of the mode that is present in the channel l . This quantity can (with some assumptions) be obtained from simulations of the geometry. q_l is the quality factor of that loss channel, or the reciprocal of what is known as the loss tangent $\tan \delta$. This quantity needs to be determined empirically for the particular combination of materials and processes used in the system of interest.

For some loss channels such as seam loss, the microscopic model of loss is not clear, so a ratio of two different quantities is used: y_{seam} and g_{seam} in the case of the seam. The specific details will be discussed in Section 2.2.6, but the relevant point here is that y_{seam} is still similar to a participation, and g_{seam} still similar to a quality factor.

Putting all of these together, the participation model for loss is given by

$$\frac{1}{Q_{\text{tot}}} = \frac{1}{Q_c} + \frac{1}{Q_{\text{rad}}} + \frac{y_{\text{seam}}}{g_{\text{seam}}} + \sum_l \frac{p_l}{q_l} \quad (2.3)$$

Several particular variants for l are discussed in the following few sections, and I note that these are by no means a limit to the model, only the channels we are currently considering.

I note that so far, we have only re-cast the loss in a different form, and thus our equation is exactly true. However, it is also not useful without making additional assumptions. Let us therefore lay out explicitly the **assumptions** generally used with the participation model:

1. The losses in the system are attributable to a relatively small number of loss channels, each of which is internally homogeneous.
2. The properties of a particular loss channel are determined by its material composition and fabrication process.
3. The participations can be consistently simulated and the set of lossy elements (but not necessarily the exact mechanisms of loss) in the system is known.

Additionally, further assumptions are frequently made about the particular forms and properties of the individual loss channels; I shall discuss these in the relevant sections.

2.2.2 Coupling

If we wish to measure a resonator or perform any kind of manipulation of its state, we must introduce a port through which microwaves can leak in and out – a resonator in complete isolation is not useful. Even if the resonator itself is “perfect” (has no internal losses), this coupling port will therefore provide a loss channel. Because of the ubiquity of coupling loss, it is common to see the total Q of a resonator be written as a combination of coupling and everything else:

$$\frac{1}{Q_{\text{tot}}} = \frac{1}{Q_c} + \frac{1}{Q_i}$$

where Q_{tot} is the total Q of the resonator (also commonly referred to as the “loaded Q ” Q_l); Q_c is the Q only due to coupling loss; and Q_i , the internal Q , combines all other loss. Another reason to separate out coupling is that unlike other sources of loss, for some measurement configurations, we have the ability to measure it directly; see section 2.5.

For microwave resonators, the coupling is commonly to a transmission line. The two main ways of achieving this coupling are capacitive (coupling to the electric

field), and inductive (coupling to the magnetic field). Fig. 2.2 demonstrates examples of these two methods for planar circuit and 3-D cavity architectures. The planar circuits, in this case, feature a **CPW** resonator coupled to an on-chip transmission line. The 3-D coupling is demonstrated for pins in the field of a resonant cavity mode (the cavity is not pictured).

Since the impedance of a transmission line is generally known, or at least is frequently assumed to be 50Ω , we can calculate Q_c using only the field distribution of the mode of interest over the port. In practice, when simulating the structure in HFSS, we can remove all lossy elements except for the port, and the resulting Q of the resonant mode will give the Q_c . It is of course also possible to manually perform the same calculation in the fields calculator, allowing the computation of several Q_c 's in one simulation.

Sometimes resonators need to be coupled very weakly, for example when we are interested in measuring their Q_i . In this case, for 3-D resonators we generally place the pin at the end of a sub-cutoff waveguide (see Fig. 2.2 (e)). It can be difficult to simulate the fields precisely enough for very weak coupling. This can be overcome with the following trick: simulate the system for several longer pin lengths (which give stronger coupling, and are thus easier to simulate). Then, fit the resulting Q_c vs. pin length relationship to an exponential, and extrapolate to the desired Q_c or pin length.

In superconducting quantum computing, there is also often a coupling to an anharmonic resonator (e.g. transmon) in order to achieve full control over the quantum state. The losses in the anharmonic resonator will then act as loss channels in our original harmonic oscillator via the hybridisation of the two modes. If the hybridisation of the two modes is sufficiently strong, and the lifetime of the anharmonic resonator sufficiently low, the harmonic oscillator may become limited by this coupling – this is known as the reverse Purcell effect (in reference to [Purcell, 1946]). In

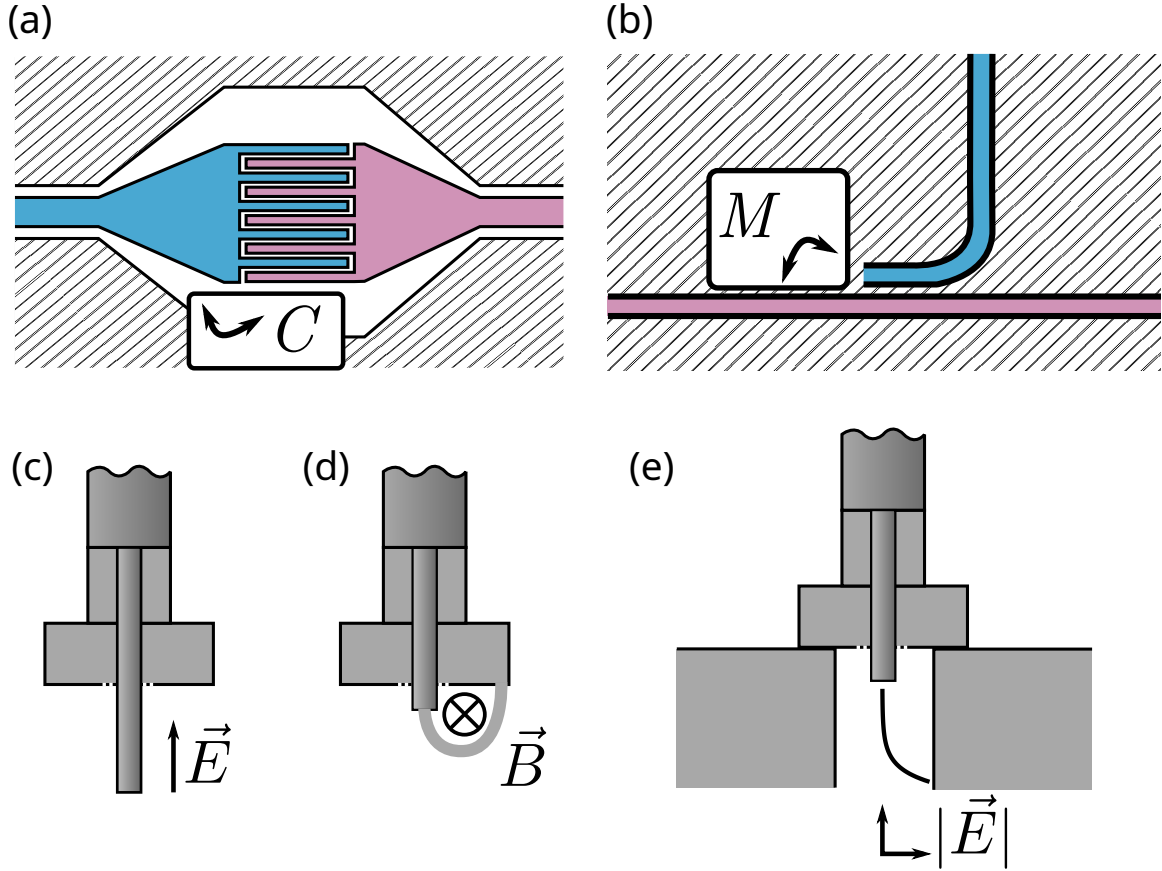


Figure 2.2: a) Capacitive coupling between a planar resonator (blue, left) and a transmission line or another resonator (pink, right). High capacitance C is achieved with the interdigitated shape of the pads. The hatched area represents the metallised co-planar ground. b) Inductive coupling between a CPW $\lambda/4$ resonator (blue) and transmission line (pink). Mutual inductance M is formed by the two parallel sections. The hatched area is once again ground, the black section is unmetallised substrate. c) 3-D analogue of a) – capacitive coupling of the pin to the electric field of a 3-D cavity mode (cavity not shown). The capacitance here is formed between the pin and the wall of the cavity. The field \vec{E} along the pin creates an emf. d) 3-D analogue of b) – inductive coupling of a pin, connected to its own ground with a loop of wire. The magnetic field \vec{B} penetrating the inductance of the loop causes an emf. See for example [Reagor et al., 2013]. e) Weak couplings can be achieved in 3-D by embedding the pin in a sub-cutoff waveguide in the cavity wall. This acts as a high-pass filter, attenuating the field of the mode exponentially with depth if its frequency is below cutoff. Here, the mode is below the bottom of the image, and its field is attenuated as we move up the waveguide.

the case of a transmon coupled to a cavity, the cavity inherits a decay rate

$$\kappa \approx \left(\frac{g}{\Delta}\right)^2 \times \gamma$$

with $\kappa = 1/T$ the loss rate of the resonator in radians/sec, g the vacuum Rabi rate, Δ the detuning between the transmon and cavity in Hz, and $\gamma = 1/T_1$ the decay rate of the transmon in radians/sec [Reagor et al., 2016].

2.2.3 Bulk Dielectric Loss

The participation of the electromagnetic mode in a bulk dielectric is another source of loss. The exact nature of this loss remains an open question, although it seems likely that the energy is somehow converted into phonons via piezoelectricity, or the weaker electrostriction. The resulting phonons then scatter, resulting in incoherent energy loss. Note that even nominally non-piezoelectric materials may exhibit piezoelectricity at surfaces due to the breaking of symmetry there.

The effect of the dielectric on electric fields is given by a complex permittivity $\epsilon = \epsilon' - i\epsilon''$, which in general depends on frequency. The magnitude of the dielectric constant determines the ratio of the electric displacement field \vec{D} and electric field \vec{E} . The angle in the complex plane $\delta = \arctan \epsilon''/\epsilon'$ determines the phase difference between the displacement and electric fields. In this manner, ϵ'' is responsible for losses in the system. $\tan \delta$ is the loss tangent of the dielectric, which is the reciprocal of its quality factor q as mentioned above. These parameters are determined empirically, and are generally difficult to compute *ab initio*.

The participation p for dielectric loss is obtained via the following integral:

$$p = \frac{\frac{1}{2} \int_{V_d} \vec{E} \cdot \vec{D} dV}{\frac{1}{2} \int_V \vec{E} \cdot \vec{D} dV} = \frac{\int_{V_d} \vec{E} \cdot \vec{D} dV}{\int_V \vec{E} \cdot \vec{D} dV}, \quad (2.4)$$

where V_d is the volume of the dielectric, and V – the total volume occupied by the

mode. The $1/2$ in the numerator comes from averaging the loss over the entire cycle (the fields are given at peak value); the $1/2$ in the denominator is just the standard formula for energy stored in the electric field, when the electric field is at peak value, there is no energy in the magnetic field. Assuming our dielectric is linear and isotropic, the displacement field $\vec{D} = \epsilon(\vec{x}, \omega)\vec{E}$, and Eq. 2.4 can be rewritten as

$$p = \frac{\int_{V_d} \epsilon(\vec{x}, \omega) |\vec{E}(\vec{x})|^2 dV}{\int_V \epsilon(\vec{x}, \omega) |\vec{E}(\vec{x})|^2 dV}.$$

A number of assumptions are commonly made in our field when dealing with this loss:

Assumptions:

1. A commonly-made assumption is that the frequency dependence of ϵ is negligible in our band of interest ($\sim 1 - 10$ GHz). As material studies methods become more advanced, it will likely become possible to test the validity of this, and take any frequency dependence into account if the assumption is determined to be false.
2. Another assumption is that ϵ is spatially homogeneous throughout the dielectric. It is also commonly assumed that the surface and bulk have similar properties, although they are also sometimes separated into distinct regions.
3. The dielectric constant is generally assumed to be isotropic. In reality, sapphire is birefringent in the microwave domain, meaning the dielectric response is described by the components of the dielectric tensor, rather than by a dielectric constant. Depending on direction, the components vary by more than 10%. This can be accounted for in simulation since the sapphire wafers have a known crystal orientation.
4. We do not take into account the possible conductivity σ of the dielectric sample.

The condition for this to be valid is $\sigma \ll \omega\epsilon''$, which generally tends to hold for good resistors for microwave frequencies. It may become a concern if the silicon used has a sufficient number of impurities to allow for conduction at milliKelvin temperatures, although to my knowledge, this has not been measured for our wafers. See [Krupka et al., 2006] for an example of such a measurement for a different type of silicon. For more information, see [Collin, 2001] Eq. (2.28).

The first assumption allows us to treat $\epsilon\vec{x}, \omega$ as $\epsilon\vec{x}$. The second assumption allows us to remove the position dependence of ϵ within the dielectric (in the numerator), taking it out of the integral. As mentioned, the dielectric is sometimes split into a small number of discrete regions, see section 2.2.4 for a common example. In the denominator, this generally results in integration over vacuum with permittivity ϵ_0 , and the dielectric with ϵ , although in practice, the energy of the mode in the simulation is set to e.g. 1 J and thus does not need to be computed explicitly. The third assumption has already been incorporated into the above form, it can be removed by treating ϵ as a tensor in the integral. The fourth assumption does not affect the participation ratio calculation, but can be removed from $\tan \delta$ via the aforementioned Eq. (2.28) in [Collin, 2001]:

$$\tan \delta = \frac{\omega\epsilon'' + \sigma}{\omega\epsilon'}$$

with ω the angular frequency of interest and σ the conductivity of the dielectric.

Using the above assumptions, the final form for the participation is

$$p = \frac{\epsilon \int_{V_d} |\vec{E}|^2 dV}{\int_V \epsilon(\vec{x}) |\vec{E}|^2 dV}.$$

2.2.4 Surface Dielectric Loss

Aside from bulk pieces of dielectric, e.g. the substrate or plastic parts in the assembly, some surfaces in the system may be covered in a dielectric as well. Since these are

not usually purposefully created in a controlled or well-characterised way, we generally treat them phenomenologically, and have only hypotheses as to the origins of the loss (although recently, there has been progress in studying the microscopic origins of this, see chapter 5).

There are three main surface types associated with surface dielectric loss: metal-air (MA), metal-substrate (MS), and substrate-air (SA), see e.g. [Wang et al., 2015]. MA is generally thought to be due to oxides which form on the surfaces of most of the metals used, organic residues left over from lithography, or adsorbates. Since the oxide is usually native (and even in the case of purposefully-grown aluminium oxide, is not grown epitaxially), it is amorphous and of unknown chemical composition. Therefore, its loss tangent may be very different from measured values for bulk oxides. The situation is even less clear with organic residues; there has not been a thorough study on the presence and composition of these. For these reasons, the loss at this surface is treated phenomenologically.

The microscopics of MS and SA are even less clear. Generally, MS is thought to arise either as a result of organic residue (if using lift-off, or a multi-step process), or an “imperfect” interface between the metal and substrate (either as non-uniform growth of the metal, or actual damage to the substrate). SA can also harbour organic residues (which will form even in an etching process), as well as surface effects of the bulk dielectric mentioned in the above section (such as e.g. anomalous piezoelectricity).

The model for surface dielectric loss is the same as for bulk dielectric loss in the section above. Unlike bulk dielectrics, surface dielectrics are generally very thin: for example, native oxides on aluminium or indium are known to be on the order of a few nanometres in thickness. Since the resonant structures we use are on the centimetre scale, explicit finite-element simulation of the surface dielectric presents a computational challenge (it is very difficult to maintain accuracy without using a computationally-prohibitive number of elements when the length scales in the simula-

tion range over so many orders of magnitude). For this reason, we typically introduce an additional assumption, namely that the surface dielectric is so thin that the electric field does not vary throughout its thickness. This allows us to turn the volume integral into a surface integral (see first equality):

$$p_{\text{diel,surf}} = \frac{\epsilon t \int_{S_d} |\vec{E}_{\text{real}}|^2 dS}{\int_V \epsilon(\vec{x}) |\vec{E}|^2 dV} = \frac{t \int_{S_d} |\vec{E}_{\text{sim}}|^2 dS}{\epsilon_r \int_V \epsilon_r(\vec{x}) |\vec{E}|^2 dV}, \quad (2.5)$$

with t the thickness of the dielectric and S_d the surface covered by it, $\epsilon_r \equiv \epsilon/\epsilon_0$, \vec{E}_{real} is the real physical field inside the surface dielectric. **However**, there is an additional complication: for technical reasons, since we are not simulating the surface dielectric, it is easier to use boundary conditions that assume $\epsilon = \epsilon_0$. If one does this, the simulation is not aware of the surface dielectric at all, and produces electric field \vec{E}_{sim} . The proper boundary conditions can then be re-introduced manually by noting that $\vec{E}_{\text{sim}} = \epsilon_r \vec{E}_{\text{real}}$ (this is the standard problem of a capacitor partially filled with a dielectric). This obtains the second equality above. From this form of the equation, we can see that (possibly contrary to one's intuition) the surface dielectric participation *decreases* with a higher ϵ_r , everything else being kept constant.

Another important thing to note here is that neither ϵ_r nor t are truly known (or even necessarily represent individual physical objects), since the microscopic loss mechanisms are not fully known. Therefore, one frequently sees assumptions about these values in the literature, e.g. for the MA interface of aluminium, $\epsilon_r = 10$ and $t = 3 \text{ nm}$ are frequently assumed, see e.g. [Wenner et al., 2011]. One must always be careful when comparing these participations to ensure that these values are correctly accounted for.

I note that we have subtly stepped away from the principle stated in section 2.2.1, namely that q contains all of the unknown physical parameters, while p can be computed entirely from the field profile. In principle, it is possible to measure the thick-

ness of the oxide (see section 5). However, measuring the ϵ of an amorphous surface dielectric is a difficult task. Additionally, it is unknown whether there are other loss mechanisms at play, and all of these are very process-dependent. Therefore, generally values for these are just assumed, as above.

A possible alternate solution would be to split the Q of surface dielectric loss differently than q/p : we could move the unknown material parameters ϵ and t into q . This would leave only quantities we can calculate from the field profile (except for the term in the denominator which represents the energy stored in the surface dielectric; this is generally a very small fraction of the total energy and so would not affect the calculations appreciably). The resulting form for loss would be

$$Q^{-1} = \frac{p}{q} = \left(\frac{\epsilon t \int_{S_d} |\vec{E}|^2 dS}{\int_V \epsilon(\vec{x}) |\vec{E}|^2 dV} \right) \left(\frac{1}{1/\tan \delta} \right) = \left(\frac{\int_{S_d} |\vec{E}|^2 dS}{\int_V \epsilon(\vec{x}) |\vec{E}|^2 dV} \right) \left(\frac{1}{1/(\epsilon t \tan \delta)} \right) = \frac{G_E}{\Lambda}.$$

The advantage of this is that the p -equivalent electric geometric factor G_E once again can be calculated without any empirical constants, which are all contained in the q -equivalent “retaininess” Λ . It also removes the need for separately keeping track of ϵ , t , and $\tan \delta$, only the product of which actually affects our measurements, and which are likely highly process-dependent and not fundamental. The disadvantage is that G_E and Λ are not dimensionless (unlike p and q) and the natural scale for them is unclear. Additionally, the new form obscures somewhat the dependence of Λ on t , which can actually be measured for several types of surface layers.

Regardless of which form is chosen, we only need to know the electric field at the surface for a sufficiently thin layer (this also applies for the magnetic field and conductor loss). However, there is a subtlety for calculating the integrals for surface dielectric loss that is not generally present for bulk dielectric loss (unless there are very large field gradients present on complicated dielectric shapes). Since the dielectric is assumed to be very thin, and thus has a large ratio of length scales, it is challenging

to accurately simulate edges and corners of the material, where the simulation can diverge. There exists a two-step simulation method for these regions, in which a 2D cross-section is first simulated very finely, and the results are combined with a 3D simulation. For more details, see the supplement of [Wang et al., 2015] or chapter 5.7.1 of [Axline, 2018].

Two-level systems (TLS)

A common source of dielectric loss, particularly in surfaces, is coupling to **TLSs**. This is a phenomenological model which postulates the existence of a bath of **TLS** of varying parameters in a dielectric. By coupling to these **TLS**, the mode of interest can either experience an enhanced decay rate (in the case of incoherent **TLS**), or actual swaps with a coherent **TLS**. The microscopic origins of these systems are an open question of great interest [Müller et al., 2019, McRae et al., 2020b]; candidates include tunneling of atoms, changes of bonds, etc.

TLS have been studied in glasses for decades (e.g. [Phillips, 1987]), and have more recently become of interest in the superconducting quantum computing community [Martinis et al., 2005, Gao et al., 2008a]. The effect of **TLS** is generally expressed as an effective loss tangent which depends on temperature, frequency, and input power:

$$\tan \delta_{\text{TLS}} = \tan \delta_{\text{TLS}}^0 \frac{\tanh \frac{\hbar \omega}{2K_B T}}{\sqrt{1 + \left(\frac{\bar{n}}{n_c}\right)^\beta}}, \quad (2.6)$$

where $\tan \delta_{\text{TLS}}^0$ is the loss tangent at low powers at absolute zero, ω the resonance frequency, T the temperature, \bar{n} the number of photons stored in the resonator, and n_c is the critical number of photons at which saturation is achieved. β is a phenomenological parameter which is sometimes set to 1, and other times is placed over the entire denominator instead. Additionally, a participation ratio or filling factor is sometimes included in the definition; we shall keep this separate from $\tan \delta_{\text{TLS}}$ for

consistency with our participation model. It is important to note that this model is largely phenomenological: although it can be derived for coupling to a bath of two level systems, there is no particular mechanism known to be responsible for this.

There are other ways of writing the above equation: \bar{n}/n_c is occasionally written in terms of input power P_{in}/P_c or applied electric field $(E/E_c)^2$. These are physically equivalent descriptions and can be used interchangeably, depending on context. For example, for storing quantum information, we are generally interested in the $\bar{n} \approx 1$ regime, so we need to compare n_c to 1. For a given set of materials and fabrication methods, it appears likely that E_c is the quantity that remains constant, however. Therefore, the geometry of the resonator plays a large role in determining whether we are likely to reach saturation of the **TLS**: a large, more dilute mode will have a lower electric field for a given \bar{n} than a more compact mode. For this reason, a micromachined cavity has $n_c \approx 10^9$, while aluminium **CPW** resonators have $n_c \approx 10^3$, although the properties of the **TLS** themselves remain similar [Lei* & Krayzman* et al., 2020], Sec. 3.4.

Generally, the **TLS** parameters are assumed to be independent of temperature and power in our region of interest. However, there have been some indications that the critical power may vary with temperature, see [de Leon, 2021]. Neglecting this, we observe three primary tendencies for the **TLS**-induced loss:

1. It is constant in temperature for $T \ll \hbar\omega/(2K_B)$, and drops as $\sim 1/(2T)$ for $T > \hbar\omega/(2K_B)$. The transition temperature is around 200 mK for an 8 GHz resonator.
2. It drops as $1/\sqrt{1 + \left(\frac{\bar{n}}{n_c}\right)^\beta}$.
3. It increases with ω as $\tanh \hbar\omega/(2K_B T)$, that is, it is linear for $\omega < 2K_B T/\hbar$, and is constant for $\omega \gg 2K_B T/\hbar$.

The first two can be fairly easily measured in experiment, allowing us to fit for

the [TLS](#) parameters. The third is typically not a factor which can be varied in an experiment, but is necessary to consider in order to compare [TLS](#) loss between modes at different frequencies. An assumption that is commonly made is that all power-dependent loss in a resonator is caused by [TLS](#) loss, see e.g. [Calusine et al., 2018, Altoé*, Banerjee*, Berk*, Hadr* et al., 2022]. This is commonly paired with various assumptions about the location and origin of this loss; commonly, it is assumed that it comes from the dielectric surfaces, although sometimes all dielectric loss (including bulk) is blamed on [TLS](#).

I want to emphasise that these are assumptions, which, to my knowledge, have not been proven. For example, although conductor loss (Sec. 2.2.5) has not yet been observed to vary in power, seam loss (Sec. 2.2.6) has, as found in this thesis, see also [Brecht, 2017] section 7.5.2 for an extreme example. Although there have recently been several works examining surface oxides in relation to [TLS](#) [Premkumar et al., 2021, Murthy et al., 2022], no causative relationship or particular mechanism for this loss has been definitively identified. This is not to say that these assumptions are wrong or that the efforts are useless, I just wish to highlight that we are still in the relatively early stages of studying this topic, and further research is necessary before we can be confident.

2.2.5 Conductor Loss

Any currents driven through a metal present another potential source of loss, called conductor loss. In fact, normal metal microwave circuits are generally limited by this loss channel in particular, resulting in Q 's in the thousands. Although superconductors are commonly perceived to offer no electrical resistance at sufficiently low temperatures, there are a number of mechanisms through which losses can occur. For example, non-equilibrium quasiparticles can allow for more damping than expected from just the temperature, and trapped magnetic flux in the form of vortices with

normal cores (type-II) or intermediate state (type-I) provides an effective resistance (see e.g. [Gao, 2008] Sec. 2.4.2 for non-equilibrium quasiparticles, [Catelani et al., 2021] for a recent treatment of magnetic loss in type-I superconductors). There are also additional losses of unknown origin, which turn out to dominate conductive loss in our superconductive cavities. In this section, I shall describe the phenomenological model used to describe conductor loss, regardless of cause. For the relatively well-understood losses due to thermal quasiparticles, see section 2.3.1. See Table E.1 for a list of properties of superconductors used in this thesis.

An open question.

The source of conductive loss in our superconducting films is currently unknown. Thermal quasiparticles are almost non-existent at these temperatures (even if we take the temperature of the cavity to be that calculated from its average photon number), vortices due to magnetic fields are not sufficient [Catelani et al., 2021], as are non-equilibrium quasiparticles. Subgap states also do not appear to work. An understanding of this source of loss would be very helpful for designing lower-loss cavities and other superconducting microwave devices.

There are multiple ways of thinking about the conductor loss. I first present the purely phenomenological model. Losses in a superconductor arise from the magnetic fields that penetrate into the surface, assuming a form $H \propto e^{-z/\lambda}$ with z being depth and λ the penetration depth. Electric fields are essentially completely screened. As usual, we write the reciprocal Q as a ratio of p/q :

$$Q_{\text{cond}}^{-1} = \frac{1}{q_{\text{cond}}} \frac{\frac{1}{2} \int_{\text{surf}} \int_0^\infty e^{-z/\lambda} |H|^2 dz dA}{\frac{1}{2} \int_V |H|^2 dV} = \frac{1}{q_{\text{cond}}} \frac{\lambda \int_{\text{surf}} |H|^2 dA}{\int_V |H|^2 dV}, = \frac{p_{\text{cond}}}{q_{\text{cond}}} \quad (2.7)$$

where λ is the penetration depth of the superconductor. I note that the λ factor does not come from assuming a homogeneous $|H|$ up to a thickness of λ the way that dielectric thickness t appears in surface dielectric loss, it is instead the actual result of taking the integral. If the thickness of the superconducting film is not $\gg \lambda$, the

approximation of taking the upper limit of the integral as ∞ is no longer valid and we must appropriately change the calculation. Note also that, as with t and ϵ_r in surface dielectric loss, we have swept under the rug the fact that p_{cond} contains λ , a parameter which we actually need to measure for our conductor.

Another way to think about conductor loss is to consider the surface impedance of the conductor. The surface impedance Z_s is the ratio of the magnetic field to the electric field at the surface and takes the form

$$Z_s = R_s + iX_s = R_s + i\omega L_s, \quad (2.8)$$

where R_s and X_s are surface resistance and surface reactance, and L_s is surface inductance. For more details, see e.g. [Van Duzer and Turner, 1981], section 3.15, [Gao, 2008] section 2.2.3, or [Zmuidzinas, 2012]; see also [Pozar, 2011] section 1.7 for the general concept of surface impedance of a conductor.

We can now directly write down

$$Q_{\text{cond}}(T) = \omega \frac{U_{\text{tot}}}{P} = \omega \frac{\frac{1}{2} \int |\mathbf{B} \cdot \mathbf{H}| dV}{\frac{R_s(T)}{2} \int |\mathbf{H}|^2 dS} = \frac{\omega \mu \lambda_0}{R_s(T)} \frac{\int |\mathbf{H}|^2 dV}{\lambda_0 \int |\mathbf{H}|^2 dS}.$$

For power lost expression, see e.g. [Pozar, 2011], Eq. (1.97). Note that the only thing that depends on temperature is the surface resistance. Note that by analogy to the electric geometric factor G_E , we can define a magnetic geometric factor (called just G for consistency with other literature):

$$G = \omega \mu \frac{\int_V |H|^2 dV}{\int_S |H|^2 dS}, \quad (2.9)$$

allowing us to write

$$Q_{\text{cond}}^{-1} = \frac{R_s}{G}.$$

We now define the kinetic inductance fraction α , which represents the fraction of

total inductance that comes from the kinetic energy of the charge carriers (Cooper pairs for a superconductor). This is equivalent to p_{cond} . For clarity, α_0 will always be evaluated at zero temperature:

$$\alpha_0 \equiv \lambda_0 \frac{\int |H|^2 dS}{\int |H|^2 dV}. \quad (2.10)$$

We then notice that $X_s(0) = \omega\mu\lambda_0$ and that the second factor is just $1/\alpha$ from Eq. (2.10), giving

$$Q_{\text{cond}}(T) = \frac{1}{\alpha_0} \frac{X_s(0)}{R_s(T)}. \quad (2.11)$$

Again, note that the only term that depends on temperature is the surface resistance (recall that α is evaluated at zero temperature).

Another way to obtain is simply by observing that for a resonator of impedance $Z = R + jX$, the Q is given by $Q = \frac{X}{R}$. In our case, the total reactance X is just X_s/α , since $\alpha = L_k/L = X_s/X$, giving $Q = \frac{1}{\alpha_0} \frac{X}{R}$, as above.

We have now seen several equivalent ways of calculating conductor loss. I once again point out that fundamentally, the original source of the loss in our systems (whether expressed as q_{cond} or R_s) is unknown. For a normal metal, $q_{\text{cond}} = 1$, which can be seen from [Pozar, 2011] Eq. 1.61 and the text following. For our superconductors at frequencies of 5 GHz, q_{cond} is on the order of hundreds (for untreated machined high-purity aluminium) to tens of thousands (for high-quality thin films).

2.2.6 Seam Loss

Any joint between two conductors, even if they are made of the same material, creates a seam. This seam can be host to a number of imperfections – for example, surface oxides or contaminants, microscopic gaps, or mismatches in the crystal structure. These imperfections can result in loss of electromagnetic energy if a current is driven through them. Since the microscopic mechanisms for this loss are varied, and generally

not fully known for any particular system, we use an empirical model to describe seam loss. This section is based on [Brecht et al., 2015], see [Brecht, 2017] sec. 5.2.5 and [Reagor, 2015] sec. 4.2.4 for alternate descriptions.

We model the seam as a 1-D curve having a uniform conductivity g_{seam} (in units of $\Omega^{-1}\text{m}^{-1}$). The seam occurs at the joint of two superconducting 2-D surfaces, so the only current that results in loss is the component that is crossing the seam – any current flowing parallel to the seam is shorted out by the superconductor. Recall that conductivity is proportional to cross-sectional area, and inversely proportional to the length of the object *along the direction of the current*. In the case of a seam, the “length” is therefore generally a quite small dimension, and is what we would normally think of as a “width” of the seam. Therefore, the conductance of a segment of the seam with is proportional to its length. For a segment of length Δl , the conductance is $g_{\text{seam}}\Delta l$. The power dissipated in this segment from a surface current having component J_{\perp} crossing the seam is, from Ohm’s law,

$$\Delta P = \frac{1}{2}I^2R = \frac{1}{2}\frac{J_{\perp}^2\Delta l^2}{g_{\text{seam}}\Delta l},$$

where I and J_{\perp} are the maximum values, giving the $\frac{1}{2}$ when averaged over the whole cycle. Taking the limit $\Delta l \rightarrow 0$ and integrating, we obtain the total power dissipated:

$$P = \frac{1}{g_{\text{seam}}} \int_{\text{seam}} \frac{1}{2}(J_{\perp}(\vec{x}))^2 dl = \frac{1}{g_{\text{seam}}} \int_{\text{seam}} \frac{1}{2}|\vec{J}_s \times \hat{l}|^2 dl.$$

Finally, substituting this into the definition of Q , we obtain the internal Q from seam loss (written in the reciprocal for easy comparison to the participation model)

$$\frac{1}{Q_{\text{seam}}} = \frac{P}{\omega E_{\text{tot}}} = \frac{1}{g_{\text{seam}}} \frac{\int_{\text{seam}} |\vec{J}_s \times \hat{l}|^2 dl}{\omega \int \vec{H} \cdot \vec{B} dV} \equiv \frac{y_{\text{seam}}}{g_{\text{seam}}}, \quad (2.12)$$

where the $\frac{1}{2}$ cancel, as usual. y_{seam} is the admittance into the seam per unit length,

with units $\Omega^{-1}\text{m}^{-1}$, and is thus defined to be

$$y_{\text{seam}} = \frac{\int_{\text{seam}} |\vec{J}_s \times \hat{l}|^2 dl}{\omega \int \vec{H} \cdot \vec{B} dV}. \quad (2.13)$$

As mentioned above, y_{seam} takes the role of the participation-like quantity: it represents how much the seam contributes to the mode and can be calculated from the geometry of the structure (albeit, it is not dimensionless). Similarly, g_{seam} is the q-like quantity: it is reciprocal to the lossiness and must be measured empirically.

We can obtain an alternate form for the above expressions by noting the interface condition for magnetic fields:

$$\vec{J}_s = \hat{n} \times (\vec{H}_2 - \vec{H}_1).$$

Since we generally initially calculate the mode structure assuming the superconductor perfectly expels all magnetic fields and then add penetration in as a perturbation, we can neglect \vec{H}_2 (this would break if the field inside the superconductor were relatively large, e.g. if penetration depth is not small compared to the linear dimensions of the mode). To get J_{\perp} , use the component of \vec{H} parallel to the seam \vec{H}_{\parallel} :

$$J_{\perp} = |\hat{n} \times \vec{H}_{\parallel}|,$$

which can then be substituted into Eq. 2.13 to obtain

$$y_{\text{seam}} = \frac{\int_{\text{seam}} |\vec{H}_{\parallel}|^2 dl}{\int \vec{H} \cdot \vec{B} dV}. \quad (2.14)$$

An important assumption made in this analysis is that we know the actual location of the seam. In reality, it is not always clear where the current will flow. For example, two halves of a bulk-machined rectangular cavity meet at a 2-D surface. We assume

that the seam is located at the innermost part of this surface, where the two inner faces of the cavity meet. However, if the two mating surfaces are sufficiently rough, the actual points of contact could be farther away (and likely do not form a continuous line). Since the scale of the roughness is microscopic, it is typically not possible to determine the location of the actual seam and incorporate it into g_{seam} – instead, g_{seam} is calculated as if the seam were in its designed location, and all the variance is attributed to y_{seam} . This can result in large variances in the measured seam quality.

One way to mitigate this is by incorporating an indium seal: a groove is machined into one of the surfaces, just around the edge. Indium wire is placed into this groove (which is designed to not be able to fully fit the whole volume of indium). The two pieces are then pressed together and bolted, compressing the indium and ensuring that the seam cannot be outside of this line of indium. This also improves the actual quality of the seam, as the compressed indium forms a better contact than solid metal surfaces. Other types of gasket (e.g. knife-edge, etc.) are also possible.

An even more complicated situation arises when the joint occurs at a 3-D object. For example, as we shall see in a later section, one way to make contact between two superconducting surfaces is by placing an indium bump (more commonly many indium bumps) between them. The individual bumps are roughly cubic, so their lateral dimensions cannot be neglected. The question of where the current flows becomes even more non-trivial in this situation. Since the goal of the model is to avoid microscopics, we choose the seam line in a way that is minimally-dependent on the details of the bumps: for a single bump, we assume the seam has length of one side of the bump; for a bump array, we assume a contiguous path along the innermost bumps. As long as we are consistent in terms of how we define the seam, we can use our model to compare different devices and make predictions for new devices. A different definition (e.g., picking the perimeter of a bump) would result in the y_{seam} and g_{seam} changing by the same amount, leaving the Q unchanged.

Finally, I note that seam losses can appear in unexpected places, and one needs to be careful to account for them. One example is seam loss in the packaging: even if the device itself does not have a seam, if the mode of interest (or another mode which can couple to it!) has some participation in the walls of the package, which is generally conductive, seam loss can become important. Additionally, devices made in multiple fabrication steps or with additional conductive features, e.g. wirebonds, can suffer from seam losses at the contacts between the different metals/steps. In summary, any time one is worried about losses in a superconducting microwave system, it is worth considering possible losses from any contacts between two distinct conductors.

2.2.7 Beyond the Participation Ratio Model

The participation ratio model described above allows us to understand, and to an extent, predict losses in superconducting resonators. However, as with any model, it is only valid in certain situations and given certain assumptions. Our recent work on multi-mode resonators (see chapter 5 for more details) has allowed us to probe our assumptions more carefully, and to make measurements which are sensitive enough to see discrepancies in the model. In brief, we make resonators with more modes than loss channels, with each mode having different participations. This would allow us to extract the different q 's using only one physical device.

However, what we frequently see instead is that the equations describing the losses are inconsistent, if we use errors of 1-2% on Q , which is the uncertainty of a Q for a single device during a single cooldown. If we assume large errors (e.g. 10-20%), the equations can be made consistent again, but this error is more appropriate for device-to-device variation, and thus precludes us from learning information about the particular device we are currently measuring (as compared to other, nominally identical devices). This prompts us to re-examine the assumptions made in the model. The main suspect is the assumption that the material properties of a single loss

channel are homogeneous. If, for example, part of the conductive surface is lossier than the rest, then the conductive contribution to the Q would no longer be correctly described by the model. There are multiple ways to deal with the situation. One is to assign wider uncertainties to the parameters and/or measured values, e.g. assume we know p_{cond} only to 50%, or that we have measured Q only to 20%. This gives more room for the equations to be made consistent. Depending on the meanings of the uncertainties one assigns, this would carry a different interpretation of the results of the measurement.

Another possibility is to weaken the homogeneity assumption. One way to do it is to split the loss channels into several regions and treat them separately, although it is generally not clear exactly how to do this. For example, in a bulk-machined piece, one may hypothesise that surfaces that were machined in different ways (e.g. milled vs. drilled, etc.) may have different properties. However, it could also be the case that the inhomogeneities are simply due to random distributions of whatever causes loss. One possible way to assess this would be to fabricate a resonator with a very low fundamental frequency, allowing us to measure a very large number of modes which have different participations in different parts of the resonator. The results could then be correlated with more advanced materials-style surface measurements of lower-quality areas (e.g. x-ray or [transmission electron microscopy \(TEM\)](#) measurements) to see whether any pattern can be found.

2.3 Variations in Temperature

Let us now discuss the ways in which the loss mechanisms are affected by the one of the two tuning knobs easily accessible in our experiments, temperature (the other being input power). Of the aforementioned mechanisms, two are known to have an explicit temperature dependence: [TLS](#) loss (as described in section 2.2.4) and

conductor loss (as described in the following section). The other loss mechanisms have no known temperature dependence, and in fact, are sometimes assumed to be explicitly temperature-independent in order to make measurements of **TLS** and/or conductor loss. A superconducting microwave resonator which is at least partially limited by **TLS** loss and has a sufficiently high T_c will behave qualitatively like the one in Fig. 2.3: as temperature is increased from base, the Q will first increase somewhat, due to the **TLS**'s saturating; then, the Q will start falling as thermal quasiparticles become more prevalent. A more complicated behaviour has been observed in one study, in which there is a brief initial drop in Q prior to the **TLS** saturation [de Leon, 2021]. This is thought to arise from changing saturation powers of the **TLS**'s, although to the author's knowledge, there is no confirmation of this explanation.

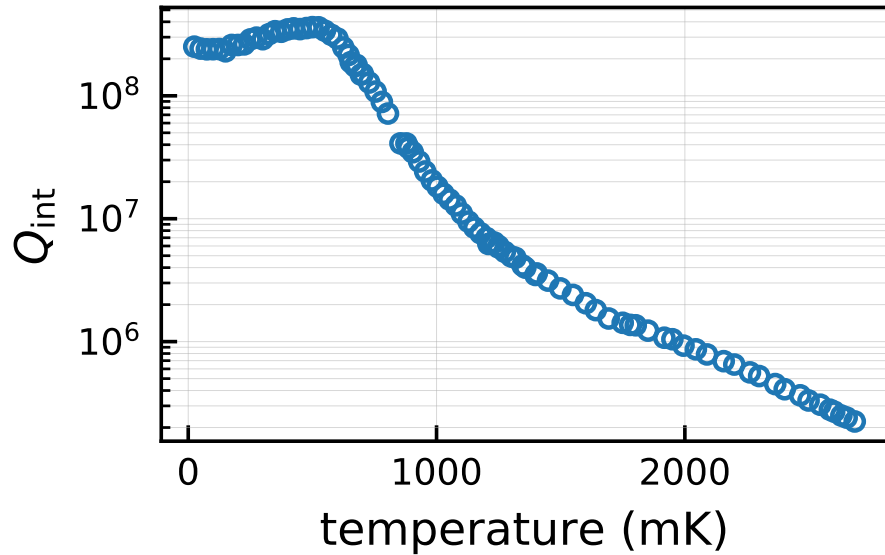


Figure 2.3: A sample temperature sweep of a **TLS**-sensitive superconducting microwave resonator. The **TLS** is seen to saturate at around 500 mK, followed by a decrease in Q due to thermal quasiparticles. This particular resonator is made of indium, and thus has a $T_c \approx 3.4$ K. Note that this 3-D cavity resonator is not strongly limited by **TLS**—some resonators (typically planar) will increase Q by an order of magnitude between unsaturated and saturated.

2.3.1 Conductor Loss

In this section, I briefly overview Mattis-Bardeen theory for thermal quasiparticle-induced conductor loss. This is by no means intended to be a complete derivation or treatment. The original paper is [Mattis and Bardeen, 1958] (see also [Abrikosov et al., 1959]), [Brecht, 2017, Reagor, 2015, Zmuidzinas, 2012] provide brief coverage, [Gao, 2008, Pöpel, 1989, Turneaure et al., 1991, Gittleman and Rosenblum, 1964, Walsh and Tomaselli, 1990] review the subject more thoroughly, and [Nam, 1967] derives expressions for conductivity and impedance.

Mattis-Bardeen theory allows us to describe the response of a superconductor to an applied electromagnetic field via the surface impedance Z_s . For a regular conductor, surface impedance can be found from simple Ohm's law. For a good conductor with a very large electron mean free path (e.g. at high frequencies and low temperatures), we need to modify this to allow the current to depend on the electric field within some volume, making the new equation non-local. Pippard extended this to superconductors by phenomenologically introducing the coherence length ξ_0 as the scale over which fields decay [Pippard, 1953]. In the Mattis-Bardeen work, this is replaced with the Mattis-Bardeen kernel obtained from [Bardeen-Cooper-Schrieffer theory of superconductivity \(BCS\)](#), which crucially includes the superconducting gap. This results in a fairly involved integration to obtain \vec{J} . The resulting equation can then be used to obtain the surface impedance numerically, as in [Gao et al., 2008a].

More explicitly, with some assumptions, we can write down an updated version of Ohm's law:

$$\vec{J} = \sigma \vec{E} = (\sigma_1 - i\sigma_2) \vec{E}$$

where the conductivity is now a complex quantity [Glover and Tinkham, 1957] given

by [Mattis and Bardeen, 1958]:

$$\frac{\sigma_1(\omega, T)}{\sigma_n} = \frac{2}{\hbar\omega} \int_{\Delta(T)}^{\infty} \frac{[f(E) - f(E + \hbar\omega)](E^2 + \Delta(T)^2 + \hbar\omega E)}{\sqrt{E^2 - \Delta(T)^2} \sqrt{(E + \hbar\omega)^2 - \Delta(T)^2}} dE + \frac{1}{\hbar\omega} \int_{\Delta(T)-\hbar\omega}^{-\Delta(T)} \frac{[1 - 2f(E + \hbar\omega)](E^2 + \Delta(T)^2 + \hbar\omega E)}{\sqrt{E^2 - \Delta(T)^2} \sqrt{(E + \hbar\omega)^2 - \Delta(T)^2}} dE \quad (2.15a)$$

$$\frac{\sigma_2(\omega, T)}{\sigma_n} = \frac{1}{\hbar\omega} \int_{\max(\Delta(T)-\hbar\omega, -\Delta(T))}^{\Delta(T)} \frac{[1 - 2f(E + \hbar\omega)](E^2 + \Delta(T)^2 + \hbar\omega E)}{\sqrt{\Delta(T)^2 - E^2} \sqrt{(E + \hbar\omega)^2 - \Delta(T)^2}} dE, \quad (2.15b)$$

where $f(E)$ is the distribution of quasiparticles; if they are in thermal equilibrium at temperature T , then it is given by the standard Fermi-Dirac distribution

$$f(E) = \frac{1}{1 + e^{E/(k_B T)}}.$$

$\Delta(T)$ is the superconducting gap at temperature T , which shall be addressed soon. σ_n is the normal-state conductivity right above T_c . Note that it is likely that we have some level of non-thermal quasiparticles (see e.g. [Houzet et al., 2019] as an example mechanism). In general, these are thought to come from higher-energy radiation coming in either through non-light-tight connections, or insufficiently filtered microwave lines.

Let us now make several remarks regarding Eq. 2.15. In writing these expressions, I have been careful to explicitly write out which terms are dependent on temperature. The second term in Eq. 2.15a is only to be evaluated in the case that $\hbar\omega > 2\Delta(T)$. Although for e.g. a typical aluminium resonator of $\omega = 2\pi \times 5 \text{ GHz}$ $\hbar\omega$ is about 10 times lower than Δ_0 , it is important to note that this is no longer true if we try to fit for temperatures sufficiently close to T_c , since $\Delta(T)$ drops to 0! We must also be careful about the signs of the square roots. We also note that these expressions give σ_1 , σ_2 in terms of σ_n , so we need to know it to get the scaling factor. These

expressions depend on no other parameters of the superconductor except the gap, which itself is fairly general, as discussed below. Finally, we provide commonly-used approximations for σ : if 1) $k_B T \ll \Delta(T)$ and 2) $\frac{E}{k_B T} \gg 1$ (the second condition is equivalent to assuming there is not an occupation much larger than 1), then σ can be approximated as [Gao et al., 2008b]

$$\frac{\sigma_1(\omega, T)}{\sigma_n} \approx \frac{4\Delta(T)}{\hbar\omega} e^{-\frac{\Delta(T)}{k_B T}} \sinh\left(\frac{\hbar\omega}{2k_B T}\right) K_0\left(\frac{\hbar\omega}{2k_B T}\right) \quad (2.16a)$$

$$\frac{\sigma_2(\omega, T)}{\sigma_n} \approx \frac{\pi\Delta(T)}{\hbar\omega} \left[1 - 2e^{-\frac{\Delta(T)}{k_B T}} \exp\left(-\frac{\hbar\omega}{2k_B T}\right) I_0\left(\frac{\hbar\omega}{2k_B T}\right) \right] \quad (2.16b)$$

with I_0 , K_0 being modified Bessel functions of the first and second kind, respectively. Note that the first condition breaks down at sufficiently large T , as $\Delta(T)$ must go through 0 at $T = T_c$. See Fig. 2.4 for a comparison of these approximations to the exact solution.

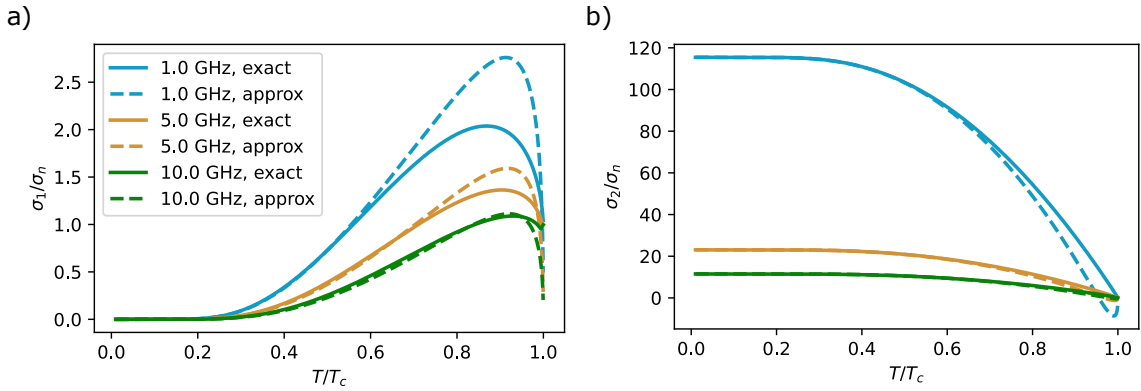


Figure 2.4: The two parts of complex conductivity, calculated via Eq. 2.15 (“exact”, solid lines) compared to the approximations in Eq. 2.4 (“approx”, dashed lines), at three different frequencies. a) is the real part σ_1/σ_n , b) is the imaginary part σ_2/σ_n . The T_c is chosen to be 1 K. We observe that the approximation works for low T/T_c , but starts to break down at higher temperatures. Note also that at $T = 0$, for $\hbar\omega < 2 * \Delta_0$, $\sigma_1 = 0$: there is no absorption without quasiparticles, unless the photons have energy to break apart a Cooper pair.

Let us now discuss the gap $\Delta(T)$. This is a pretty standard calculation which can be found in superconductivity textbooks, e.g. [Tinkham, 2015] section 3.6 or

[Van Duzer and Turner, 1981] section 2.11. I shall only quote the main results. The temperature dependence of the gap is expressed implicitly by the integral equation (Eq. 3.27 in the original **BCS** paper [Bardeen et al., 1957])

$$\frac{1}{N(0)V} = \int_0^{k_B\Theta_D} \frac{\tanh\left(\frac{1}{2}\sqrt{\xi^2 + \Delta(T)^2}/(k_B T)\right)}{\sqrt{\xi^2 + \Delta(T)^2}} d\xi, \quad (2.17)$$

where $N(0)$ is the density of states at the Fermi level, V is the interaction strength of the potential in the **BCS** theory, Θ_D is the Debye temperature of the metal (and therefore $k_B\Theta_D/\hbar$ is the Debye frequency, which is the cutoff for the integral). $N(0)V$, Θ_D and T_c can be looked up in a table for a given material, but we can do better: by setting $T = T_c$ and $\Delta(T_c) = 0$ in Eq. 2.17, we can analytically solve the integral and obtain a self-consistency relation, allowing us to eliminate one of the parameters (note that this assumes weak coupling, $2T_c \ll \Theta_D$ which is true for e.g. Al, but *not* as true for e.g. Nb), see. Eq. 3.27 in [Bardeen et al., 1957]:

$$\frac{1}{N(0)V} = \ln \frac{4e^\gamma \Theta_D}{2\pi T_c},$$

where γ is the Euler-Mascheroni constant, $e^\gamma \approx 1.78$. We can now plug the result into Eq. 2.17 to obtain an implicit integral equation for $\Delta(T)$. Via u-substitution, it can easily be seen that this equation scales linearly in Δ_0 , the gap at zero temperature, as well as T_c , which means that we obtain an equation for $\Delta(T)/\Delta_0$ vs. T/T_c as a function of only one parameter, Θ_D , and since the integrand becomes small at large ξ , the function depends quite weakly on the exact value of Θ_D . Thus, the scaled gap vs. scaled temperature is quite similar for different weak-coupling superconductors; see Fig. 2.5. Finally, let us note some useful limits: for small T/T_c (see e.g. [Gao

et al., 2008a] Eq. 2.53),

$$\frac{\Delta(T)}{\Delta_0} \approx 1 - \sqrt{2e^\gamma T/T_c} \exp\left(-\frac{\pi}{e^\gamma T/T_c}\right),$$

demonstrating a difference from 1 exponentially suppressed in $e^{-\frac{\Delta}{k_B T}}$. This is due to the fact that there are essentially no thermally-excited quasiparticles until T gets large enough, due to the Fermi-Dirac distribution.

For $T/T_c \lesssim 1$ (e.g. [Tinkham, 2015] Eq. 3.54),

$$\frac{\Delta(T)}{\Delta_0} \approx 1.74 \sqrt{1 - \frac{T}{T_c}}.$$

A note on the constants.

In the above equations, we have assumed theoretical values for many physical properties. For example, BCS gives us $\Delta_0 = \frac{\pi}{e^\gamma} k_B T_c \approx 1.76 k_B T_c$. In reality, these values can vary depending on material, and some of the other properties may depend on e.g. temperature. One need look no further than the back cover of [Van Duzer and Turner, 1981] to see variations in Δ_0/T_c . One must be careful even with the tabulated values, however, since there is no such thing as “aluminium” – the properties will depend on the exact composition (alloy vs. pure), thickness of superconductor, process in which it was prepared, and conditions under which it was measured. Therefore, if one really needs precise values, then one should carefully read the source papers for these properties and determine whether the conditions are sufficiently similar; even better is to measure the properties, although of course this is much more difficult. One can instead just keep in mind that a lot of the numbers in the above equations may not be exactly applicable to one’s situation.

Now that we have $\Delta(T)$, we can use it to calculate σ from Eqs. 2.15. In practice, these equations are somewhat computationally expensive. Numerical issues in the calculation of $\Delta(T)$ at both small and large T/T_c force us to split the evaluation into three regions, with the approximation regions being calculated directly, and the middle region being pre-computed and used as a spline. σ is even more expensive to compute, so also pre-compute the values and store them into tables. Luckily,

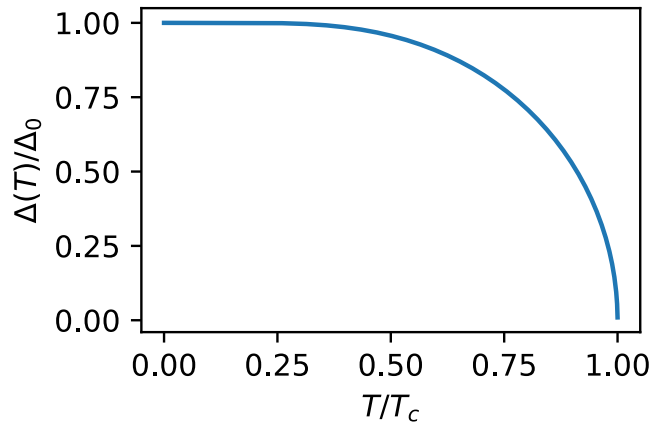


Figure 2.5: Superconducting gap scaled by the gap at zero temperature, vs. temeprature scaled by T_c . The shape is mostly universal for weak-coupling superconductors: there is a weak dependence on the Debye temperature, but it is not really visible unless it is changed drastically. Of interest are the fact that the gap does not really drop below Δ_0 until at least around $T_c/3$, and the fact that near T_c , it is falling almost vertically.

$\Delta(T/T_c)/\Delta_0$ is fairly quick to generate for a particular material (with only Θ_D as a parameter), and σ is universal for weak-coupling superconductors, as long as the appropriate substitutions are performed.

Having obtained the complex conductivity, we have one step remaining: using it to compute measurable quantities. In our case, the quantity in which we are interested is surface impedance (see section 2.2.5). This is not a trivial task. It is possible to obtain and numerically solve equations for $Z_s = R_s + iX_s = R_s + i\mu_0\omega\lambda_{\text{eff}}$ in a fairly general case (still depending on assumptions about boundary conditions), see e.g. [Gao et al., 2008a] section 2.2. We shall not attempt to do this, but just state the results for several limiting cases, in which a closed-form solution can be obtained [Zmuidzinas, 2012].

- For thick films, with thickness $t \gg \lambda_{\text{eff}}$:
 - In the local (also called dirty) limit, $\xi_0 \ll \lambda_{\text{eff}}$ or $l \ll \lambda_{\text{eff}}$, this takes the

form

$$Z_s(\omega, T) = Z_s(\omega, 0) \sqrt{\frac{i\sigma(\omega, T)}{\sigma_2(\omega, 0)}} = \sqrt{\frac{i\mu_0\omega}{\sigma(\omega, T)}}, \quad (2.18)$$

which has the same form as for a regular conductor except with our complex conductivity. Note that $\sigma_2(\omega, 0) = \frac{\pi\Delta_0}{\hbar\omega}$, as can be seen easily from Eq. 2.16b. Since $Z_s(\omega, 0) = i\mu_0\omega\lambda_0$, we can see that $\lambda_0 = \sqrt{\frac{\hbar}{\pi\Delta_0\mu_0\sigma_n}}$. Examples of this case are plotted in figure 2.6.

- In the extreme anomalous (clean) limit, $\xi_0 \gg \lambda_{\text{eff}}$ and $l \gg \lambda_{\text{eff}}$, we obtain

$$Z_s(\omega, T) = i\mu_0\omega\lambda_0 \left[\frac{\sqrt{3}l}{2\pi\lambda_0} \right]^{1/3} \left(\frac{i\sigma(\omega, T)}{\sigma_2(\omega, 0)} \right)^{1/3}. \quad (2.19)$$

- For thin films, with $t \ll \lambda_{\text{eff}}$, in the local case:

$$Z_s(\omega, T) = \frac{1}{\sigma(\omega, T)t}. \quad (2.20)$$

For all the cases, the following holds:

$$\frac{\delta Z_s(\omega, T)}{Z_s(\omega, 0)} = \gamma \frac{\delta\sigma(\omega, T)}{\sigma(\omega, 0)}, \quad \gamma = \begin{cases} -1/2 & \text{thick film, local limit} \\ -1/3 & \text{thick film, extreme anomalous limit} \\ -1 & \text{thin film, local limit} \end{cases} \quad (2.21)$$

We can use the impedance to find the expected changes in frequency and Q with temperature. I shall reproduce Eq. 2.54 of [Gao et al., 2008a] here, as this is what we use:

$$\frac{f(T) - f(0)}{f(0)} = -\frac{\alpha_0}{2} \frac{X_s(T) - X_s(0)}{X_s(0)} \quad (2.22a)$$

$$\frac{1}{Q_{\text{cond}}(T)} - \frac{1}{Q_{\text{cond}}(0)} = \alpha_0 \frac{R_s(T) - R_s(0)}{X_s(0)} \quad (2.22b)$$

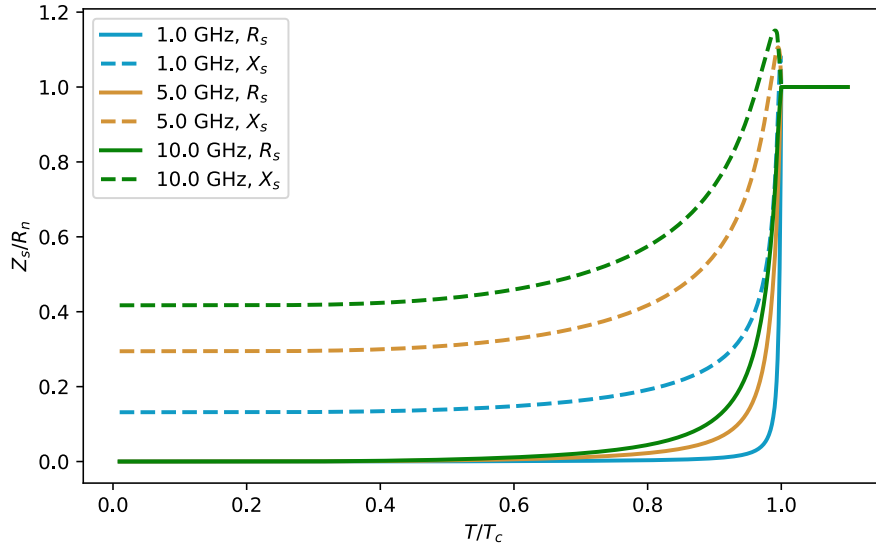


Figure 2.6: A plot of the real (solid) and imaginary (dashed) components of the surface impedance at three frequencies for a tick film in the local limit. Note that for $T > T_c$, $X_n = R_n$, as the Q_{cond} of a normal metal is 1.

Note that $R_s(0)$ should be effectively 0 due to Mattis-Bardeen, however we have some unexplained surface resistance which makes $Q_{\text{cond}}(0) \neq \infty$. We can then use Eq. 2.22 to fit our measured resonator parameters as a function of temperature. Since most of the theory describing the temperature change is fairly universal, we can do this fairly well with only two fit parameters: T_c and α_0 . Recalling our discussion of p_{cond} from earlier, note that since this method provides a way to measure α_0 , we have a way of validating our assumptions about λ_0 . In particular, if we simulate a value p_{cond} using λ_{sim} as our penetration depth and then obtain α_0 from the fit, we know that the true penetration depth λ_0 is given by

$$\lambda_0 = \lambda_{\text{sim}} \frac{\alpha_0}{p_{\text{cond}}}. \quad (2.23)$$

2.4 Designs of superconducting microwave resonators

2.4.1 Requirements and Wish List for a Good Resonator

There are several features which we must have, and several features which we would like to have in a good resonator for storing quantum information. Some of this has already been expressed earlier, but we now collect and summarise the main points.

The **requirements** are:

1. A linear drive. We must be able to excite the resonator (by driving it with a microwave tone), thereby displacing the mode.
2. A coupling to a non-linear system for control. A linear drive on its own can only generate classical states, which one can understand by considering that all of the transitions have the same energy difference. In order to be able to generate quantum states and perform quantum operations we thus need a sufficiently strong coupling to a non-linear system, which can dress the resonator states and split the transitions.

The **desires** are:

1. Long lifetime relative to operation speed. As mentioned in section 2.1.2, the concept of “lifetime” is somewhat ambiguous. In general, the longer, the better, as long as we can keep the operation speed constant (of course, in the long term, faster operation speed for a given lifetime is also desirable, as this would make the computations run in less time).
2. Modularity. We would like to be able to make our devices of several parts, rather than into one monolithic block. This allows us to interchange parts, whether due to failure or simply a need for different properties, without re-making the entire system. It also allows us to lower single-device yield requirements, since

you only need all the pieces of one module to work together at the same time, not of the whole system.

3. Scalability. We need our devices to be made in way which will work for the many thousands (or millions!) of resonators we will need for a fully-functional quantum computer. We also need for the rest of the circuitry, including interconnects, to be compatible with such large numbers of elements.

2.5 Measuring the Properties of a Resonator

We conclude this chapter with a section on how we actually measure our resonators. Our methods fall into two main categories: spectroscopy (frequency-domain measurement) and time-domain measurements. For all of the following, the resonator shall be anchored securely to the mixing plate of a dilution refrigerator cooled to its base temperature of 15-20 mK. All of the communication with the resonator will be carried out through coaxial microwave cables ([SubMiniature version A \(SMA\)](#), in our case).

2.5.1 Frequency-domain

One way to measure the resonator is via spectroscopy, or frequency-domain measurements. These are generally carried out with a [vector network analyser \(VNA\)](#) (although this is not a requirement). The resonator is hooked up in one of the following configurations (see Fig. 2.7), and the appropriate S-matrix elements are measured (see. e.g. [[Pozar, 2011](#), [Collin, 2001](#)]) while frequency is swept around the resonance. The results are fit to a model as described in each subsection.

If we wish to obtain the internal Q or lifetime of the resonator, we need to make sure that it is not strongly overcoupled, that is, avoid the situation where $Q_c \ll Q_i$, as in that case, the internal losses of the resonator will be difficult to distinguish compared to the much larger losses through coupling, see section 2.2.2. In practice,

for $Q_c > Q_i/10$ or so, we can generally get a decent idea of Q_i , although of course $Q_c \gtrsim Q_i$ is preferable. If $Q_c \gg Q_i$, it can become difficult to find the mode at all, so care must be exercised in designing the strength of one's coupling. If the above is followed, it is generally possible to fit for the frequency f_r , as well as Q_i and Q_c of the resonator. In the following, we use a particular model for the shape of the resonance, which we then fit to a circle. The model itself can be derived from a circuit representation [Petersan and Anlage, 1998, Khalil et al., 2012, Probst et al., 2015, Gao et al., 2008a], or with input-output theory, e.g. [Chen et al., 2022]. We shall use the circle-fitting approach from [Probst et al., 2015], adjusted appropriately.

Reflection

In reflection, a microwave tone is sent to the resonator, and the reflected power is measured. In room-temperature measurements, the same physical port and transmission line can be used for this, e.g. via measuring S_{11} on a **VNA**. In cryogenic measurements, the input line needs heavy attenuation, and since we frequently measure down to single-photon powers, the output line has a lot of amplification. For this reason, the reflected signal is usually directed to a separate output chain via a circulator or a directional coupler. Although this setup has us measuring e.g. S_{21} on the **VNA**, it is still exactly the same measurement.

The measured signal is thus reflected power vs. frequency. For the simple case depicted in Fig. 2.7 a), the amplitude of the signal takes a Lorentzian shape, while the phase is a sigmoid. We can understand this in the following way: when the signal is far off-resonant, the impedance of the resonator goes to 0, with sign depending on which direction we go (the inductor shorts to ground at low frequencies, the capacitor – at high frequencies). All the signal therefore reflects from the impedance mismatch, giving $|S_{11}| = 1$, while the phase changes sign. What happens on resonance depends on the ratio between Q_c and the internal Q of the resonator, $Q_i = R\sqrt{\frac{C}{L}}$. There are

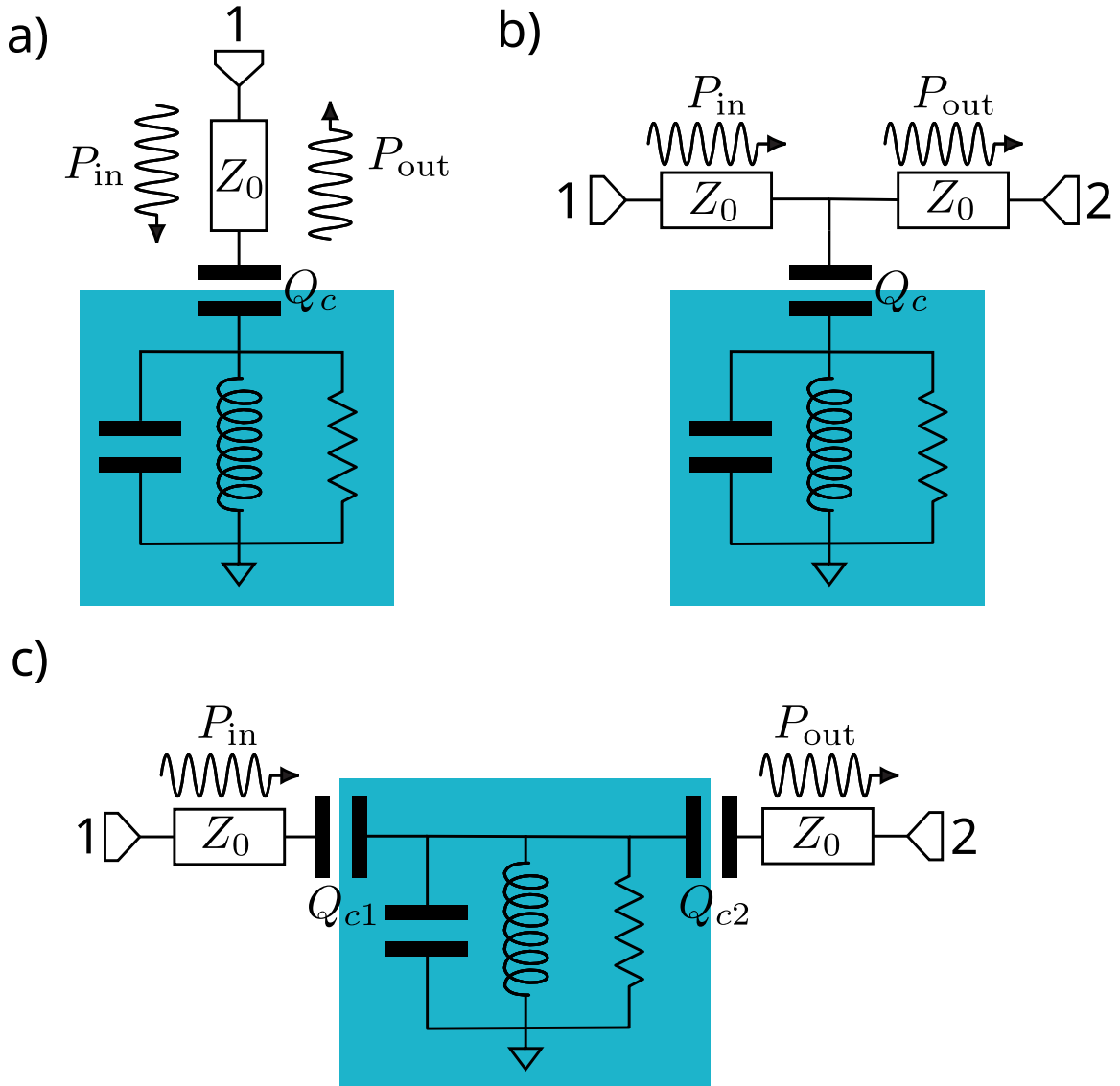


Figure 2.7: The three main circuit configurations used to measure a microwave resonator: a) Reflection: a signal is sent from port 1, reflects from the resonator, and returns to port 1. In cryogenic measurements, two different lines are generally needed for the input and output, with a circulator or directional coupler routing the reflected signal to the output chain. b) Hanger: a signal is sent from port 1, encounters a shunt to ground through the resonator via a tee, and continues to port 2. Several resonators can “hang” between the ports, allowing for easy multiplexing. c) Transmission: a signal is sent from port 1, travels through the resonator and to port 2. The resonator is marked in blue in all three diagrams. a) and b) have one coupling capacitance Q_c , c) has two – Q_{c1} and Q_{c2} . The transmission lines connecting the resonator to the ports have characteristic impedance Z_0 (we do not consider the case that the two lines present in b) and c) are different, since in practice, they are almost always $50\ \Omega$).

three relatively straightforward cases:

- The resonator is strongly undercoupled, $Q_c \gg Q_i$. In this case, it is as if the resonator were not there at all, and the signal is just reflected back. Such a resonator will be very difficult to find in magnitude. Searching in phase might help, although this still only works up to a degree, at some point the resonator is just too undercoupled to see.
- The resonator is strongly overcoupled, $Q_c \ll Q_i$. In this case, energy will travel into the resonator much faster than the resonator can dissipate it, meaning that it will still reflect, although with the opposite sign.
- The resonator is approximately critically coupled, $Q_c \approx Q_i$. The energy travels into the resonator at the same rate as the resonator dissipates it, meaning there is little reflection.

There are also several non-idealities which can affect the form of the reflected signal. The full $S_{11}(f)$ for reflection is given by:

$$S_{11}(f) = ae^{i\alpha}e^{-2\pi if\tau} \left[1 - \frac{2Q_l/|Q_c|e^{i\phi}}{1 + 2iQ_l(f/f_r - 1)} \right]. \quad (2.24)$$

The non-ideality parameters are as follows: a is the total attenuation/gain of the signal chain, α – a constant phase shift, τ – the electrical delay due to the cables (which causes a frequency-dependent phase shift, and ϕ is the asymmetry of the resonance, which is equivalent to a complex phase of Q_c ($Q_c = |Q_c|e^{-i\phi}$). The exact cause of $\phi \neq 0$ is described somewhat differently in different publications; in general, it is attributed to some impedance mismatches or reflections in cables. f_r is the resonance frequency of the resonator, and $Q_l^{-1} = Q_i^{-1} + \Re(Q_c^{-1})$.

Except for the $e^{-2\pi if\tau}$ term, the S_{11} function is most of a circle on the complex plane. We shall now briefly examine what the different parts of the function do,

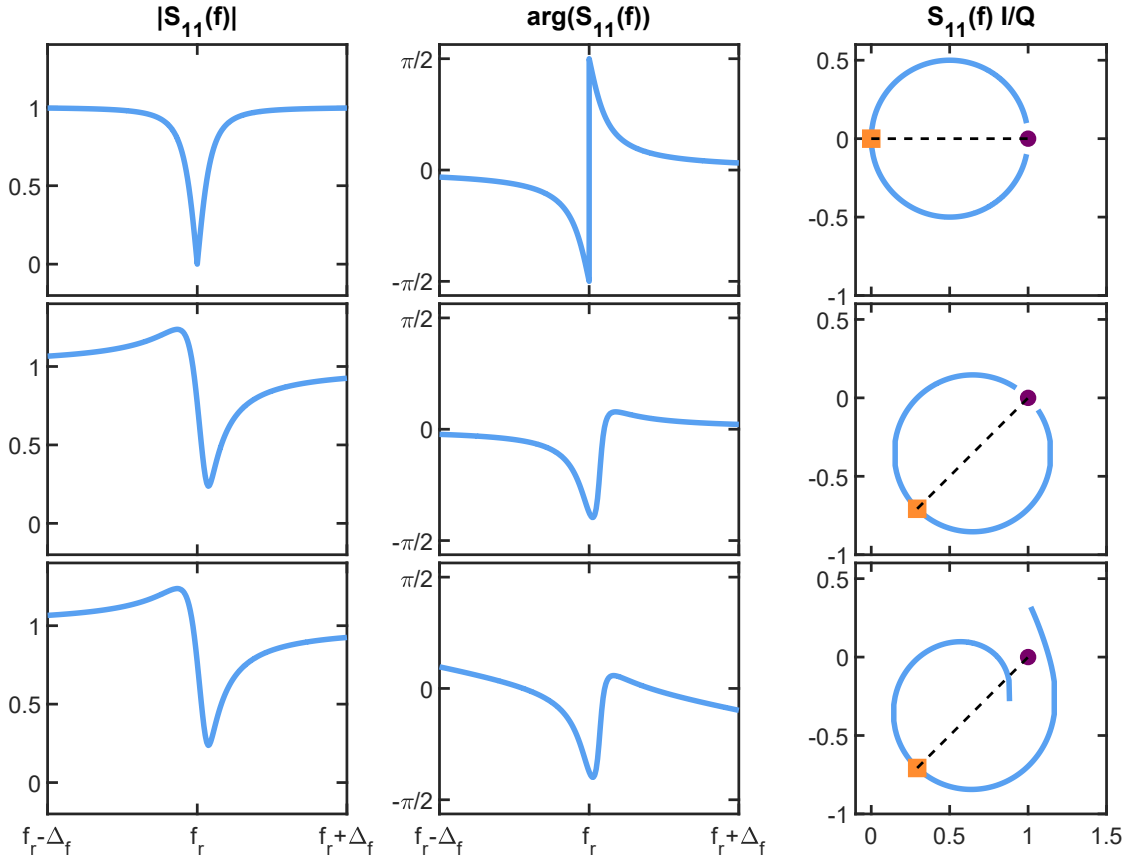


Figure 2.8: A simulated sample reflection measurement. The leftmost column is $|S_{11}(f)|$, the middle column is $\arg S_{11}(f)$, the rightmost column is S_{11} in the complex (I/Q) plane. In the I/Q plane plots, the orange square is the point on resonance, and the purple circle is the infinite-frequency limit point. The dashed line connecting them is a visual guide for the angle. The first row is an ideal, critically-coupled resonator of $Q_i = Q_c = 10^6$, $f_r = 5 \times 10^9$. The second row adds an asymmetry of $\phi = \pi/4$, which turns the circle around the point at infinite frequency (in contrast, a phase offset α would just add directly to the phase, rotating the graph around the on-resonant point). Note that this causes $|S_{11}|$ to appear to exceed 1 in a certain region due to the internal impedance mismatches. The last row adds 1.2 μs of cable delay (note that this is exaggerated for visibility compared to the standard 60-80 ns observed). This presents as an overall slope to the phase, or deviation from the circular shape.

although the author strongly recommends spending some time trying out plotting it (both the real/imaginary parts, and in the complex plane) with different parameters in order to get a feel for it, see also [Probst et al., 2015] for the full method. The part in the brackets is an asymmetric oscillator: it is a circle of diameter $Q_l/|Q_c|$ pivoted around $S_{11} = 1 + 0i$ by an angle ϕ . The $f = \infty$ point is at $S_{11} = 1$, so the circle does not quite meet there in any finite-frequency sweet; the opposite point on the circle is at $f = f_r$. $e^{i\alpha}$ then rotates everything by an angle α about the origin, followed by a scaling a . The $e^{-2\pi if\tau}$ term is a little different, it provides extra loops in the circle.

Let us now briefly discuss the fitting procedure, see [Probst et al., 2015] Fig. 3 for an illustration. Fortunately, the cable delay term can generally be calibrated away fairly easily – although the electrical length itself also depends on frequency, our resonances are generally sufficiently high-Q that we can neglect this. Therefore, we can take a wider sweep of phase around the resonance (generally, we use hundreds of MHz to a GHZ span for this) and fit the data to a line to extract $2\pi\tau$. We can then multiply the data by $e^{-2\pi if\tau}$, removing the cable delay and obtaining a circle. We can then fit the data to a circular model and displace it such that the centre of the circle is at the origin. At this point, the phase takes the following form:

$$\arg S_{11}(f) = \theta_0 + 2 \arctan \left(2Q_l \left[1 - \frac{f}{f_r} \right] \right) \quad (2.25)$$

From this, we can extract the necessary parameters, and finally shift the circle back to the “ideal” position.

We have thus obtained the parameters of the model, a , α , τ , Q_l , $|Q_c|$, ϕ , and f_r . Generally, we are interested primarily in f_r , and Q_i . f_r can be obtained directly from this (note that in an asymmetric resonator, the lowest point of S_{11} is not actually f_r , so we do need to perform the fit). Q_i , on the other hand, needs to be extracted from Q_l and $|Q_c|$. As mentioned above, this can only be done reliably if we are not too

overcoupled, otherwise, our calculation involves taking the reciprocal of a very small number and is thus very sensitive to error.

Hanger

In a hanger measurement, the resonator provides a shunt to ground to a microwave tone sent between two ports. This measurement setup is quite similar to the reflection measurement, but has the advantage that several resonators can be multiplexed easily. Since there are now explicitly two ports, we measure the S_{21} of the system, which only differs from the reflection case by a factor of 2:

$$S_{21}(f) = ae^{i\alpha} e^{-2\pi if\tau} \left[1 - \frac{Q_l/|Q_c|e^{i\phi}}{1 + 2iQ_l(f/f_r - 1)} \right]. \quad (2.26)$$

The factor of 2 decreases the range of the amplitudes, so we must take more data to get as good of a fit compared to reflection. This is generally not a large problem, but may provide a reason to prefer reflection over hanger for experiments with only one resonator.

Transmission

In transmission, the signal from port 1 goes *through* the resonator and then to port 2. This case is somewhat different from reflection and hanger. First, reflection and hanger are self-calibrating – far off resonance, we expect the S_{11} or S_{21} to be 1, and any variation can be attributed to a . This is not the case for transmission: far off resonance, the resonator provides a zero-impedance shunt to ground, meaning S_{21} is 0. This means that a transmission measurement requires a calibration of the lines in order to extract Q , which can be done either with multiple measurements, or by having a switch or some other non-reciprocal element in the system. Second, transmission now has two coupling Q 's, which creates more opportunity for imperfections and

would technically require measuring more S-parameters in order to disentangle them (which is complicated in a cryogenic system, due to the aforementioned attenuation and amplification). The equation for transmission is

$$S_{21}(f) = ae^{i\alpha} e^{-2\pi if\tau} \left[\frac{2Q_l/|Q_c|e^{i\phi}}{1 + 2iQ_l(f/f_r - 1)} \right]. \quad (2.27)$$

Transmission has a potential application in situations where it's hard to find the resonator in reflection or hanger, and measuring whether or not S_{21} is zero is easier than comparing small deviations around a non-zero value. It also does allow for multiplexing. In practice, we generally refrain from transmission measurements.

T_1 or T_2 ?

What is the correct interpretation of the Q_i extracted from such spectroscopic measurements? We extract Q information from the breadth of the peak we detect. However, if there is frequency jitter that is faster than our measurement, then we shall see it either as discontinuities in the trace or a broadened trace, depending on the frequency of the jitter as well as the IFBW of the [VNA](#) and the total sweep time. In the discontinuity case, we need to average a lot to get the trace to fit our model, once again resulting in a broadened peak. Therefore, we see that frequency jitter will lead us to a decreased Q , and that we are measuring a lifetime that is sensitive to frequency noise and is thus T_2 -like. However, also note that we are measuring an energy, not an amplitude lifetime, and therefore the actual timescale is $T_2/2$.

Of course, there is somewhat of a grey area regarding the distinction between T_1 and T_2 . If we can observe the resonator quickly enough to distinguish individual traces between it jumping, then we could fit each trace separately and then average the results. The result would be more of a T_1 measurement. Therefore, we see that the distinction really depends on a frequency scale. I note that this is not hypothetical

– we commonly observe our resonators jittering, and have attempted various ways of clamping that could improve the situation. Some of our measurements have been made with the pulse tube of the dilution refrigerator turned off (the fridge can stay cold for at least 15 minutes in this state) in order to dampen the vibrations, which improves the jittering in some cases (and does nothing at all in other cases!) The causes of this are not always clear – a loose clamp can be an obvious cause of physical vibration, but such causes are not always present.

2.5.2 Time-domain

The other main way to measure a resonator is with a time-domain measurement. As the name implies, in this case, the resonator is interrogated with a signal, and then its response is measured as a function of time. The test equipment in this case needs to be able to record data on the timescale of small fractions of a microsecond, if we wish to be able to truly characterise resonators with relatively short lifetimes (tens of microseconds), although in principle, one could get away with less resolution for a higher-Q resonator. For this thesis, an [field-programmable gate array \(FPGA\)](#) was used to both generate the signals and record the data, although one can get away with less complicated equipment, e.g. an [arbitrary waveform generator \(AWG\)](#) and a digitiser.

Ringdown

The primary method used to measure a resonator is called ringdown. The basic idea is simple: energy is loaded into the resonator with a resonant pulse. Once the resonator is displaced, it will decay back to the vacuum state, emitting an exponentially-decaying amount of energy – this process is referred to as the ringdown. The energy coming out of the resonator is collected, and can then be fitted to an exponential curve. This can be done with any of the configurations described above.

There are several complications to the process. First, there is once again the question of T_1 vs. T_2 . Unlike the case of the frequency-domain measurement, we can easily choose which one we obtain depending on how we average. The difference is the order of averaging: in a time-domain measurement, we generally need to collect many traces of points in IQ space (complex data). We then have two options: we can first calculate the amplitude of each set, and then average the results, or we can average the IQ data across all the sets, and then calculate the amplitude. In the first case, a jitter in frequency will not affect the resulting lifetime (meaning we have T_1), whereas in the second case, it will, so we have T_2 . One easy way to see how this works is to consider a dataset where each point is either +1 or -1. Averaging the amplitudes of the data gives 1, since the phase does not matter. On the other hand, finding the amplitude of the averages gives 0, since the phases have cancelled out.

Next, we note that the method as described above can only give us the Q_l of the resonator, since we have no way of distinguishing what fraction of the energy is being lost due to internal vs. external losses. There are two ways of dealing with this. One is by making a [VNA](#) frequency-domain measurement of the resonator in its current configuration to determine the Q_c , and then use the time-domain measurement. Why bother with the time-domain measurement, since we've already done a frequency-domain one? There are several potential reasons: in our setup, time-domain measurements are faster, so if we wish to collect more data (e.g. power/temperature sweeps), we may want to do most of the data collection with the [FPGA](#). If the resonator is jittering, it is also much easier to take T_1 measurements in this way. This is the method we use in this thesis.

The other way to get Q_c is by measuring not only the ringdown, but also the *ring up* of the resonator. This means that we start measuring the power coming out of the resonator from right before we have started driving it, so we can see it changing as the resonator is displaced from vacuum (the ring up) as well as the ringdown. We

can write a model for what this should look like, allowing us to disentangle Q_c from Q_i . This can be done via input-output theory, or via explicitly solving for the signal as a function of time (see e.g. [Heidler et al., 2021] for a description).

Transmon Coupling

Finally, let us briefly mention the fact that we can measure the resonator indirectly through another system coupled to it, in our case, a transmon. I shall describe this in more detail in chapter 4, but in short, the idea is that we can perform gates between the two systems such that the information about the state of the resonator is somehow encoded in the state of the transmon. We can then read out the transmon without ever having the ability to read out the resonator directly. This is done not because it is a superior way to measure the resonator, but because this is the structure of the final system we are trying to design (recall, we need to be able to couple our resonator to a non-linear control element). Equipment-wise, this method is the most involved, as performing these gates requires the ability to generate very short (timescale of nanoseconds) pulses, and, depending on exactly what one wants to do, may even require feedback/forward.

CHAPTER 3

Micromachined Cavities and High-quality Superconducting Microwave Seams

In this chapter, I shall discuss aspects of a hybrid architecture for superconducting quantum computing that combines some advantages of lithographically-defined planar devices with those of 3-D cavities: [multilayer microwave integrated quantum circuits \(MMIQC\)](#) [Brecht et al., 2016]. As discussed in section 2.1.3, lithographically-defined devices have advantages in scalability and precision, while 3-D cavities have higher Q and protection from cross-talk. The main idea is that we can build quantum circuits on a stack of silicon chips, with cavities being etched into a chip and metallised, and interconnects routed to one of the outer surfaces to permit access to inner elements. In this chapter, I shall focus on the key building block of the [MMIQC](#), the micromachined cavity; for more in-depth discussion of the architecture itself, see [Brecht, 2017]. This chapter is partially based on [[Lei* & Krayzman*](#) et al., 2020].

3.1 Micromachined Cavities

The micromachined cavity (Fig. 3.1) is a type of hybrid 3-D/thin-film resonator. It is a core element of the [MMIQC](#) since it is the object which stores the quantum information. The body of the cavity is wet-etched out of a silicon chip using KOH, which has a very high selectivity to different crystal orientations of silicon. This results in the characteristic trapezoid shape (when the surface of the silicon chip is $\langle 100 \rangle$), with an angle of 54.7° . The etched surface, as well as the surface of the chip making the roof of the cavity, are then metallised with a superconductor. In our case, we thermally evaporate indium directly onto the chips. Indium is a superconductor with a reasonable T_c of 3.4 K, and has the property that it cold-welds to itself when pressed at room temperature, as well as remaining ductile to cryogenic temperatures. This allows us to form a high-quality microwave seam at the joint between the two chips; this will be discussed in much more detail throughout the rest of this chapter.

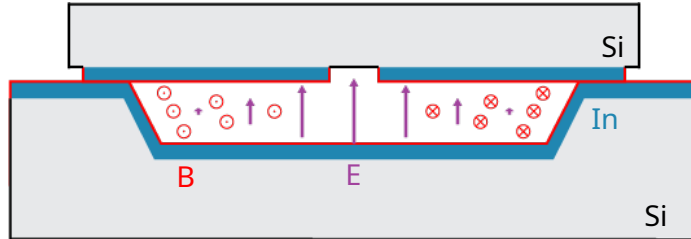


Figure 3.1: A crosssection of the micromachined cavity. It is made of two silicon chips, with the bottom one having a cavity micromachined into it. The two chips are metallised with a superconductor (in this case, indium), and pressed together. Note that the surface of indium is coated in an oxide (and possibly contaminants), shown in red. The electric and magnetic fields of the TE101 mode are also shown. From the top, the cavity shape is rectangular.

The mode which we generally use to store information is the TE101 mode. Although the micromachined cavity is not actually rectangular to the slope of the side-walls, the mode shape is essentially the same as that of a rectangular cavity TE101 mode, see Fig. 3.2. In order to maintain a fundamental frequency of under 10 GHz, the dimensions of the cavity must therefore be at least 2 cm (with the third dimension

being constrained by the thickness of the chip). Coupling to this mode is achieved via the hole in the metallisation on the top chip, which is made lithographically (see inset in Fig. 3.3 (a)). Note that the hole is only in the conductor, not in the silicon itself.

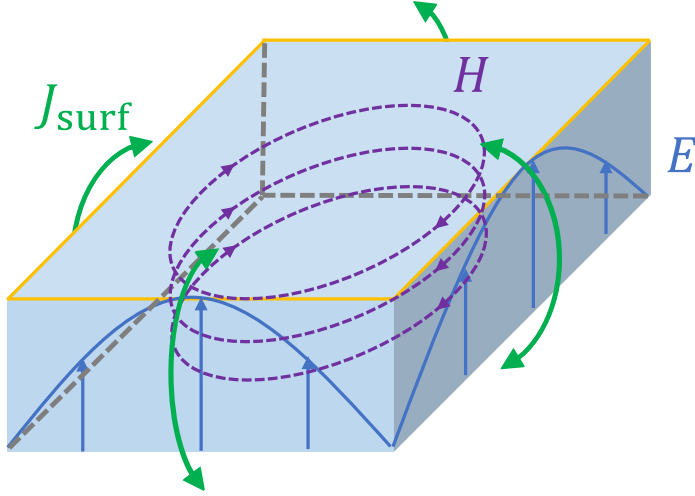


Figure 3.2: The TE101 mode of a rectangular cavity. The electric field (blue) is uniform in the up/down (\hat{y}) direction, the magnetic field (purple) circulates around the centre of the cavity, and surface current (green) flows around the thin walls. The frequency of the mode is set by $\sqrt{a^{-2} + b^{-2}}$, with a and b the dimensions of the cavity along \hat{x} and \hat{z} . Therefore, the *middle* dimension contributes the most, and thus both the length and the width of the cavity cannot be made smaller than 2 cm without raising the frequency above 10 GHz. The orange line represents the location of the seam for the micromachined cavity.

An important feature of the TE101 mode is the location of the seam. Since it is not practical to etch a cavity into the side of a chip, the seam of a micromachined cavity must be placed similarly to the orange seam depicted in Fig. 3.2. The challenge with such a seam location is that as we can see from the diagram, most of the surface current of the mode must cross the seam with a large perpendicular component. As we can recall from Eq. 2.12, this means that such a mode will have a very large y_{seam} , and thus be very sensitive to the seam quality. This applies to many structures in the **MMIQC**, since they all are confined to being on/in a chip, which prohibits placing joints at locations where the current does not cross. For this reason, it is crucial

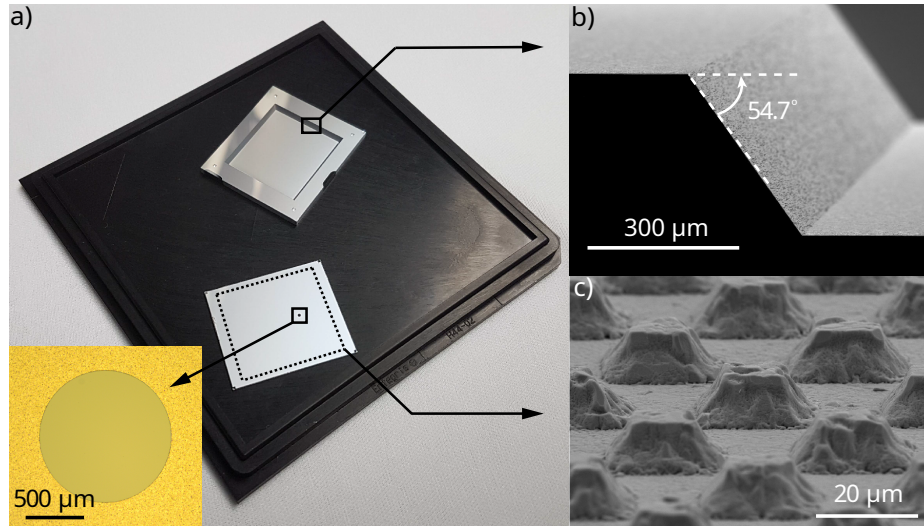


Figure 3.3: A micromachined cavity. (a): A photograph of a disassembled micromachined cavity. Inset: the hole in the metallisation for coupling. The indium bumps around the perimeter are indicated with the dotted line. (b) An SEM of the sidewall of the cavity, demonstrating the characteristic 54.7° angle formed by the KOH etch. (c) An SEM of the indium bumps used to form a high-quality microwave seam. Reproduced from *Appl. Phys. Lett.* 116, 154002 (2020), with the permission of AIP Publishing.

to be able to create ultra-low-loss seams in the microwave regime for the [MMIQC](#) architecture, and for the micromachined cavity in particular.

3.2 Ultra-low-loss Microwave Seams with Indium Bump Bonding

Microwave seam loss is a concern not only for quantum computing, but also in particle accelerators which use very high-Q superconducting microwave cavities. Several methods have been developed for this, including diffusion-bonding [Isagawa, 1978] and electron beam welding [Allen et al., 1971]. Indeed, they permit niobium cavities with very high Q's in the microwave regime [Romanenko et al., 2020]. However, none of these methods have a clear strategy for application to on-chip devices, and are likely not directly compatible with transmon qubits.

Therefore, we chose instead to modify an existing method of making mechanical and electrical connections between chips which is known to work under cryogenic conditions: indium bump bonding. This method is common enough for there to be commercial equipment for it; one sample use is in cryogenic detectors [DeNigris et al., 2018]. Indium is a superconductor with a reasonable T_c of 3.4 K, cold-welds to itself at room temperature, and remains ductile even at cryogenic temperatures [Datta et al., 2005] – properties that make it suitable for a low-loss interconnect. Additionally, indium bumps can be formed using standard photolithography and thin-film deposition, while the bonding itself can be automated using the aforementioned equipment. It is also non-destructive to other circuit components, and thus relatively straightforward to adapt both to existing superconducting quantum circuits and to scalable fabrication. For these reasons, indium bump bonding has recently started being used for 3-D integration [Rosenberg et al., 2017, Foxen et al., 2017, O’Brien et al., 2017, McRae et al., 2017] in the field, however, a measurement of the microwave quality of the seam had not been carried out prior to this work.

The concept is fairly straightforward: indium bumps (around $15 \mu\text{m} \times 15 \mu\text{m} \times 10 \mu\text{m}$, in our case) are fabricated lithographically, see Sec. 3.3 for more details. They are then compressed by around 50%, resulting a deformation large enough to break through the surface oxide, and make direct metal-to-metal contact to the other surface. If they are placed closely enough together, the seam can also be light-tight, see Fig. 3.3 (c). Although it is in principle possible to bond bumps to bumps, we bond to a flat indium surface. This not only requires one fewer round of fabrication, but also allows us much greater tolerance to lateral displacements between the two chips.

3.2.1 Measuring Seam Quality

Now that we have decided on a technology for creating our microwave seams, we need to be able to measure the resulting quality. One approach is to simply make our final

device (namely the micromachined cavity) and measure its Q . However, this would not actually give us a measurement of the quality of the seam, just a lower bound, found by attributing *all* of the cavity's loss to the seam. Furthermore, we wouldn't know whether the cavity is limited by the seam or not, and thus have no idea whether we have succeeded in achieving a sufficiently high g_{seam} . Even if we wanted to improve the seam quality by trying different fabrication techniques, designs, etc., we would not necessarily even be able to tell whether our efforts are making any difference, if the cavity is limited by some other loss mechanism. If we wanted to improve the quality of our cavity at some point in the future, we would not know which loss mechanism needs to be improved first.

Therefore, we instead take a different approach: we make several devices which are nominally identical except for their y_{seam} . We make sure to include a device with as high of a y_{seam} as possible, to purposefully make it sensitive to seam loss. Using this series of devices, we should then be able to either actually measure the seam loss, if we see Q_i dropping with increasing y_{seam} , or place a much higher lower bound on the quality of the seam than the micromachined cavity would allow us, if even our most sensitive device doesn't seem to be any worse than the others. In the first case, we should be able to calculate the effects of seam loss on our cavity and then act appropriately; in the second case, we should at least know that our cavity is not limited by the seam.

The devices that we have chosen for this task are stripline resonators made of a number of sections alternating between two bonded chips, with the sections connected by indium bumps; see Fig. 3.4. Compare to the devices in [Brecht, 2017] Sec. 7.4, which used electroplated indium, and thus had normal metals, and also did not reach as high of a y_{seam} as in this work. When the two chips are bonded together, the stripline recovers its original shape. Since the $\sim 10 \mu\text{m}$ bumps have been compressed by around 50%, the chips are now separated by only around $5 \mu\text{m}$; the bumps may add

a small bit of inductance here, but no real change to the mode is expected. Bumps for mechanical support are also visible around the perimeter of the chip – these are necessary, since without them, the top chip would be connected to the bottom only by the small number of individual bumps making the seam. The mechanical support bumps carry no current and do not contribute to the mode.

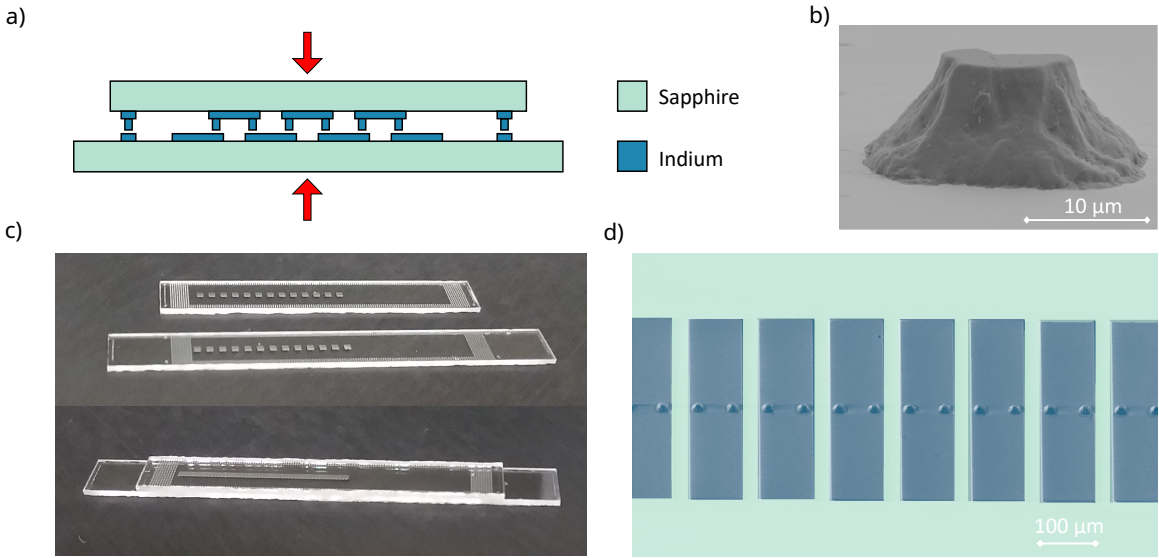


Figure 3.4: a) Diagram of the interrupted stripline split between two chips. The two outer bumps represent the mechanical stability bumps, which play no role in the electrical mode and exist solely to provide additional area on which the top (daughter) chip can rest. b) An SEM image of a sample indium bump. c) A photograph of the two chips before (top) and after (bottom) bonding. We see the stripline recovers its shape between the two chips. d) An SEM image of the stripline, interrupted by bumps.

The two chips are then pressed together in the SET FC150 commercial bonder. The force is chosen such that the resulting pressure is the same as what can be achieved for the micromachined cavity (the micromachined cavity has many more bumps, and thus is limited in pressure by the maximum amount of force that the machine can provide). Since the total area of the bumps is around 3 mm^2 , the force we used was 75 kg, giving around 250 MPa of pressure. Pressures lower than several 10's of MPa resulted in bonds that would not hold mechanically. The force was ramped up from 0 in 5-10 segments, with the ramping taking several minutes, and

then being held at the end of each segment for several minutes. We did not attempt to find an optimal ramp. I do note that pressing too quickly resulting in even more smudging than usual (the interrupted striplines had a very high aspect ratio, and even with slow ramping the bonded devices shifted by several microns). This could be determined by comparing the locations of the alignment marks on the two chips in a light microscope after they were bonded, see Fig. 3.5. Additionally, scrubbing seems to have just destroyed the bumps, as was not attempted more than once.

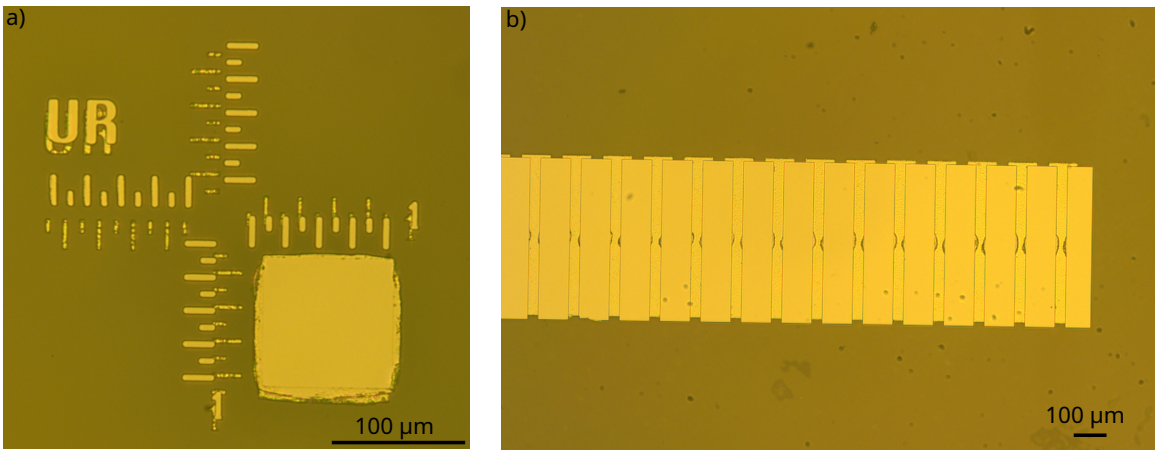


Figure 3.5: a) The two alignment marks used for bonding seen on the two bonded chips. A misalignment is visible, as well as the compressed square pressing outwards. The misalignment is larger than that of the bonding device and likely occurs as the indium flows during the bonding. b) Misalignment seen on a bonded stripline. We can also see the compressed bumps pressing out, demonstrating that they were sufficiently deformed.

Finally, I note that the devices were measured in a multiplexed package styled after [Axline et al., 2016]. By making the different devices slightly different frequencies, we were able to measure 4 devices within one package in the same cooldown.

We fabricate several versions of the device, with varying numbers of evenly-spaced segments, and varying numbers of bumps per segment. Clearly, y_{seam} must increase with number of segments, and decrease with bumps per segment. To actually calculate y_{seam} , we have two options. First, we can use HFSS to perform finite-element simulation. In this case, it is simplest to treat the stripline as a 2-D rectangle, with

bumps represented by much narrower sections. This lets us avoid dealing with the complicated motion of current through the bump, as we can simply integrate the current crossing the narrow regions. As mentioned above, we have to do this anyway for defining seam loss, since we don't know the microscopics of the current motion. As long as we are consistent in how we define the seam, the results obtained this way will be meaningful. Therefore, we choose the nominal width of the bump as the width of the narrow region.

We can also write down an analytical approximation. Recall Eq. 2.13. Let us assume that our stripline has length l , width W , is interrupted in N places, with n bumps of width w at each interruption. Let us further assume that $n * w \ll W$. Finally, let us define a coordinate x starting from one end of the stripline, and running through l on the other end, and a coordinate z doing the same thing over width, from 0 to W . At each interruption,

$$J_{\perp}(x, z) = \frac{I(x)}{nw},$$

if and only if (x, z) represents a point inside a bump, by definition of surface current and the small-bump assumption. Integrating over the length of the seam,

$$\int_0^W J_{\perp}(x, z)^2 dz = nw \frac{I(x)^2}{(nw)^2} = \frac{I(x)^2}{nw}.$$

Since there are N seams, to obtain the total numerator for y_{seam} , we must sum over all $x_i = i \frac{l}{N+1}$, $i \in [1, N]$ evenly-spaced interruptions:

$$\frac{1}{nw} \sum_i I(x_i)^2.$$

Let us now consider the denominator. We can express twice the total energy in the system as $\frac{L}{l} \int I(x)^2 dx$, with L/l the inductance of the stripline per unit length

(ignoring inductance of the bumps). Since we are concerned with the normal modes of a $\lambda/2$ stripline resonator,

$$I_m(x) = \sin(k_m x) = \sin(m\pi x/l),$$

with m the integer index of the mode.

$$\int_0^l I_m(x)^2 dx = \int_0^l \sin^2(m\pi x/l) dx = \frac{l}{2}$$

(there is a nice way of thinking about that integral – we know the average value of $\sin(x)^2$ over an integer number of periods must be $1/2$, since $\sin(x)^2 + \cos(x)^2 = 1$, so integrating from 0 to l must give $l/2$). Finally, the frequency of a resonator is $\omega_m = \frac{m}{\sqrt{LC}}$. Putting it all together, we obtain

$$y_{\text{seam}} = \frac{1}{nw} \frac{\sum_i \sin^2(m\pi x_i/l)}{\frac{m}{\sqrt{LC}} \frac{L}{l} \frac{l}{2}} = \frac{2}{nw} \frac{\sum_i \sin^2(m\pi x_i/l)}{m \sqrt{\frac{L}{C}}}.$$

We now notice that $\sqrt{L/C} = Z_0$, the impedance of the mode. We can solve for the mode impedance in many ways. One way to do it with only a 2-D electrostatic solver is to notice that $\frac{1}{LC_0} = c$, where C_0 is the capacitance with all dielectrics replaced by vacuum, and c is the speed of light. By solving for C and C_0 with a 2-D electrostatic solver (one simulation with dielectric, the other without), we can obtain

$$Z_0 = \frac{1}{c\sqrt{CC_0}},$$

see e.g. [Green, 1965]. We can get away with a 2-D simulation because the 2-D cross-section of the stripline is essentially constant, neglecting the bumps. With our

knowledge of $Z_0 \approx 110 \Omega$, we can now solve for y_{seam} :

$$y_{\text{seam}} = \frac{2}{nw} \frac{\sum_{i=1}^N \sin^2(m\pi i/(N+1))}{mZ_0} \quad (3.1)$$

Measurement Results

Now that we have described the devices we shall use as well as how to obtain their y_{seam} , all that is left is to actually measure the devices, and see what we can learn about g_{seam} . We present the data, along with some data on bulk-machined cavities for comparison, in Fig. 3.6.

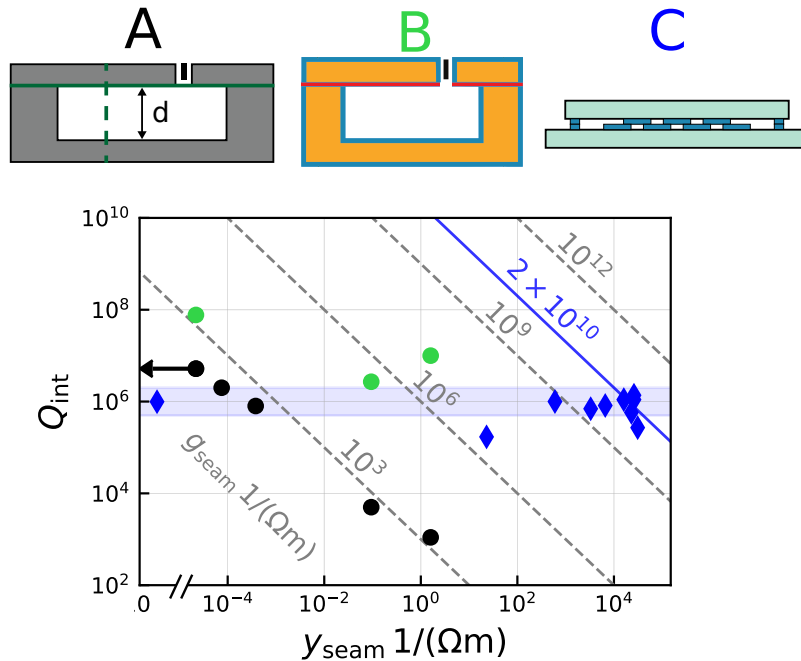


Figure 3.6: Log-log plot of internal Q vs. y_{seam} for three series of devices. All of the devices within each series have similar designs, except for y_{seam} . Series A: black circles, aluminium 6061 cavities cut in different places and bolted together. Series B: green circles, same as A, but now in copper electroplated with indium. Series C: blue diamonds, interrupted striplines described above. For data for A and B, see [Brecht et al., 2015]. Adapted from Appl. Phys. Lett. 116, 154002 (2020), with the permission of AIP Publishing.

This plot shows how internal Q changes with y_{seam} for three series of devices. Series A represents aluminium 6061 cavities that have been cut in different places and bolted

together. The point with the lowest y_{seam} , marked with an arrow pointing left, represents a cavity cut along a plane of symmetry such that no current should cross the seam in the ideal case. In reality, machining imperfections can cause an asymmetry; the value given is that assuming the imperfections are as large as possible within the machining specification. Series B represents similar cavities that are instead made of copper and electroplated with indium (the copper serves only to allow electroplating and should not participate in the mode). These two series are from [Brecht et al., 2015]. Series C represents the interrupted striplines described earlier in this section.

For the cavities, the devices in each series have similar participations, except for the seam. For the striplines, the devices are nominally identical except for y_{seam} . If the a series of devices is limited by the seam, we would expect Q_i to fall as y_{seam} increases; if it is limited predominantly by the seam, then Q_i should lie along a line of constant g_{seam} (the diagonal lines on the plot). We observe that for the 6061 cavities, increasing y_{seam} does indeed lower Q_i in a way that is consistent with a g_{seam} of $10^3/(\Omega m)$. This suggests that they are indeed limited by seam loss (for this to be a proof, we would need the other participations to be identical). When identically-shaped cavities are made using indium (series B), we see the Q_i no longer has a clear relationship to y_{seam} . Therefore, the cold-welding of indium has improved the quality of the seam to at least around $10^7/(\Omega m)$, although note that this is only a bound.

For the interrupted striplines, I first note the device with 0 y_{seam} : this was a control device in which the *entire* stripline was on one of the two chips, with no interruptions. The other chip was still fabricated and bonded to the first one to ensure all of the participations were the same as for the non-control devices. Therefore, this chip must actually have y_{seam} of *exactly* zero, since there is no seam at all! The band drawn around the device indicates the natural spread of Q_i that is expected from device-to-device variation (in this case, a factor of 2 was used, since flip-chip striplines seem to suffer from a somewhat larger variability in quality). Now, let us look at the

test devices. We see that almost all of them lie within the control band, with two exceptions, and one is the lowest y_{seam} tested. Furthermore, the cluster at high y_{seam} values indicates that the one lower- Q device at high y_{seam} does not actually indicate limitation due to the seam, but just standard device-to-device variation.

We therefore observe that although we have made test devices with y_{seam} orders of magnitude larger than the cavities', we *still* were not able to reach a regime where the seam limits the devices. We therefore cannot provide a true measurement of g_{seam} , but instead a lower bound on the quality, namely, $2 \times 10^{10}/(\Omega m)$. Note that this is at least $1000\times$ larger than the bound obtained for the machined cavities. Also note that this is bound is not obtained from the best device measured, but instead represents 4 devices, and is thus the bound on what we can repeatably achieve.

Let us now return to the micromachined cavity. The y_{seam} of a micromachined cavity is around $10/(\Omega m)$, depending on the device parameters. We observe that a g_{seam} of at least $2 \times 10^{10}/(\Omega m)$ would permit the micromachined cavity to have a Q_i of at least around 2 billion, if the other losses were sufficiently small, and assuming that the seam quality of the micromachined cavity is the same as for our interrupted striplines. Since this is just a lower bound, it may be the case that the effects of seam loss would not be noticeable in a micromachined cavity until even higher Q 's. As we shall see, this is higher than the Q 's of the micromachined cavities that we manage to attain. Therefore, we conclude that our indium bump bonded seam is sufficiently high-quality at microwave frequencies that improving it would make no difference, given the current quality of our other loss channels.

3.3 Micromachined Cavity Fabrication

3.3.1 Fabrication of the Cavity Itself

I now describe the process used to fabricate micromachined cavities for experiments in this thesis, see Fig. 3.7 for reference and Appendix A for more details on the process. The cavity is made of two chips which are then bonded together. The silicon wafers used to make the bottom chips are first cleaned with solvents ([1-methyl-2-pyrrolidone \(NMP\)](#), acetone, methanol), then the oxide is removed with 10:1 [buffered oxide etch \(BOE\)](#). Around 300 nm of silicon nitride is then deposited using [plasma-assisted chemical vapour deposition \(PECVD\)](#) (a). We then pattern positive photoresist (S1813), forming the top of the cavity (b). We then etch the nitride with a CHF_3/O_2 [reactive ion etch \(RIE\)](#) and remove the photoresist with solvents ([NMP](#), acetone, methanol, [isopropanol \(IPA\)](#)) (c). This results in a nitride etch mask on our silicon, which will prevent the substrate from being etched outside of the defined cavity region. We then etch the silicon in 30% KOH at 80 °C (d). The time of the etch depends on the desired depth – the etch rate is around 55 $\mu\text{m}/\text{hr}$, so our etches take between $\sim 2 - 27$ hours to achieve our desired cavity depths of 100 – 1500 μm . We then clean off the salts which have grown on the silicon using $\text{H}_2\text{O}:\text{HCl}:\text{H}_2\text{O}_2$ solution in 5 : 1 : 1 concentrations. Finally, we thermally evaporate 1.2 μm of indium on the surface (e).

The top chip is also fabricated from a silicon wafer, although in principle, the substrate could be something else, e.g. sapphire, since we do not need to etch it. This wafer also starts with a standard solvent clean, although we don't need to do the [BOE](#) etch since we're not trying to grow silicon nitride (f). We then define the coupling hole with photolithography, this time using a negative resist (AZnLOF2035) since we're going to do liftoff (g). We then evaporate around 1 μm of indium on the surface, and lift the resist off in [NMP](#) or TechniStrip Ni555 (a special solvent for our resist) (h). We then perform another layer of photolithography to define a liftoff

pattern for bumps, this time with the thicker AZnLOF2070 (i). We then evaporate around 9 μm of indium and lift the resist off, leaving indium bumps for the seam (see the next section), (j). Since our bumps are so tall, we need the resist to be quite thick, at least around 14 μm , in order to be able to lift off. In order to make good contact between the bumps and the indium layer underneath, we argon ion mill the film in the indium evaporator before deposition the second layer – this is thought to remove the oxide, allowing for metal-metal contact.

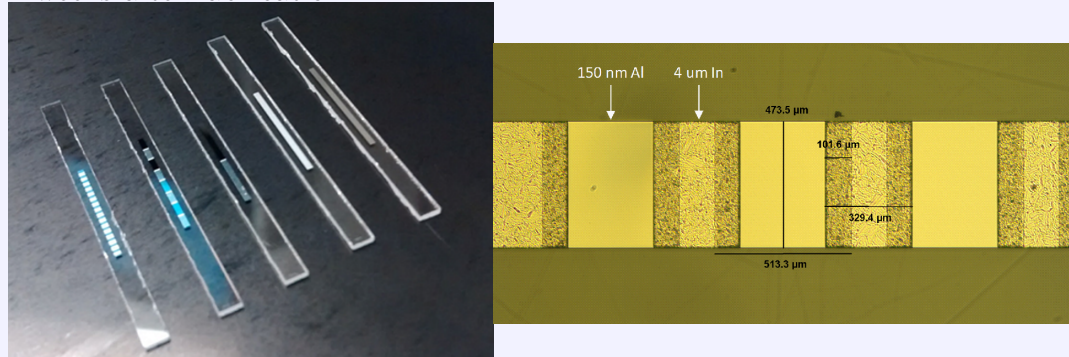
Under-bump metallisation.

I note that a number of groups use an under-bump metallisation layer (see e.g [Foxen et al., 2017]) between aluminium and indium. The claim is that aluminium and indium will interdiffuse, forming an intermetallic, with [Wade and Banister, 1975] being commonly cited. I am not a metallurgist, and thus present the following quote from the book without comment (pg. 1003):

10. ALLOYS

Most metals and metalloids readily alloy with aluminium; relatively few (Be, Ga, Si, Ge, Sn, Zn and Hg) form simple eutectic-type systems with aluminium. The elements Na, K, Rb, Cs, In, Tl, Pb and Cd have only a limited solubility in the liquid metal; they form simple, monotectic-type systems. In these cases, no binary intermetallic phases or compounds are known with aluminium^{10a,27}.

Additionally, we made several test devices with In/Al seams, with varying y_{seam} . The Q_i of all of them was around 2 million, and thus the devices did not seem to be seam-limited. The g_{seam} limit extracted from the measurement for an In/Al was $g_{\text{seam}} \geq 2.8 \times 10^8 / (\Omega m)$. The measurements were carried out around 2 weeks after fabrication.



For us, aluminium and indium come in contact when fabricating aperture transmons for coupling with the cavity, see [Brecht et al., 2017].

3.3.2 Bonding Process

Now that we have finished fabrication of the top and bottom chips, we need to bond them. We first both chips with atmospheric plasma comprising a mix of helium, nitrogen, and hydrogen (k). This is the commercial system ONTOS. The stated functionality of the treatment is to replace the indium oxide on the surface with indium nitride, which is supposed to be more brittle and thus easier to break through during bonding. We did not verify these claims, but we did confirm that the process did not decrease the quality of the seam (see next section), change the room-temperature resistance of transmons, and seemed to make the seam quality more consistent (although we did not study this carefully). Immediately following the plasma treatment, we bonded the two chips together using the SET FC150 commercial bonder (l). We used the maximum available force, $200\text{ kg}\times\text{g}$. The area of the bumps was such that this provided a pressure of several hundred MPa (in our experiments, we found that around 250 MPa was generally sufficient). We did not heat the chucks or use any scrubbing. After compression, the bumps were reduced in height by around 50%, as verified via [SEM](#) from the side. As a last step, a thin indium wire was carefully pressed around the outer perimeter of the top piece, to ensure light-tightness. It also appears that this step may have helped with vibrations of the mode.

Let us now briefly discuss the differences between the micromachined cavity described here, and the previous generation [[Brecht et al., 2015](#)]. Previously, the indium was electro-plated, not evaporated. This creates two potential differences: first, a normal metal (copper or gold) must first be deposited on the silicon as a seed layer for the electroplating, which is not necessary with evaporation. Additionally, the indium is sourced from an indium sulphamate plating bath, which contains organic surfactants with unknown properties, whereas in evaporation, a pure indium target is used. Additionally, in the previous experiment, the top of the cavity was formed by a [PCB](#) rather than another silicon chip. Finally, bonding was achieved via flat-to-flat con-

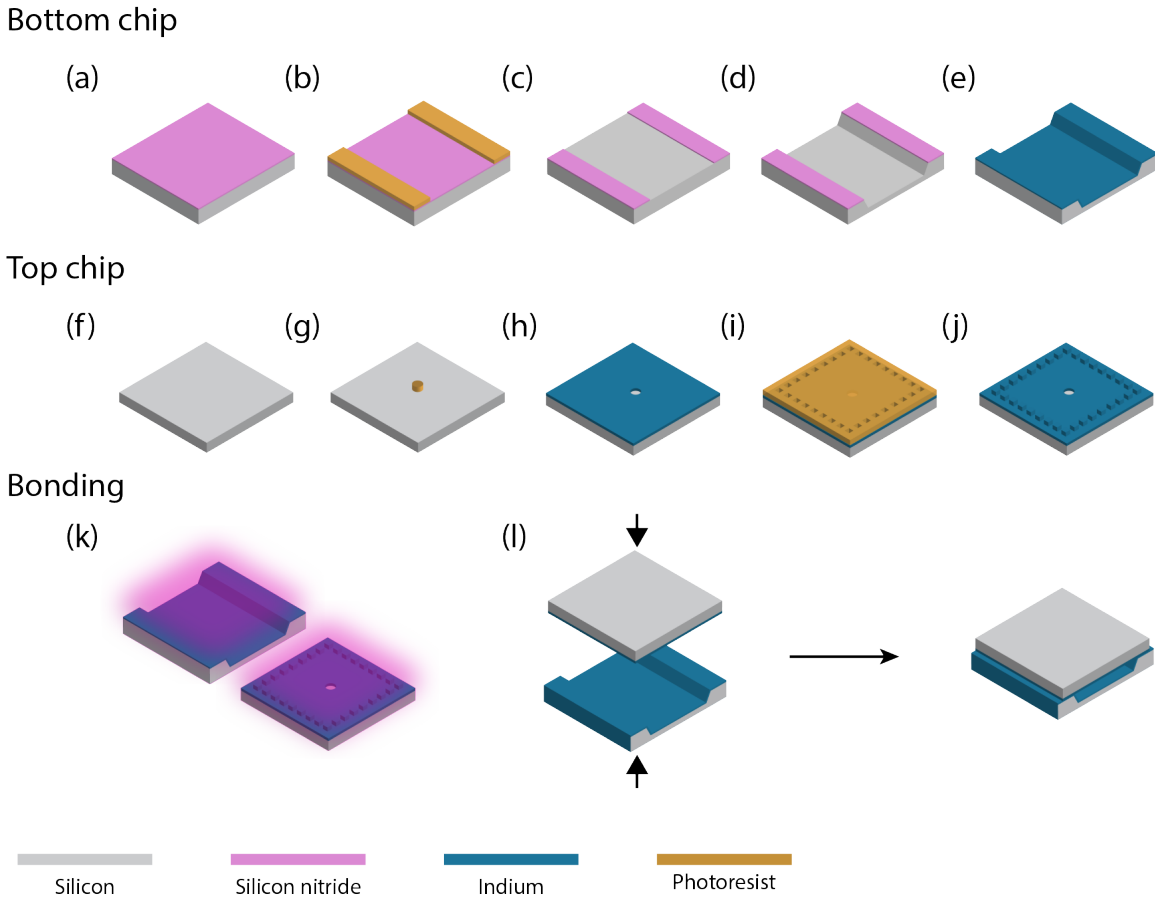


Figure 3.7: The fabrication process of a micromachined cavity. See the text, section A.2.2 for a description of the process. Reproduced from Appl. Phys. Lett. 116, 154002 (2020), with the permission of AIP Publishing.

tact of indium, which does not leave room for deformation and thus does not enable breaking of the oxide. As we shall see later in this chapter, the new cavity has a lifetime improved by two orders of magnitude compared to this previous design.

3.3.3 Coupling to a Micromachined Cavity

Finally, I describe the method by which we couple to a micromachined cavity. As with other resonators, we use a pin attached to an **SMA** connector to couple capacitively to the electric field. The actual coupling is achieved through the aforementioned aperture in the metallisation (it is small enough to prevent significant hybridisation with the copper cavity). We can change the length of the pin to change the coupling. Note that

we need to have a very high coupling Q in this case, since the micromachined cavity turns out to be very high- Q . There is another copper piece (not pictured) which bolts into the first one to form a full enclosure around the micromachined cavity. The structure does not participate in the storage mode, and its modes are engineered to be far from it. The copper package serves as a way of bolting the micromachined cavity to the dilution fridge, as well as to help with thermalisation. It is not a fundamental part of the cavity.

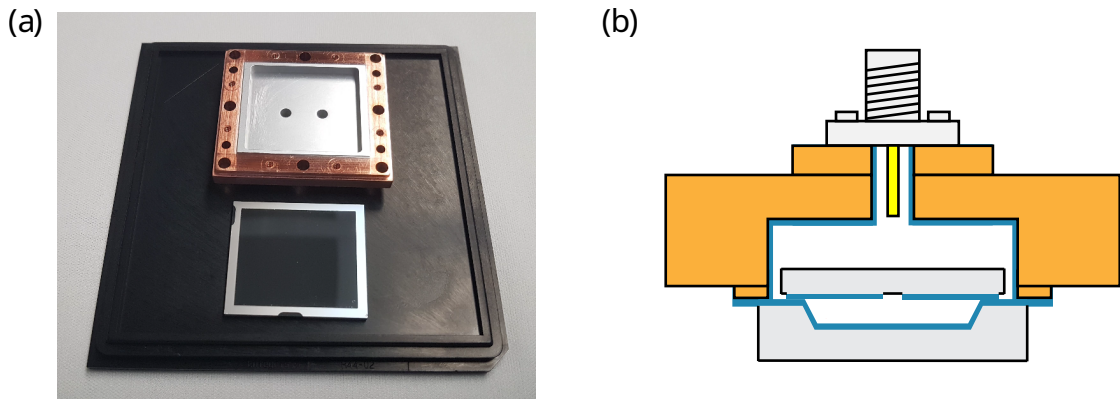


Figure 3.8: (a): Assembled micromachined cavity (bottom), ready to be bonded to its coupler (top). (b): Diagram of the coupling mechanism for the micromachined cavity. A copper cavity is partially coated with $10\text{ }\mu\text{m}$ of indium via evaporation (the rest of the cavity is masked with kapton tape). The cavity is then bonded to the micromachined cavity, flat-to-flat: it is not necessary for the copper cavity to be particularly high- Q . A standard coupling pin is then inserted into the copper piece.

3.4 Micromachined Cavity Measurements

The cavity is set up for measurement in reflection. The measurement chain is fairly standard: the cavity is mounted to the base stage of a cryogen-free dilution refrigerator (base temperature around 15 mK), inside a Cryoperm magnetic shield. Aside from cable attenuation, there is a 20 dB attenuator on the 4 K stage, and a 30 dB attenuator at base on the input line. The signal is then routed through a 10 dB directional coupler: the input signal enters the coupled port, is directed to the input port

of the coupler, which is attached to the micromachined cavity. The signal reflects off the cavity, and 90% of it is directed to the through port of the coupler. It is then directed through two isolators, followed by a [high-electron-mobility transistor \(HEMT\)](#) amplifier at the 4 K stage. The signal is finally routed outside the fridge, where, depending on the measurement, it may be amplified by an additional low-noise room-temperature amplifier.

We fabricated several cavities of different depths (100 μm – 1500 μm). The deeper cavities required thicker silicon wafers (2 mm max), and sometimes over 24 hours of etching. We performed both frequency-domain (Sec. 2.5.1) and time-domain (Sec. 2.5.2) measurements. Fig. 3.9 shows a sample measurement for a cavity of depth $d = 1500 \mu\text{m}$. a) shows frequency-domain measurements at two signal powers which differ by 10 orders of magnitude, demonstrating that the cavity does not change in this range. Note that the internal Q is over 300 million, this is several times better than even bulk stub cavities! The corresponding lifetime is over 5 ms, which at the time, was the longest published lifetime for a superconducting microwave cavity in the single-photon regime with a demonstrated coupling to a transmon. Note also that the cavity is very close to being critically coupled, meaning Q_i is well-resolved. b) shows a time-domain ringdown measurement for the same cavity. Note that the τ obtained from the fit is a loaded decay, meaning that it includes the coupling loss. Also note that it is consistent with the frequency-domain measurement, which gives a $Q_{\text{tot}} \approx 150 \times 10^6$. This indicates that pure dephasing is negligible in the system, and confirms our measurement techniques.

Let us now consider how the losses of the cavity scale with d , the only variable parameter between the different cavities. Intuitively, both surface and conductor participations should scale as t/d and λ/d , respectively, since $t \ll d$ and $\lambda \ll d$. We can verify this by calculating the participations explicitly for the TE101 mode of a rectangular cavity, which is essentially what a micromachined cavity is, since d is

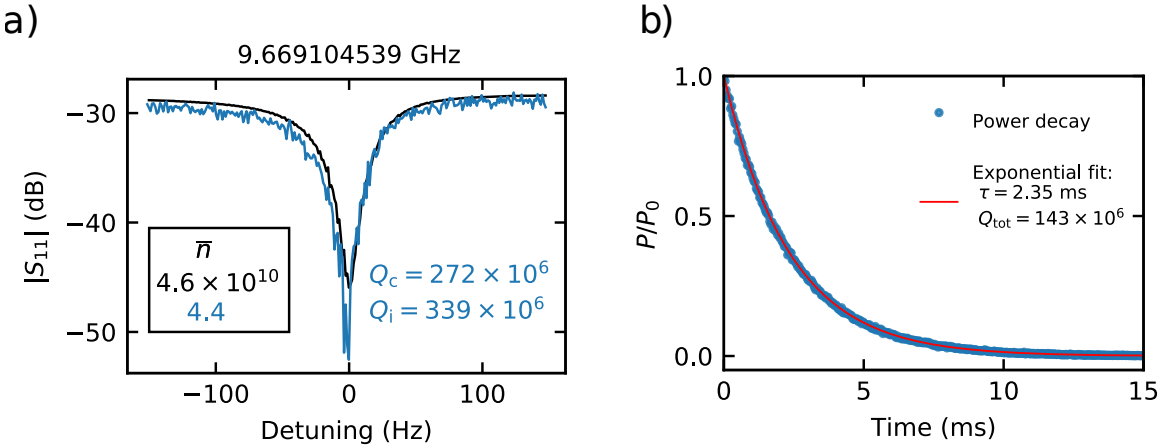


Figure 3.9: Sample frequency-domain (a) and time-domain (b) measurements of a micromachined cavity with depth $d = 1500 \mu\text{m}$. In a), the black line represents data taken at an average occupation of 4.6×10^{10} photons, the blue – at 4.4 photons. Note that the two are very similar, demonstrating the stability of the mode over many orders of magnitude of input power. Also note that the mode is almost critically coupled, meaning the Q_i is well-determined. In b), the blue points are the raw data of a ring-down measurement, and the red line is the exponential fit. Note that this includes loss to coupling: we can find the internal decay time by taking Q_c into account. Adapted from Appl. Phys. Lett. 116, 154002 (2020), with the permission of AIP Publishing.

much smaller than the other two dimensions, call them a and b . The fields can be found from solving Poisson's equation:

$$\begin{aligned} E_z &= E_0 \sin\left(\frac{\pi x}{a}\right) \sin\left(\frac{\pi z}{b}\right) \\ H_x &= -i \frac{\pi E_0}{k\eta b} \sin\left(\frac{\pi x}{a}\right) \cos\left(\frac{\pi z}{b}\right) \\ H_y &= i \frac{\pi E_0}{k\eta a} \cos\left(\frac{\pi x}{a}\right) \sin\left(\frac{\pi z}{b}\right), \end{aligned}$$

where $\eta = \sqrt{\frac{\mu_0}{\epsilon_0}}$, $k = \frac{\omega}{c} = \sqrt{\left(\frac{\pi}{a}\right)^2 + \left(\frac{\pi}{b}\right)^2}$. From this, we calculate the participations:

$$\begin{aligned} p_{\text{cond}} &= \frac{\lambda \int_S |\vec{H}_\parallel|^2 ds}{\int_V |\vec{H}|^2 dv} = \frac{\omega \mu_0 \lambda}{\eta} \frac{2\pi^2}{k^3} \left(\frac{1}{b^2} + \frac{1}{a^2} \right) \frac{1}{d} \propto \frac{1}{d} \\ p_{\text{surf}} &= \frac{t \int_S \epsilon |\vec{E}|^2 ds}{\int_V \epsilon |\vec{E}|^2 dv} = \frac{2t}{\epsilon/\epsilon_0} \frac{1}{d} \propto \frac{1}{d} \\ y_{\text{seam}} &= \frac{4\pi^2}{\eta k^3} \left(\frac{1}{b^3} + \frac{1}{a^3} \right) \frac{1}{d} \propto \frac{1}{d} \end{aligned}$$

From this we see that all of the three loss channels scale as $1/d$ for the micromachined cavity. Therefore, we expect the Q of the cavities to increase linearly with d . Let us now look at the data for all of the measured cavities, see Fig. 3.10. We see that indeed, the Q increases as expected. We also see that the cavities are fairly consistent in quality, across multiple batches, multiple cooldowns, and multiple nominally identical devices. For our deepest cavities, we obtain Q consistently over 200 million. In principle, we could obtain even higher Q 's by etching deeper cavities into thicker silicon wafers.

Let us consider whether the cavities were limited by the seam. Fig. 3.10 b) plots the micromachined cavity results on the familiar seam plot. Although it appears that all of the points lie along a line of constant y_{seam} , this is actually not an indication of being limited by the seam. Recall that that is only true if y_{seam} is the only loss channel that changes between the different devices. In this case, *all* of the loss channels scale exactly the same way with d , the only parameter. Therefore, *any* of the three known loss channels limiting the cavities would look like this! Since the cavities are still more than an order of magnitude away from the lower bound of indium bump bond y_{seam} , it is probable that the cavities are instead limited by surface dielectric or conductor loss, and our seam is indeed not a large contribution.

Aside from just measuring Q_i for various cavities, we have two more control knobs which we can vary in the experiment: input power and temperature. Fig. 3.11 (a)

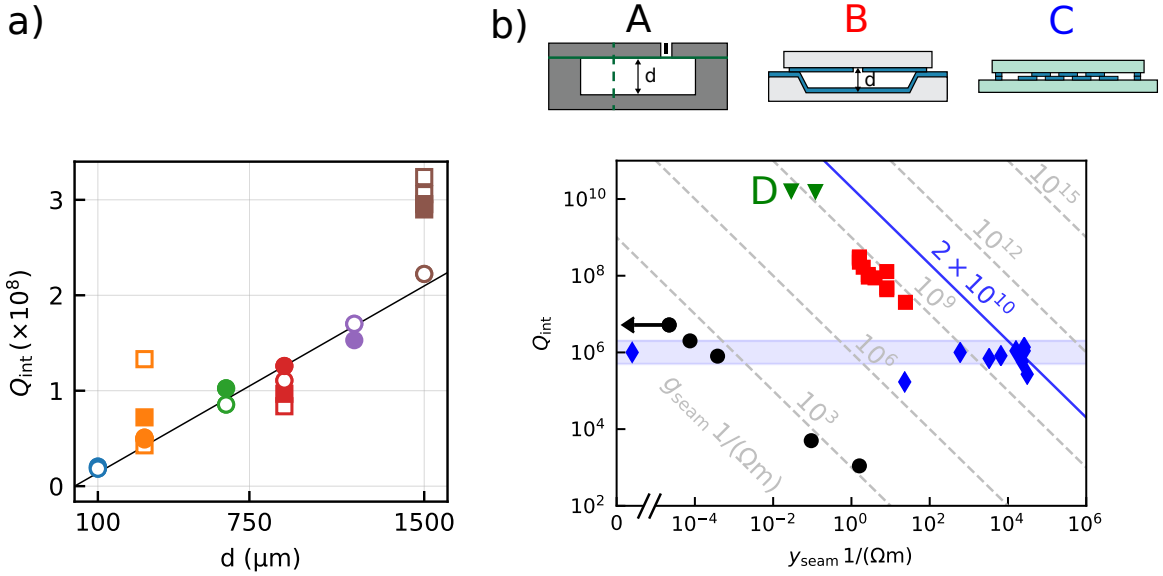


Figure 3.10: Results of measurement of several micromachined cavities. a) Extracted Q_i as a function of depth, for all of the measured cavities. The cavities were made in two batches, represented by squares and circles. They were also measured over two cooldowns separated by more than three months, represented by open and filled markers. The cavities were made in six nominal depths: 100, 300, 650, 900, 1200, and 1500 μm , represented by the different colours. The solid line is a fit for devices from the second batch, with $Q_i(d = 0) = 0$. b) The seam plot with micromachined cavity data included. The black devices are the aluminium 6061 cavities, red – the micromachined cavities, blue – the interrupted seam striplines, and green comes from [Romanenko et al., 2020]. Note that the micromachined cavities do not reach the g_{seam} limit from the interrupted striplines. Although the cavities lie along a line of constant g_{seam} , we must note that all of the participations of the cavity scale together, which means that they are likely limited not by seams but another loss mechanism. Adapted from Appl. Phys. Lett. 116, 154002 (2020), with the permission of AIP Publishing.

shows us power sweeps for the various cavities. The abscissa is written in terms of average photon number rather than power, as given by (for reflection):

$$\bar{n} = \frac{P_{\text{in}}}{\hbar\omega_0^2} \frac{4Q_l^2}{Q_c}. \quad (3.2)$$

We use photon number instead of power because our operating regime for quantum information storage is defined in terms of \bar{n} and is around 1. Since we do not have direct access to \bar{n} , we need to fit the resonances to extract Q_l and Q_c to convert from P_{in} , which we set directly in the experiment. Note that this is simply a re-scaling: \bar{n}

is linear in P_{in} .

We have measured the cavities over around ten orders of magnitude of circulating photon number. We have measured many of them down to single-digit photon numbers, and we see very little change in Q_i , allowing us to assume that the value at ten photons is likely the same as at one photon. We observe that the change in Q is much smaller than that found in planar resonators, e.g. [Pappas et al., 2011, Quintana et al., 2014, Calusine et al., 2018], changing by less than a factor of 2 over the whole range of photon numbers tested. This is similar to other 3-D resonators. Since we have not measured the full **TLS** curve, we can only estimate the critical photon number n_c , which looks to be around 10^9 for the micromachined cavity. We note that if we **TLS**'s themselves are identical in the different devices, n_c should scale with the volumes. Presumably, identical **TLS**'s should be saturated by the same electric field, and the larger the mode volume, the more dilute the field is, and the more energy is needed to achieve the same critical field. The mode volume of a micromachined cavity is on the order of millions of times larger than a typical **CPW** resonator. The maximum value of the electric field at a single-photon power is on the order of mV/m for a micromachined cavity, and hundreds of mV/m to a V/m of a **CPW** resonator. The critical photon number for a **CPW** resonator can be on the order of 1000 [Dunsworth et al., 2017], which is therefore consistent with our **TLS** having similar properties. We do not expect other loss mechanisms to be dependent on \bar{n} , although resonators with seams do occasionally become non-linear at relatively low powers. Therefore, since we see a change in Q_i with increased \bar{n} (and therefore saturating **TLS**), it is likely that the **TLS** are one of the factors limiting the Q_i of the cavities.

Fig. 3.11 (b) shows us temperature sweeps for the cavities. This is achieved via a simple resistive heater at the base of the fridge. We see two regimes: up to around 500 mK, the Q_i is increasing with temperature. This is the thermal saturation of **TLS**'s. Since **TLS** loss is the only loss channel that should change with temperature

(until we get to a larger fraction of T_c , when there starts to be a non-trivial fraction of thermally broken Cooper pairs, this confirms that **TLS** loss is one of the limiting factors of the cavity. We can fit this loss using Eq. 2.6:

$$\frac{1}{Q_i} = \frac{1}{Q_i(T=0)} + p_{\text{TLS}} \tan \delta_{\text{TLS}}^0 \tanh \left(\frac{\hbar \omega}{2k_B T} \right) \nu,$$

where p_{TLS} is the participation in the physical medium containing the **TLS**'s, widely believed to be surface dielectric, and ν being the \bar{n} -dependent factor, which is constant for every trace as it is taken at a constant power, and is also very close to 1, as $\bar{n} \ll n_c$ for our measurements. The result of the fits (up to $T = 500$ mK is shown with the lines. If we assume that p_{TLS} is indeed given by the participation in a 3 nm-thick surface oxide with $\epsilon_r = 10$, we obtain a $\tan \delta_{\text{TLS}}^0 = (5.6 \pm 1.6) \times 10^{-3}$. This is comparable to the $\tan \delta_{\text{TLS}}^0$ found for aluminium resonators which is around 10^{-3} [Pappas et al., 2011, McRae et al., 2020a].

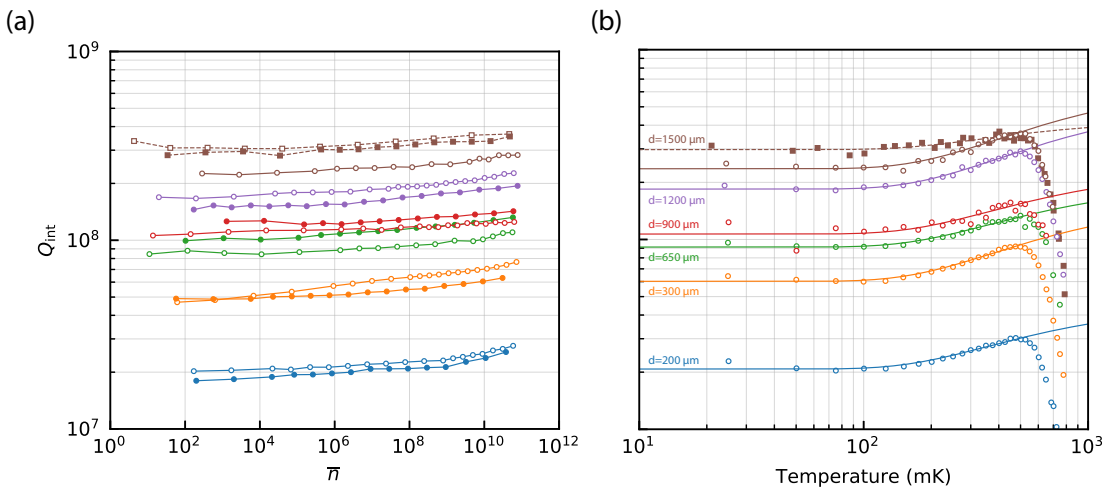


Figure 3.11: Power (a) and temperature (b) sweeps of Q_i for micromachined cavities. The power sweeps span around ten orders of magnitude, revealing a very small change, compared to planar resonators. This change is likely attributable to **TLS** loss in the surface dielectrics. The lines are guides to the eye. We likewise see a small change in temperature (up until several hundred mK, at which point Mattis-Bardeen takes over). We can fit this to the **TLS** model, as shown by the lines. Adapted from Appl. Phys. Lett. 116, 154002 (2020), with the permission of AIP Publishing.

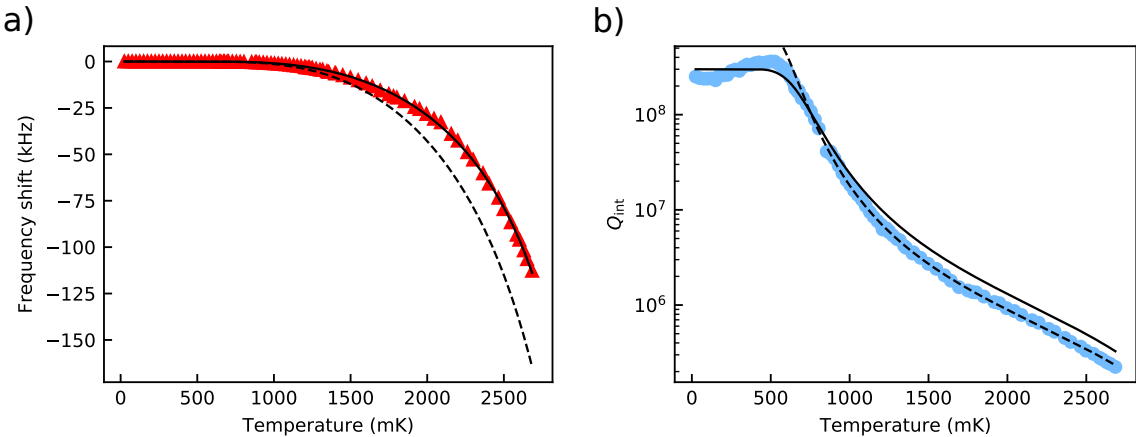


Figure 3.12: Plot of fits of the resonant frequency (left) and internal quality factor (right) as a function of temperature of a micromachined cavity of depth 1490 μm . The solid line uses parameters extracted from the frequency fit and the dashed line uses parameters extracted from the Q fit. The fit is obtained using the Mattis-Bardeen result. For the Q fit, we only use $T > 700 \text{ mK}$, as the lower temperatures are influenced by [TLS](#), see above. The frequency fit has two free parameters: T_c and p_{cond} , which correspond to scaling in the x and y directions, respectively. The Q fit has Q_0 as an additional parameter. The fits presented here assume the local limit of the superconductor; we do not present plots of the fits in the extreme anomalous limit as they would be indistinguishable from these. We extract T_c between 3.2 and 3.4 K and λ between 32 and 68 nm. Reproduced from Appl. Phys. Lett. 116, 154002 (2020), with the permission of AIP Publishing.

The second regime occurs at the higher end of the temperature scale – this is when Mattis-Bardeen loss comes into play, see section 2.3.1. To better explore this region, it is necessary to sweep through higher temperatures. Ideally, one would cross T_c to fully cover the curve, however, this generally requires multiple measurements, as the Q_i drops significantly as T increases, so either we are strongly overcoupled at low T , and thus cannot extract a Q_i , or we are too strongly uncoupled at high T to be able to measure the mode. Since the T_c of our indium is around 3.4 K, getting to this temperature is somewhat more involved – we need to turn off the dilution fridge turbomolecular pump, since the pressure gets to high. We also sometimes need to manage the helium mix, and it is more difficult to stabilise the fridge at these temperatures.

| Fit, limit | T_c (K) | λ (nm) |
|----------------------|-----------------|------------------|
| Frequency, local | 3.29 ± 0.01 | 32.35 ± 0.66 |
| Frequency, anomalous | 3.17 ± 0.01 | 42.98 ± 0.72 |
| Q , local | 3.35 ± 0.03 | 51.80 ± 2.44 |
| Q , anomalous | 3.24 ± 0.04 | 67.92 ± 4.01 |

Table 3.1: Mattis-Bardeen fit results in two limits for a micromachined cavity.

A sample temperare sweep of a micromachined cavity is shown in Fig. 3.12. a) shows the frequency shift and b) the change in Q . Note that the region from 0 to around 500 mK in the Q graph is dominated by TLS loss. We can fit each plot to the Mattis-Bardeen theory as presented earlier. Frequency can be fit with two parameters: T_c and $p_{\text{cond}} = \alpha$; Q_i requires an additional parameter of Q_0 to capture all of the other loss mechanisms at $T = 0$. We can fit frequency and Q_i separately, and then use that to predict the other curve. In Fig. 3.12, the solid line represents the frequency fit, while the dashed line represents the Q fit. We can see that the two fits do not quite match each other, indicating that there is something unaccounted for by our theory. This is still an open question: it is possible to make this work via an extra empirical parameter, e.g. scaling α differently for frequency and Q , but that is not motivated by physics. Furthermore, sometimes, both fits fit both graphs.

We cannot distinguish which fit is better, therefore we present the results of all in Table 3.1. Between the two fits, we extract a T_c between 3.2 K and 3.4 K, and penetration depth between 32 nm and 68 nm. These are close to expected values. The table value for indium T_c is 3.4 K, so we likely can trust our values. Although the λ range is a factor of two, it is still a useful metric. In fact, this is close to what is expected for aluminium (50 nm being generally given as a nominal value).

3.5 Micromachined Cavity Outlook

In summary, we have demonstrated that a micromachined cavity can reliably attain lifetimes in the several millisecond range. This is several times larger than what is routinely achieved with high-purity bulk-machined cavities, even though the micromachined cavity has a less favourable geometry (d is smaller than is typical in machined cavities). This is likely the case because the thin-film superconductors deposited on a crystalline substrate have lower losses than bulk superconductors which have been machined. Furthermore, the micromachined cavity is fabricated using lithographic methods and standard, easy-to-automate bonding.

The coupling of a micromachined cavity to an aperture transmon [Minev et al., 2016] has already been demonstrated [Brecht, 2017]. The immediate next step would be to demonstrate coupling to an aperture transmon with the improved cavity, which has a lifetime 100 times larger than the previous design. In principle, one should be able to use the method from the previous work directly with the new cavity, especially since the indium/aluminium seam has been found to be high quality without any additional layers. If a Purcell filter is needed, it can be easily added via another cavity above the readout, since it does not need to be high-Q. Then, making devices with multiple micromachined cavities side-by-side (or stacked vertically) would be an important step in demonstrating the scalability of the architecture. It may also be useful to couple them to planar resonators, as in [Brecht et al., 2015], although fabricated on a crystalline substrate rather than a [PCB](#). Finally, through-silicon vias would provide an additional tool in the [MMIQC](#) architecture, see e.g. [Mallek et al., 2021, Grigoras et al., 2022].

CHAPTER 4

Suspended Coaxial Resonators

In the previous chapter, we discussed a fully-lithographic way of producing high- Q superconducting microwave cavities. Although I anticipate that in the long term, when development is happening in foundries rather than university cleanrooms, or perhaps when devices include hundreds of resonators rather than fewer than ten at most, such an approach will prove to be scalable, in the near term, the advantages do not seem to outweigh the costs of switching to a new architecture. Therefore, it is important to develop resonators for the intermediate regime, which will allow superconducting bosonic quantum computing experiments to move beyond the several-device limit. We still seek to improve the scalability of the devices, both in terms of production, and in terms of configurability. As before, high Q is desirable feature.

In this chapter, I shall discuss several ways to approach this that fall under the broad category of suspended coaxial resonators: coaxial resonators in which the centrepin is made separately from the outer conductor, and held in place inside of it. Broadly speaking, these devices have several advantages. Since the centrepin is a separate piece, it is generally possible to replace it without having to replace the

entire rest of the assembly. This is very helpful for devices with more than one or two resonators, in cases where we need to change the frequency of one, or perhaps replace it because it has been damaged, which is much easier and cheaper than making the entire system over from scratch. We also gain the ability to make the outer conductor and centrepin from different materials, or subject them to different treatments, which can be used both for materials characterisation, and to improve the quality of a device, if, for example, a material or process can be used in one of the pieces, but would be impractical or impossible in the other. It is also allows us to avoid the complicated machining of a stub at the bottom of a cavity. Finally, we gain a useful dimension compared to coaxial stub cavities, as it may be possible to stack multiple resonators within one enclosure along the axis, as well as tiling them in the transverse plane. See Fig. 4.1 for a comparison of a tiling of 3×3 stub cavities vs. a cartoon of how suspended coaxial resonators may be tiled along the different dimension.

In section 4.1, I describe several approaches of holding a rod in a tunnel to form a resonator, and provide measurement results. In section 4.2, I describe ways to hold a chip-based stripline “centrepin”, and provide data from measurements. Finally, in section 4.3, I summarise the results and describe potential future work.

4.1 Suspended Rod Resonators

A natural way to make a suspended coaxial resonator is by suspending a superconducting rod inside of a tunnel. Electromagnetically, this looks just like a stub cavity that has been reflected across the bottom ground plane, see Fig. 4.2. Of course, the road cannot float in air (well, vacuum), and must be held in place with some sort of dielectric (a conductor would significantly modify the mode, and likely ruin the Q with seam losses). There are many different ways to do this, from the straightforward “hold it in place with a PTFE clip” to the more exotic “hang it by Kevlar threads

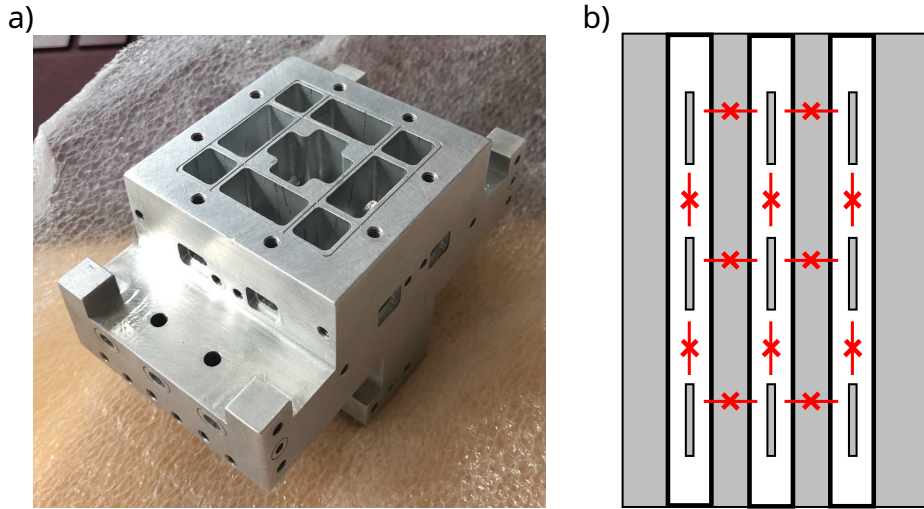


Figure 4.1: a) Photograph of a 3×3 tiling of stub cavities (courtesy of Chris Wang). The stubs are located at the bottom of each tunnel, and are not visible from this angle. Note that this is a monolithic structure: to replace any of the resonators, the entire device must be fabricated from scratch. Additionally, note that the cavities can only tile in two dimensions: it is not possible to fit more than two stub cavity resonators on top of each other (two is possible if they are machined to be back-to-back). b) A cartoon of a possible realisation of stacking of suspended coaxial resonators along the long dimension. The resonators are held in place in a tunnel (the mechanism can vary, and is not depicted), with multiple resonators fitting into one tunnel. They are coupled via Josephon-junction based elements (on chips which are also not depicted) in much the same way as in a). As with stub cavities, tiling in and out of the page is also possible.

epoxied to screws". In this section, I shall describe several different ways to hold the rod with plastic clips.

4.1.1 Plastic Clamp, Rod Considerations

When deciding how to clamp the rod, several factors must be taken into account.

1. The clamp must not significantly decrease the Q of our mode
2. The clamp must work at milliKelvin temperatures
3. The clamp must be resistant to vibration (the exact frequencies at which this must be true are somewhat unclear, although it seems that several tens of Hz to

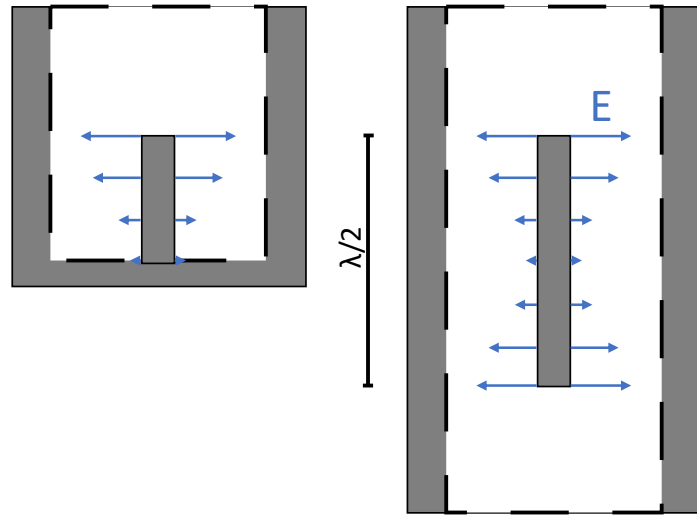


Figure 4.2: A coaxial stub cavity (left) has exactly the same mode structure as a suspended coaxial rod (right), neglecting the supports. Note that since the stub cavity is grounded at one end and open at the other end, it forms a $\lambda/4$ resonance, compared to the $\lambda/2$ of the rod.

several kHz covers the common range of vibrations seen in resonators, as well as a large part of the frequency content of the pulse tube)

The first criterion could be fulfilled by a material such as sapphire or silicon, but it is difficult to imagine making a functional clamp from them. Therefore, we can make do with a somewhat lossier material and place it in regions of low electric field to minimise participation (note that this won't let us get away with something too lossy: if $\tan \delta = 10^{-3}$, we would need an unrealistically small participation of 10^{-4} to even get a Q limited to *at most* ten million. As mentioned above, some exotic method such as Kevlar threads might work, but this is non-trivial to achieve in practice, so we started with something more straightforward. From so-far unpublished results with the dielectric dipper [Read* & Chapman* et al., 2022], we know that for some types of PTFE we can expect $\tan \delta \approx 10^{-7}$. Of course, there are many different kinds of PTFE, and cryogenic microwave loss tangent is certainly not a factor for which anyone generally controls, so we can expect it to vary quite a bit; nevertheless, this should be a good starting point.

To address the second requirement, we must take into consideration the fact that when cooled to milliKelvin temperatures from room temperature, PTFE shrinks by around 2%, while aluminium shrinks by around 0.4%. This means that if we simply hold our rod inside an aluminium package with a piece of PTFE, the relative contraction will likely cause the connection to become loose. One way to overcome this is by using spring-like clamps, which are pre-compressed by more than the expected relative shrinkage. We expect these to still provide a returning force even at cryogenic temperatures. We can also cleverly engineer our clamps such that they tighten, rather than loosen, when cooled.

To address the third requirement, we must consider the different degrees of freedom of the centre rod, and eliminate them using the clamps. It is fairly straightforward to prevent motion in the transverse plane, just by filling part of the space between the rod and outer conductor. Preventing tilting is more challenging, but if we make sure to have more than one clamp spaced sufficiently far apart, it is still not too difficult. The most challenging is the “battering ram” mode, in which the rod moves along its axis. We cannot place dielectric on the edges of the rod, as the electric field will always have an antinode there. Therefore, we have to rely on the friction from the clamps, which themselves can be anchored to transverse rails in the outer conductor. To understand what we are trying to prevent, we note that although an ideal coaxial resonator is first-order insensitive to motion in the transverse plane, there are always some asymmetries, and also note that since we want Q 's in the tens of millions, even small shifts can cause noticeable effects. Motion along the axis, on the other hand, can affect coupling Q , which is actually exponentially dependent on position.

When it comes to the rod itself, our concerns are twofold:

1. q_{cond} and q_{MA} of the material should be high
2. The mechanical properties should be compatible with the clamping mechanism.

Both of these depend strongly on what material is used for the rod. There are three obvious choices: a cold-worked (e.g. rolled or extruded) wire, a machined rod, or a superconducting coating on top of some other material. We tried the first two, for something similar to the third option, see Sec. 4.2. Some notes on potential differences: the different fabrication processes may result in different properties of materials, even if they are nominally of the same composition, so 4N aluminium wire will likely be different from a machined piece of 4N aluminium. Wire that is too thin will also bend.

4.1.2 Single-piece Clips

The easiest way to suspend a rod is with a single piece of PTFE for each clamp. The simplest shape for a clamp is a PTFE cylinder with a hole for the rod in the centre. This can be made from cutting a PTFE dowel with a razor and then drilling a hole, or from cutting part of the dielectric in a coaxial cable. It may be necessary to cut part of the cylinder off in order to fit it into the tunnel. A more intelligent approach is to design a clamp, such as the one in Fig. 4.3 a)/b), which can grab the rod and also compress when inserted into the tunnel. These are traditionally machined from bulk PTFE. Since the PTFE shrinks more than most metals, it will grab onto the rod, and if it has been compressed by more than it will shrink, it will also remain compressed when cooled, retaining restoring force on the walls. We can hold such a clamp in place with plastic screws such as in Fig. 4.3 c), further preventing motion along the axis.

Since we want to minimise the participation in the dielectrics, we can choose to use the λ mode, which has two electric field nodes in which we can place the clamps, as in Fig. 4.3 d). By measuring both this mode, and the mode above (or below), which will have a much higher participation in the dielectric, we could determine whether we are limited by the dielectric clamps. Note that in reality, the dielectric

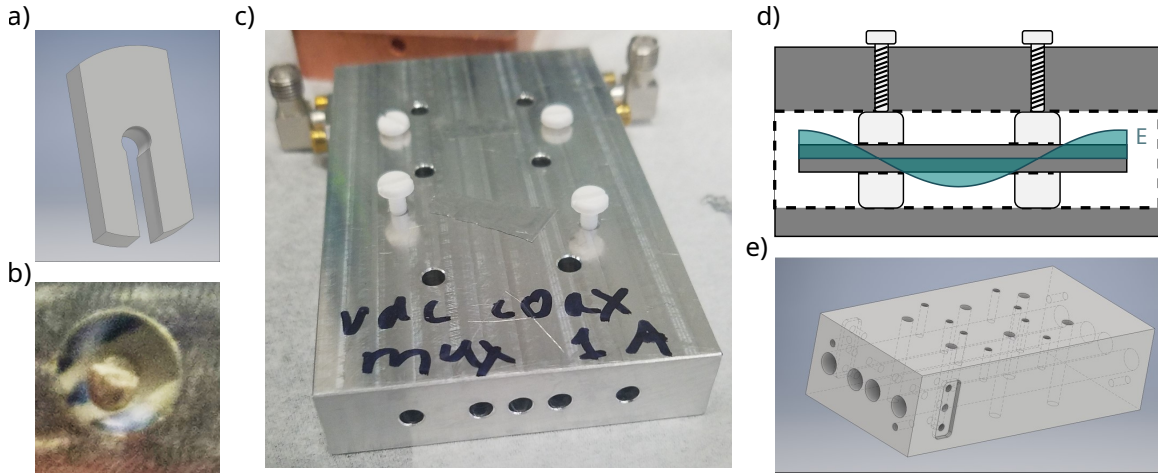


Figure 4.3: a) CAD drawing of a machined PTFE clip. The rod is inserted into the centre hole, then the whole clip is inserted into the outer conductor. The fork end of the clip is compressed by this. b) A photograph of a clip from a) in action. Note the bending of the two tines. c) A photograph of a first-generation package for the suspended rod resonator, including plastic screws for holding the clamps in place. d) A diagram of λ mode of a suspended rod resonator. Note that for this mode, the clamps are at the electric field nodes, suppressing dielectric participation. e) A CAD drawing of a second-generation package for suspended rods, this time wider, such that the participations are essentially the same as for a standard stub cavity.

constant of the clamps will somewhat distort the mode from the standard cosine, not pictured. To minimise the participation, we have to make the clamps as narrow as possible. Luckily, the participation scales as t^3 for small thickness t : the electric field is linear in t near the minimum of $|\vec{E}|$, and thus $\int_{-t/2}^{t/2} |\vec{E}|^2 dt \propto t^3$. For typical dimensions, a thickness on the order of a couple of millimetres is sufficient for sub-percent participation.

We made two types of package for this experiment: aluminium 6061 packages with relatively thin tunnels, Fig. 4.3 c), and an etched (see A.4) high-purity aluminium package with wider tunnels, resulting in participations like in the standard stub cavity designs, Fig. 4.3 e). The thick tunnels also allow us to use thicker centre conductor rods, such as ones made of machined 5N aluminium. Note that we expect etched 5N Al to have higher material quality than 6061 or unetched 5N Al, as per stub cavity results (and other measurements). We also tested a variety of centrepins, namely:

hand-cut wires of aluminium, niobium, tantalum, and NbTi, as well as machined aluminium.

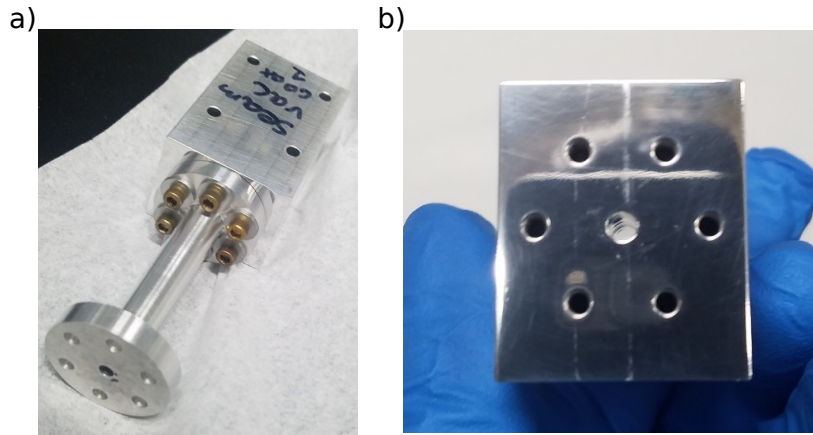


Figure 4.4: a) Photograph of an assembled suspended rod resonator with a seam. The two parts have different shapes only for ease of assembly and machining, there is no fundamental difference between the two. b) Polished face of one of the two parts before assembly.

We also made a package containing a seam right at the centre, in order to test the use of rod resonators as a bus (e.g. [Burkhart et al., 2021]). Fig. 4.4 a) shows a photograph of such a device. Inside the tunnel is a suspended rod; the seam between the two pieces is directly at the centre of the mode of the rod. The two pieces making up the outer conductor have different shapes due to practical concerns, there is no fundamental reason for any difference between the two. In order to improve the quality of the seam (recall, g_{seam} for plain aluminium 6061 is around $1000/(\Omega m)$, and y_{seam} will be quite high for this mode), we polish the mating surfaces. In other experiments, we have found that by careful polishing, we can attain g_{seam} of several $\times 10^5/(\Omega m)$. As before, we can measure several modes in order to distinguish the seam loss from other losses: for non-seam-sensitive modes, y_{seam} ranges from $(0.5 - 1) \times 10^{-3}/(\Omega m)$, whereas the seam-sensitive mode has $y_{\text{seam}} = 0.4/(\Omega m)$. We polish the surface by manually lapping it with progressively finer grits of sandpaper (with water), and then finishing off with a cloth and a chemical abrasive cream called Pikal care. Although we did not do it for this device, it is possible, with additional rounds of Pikal care

and sufficient skill to polish the aluminium to a mirror-like state. For better results it is also good to use a very flat surface, such as a special sheet of glass, under the sandpaper.

Having assembled several resonators of slightly different frequencies (controlled via different lengths of the centre conductor rod) into one multiplexed package, we measure their frequencies and Q 's in hanger configuration. Fig. 4.5 shows the data for suspended rod resonators in the 6061 aluminium package (Fig. 4.3 c)). We used four different materials for the centrepin: high-purity aluminium wire, 3N niobium wire, 3N8 tantalum wire, as well as a piece of superconducting coaxial cable centrepin made of NbTi. All of the wire was solvent cleaned, and none was etched. For each of the resonators, we were able to measure the λ mode (Fig. 4.3 d)), which is mode 2, as well as the next harmonic, mode 3. Mode 2 of each device lies to the left of the dashed line, while mode 3 – to the right. We note that the clips are positioned such that mode 2 has very low participation in them (on the order of a percent), while mode 3 has much higher participation (tens of percent). Therefore, if a device is limited by the clips, we would expect mode 3 to have much lower Q (the other participations are similar, though not identical). We also note that most of the devices had clips as in Fig. 4.3 a), except for one Al wire which had instead clips made from coaxial cable dielectric.

There are several results of note. First, it appears that Al and Ta make for better resonators than Nb and NbTi, reaching Q 's of around a million. Next, we note that there does not appear to be a significant drop in Q from mode 2 to mode 3, indicating that the clips do not limit us at Q of a million. Cooldown-to-cooldown variation is sometimes large (a factor of ~ 2), and sometimes negligible. In one of the cooldowns, we cycled the fridge above T_c of the superconductors several times, after which all of the Q 's improved, some by a factor of 3. We also note that some of the resonators experience very large vibrations. For example, the tantalum wire's resonance shakes

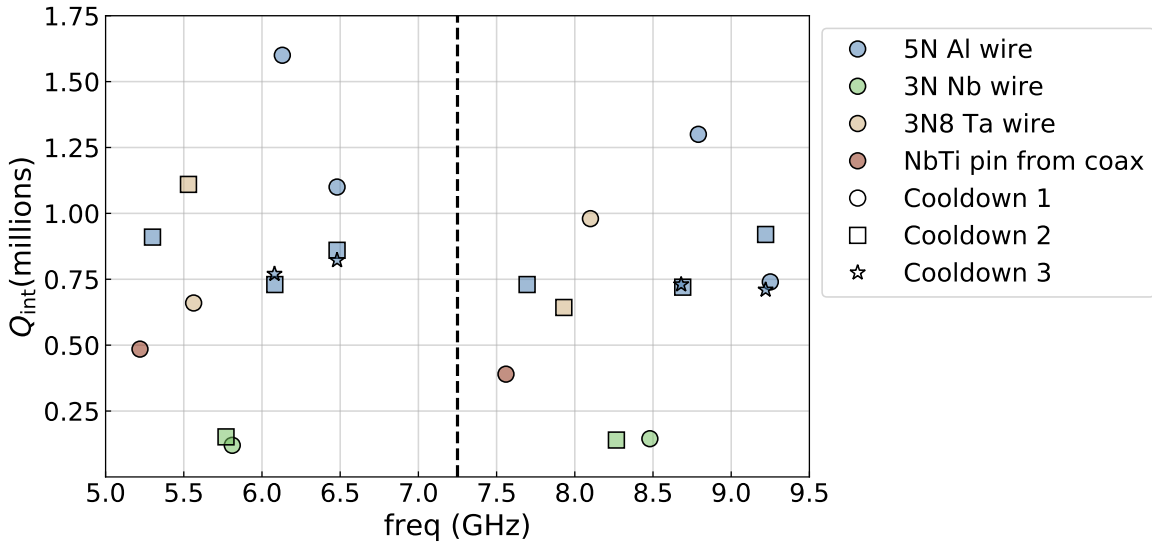


Figure 4.5: Measurements of suspended rod resonators with various centrepin materials in an aluminium 6061 package. The different materials are indicated by colour, and comprise three wire materials and NbTi cut out of a superconducting coaxial cable. Some of the devices were measured in multiple cooldowns, indicated by the marker shape. Each resonator had two modes in the bandwidth of all of the equipment; all of the first modes are left of the dashed line, and the second modes are right of the dashed line. For each given material and cooldown, the first and second modes of the devices are in the same order in frequency, allowing devices to be directly matched. The first mode is the one shown in Fig. 4.3 d), with several percent participation in the dielectric clips, while the second mode is the next harmonic, with much higher participation in the clips. Almost all of the dielectric clips are as in Fig. 4.3 a), except for the $\sim 6.5/9.3$ GHz 5N Al wire device in all three cooldowns, which used a spacer cut from coaxial cable dielectric. All of the wires were cleaned with solvents but not etched.

visibly (as in, the frequency moves over less than a second and is visible in the VNA).

When the pulse tube is turned off, the shaking improves, and the extracted Q is almost twice as high. We also performed ringdown experiments on some of the resonators. Generally, the T_2 was almost twice T_1 , although some of the none-Al samples seemed to have visible dephasing. This was likely due to visible shaking of the mode. Finally, I note that we did not measure the resonators down to single-photon level. Instead, we measured the power-dependencies of the Q 's and stopped when it seemed that the Q was changing sufficiently little – in practice, this tended to be around $10^2 - 10^5$ photons, see Fig. 4.6. If we assume that the power dependence is caused by TLS loss

in the MA, this is roughly consistent with critical photon number expected for a 3-D resonator with a fairly small gap. There was no drastic difference between the metals used, although we did not carry out a careful analysis.

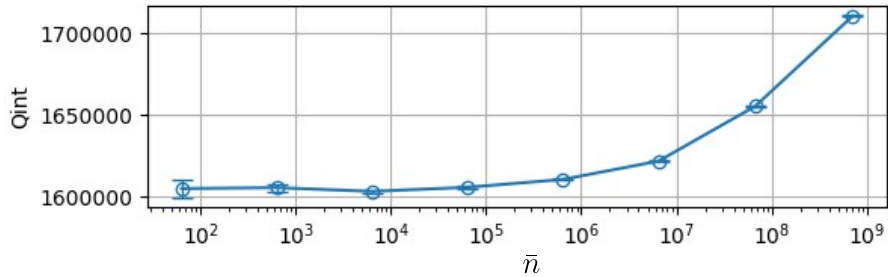


Figure 4.6: Power dependence of the Q_i of the 6.2 GHz suspended 5N Al wire from cooldown 1, see Fig. 4.5. Note that it becomes fairly flat at around 10^7 photons.

Next, I mention the measurement results for the seam package (Fig. 4.4), which was 6061 Al with an aluminium wire as the rod. We were also able to measure two modes for this device, although instead of modes 2 and 3, we measured modes 3 and 4. The frequencies were 5.59 GHz and 7.53 GHz, with respective Q_i 's of 330,000 and 920,000. Mode 3 is seam-sensitive, with $y_{\text{seam}} = 0.4/(\Omega \text{m})$, while mode 4 is insensitive; assuming a 10 mil machining offset to the seam, $y_{\text{seam}} = 10^{-3}/(\Omega \text{m})$. This is consistent with mode 3 being limited by a seam with conductance $g_{\text{seam}} = 1.3 \times 10^5/(\Omega \text{m})$. Although we would likely not want to use this device as a resonator, it actually shows large promise as an inter-device bus: even with the seam in the worst place, and with the simplest possible construction, we were able to achieve a Q_i almost ten times larger than in [Burkhart et al., 2021]. The importance of being able to do this with a seam present is that unless the entire network is constructed monolithically (which is antithetical to a modular architecture), a bus connecting multiple parts must necessarily have a seam. I also note that we were able to achieve a seam with $g_{\text{seam}} \geq 1.3 \times 10^5/(\Omega \text{m})$ with hand-polishing, without even attaining a mirror-like finish.

Let us now discuss the results for the suspended rods in an etched 5N aluminium

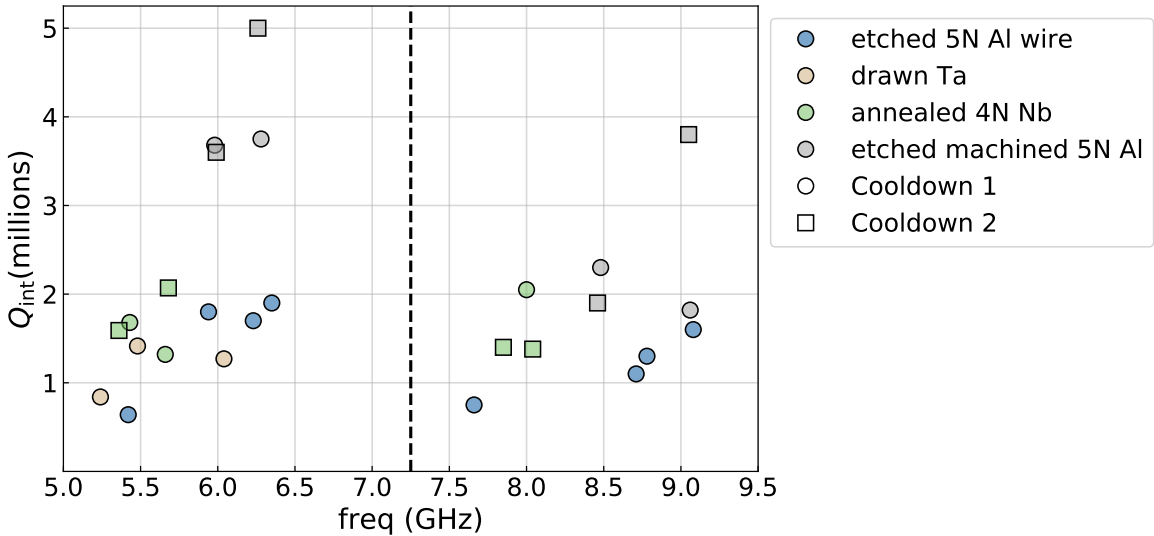


Figure 4.7: Measurements of rod resonators in an etched 5N aluminium package. The different materials are indicated by colour, and comprise two etched types of 5N aluminium (wire and machined rod), drawn Ta rods, and annealed 4N Nb rods. As in Fig. 4.5, two modes were measured for some resonators, with mode 1 left of the dashed line and mode 2 – right. Some devices were measured in two different cooldowns, indicated by marker shape.

package: Fig. 4.7. Note that we have increased the dimensions to approximately match that of a stub cavity, which will allow us to have more favourable participations in the case of a thin wire, and to accommodate thicker rods. As before, we have several different materials used for the rod, some of which are measured in multiple cooldowns. Again, we measure modes 2 and 3, with 2 left of the dashed line. In this case, the materials are: drawn Ta rods, annealed 4N Nb, etched 5N Al wire, and etched machined 5N Al rods. As we expected, the machined rods perform better than the other materials; there are no other clear trends. For the highest- Q devices, mode 3 does seem to have a lower Q than mode 2, but a Q of almost 4 million was measured once there, so it does not seem that we are limited by the PTFE at least at that level. It is worth noting that we once again see vibrations, especially in the Nb rods, see Fig. 4.8 for an example of a VNA trace demonstrating this behaviour.

One additional type of measurement we can perform is a temperature sweep. If the inner and outer conductors are made of different materials, we can even see the

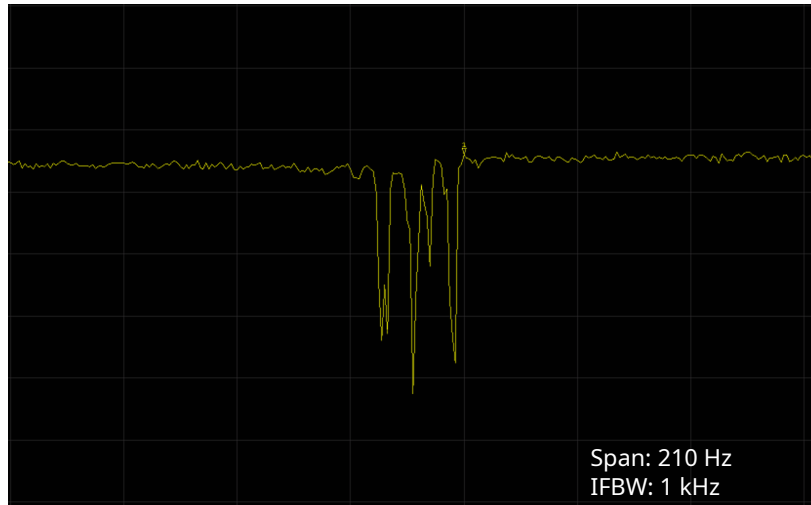


Figure 4.8: The shaking of a mode in a suspended Nb rod resonator, as seen on the [VNA](#). This is a single sweep: after averaging many times, the result is a much wider but smoother curve.

transitions separately, see Fig. 4.9 a) for an example. Here, we sweep temperature on a Ta rod in a 6061 Al package. The two transitions are clearly visible, although Ta is harder to see due to the mode becoming severely undercoupled at higher temperatures, as well as the fridge becoming harder to stabilise. We can then use Mattis-Bardeen to fit the temperature sweep, e.g. Fig. 4.9 b). Note that in this case the temperature sweeps are only valid up to a little under T_c because we did not properly take into account the presence of the second superconductor, however, it would be fairly straightforward to modify the code to fit both. We did not attempt to perform careful fitting, since machined 5N Al turned out to be noticeably better than the other metals, so we did not need to know their properties as well. However, from the fits, we were able to confirm that our high-purity etched Al has approximately the expected penetration depth of 50 nm, whereas the 6061 Al used for the package has a larger penetration depth of 200-250 nm. This can be seen from the Q_i fit: since normal metal has a $q_{\text{cond}} = 1$, $p_{\text{cond}} \leq 1/Q_i$ where the Q_i is taken just above T_c for the lower T_c metal. The bound should also be quite tight if the Q_i changes drastically between 0 and this temperature, and if the other metal's T_c is a lot larger than the

T_c of the lower- T_c metal.

Let us summarise the results obtained. Using simple tunnels drilled in an Al package together with wire and PTFE clips, it is fairly easy to get resonators with Q_i on the order of a million. It is also straightforward to make sufficiently good seams such that if one were placed in the worst possible place on such a resonator, the Q_i can still be in the hundreds of thousands – it can likely be around a million with more intelligent placing of seams. By using machined 5N Al for both the outer and inner conductors, we can increase the Q of the resonators to several million. We can also swap the suspended rods in the resonators as needed. Finally, we can use the fact that the centre conductor can be made of a different material than the outer conductor to perform some material characterisation, namely find T_c and penetration depth of the materials. On the other hand, the resonators made this way are not very reliable: their Q can vary by several times cooldown to cooldown. They are quite challenging to assemble (the clips need to be pushed in a specific order to make sure they end up where they are supposed to, it is difficult to gauge exactly where the pin is). They also suffer from vibration issues. Finally, the machined 5N parts are not as good as expected. The exact causes are unclear, possibilities include the fact that either the conductors or the clips are damaged during assembly (with the clips possibly leaving PTFE residue on the conductors), as well as the fact that cleaning and etching these tunnels may not work as well as for the shorter stub cavities (black residue, presumably from machining, can be seen and is difficult to remove).

4.1.3 Two-piece Clips

In order to mitigate some of the challenges encountered with the one-piece clips described above, we developed another suspension mechanism for rods. The two main changes are that the package is now made of two parts, removing the need for sliding the centre conductor through it, and that the clips are designed more carefully,

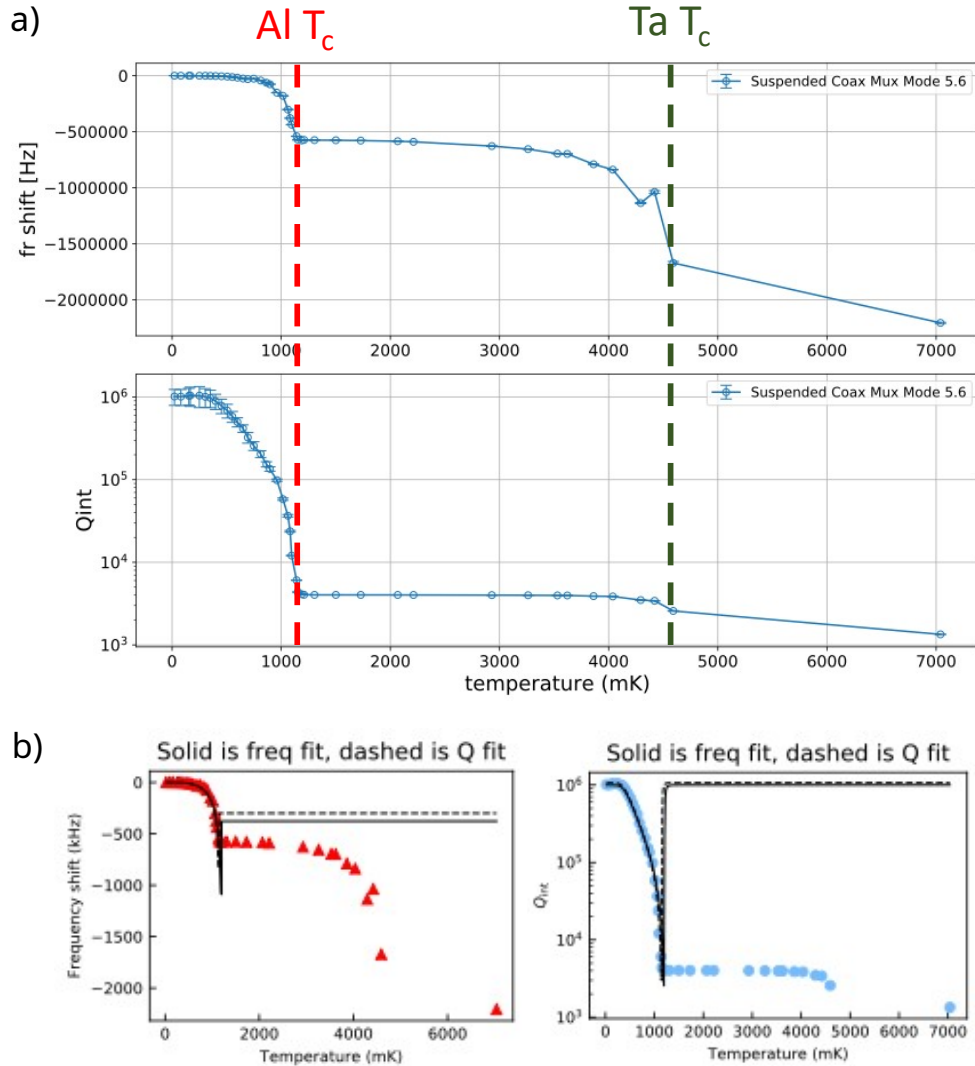


Figure 4.9: Temperature sweep of a suspended Ta wire in a 6061 Al package. a) Frequency shift and Q_i of the resonator as a function of temperature. A clear transition can be seen at the point where the aluminium outer conductor goes through T_c (near the known value of 1.2 K for bulk Al), while the Ta rod still remains superconducting. Resolving the Ta transition is more difficult, since the Q has dropped so much that it becomes difficult to resolve the mode; also, stabilising the temperature of the fridge becomes more and more difficult as the temperature increases. Nevertheless, a transition can still be seen near the measured value of ~ 4.5 K for bulk Ta. b) Fits for the frequency and Q_i of the above (note: **fits are only valid to slightly under T_c**). It would be fairly straightforward to modify the Mattis-Bardeen fitting procedure to account for two metals, although this was not done. Note that since normal metal has $q_{\text{cond}} = 1$, it is possible to upper bound p_{cond} of the lower- T_c metal via $1/Q_i(T = T_{c,\text{lower}} + \epsilon)$. Here, we see that Al 6061 has a higher p_{cond} than expected by a factor of around 5, indicating that the penetration depth is larger than the simulation value of 50 nm by about that factor.

of two pieces. In this section, I describe the new design and some considerations that went into it. I shall not present any measurements, since this device was not actually made – instead, we made suspended stripline resonators, as described in section 4.2.

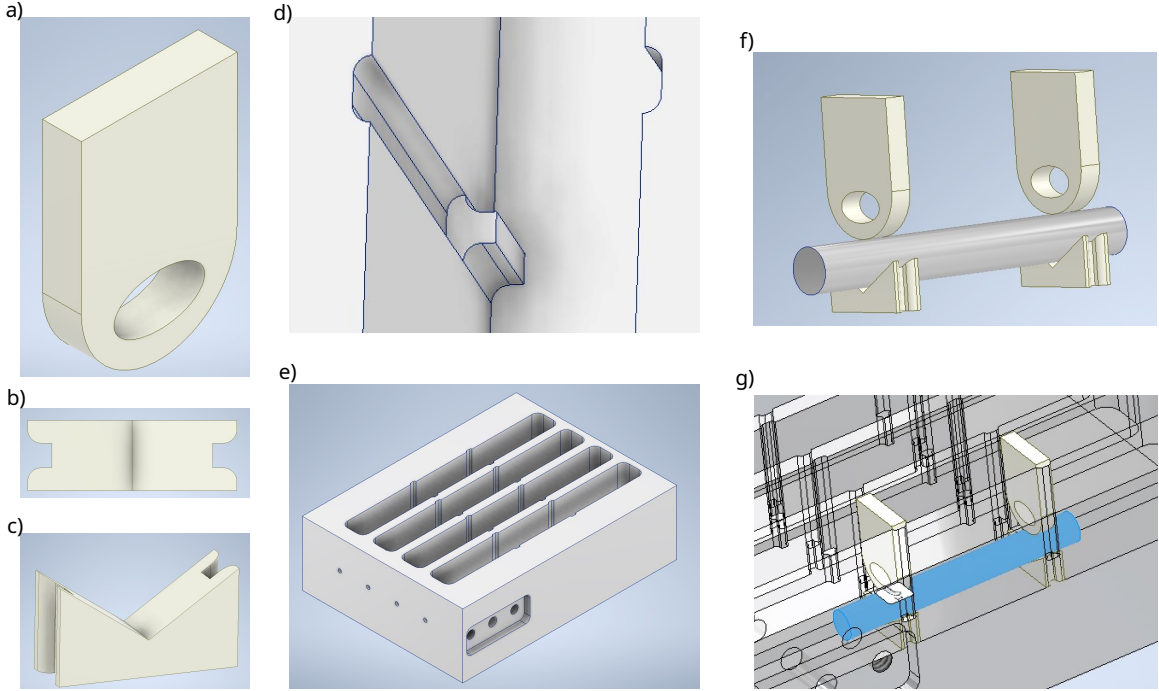


Figure 4.10: [CAD](#) drawings of a rod suspended with two-piece clips. a) Isometric view of the top clip. The hole allows the arch to compress. b) Top view of the bottom clip. c) Isometric view of the bottom clip. d) Railing in the side of the package for the clip. The bottom clip grips onto the protruding railing with the slots in its sides, and will shrink onto them when cooled. The top clip slides into the slots in the package. e) A multiplexed package for four rods. The holes in the sides allow for precise positioning of the rod. f) Assembly of the rod and two clips. The bottom clip's triangular shape prevents the rod from sliding in the transverse plane. g) Assembly of the rod (here coloured blue) and two clips mounted inside the package.

The design can be seen in Fig. 4.10. a) through c) show different views of the clips. Let us recall our requirement list for clips from the previous section. To avoid spoiling the Q_i of the mode, we keep our clips thin, 2-3 mm. The top clip is slightly narrower than the bottom, in order to ensure stability. To retain restoring force at cryogenic temperatures, we make a hole in the top clip. This allows the remaining arch to compress by more than the thermal contraction. There are a number of features to deal with motion in various directions. The bottom clip is a triangle, against which

the top clip will push the rod. This prevents motion of the rod relative to the clips in the transverse plane. Next, note that the bottom clip has slots for corresponding rails in the package. When cooled, the clip will grip onto the rails due to differential contraction, preventing motion of the clip relative to the package. The top clip is guided by slots in the package. Finally, the top clip will be pushed down by the lid of the package (not pictured), which will be bolted to the main package part. This style of package, dubbed “seammux”, was originally created for multiplexing several chips in hanger configuration, see [Axline, 2018] pg. 82. Although there is a seam present, its effects can be minimised by placing the seam farther away from the centre conductor than the other ground planes (as well as by increasing g_{seam} , see discussion in citation above). In this case, the seammux is modified to accommodate suspended rods. Since this design does not require sliding the rods through a tunnel, and is much more open (presumably leading to better etching), it should be able to achieve Q factors comparable to that of the stub cavity, assuming similar dimensions.

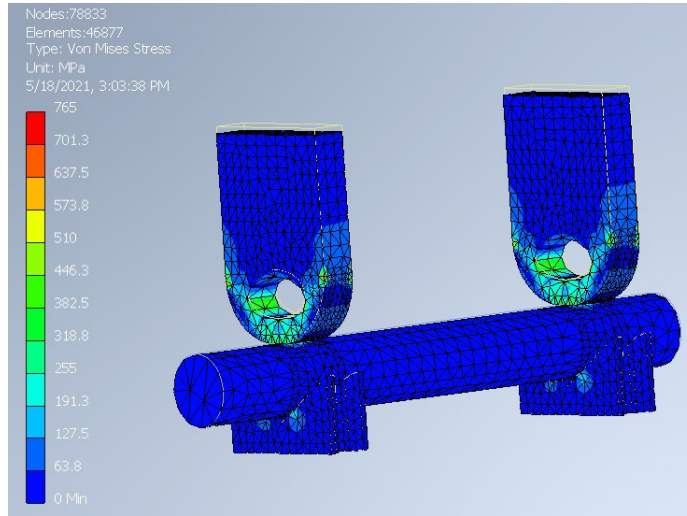


Figure 4.11: Inventor model of stress in the two-piece clip. Mechanical properties for the materials need to be found in literature, as they change depending on temperature.

Let us now briefly discuss the mechanical considerations that went into the clip design. In order to make sure the clip holds the rod as tightly as possible without permanently deforming, we need for the stress inside the **PTFE** to not exceed the

compressive yield strength, the point on the stress-strain curve where any additional strain results in non-elastic deformation (i.e. plastic deformation, in which the object no longer returns to its original shape after the strain is removed). Of course, if we're okay with single-use clips, we could go a bit further to its ultimate compressive strength, exceeding which would break the clamp. We can approximate the maximum stress in the arch (which is clearly where largest stress should be) using Euler-Bernoulli beam theory, and approximating the arch as a beam of rectangular cross-section. The displacement will be set by the difference between the height of the package, and the combined height of the two clips and rod, remembering to take thermal contraction into consideration when necessary. Performing this calculation using the modulus of PTFE from [Reed et al., 1973], get an approximate maximum stress of a few hundred MPa. We can also simulate the structure. This can be done in Inventor (although at a very basic level without purchase of additional simulation software), or in COMSOL structural mechanics. Fig. 4.11 presents such a simulation in Inventor, showing a rough agreement with our approximate calculation. The last important factor is friction: the mechanical properties of PTFE change when it is cooled: it shrinks significantly, becomes harder, and likely, its coefficient of friction changes. Although it's difficult to find tribological studies in a relevant regime, one can easily verify that PTFE becomes much more difficult to grip when cold by dunking it in liquid nitrogen and attempting to pull it with tweezers. However, I was unable to find a measurement of the coefficient of friction in conditions sufficiently similar to mine.

Although the above mechanical analysis is not complete, it would likely be possible to hold the rod with clips such as these, although vibrations may still be a problem. In practice, I would not continue trying to simulate the system, but rather just build it and measure it. Electrically, there is no reason why the result should not be as good as a stub cavity. However, I did not end up actually making such a device. The mechanical considerations made the design fairly complicated, and it turned out that

there is a better way to make a centre conductor, as described in the next section.

4.2 Suspended Stripline Resonators

In this section, I describe a different design for a suspended coaxial resonator: the suspended stripline. Electromagnetically, the structure is fundamentally the same: a centre conductor suspended coaxially in the outer conductor. However, for the physical centre conductor itself, we shall use a new structure. We take a cross-shaped crystalline chip (more detail to come in the next section) and evaporate metal on all sides of one of the bars, see Fig. 4.12. This forms the centre conductor, while the other bar forms the dielectric supports, the two being thus combined into one object.

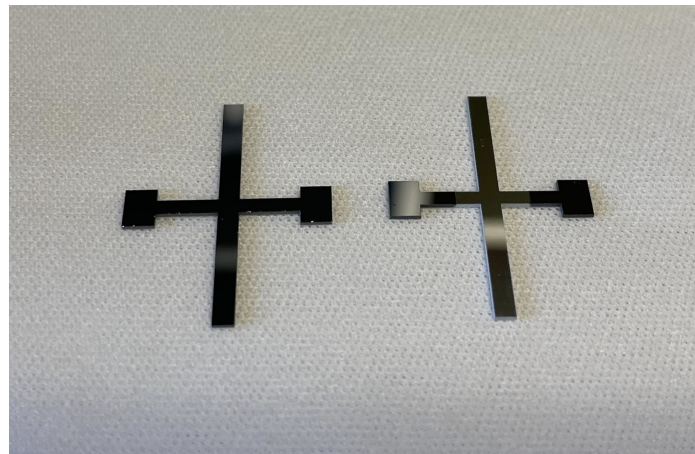


Figure 4.12: Two silicon chips lasercut into crosses for use as suspended stripline centre conductors. The left is plain, the right has had aluminium evaporated all around its vertical bar, as well as halfway down the side bars.

Compared to a suspended rod, a suspended stripline has two advantages. First, the conductor is a thin film on a crystalline substrate rather than a bulk metal, and thus is expected to have a higher quality. Second, the dielectric supports are smaller, less lossy, and also attached to the conductor, helping with mechanical stability. Compared to a regular (3D) stripline [Axline et al., 2016], a suspended stripline can have much lower substrate participation, permitting a higher Q . A regular stripline

stores something like 50% of its energy in bulk dielectric ($p_{\text{dielectric}} \approx 0.5$). For standard EFG sapphire we typically use, $\tan \delta_{\text{bulk}} = 6 \times 10^{-8}$ [Read* & Chapman* et al., 2022]. This would limit a stripline to a Q_i of around 30 million just from the bulk dielectric, without considering the SA interface. It may be possible to improve this by a factor of several using the more expensive and hard-to-obtain HEMEX sapphire, but the presence of dielectric still places a fundamental bound on the quality of the resonator. For the suspended stripline, by using modes with electric field nodes at the centre (i.e. the $n\lambda/2$ modes), we can decrease the dielectric participation to significantly under 1%, giving us a much larger fundamental limit (this is the same thing we did with the suspended rods, except we now have dielectric clamps only at the centre instead of at two places, so the modes of choice are different). For these reasons, we expect a suspended stripline to have a high Q and be relatively resistant to mechanical motion, while keeping the scalability advantages described at the beginning of the section. In section 4.2.1, I shall describe the design of the centre conductor. In section 4.2.2, I describe the design and present the measurements for a package with a seam; in section 4.2.3 – for a seamless package.

4.2.1 Suspended Stripline Centre Conductor

Let us first discuss how we actually obtain the chips we use to make our centre conductors. Currently, we use the services of an external company to laser ablate silicon or sapphire wafers into the shape seen in Fig. 4.12. Sapphire is harder to cut than silicon, and is thus more expensive. For this reason, we used 500 μm -thick silicon chips, and 100 μm -thick sapphire chips. Both types of chips were cut successfully (although the thin sapphire proved to be quite fragile and many chips broke).

Since we will be coating the chips in metal from all sides, the quality of the sidewall is important. Micrographs of the edges of the chips are pictured in Fig. 4.13. Some amount of re-deposition and damage on the sidewall are visible. Note that sapphire

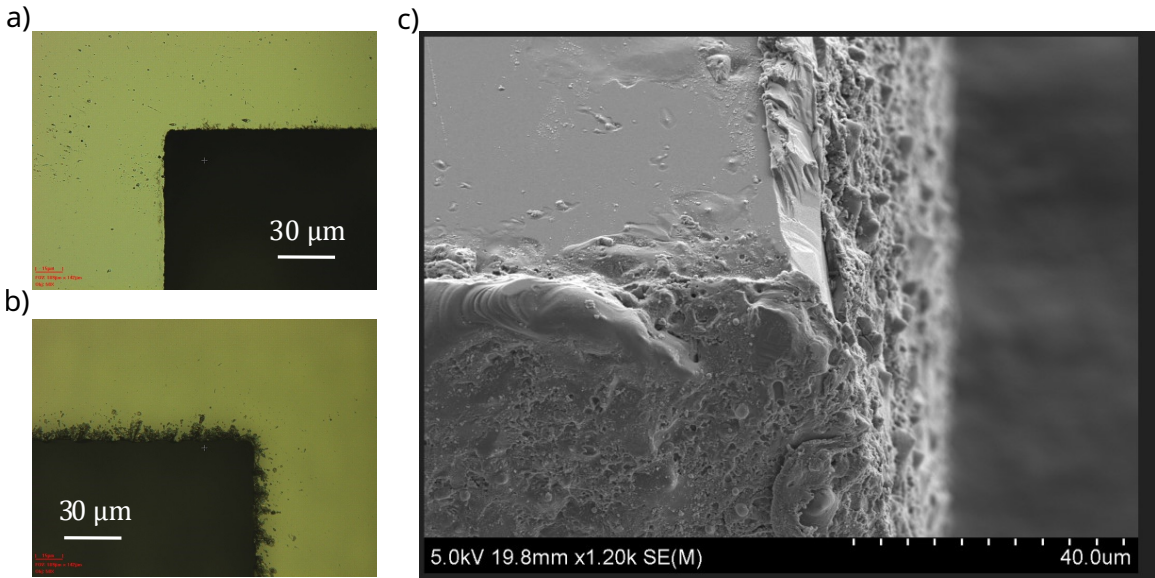


Figure 4.13: a) Optical micrograph of an inner corner in a laser-cut silicon chip. Re-deposited matter and roughness on the edges are visible. b) Optical micrograph of an inner corner in a laser-cut sapphire chip. The roughness is much worse than for the silicon chip. c) SEM of the corner of a laser-cut silicon chip. Several-micron-scale peaks are ubiquitous. Note that the edges of diced chips tend to have much larger scallops (tens of microns), at least for sapphire. This image is taken after metallisation with a few hundred nanometres of Al; it does not look noticeably different prior to metallisation.

has rougher edges due to the difficulties associated with cutting it. Nevertheless, the scale of the damage appears to be less than for traditional dicing. We have tried covering the chips with photoresist to protect them from re-deposition during the laser cutting, and then stripping off the resist afterwards. This appears to somewhat decrease the amount of visible re-deposited particles, but does not eliminate it – it is unclear whether this is better. Since our process does not require lithography, we are free to aggressively clean the chips before metal deposition, whether it be piranha, BOE, or even full **RCA clean**. We did not attempt to determine whether this increases the quality factors of the resulting devices.

After the chips are fabricated, they need to be coated in a superconductor. We do this by evaporating aluminium onto the chip while it is rotating at 45° to the evaporation direction, see Fig. 4.14 a). To do this, we have made a custom 45-

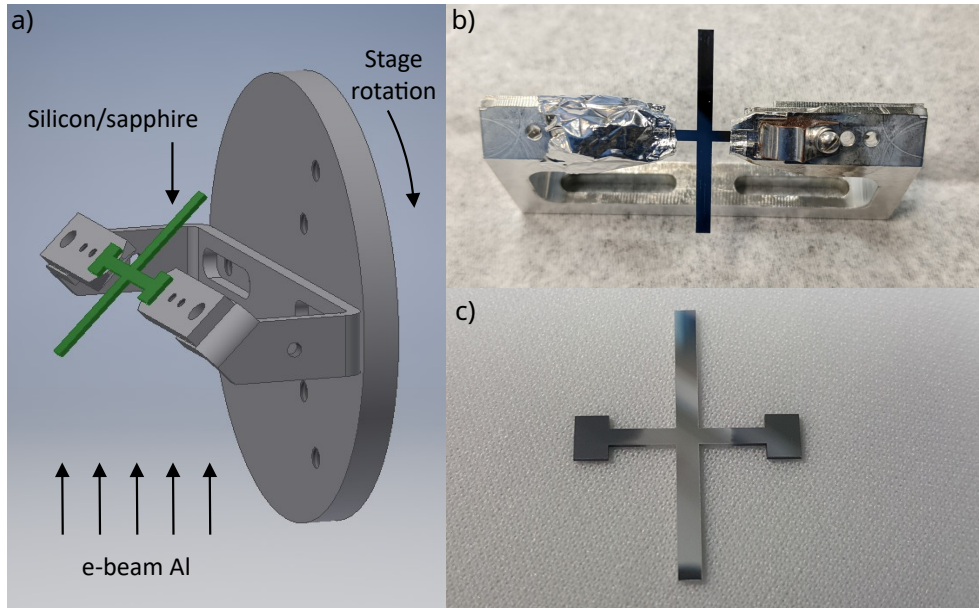


Figure 4.14: a) CAD drawing of a suspended stripline chip in the metal evaporator. The stage rotation allows for the central bar to be coated evenly from all sides (the number of rotations during one evaporation is much larger than one). b) A photograph of a sapphire chip in the clamp used for the evaporation, with aluminium already evaporated onto it. The right side shows the BeCu clip used to hold the chip to the clamp, the left side also shows the aluminium foil used to shadow the evaporation. c) A silicon chip with aluminium evaporated on it. The right side was shadowed well, forming a straight line, while the left was not, resulting in extraneous metal.

degree holder for the chip which mounts to the sample stage of our evaporator. The evaporator itself has two rotation axes, allowing us to tilt the sample and then rotate during the evaporation. The sample is held to the mount with a BeCu clip on each side. Since we do not want to metallise the parts of the chip to be clamped, we mask them from evaporation with aluminium foil. Fig. 4.14 c) shows that it is possible to get good masking if one is sufficiently careful. It would, of course, also be possible to do this lithographically with liftoff or etching, or just to dip the chip into etchant carefully afterwards. Both of these methods introduce extra factors which may contribute to loss and were not found to be necessary.

4.2.2 Suspended Stripline Seam Package

I now describe a package for suspended stripline resonators which is made of two parts, and thus contains a seam. This work was predominantly carried out by my colleague Chan U Lei; I include it in this thesis for completeness. The two parts are machined too have a cavity with sloped sidewalls and places to clip the suspended stripline and a non-linear control element (e.g. a transmon), see Fig. 4.15. The shape of the walls allows us to evaporate superconducting metals onto the surface of the cavity, giving us access to high-quality thin films, as well as a wider range of materials. Although this package has a seam, the expected $y_{\text{seam}} \approx 10^{-4}/(\Omega\text{m})$ for the storage mode, which should enable sufficiently high Q 's: if we polish or diamond turn the mating surfaces, we should be able to do better than $y_{\text{seam}} = 10^5/(\Omega\text{m})$, so we should not be limited in Q at the level of around a billion.

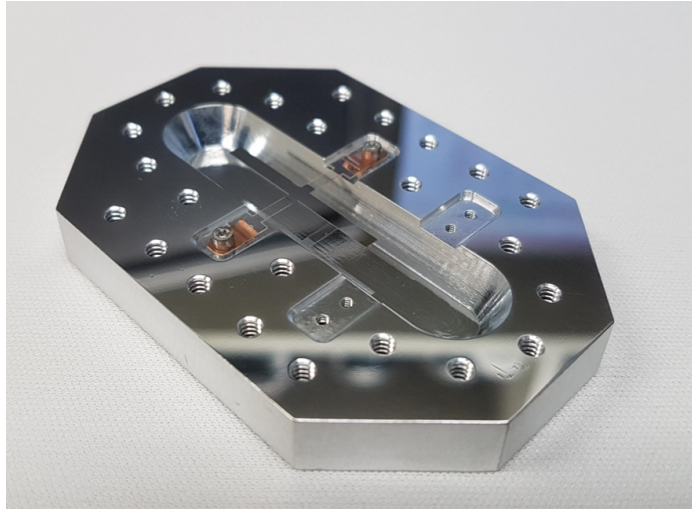


Figure 4.15: Sapphire stripline suspended in a seam package. It is held in place with a BeCu clip on each side. The walls of the cavity are slanted, allowing us to deposit metal on them. A space is left for a chip containing a transmon. The top part of the package (not pictured) is almost identical to the bottom, the one main difference is a coupling port placed directly over the centre of the suspended stripline chip. The cavity is polished ending with Pikal care, and the mating surfaces are diamond-turned.

Table 4.1 lists the simulated participations for a particular variation of the storage and readout modes of the suspended stripline in a seam package. Since we used

| Participation | Storage mode | Readout mode |
|-----------------------------|---------------------------------------|---------------------------------------|
| p_{diel} | 4.4×10^{-5} | 1.2×10^{-1} |
| $p_{\text{cond,stripline}}$ | 3.0×10^{-5} | 3.1×10^{-5} |
| $p_{\text{cond,package}}$ | 6.2×10^{-6} | 5.7×10^{-6} |
| $p_{\text{MA,stripline}}$ | 2.1×10^{-7} | 1.7×10^{-7} |
| $p_{\text{MA,package}}$ | 2.7×10^{-8} | 3.4×10^{-8} |
| y_{seam} | $1.1 \times 10^{-4}/(\Omega\text{m})$ | $1.4 \times 10^{-3}/(\Omega\text{m})$ |

Table 4.1: Participations for the seam package for a suspended stripline resonator. The storage and readout modes have almost identical participations, except the readout mode has thousands of times higher p_{diel} , and a factor of ten higher y_{seam} .

slightly different chips, the participations vary somewhat, but the general trends are the same. Note that the two are almost identical, except the bulk dielectric participation of the storage mode is thousands of times smaller than for the readout mode, as intended by the design. The admittance into the seam is also a factor of ten lower. The participation in the clips is negligible. We can use the participations together with our best ideas about what the quality factors are (see chapter 5) to write an expectation for the Q of the storage mode, which should be over 100 million, depending on the exact materials used.

Let us now discuss the measurements. We have made two packages: they are both of 6061 aluminium, with one having four evaporation of 400 nm of Al each, and the other – 4 evaporation of 200 nm of Al each. The aluminium is e-beam evaporated after 3 minutes of argon ion milling in order to improve remove the surface oxide and create better adhesion. The four evaporation are performed at different angles with the sample rotating 90° between them such that each slanted cavity face is towards the evaporation direction once (pretending that the cavity is rectangular and not filleted).

Table 4.2 shows the results of the measurements. First, we note that most of the devices had Q_i in the tens of millions, and two – over 100 million, demonstrating that this architecture can compete with stub cavities. Next, we note that the best devices were made on sapphire. This is interesting, since the storage mode has almost

| Package | Stripline chip | Stripline metallisation | $Q_{i,\text{refl}}$ | $Q_{i,\text{ring}}$ | Jitter |
|---------|-------------------------|-------------------------------|---------------------|---------------------|--------|
| 400 nm | 500 μm Si | 2 μm Al, no oxid | 44×10^6 | — | No |
| 400 nm | 500 μm Si | 2 μm Al, no oxid | 48×10^6 | — | No |
| 200 nm | 500 μm Si | 600 nm Al with oxid | 37×10^6 | — | A bit |
| 400 nm | 500 μm Si | 800 nm Al with oxid | 37×10^3 | — | No |
| 400 nm | 100 μm sapph | 600 nm with oxid | 108×10^6 | 140×10^6 | Yes |
| 200 nm | 100 μm sapph | 600 nm with oxid | 127×10^6 | 145×10^6 | Yes |
| 200 nm | 100 μm sapph | 600 nm Al no rot with oxid | 9.6×10^6 | — | Yes |
| 200 nm | 100 μm sapph | 800 nm Al with oxid | 37×10^6 | 33×10^6 | No |

Table 4.2: Measurements of suspended striplines in seam packages in reflection and ringdown. Two packages and several chips were used. All but the first two chips received a “capping” oxidation step in the aluminium evaporator in order to have more controlled oxide rather than native growth. One of the chips was not rotated during evaporation. Many of the devices demonstrated large amounts of jitter on the [VNA](#), indicating some sort of shaking. This tended to improve (but not necessarily disappear entirely) with the pulse tube turned off.

no participation in the substrate, and should therefore be insensitive to its material. There are two explanations: the aluminium grown on sapphire has different properties from the one grown on silicon, and that the sidewalls of the chips cause loss. The first does not seem particularly likely, as we have not observed any difference between the two, although we cannot rule it out without a materials study of the two. The second seems more plausible: we have seen that the sidewall of the chips is quite rough in Figure 4.13, and it seems likely that aluminium evaporated onto such a surface *would* have different properties than aluminium grown on a flat chip. Since the sapphire is five times thinner than the silicon, it has much less of this sidewall, leading to a decrease in the losses from this surface. I do note that this is also speculation, and further testing would be needed to prove this.

For unknown reasons, one of the devices was three orders of magnitude worse than the others; no cause for this could be found. Finally, we note that many of the devices displayed large amounts of jittering in the [VNA](#). This could be ameliorated, but not entirely removed, with turning off the pulse tube. The last device was clamped more tightly by placing a 100 μm -thick sapphire chip as an additional spacer. This seems to

have improved the vibration, but one of the arms of the chip was found to be broken upon opening the package. The vibrations could not be removed even by mounting the package to the dilution fridge with springs.

4.2.3 Suspended Stripline Seamless Package

An alternative approach is to create a package for the suspended stripline which does not have a seam. Advantages include not having to worry about the seam loss, as well as potentially simpler machining (although this was arguably not the case for our implementation). There may also be additional treatments which are possible with this geometry but not with the seam package, e.g. reaming out the tunnel. We were additionally able to incorporate a better clamping mechanism which removed the vibration issue; it is in principle possible to make something similar in the seam package as well.

A photograph as well as diagrams of our package are depicted in Fig. 4.16. The photograph depicts a view into the tunnel with the chips placed inside. There are two slots made in the walls of the package with wire EDM; one of the slots houses the transmon chip (magenta), the other – the centrepin chip (yellow, with metallisation in green). The rectangular cavity used as a Purcell filter (blue) is visible in the back. I also depict the seam that will be formed when the endcap is attached to the visible main piece. The dashed lines indicate the cross-sectional views, which are presented in diagram form.

The top view shows the two chips as well as the cavity. Several elements of the design have been removed from this view for clarity. We see the three pieces of the package: the main piece, housing the two chips as well as half of the Purcell cavity, the other half of the Purcell cavity, and the endcap. The endcap is placed far enough away in the region where the field exponentially attenuates that the seam loss is negligible, the same mechanism as for the stub cavity [Reagor et al., 2016]. The Purcell filter

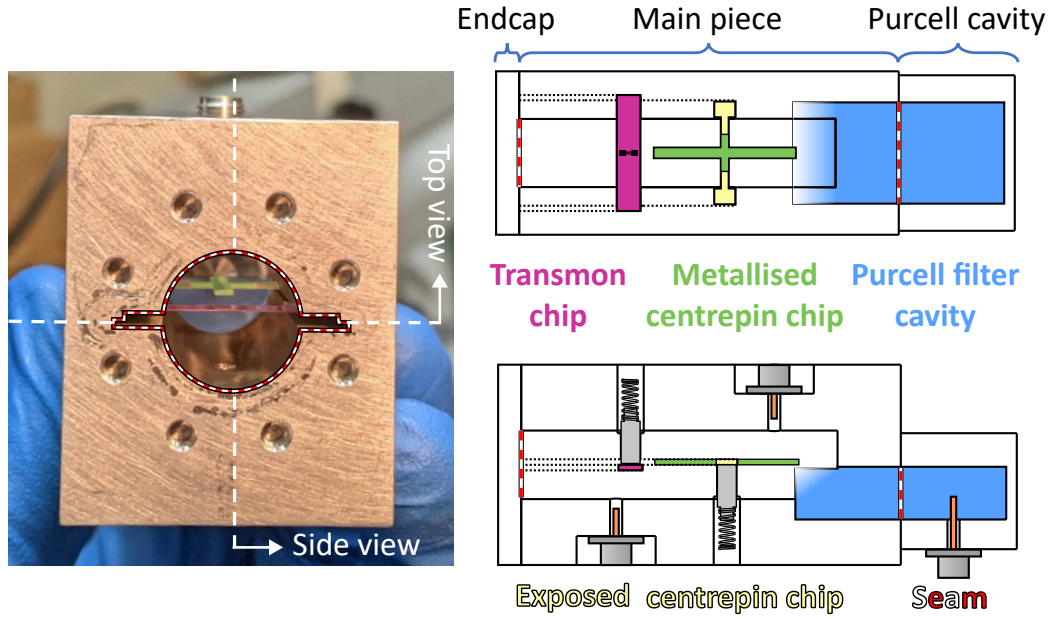


Figure 4.16: Seamless package for a suspended stripline. Left: photograph of the inside of the package, with the transmon chip, stripline chip, and Purcell filter cavity artificially coloured. The seam between the main piece and endcap is indicated with a red/white line. The two cross-sectional views are indicated with dashed white lines. Right: cross-sectional views of the package: top view on top, side view on the bottom. The chips, seam, and Purcell filter are coloured the same way as in the photograph. The side view also shows the three coupling pins, as well as the clamps and springs for the two chips (these are hidden in the top view for clarity). There are two seams between the three package pieces: one between the endcap and main piece (in the exponentially attenuated field region), and one in the middle of the Purcell filter (which has a low Q_c by design).

is realised in this design as a rectangular cavity, demonstrating the possibility of a 3D Purcell filter. It could also have been designed as an on-chip resonator, although unlike the coaxline design, it would have to be on a different chip from the storage mode. Although the seam cuts through the Purcell cavity, this is not a concern, as the Q of the cavity will be very low due to coupling by design.

The side view shows the same chips and cavity, but also adds the coupling pins and clamping mechanisms. We have three coupling pins: one for driving the transmon, one for driving the storage and readout modes, and one for readout through the Purcell filter. Note that the centre coupler couples comparably to the storage and readout modes, since we are using two modes of the same physical object and the pin

is near the edge. For this reason, the pin cannot be coupled strongly without spoiling the Q of the storage mode. It may theoretically be possible to place the pin such that it couples strongly to the readout and weakly to the storage mode (by putting it at the E field node of the storage), removing the necessity for a Purcell filter, but in practice, the precision in placement necessary to achieve this is too great. The two chips are clamped by pressing them with machined PTFE rods against a solid metal surface of the slot. The PTFE rods are pushed by BeCu springs, which are pre-compressed with screws. BeCu springs work at cryogenic temperatures, maintaining the restoring force at the base temperature.

This system has the standard circuit quantum electrodynamics (cQED) configuration, allowing us to directly implement the usual techniques for the field. We write the approximate undriven Hamiltonian in the dispersive limit, keeping only the terms which we consider for our measurements (i.e. ignoring higher-order terms):

$$\frac{H}{\hbar} = \omega_r a^\dagger a + \chi a^\dagger ab^\dagger b + \omega_t b^\dagger b + \frac{K}{2} a^{\dagger 2} a^2 + \frac{\alpha}{2} b^{\dagger 2} b^2 \quad (4.1)$$

where $\omega_{r/t}$ are the frequencies, a and b are the annihilation operators, and K and α – the self-Kerrs/anharmonicities of the resonator and transmon, respectively. χ is the cross-Kerr. α and χ are negative in our system, and K is very small. Note that there is also a coupling of identical form between the readout resonator and the transmon. We shall not discuss the derivation or the meaning of the Hamiltonian since this has been covered extensively elsewhere, see e.g. [Girvin, 2011].

I now use the coupling between the transmon and the resonator in order to measure the resonator's properties. In the process, I create and control quantum states in the resonator, demonstrating its use as a quantum memory. The measurements are similar to those performed in [Reagor et al., 2016] and are at this point standard in the lab. Custom FPGA code was used to generate the pulses and perform readout,

see [Reinhold, 2019] for a description of this.

The wiring diagram for the experiments is given in Fig. 4.17. This is fairly standard wiring for a cQED experiment. Note the eccosorb both inside and outside the μ metal shield, for increased filtering of high-frequency noise. There was no particular reason to use a +40 dB amplifier followed by 13 dB of attenuation; I simply did not have an amplifier of exactly the right amplification. Although this increases the amount of noise, the [signal-noise ratio \(SNR\)](#) was more than sufficient for the experiments. The quantum-limited amplifier used in this experiment was the [SNAIL parametric amplifier \(SPA\)](#) [Frattini et al., 2018].

I now present representative samples along with brief explanations of the most important measurements carried out. Fig. 4.18 presents two ways to measure T_1 of the resonator. The first is by preparing the resonator in the $|1\rangle$ state with [SNAP](#), then fitting its decay to an exponential. The π pulse on the transmon is selective on $n = 0$ in the resonator. Therefore, the result of the measurement (P_e) is proportional to the population of the cavity in the $|0\rangle$ state. The Wigner reveals that our state preparation is not perfect. By doing qubit spec right after [SNAP](#), we see that the state we prepare is actually almost 20% $|0\rangle$. There is very little $|2\rangle$. This is consistent with our initial value of $P_e(t = 0)$. Additionally, our imperfect readout results in reduced contrast, which is why the tail does not go to 1. Note that neither of these effects affects our measurement of T_1 : they simply provide a multiplicative and additive factor to the exponential. For this reason, I did not attempt to tune up the pulses more perfectly.

The other way of measuring T_1 is presented in Fig. 4.18 c) and d). Here, we prepare our resonator in a coherent state with a displacement, and then measure its decay. Since a displacement is quite straightforward, we see that we do a better job of preparing a coherent state than we did with $|1\rangle$. Indeed, $P_e(t = 0)$ is now very close to 0. As the state decays, α decreases exponentially. As before, we are encoding the

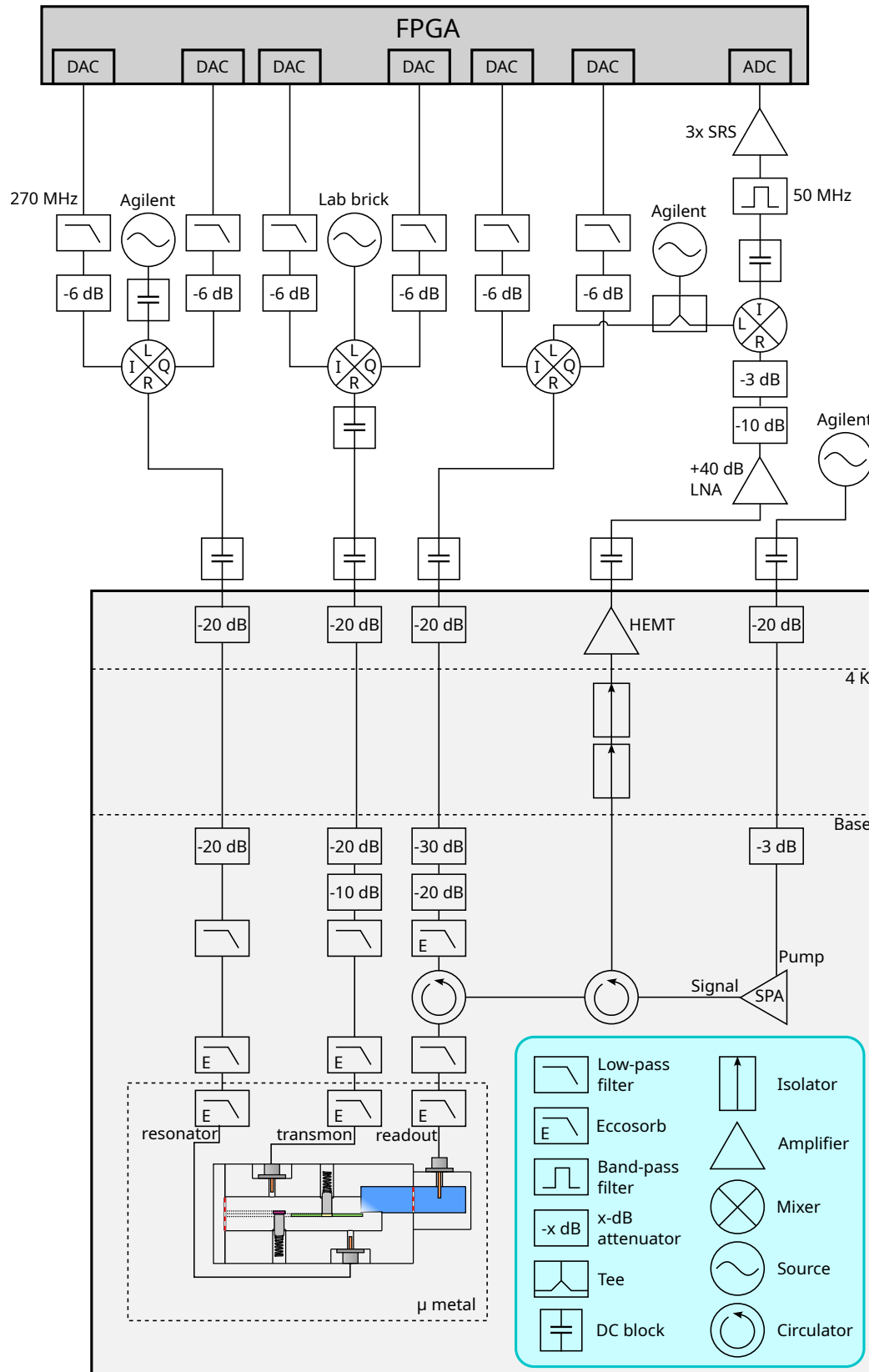


Figure 4.17: Wiring diagram for suspended stripline measurements.

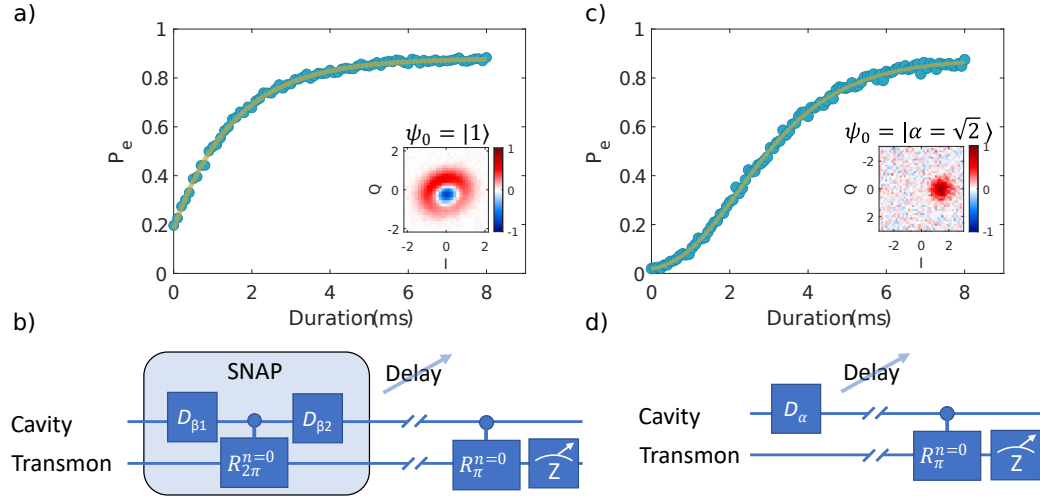


Figure 4.18: Two T_1 measurements of a suspended stripline. a) Measurement of the decay of $|1\rangle$ fit to an exponential. Inset: Wigner function of the initial state. We see that it deviates somewhat from the ideal $|1\rangle$, but is fairly close. b) Gate sequence for the experiment. First, generate the initial state via [SNAP](#) [Heeres et al., 2015], with $\beta_1 = 1.14$, $\beta_2 = -0.58$. Then, wait a variable amount of time. Finally, perform a π pulse on the transmon selective on $n = 0$ and read out to obtain the $|0\rangle$ population of the cavity. c) Another way to measure T_1 : decay of a displaced state back to vacuum. Here, the $|0\rangle$ population of the cavity increases as a double exponential, since α decays exponentially, and the overlap with a coherent state is exponential in α . Inset: Wigner function of the initial state $|\alpha = \sqrt{2}\rangle$. d) Gate sequence for the experiment. First, displace the cavity (in this case, to $\alpha = 2$). Wait a variable amount of time. Finally, measure the $|0\rangle$ population of the cavity using the transmon.

proportion of $|0\rangle$ in the resonator state into P_e . Since the overlap $\langle 0 | |\alpha \rangle$ is exponential in $|\alpha|^2$ (which can be easily seen from the form of a coherent state in the Fock basis), $P_e(t)$ is a double exponential. As before, we see the effects of imperfect readout in reduced contrast.

Fig. 4.19 shows a T_2 measurement. We first prepare $\frac{1}{\sqrt{2}}(|0\rangle + |1\rangle)$ with [SNAP](#). Here, we see that the state is somewhat rotated compared to the ideal. Again, this will not affect our measurement, but simply change a phase parameter in the fit. After a variable delay, we perform a displacement with an artificial detuning. This acts similarly to a Ramsey pulse, providing oscillations. As before, we measure the probability that the resonator is in $|0\rangle$. We then fit the result to an exponentially decaying sinusoid. As before, imperfect readout decreases the measurement contrast.

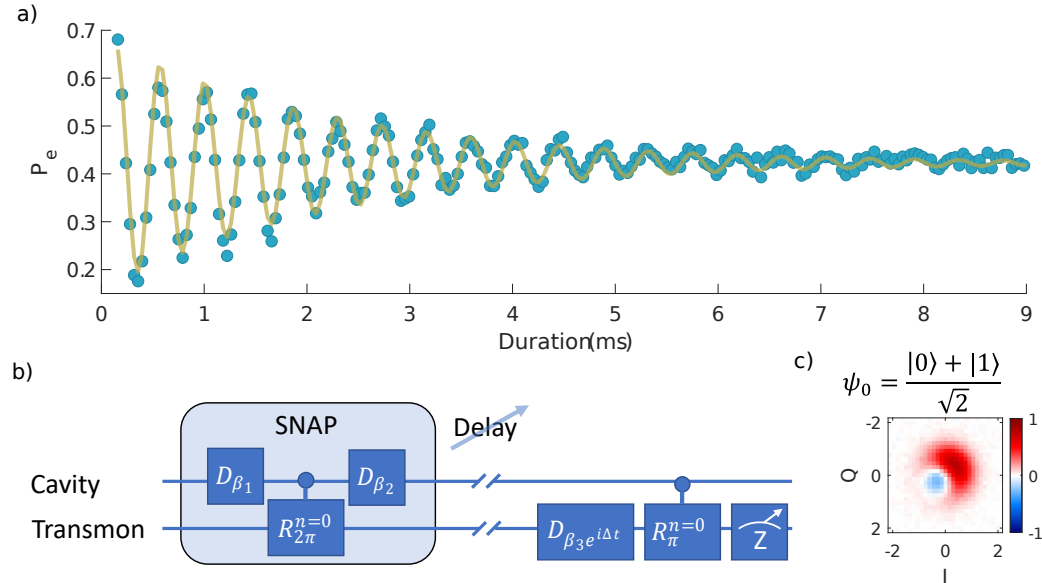


Figure 4.19: T_2 measurement of a suspended stripline resonator via a Ramsey measurement with an artificial detuning. The data is fit to an exponentially-decaying sinusoid. b) The gate sequence for the experiment. The initial state $\psi_0 = \frac{1}{\sqrt{2}}(|0\rangle + |1\rangle)$ is created via **SNAP**, with $\beta_1 = 0.56$, $\beta_2 = -0.24$. After a delay, we perform a displacement of variable phase with $\beta_3 = 0.8$. The variable phase acts as a detuning, providing the oscillations.

I now present the main results of the measurements, which can be seen in Table 4.3. Three centrepins were tested in two packages, with the same transmon chip (fabricated on 100 μm sapphire) used in all experiments. One package was 6061 aluminium, the other – 5N aluminium etched in the standard way (see A.4). Each row is a separate cooldown, with measurements occurring over several days. Some parameters changed day-to-day (or within a day), represented by ranges in the data. For the resonator, T_1 and T_2 were measured as described above, \bar{n} was measured by performing transmon spectroscopy after starting in the vacuum state and comparing heights of the $|0\rangle$ and $|1\rangle$ peaks. Note that the two methods of measuring T_1 generally gave consistent results (considering the error bars of usually around 10% and the inherent measurement-to-measurement variation).

I note that all of the devices measured have lifetimes over 0.5 ms (Q of around 20 million), including all of the devices with a 6061 aluminium package. This is already

| Device | | Resonator | | | | Transmon | | | |
|--------|------|--------------|--------------|------------|-----------|------------------|------------------|--------------------|-------|
| Chip | Al | T_1^F (ms) | T_1^C (ms) | T_2 (ms) | \bar{n} | T_1 (μ s) | T_2 (μ s) | T_2^E (μ s) | P_e |
| Si#2 | 6061 | 0.6 | — | — | — | 42 | 14 | 52 | 5% |
| Si#1 | 6061 | 0.6-0.8 | 0.5-0.8 | 0.9-1.2 | 0.08 | 15-31 | — | 15-45 | 0.3% |
| Si#1 | 5N | 0.6-0.7 | 0.6-0.7 | 0.7-0.9 | 0.03 | 34-51 | — | 34-68 | 1% |
| sapph | 6061 | 1.3-1.5 | 1.5-1.6 | 2.1-2.4 | 0.05 | 23-51 | 12-41 | 24-58 | 0.5% |
| sapph | 5N | 0.7 | 0.6-0.8 | 0.9 | 0.08 | 38-40 | — | 48 | 1.6% |
| sapph | 6061 | 1.0-1.4 | 1.3-1.6 | 0.2 | 0.11 | 22-31 | 5 | 10-13 | 4% |

Table 4.3: Measurement results for suspended striplines in seamless packages. For the resonator, T_1^F was measured via Fock state decay, while T_1^C was measured via coherent state decay. The $\chi/(2\pi)$ was around 700 kHz for the silicon centrepin chips, and around 500 kHz for the sapphire chip; the difference is likely primarily due to the different thicknesses of the chips. The same transmon chip was used for all experiments. Note that a PTFE clamp was stuck in the 5N package after its first use (Si #1), and thus the clamp hole was re-milled and the whole package was re-etched. It was not possible to measure T_2 for the transmon in some of the experiments due to beating. The resonator modes were around 5.4 GHz, the transmon – at 6.3 GHz, and the readout around 8.9 GHz.

notable, as it is comparable to the stub cavities currently used but does not require high-purity aluminium or etching and has a demountable centrepin. Furthermore, I note that the sapphire centrepin was measured to have a T_1 consistently over 1 ms in the 6061 package, which presents a further improvement over current technology. The T_2 is consistent with being limited by the transmon excited state population, indicating that we are not suffering from major vibrations. We also see that the same package can be used with different centrepins, and the same centrepin can be demounted and later remounted and measured without significant degradation, demonstrating the modularity of this design.

The 5N cavity does appear to be lower quality than the 6061 cavity, which can be seen from the sapphire chip measurements. The causes of this are unknown. Two possibilities are that something about the particular machining of this cavity makes the 5N quality worse, or that I was simply unlucky – it is not uncommon for the quality of high-purity aluminium cavities to vary significantly. This is another reason to move away from high-purity Al, aside from the cost, difficulty of machining, and

required etching. Another difficulty with the high-purity Al package is that the milling of the holes for the clamps was less precise, causing one of the PTFE pieces to get stuck. It then had to be milled out, and the package re-etched. Additionally, the “wings” by which the chips are held become somewhat damaged in the process, which can be seen when they are removed, although they can still be measured again and do not lose quality. These factors suggest that the clamping mechanism could benefit from further design consideration.

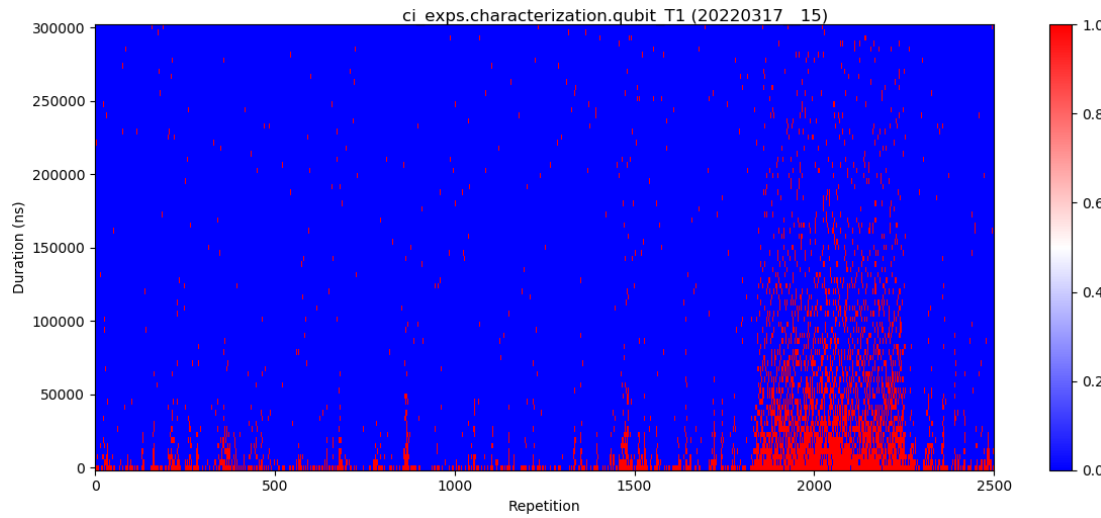


Figure 4.20: Many repetitions of the transmon T_1 measurement. The pulse tube is initially turned off, turned on at around repetition 1800, then back off around 2300. There is a noticeable increase in T_1 when the pulse tube is turned off.

For the transmon, T_1 and T_2 were measured in the standard way, excited state population is measured with RPM [Geerlings et al., 2013] (note the relatively cold transmon – likely due to the filtering). For about half of the experiments, T_2 could not be measured without echo due to beating. I note also that the transmon frequency tended to jump by up to a few hundred kHz in most cooldowns on the scale of around once per day. Occasionally, the transmon peak actually slightly split into two, which indicated the presence of two frequencies – this could be confirmed by comparing the separation of the peaks vs. beat frequencies. Switching between different frequencies is observed in the traditional stub packages as well; sometimes

cycling through T_c helps (in this experiment, it was unclear whether it helped). Even more pathologically, the transmon measurements tended to spontaneously change, sometimes depending on whether the pulse tube were on or off (see Fig. 4.20 for an example). The cause of this phenomenon is unclear, although it once started after the fridge was bumped, pointing at the mechanical vibrations from the pulse tube as the likely culprit. However, there is no clear mechanism by which T_1 should be affected by mechanical vibration. It is possible that the clamping mechanism needs to be improved, or that the unusually-thin chip used for the transmon in this case perhaps suffers more from vibration than usual chips. Finally, I note that in the last measurement, the transmon was significantly hotter than in the previous, resulting in a very low T_2 for the resonator. There is no clear cause to this, as nothing was changed between this measurement and the previous, except for the package (this did involve re-taping over the seams in the package with aluminium tape). This further highlights our lack of understanding of the exact causes of excitation in the transmon.

4.3 Suspended Coaxial Resonators Outlook

In this chapter, we have discussed several ways to make suspended coaxial resonators. We have found that suspended rods, although relatively easy to make, do not have very long coherence times. Their best usage would be in a place where the Q does not need to be very high, such as for certain implementations of a bus resonator. It may be possible to improve the Q of the rods by making them from etched machined high-purity Al. However, the clamping mechanism becomes sufficiently complicated as to negate the ease of making these devices. We were also able to test devices made of different materials, and do basic materials characterisation with the resulting structure.

For storage of quantum information, it appears that suspended striplines are the

much better choice. We were able to achieve an improvement over currently-used stub cavities with a sapphire chip in a seamless 6061 aluminium package. I believe that looking forward, it is better to avoid 5N aluminium and the difficulties associated with it, even if the resulting quality ends up being somewhat lower. The relative consistency alone will be necessary when we start doing experiments with more than one or two devices. We were also able to show that our device is more modular: we can replace the centrepins as needed. We also demonstrated a 3D Purcell filter, as well as the use of two modes of one resonator for different purposes.

Regarding the choice of package, I think we should not write off the seamed design: it's possible that by adapting the new style of clamping to the seam package, we could reduce the vibrations that plagued it (although it's also possible that that was due to the seam and not the clamping mechanism). If we can get rid of the vibrations, the ability to evaporate thin films onto the surface of the seam package is quite attractive. One can even envision a seam package that is micromachined in a silicon chip. As for the seamless package, it would likely be beneficial to re-design it in a way that avoids the need for [EDM](#) in order to make it easier to produce. Another potential improvement would be to allow for more precise control over coupling. One way would be to create a few defined positions for motion along the axis, another would be to use spacers to move the chips relative to each other in the transverse plane (up and down in Fig. [4.16](#) side view).

As to the chips, I believe the sidewall is likely to blame for the difference between the silicon and sapphire qualities. This means that it's possible that it is still a limiting factor. Possible ways to deal with this include etching (likely wet-etching will be easier than dry) the surface post-lasercutting to smooth it, or just etching out the chip in the first place. One can envision micromachining the chips in the same, except for the tilt of the sidewalls, as we have lasercut. This would require lithography, but we could aggressively clean the chip afterwards.

Overall, suspended stripline resonators are a good candidate for near-term scalable quantum memories for bosonic encodings. We have outlined a number of specific improvements to the architecture above. The next fundamental steps would be to demonstrate actual multiplexing. We have been performing experiments with several cavities for a long time, and although there is still much to be learned from such experiments, a functional quantum computer will require many thousands of qubits. Although it is likely that suspended striplines may not be the final qubit design in a full-scale computer, they do provide us with a way to start increasing the size of our experiments in the near future.

CHAPTER 5

Materials Studies for and Using Superconducting Microwave Resonators

As we have seen throughout this thesis, knowing and having control over the properties of materials is crucial in the design and fabrication of superconducting resonators (and of course in many other areas). In particular, there has been a lot of work in the superconducting quantum computing community (as well as in detector and accelerator communities) on measuring and understanding the losses in superconducting systems, see e.g. [McRae et al., 2020b] for an overview. Although many material-related improvements in coherence have been achieved, we still do not understand the microscopic causes of most of the relevant loss mechanisms. Additionally, we generally do not have a robust way of measuring the losses of individual channels.

In this chapter, I first discuss using multimode resonators to measure material properties in Sec. 5.1. This removes the variability associated with making large numbers of devices (the alternate approach) while in principle maintaining the abil-

ity to actually measure, rather than just bound, the qualities of the different loss channels. I then describe some work in cooperation with [Brookhaven National Laboratory \(BNL\)](#) on using traditional materials characterisation methods (e.g. [TEM](#), [x-ray diffraction \(XRD\)](#), etc.) to attempt to learn more about the microscopic causes of loss. The results obtained are preliminary and unpublished; I present them as a demonstration of the types of experiments that can be performed.

5.1 Multimode Resonators as a Materials Loss Characterisation Platform

5.1.1 Basic Principle

The simplest characterisation method for the quality factor of a loss channel with a resonator is the lower bound: simply pretend that all of the loss for the mode comes from this channel. Recall the participation ratio model from Sec. [2.2.1](#). Neglecting the other loss channels, we obtain:

$$\frac{1}{Q_i} = \frac{p}{q} + \sum_{\text{others}} \frac{p_i}{q_i} \geq \frac{p}{q}$$

$$Q_i \leq \frac{q}{p}$$

$$q \geq p \times Q_i,$$

which gives us a lower bound on quality q of our selected channel. However, this is generally not enough information in order to be able to improve the material quality. With just a bound, one may test several processes and check whether the bound changes, but this only works in the case that we have chosen a dominant error channel (and are not modifying the other dominant error channels). Since this is generally not true, it is very possible to miss real changes in q from process variations by this

method. It is sometimes possible to find a mode that only participates in one loss channel, and thus the bound for which is actually a measurement [Reagor et al., 2013], but this is quite uncommon, and does not tend to be robust to deviations from the ideal design. Therefore, we need some way to truly measure the q 's.

We can get a hint for how to do this by recalling the suspended stripline experiment, in which different modes (the storage and readout) have drastically different participations in different loss channels. In general, Eq. 2.3 (the participation model equation) can be written for several different modes or devices. In this case, the Q_i of each mode/device is measured separately, and we obtain m equations for m modes/devices in n variables for n loss channels, which we can express in matrix form [Calusine et al., 2018, Read* & Chapman* et al., 2022]:

$$\begin{pmatrix} Q_1^{-1} \\ Q_2^{-1} \\ \vdots \\ Q_m^{-1} \end{pmatrix} = \begin{pmatrix} p_{11} & p_{12} & \cdots & p_{1n} \\ p_{21} & p_{22} & \cdots & p_{2n} \\ \vdots & \vdots & \ddots & \vdots \\ p_{m1} & p_{m2} & \cdots & p_{mn} \end{pmatrix} \begin{pmatrix} q_1^{-1} \\ q_2^{-1} \\ \vdots \\ q_n^{-1} \end{pmatrix}.$$

We can name the matrices in the above to re-express it as

$$\boldsymbol{\Xi} = \mathbf{P}\boldsymbol{\xi}, \quad (5.1)$$

where $\boldsymbol{\Xi}$ is the m -dimensional vector of Q_i^{-1} and $\boldsymbol{\xi}$ is the n -dimensional vector of q^{-1} ($\boldsymbol{\xi}$ is used to avoid ambiguity with e.g. \mathbf{Q}^{-1}), and \mathbf{P} is the $m \times n$ -dimensional matrix of participations. Note that some elements of \mathbf{P} and $\boldsymbol{\xi}$ may have units, such as in the case of seams; this is okay as long as their product is dimensionless. From this form, we see that if $n \geq m$, then we can in principle invert the matrix \mathbf{P} (if it is not singular) to solve for $\boldsymbol{\xi}$ from the measured $\boldsymbol{\Xi}$ and the simulated \mathbf{P} . The two primary ways of increasing m are by fabricating several types of devices, or using multiple modes of a single device (or a combination of the two). It is also possible to take

a third option by reconfiguring the system between measurements in one cooldown. This has been done in [Read* & Chapman* et al., 2022], but is not very common, as it is quite challenging to carry out and can only be used in particular cases.

The first method has been used to study losses in superconducting circuits, e.g. [Wang et al., 2015, Woods et al., 2019]. This allows us to have more options in terms of device design, since we don't have to design multiple modes at the same time. However, it also introduces a lot of variability: since we are measuring multiple devices, frequently in multiple cooldowns, our results incorporate device-to-device variation as well as cooldown-to-cooldown variation, obfuscating the actual differences in loss. Additionally, sometimes different processes are needed to obtain the desired difference in participations, which adds another variable factor.

The second method is also not new, see e.g. [Turneaure and Weissman, 1968], which uses two modes of a cylindrical Nb cavity, which today we would describe as p_{cond} - and p_{MA} -sensitive. The advantage is that only a single structure is required, eliminating device-to-device variability. Additionally, if it is possible to couple to enough modes at once, all of the measurements could be performed in one cooldown. Trying to couple to many modes at once while keeping the participations of the modes sufficiently different can make these devices somewhat more difficult to design.

The fewer loss channels there are, the fewer different measurements are needed to tell them apart. This means that it is generally easier to do this for 3D cavity resonators, as they have no substrate. Devices with a substrate present an additional difficulty aside from simply having more loss channels: it is very difficult to design devices in which **SA**, **MS**, and **MA** scale differently. In general, making **P** sufficiently well-conditioned is one of the main challenges in this type of work.

5.1.2 Ellipsoidal Cavity

In this section, I present the ellipsoidal cavity, a multimode resonator for separating the loss channels relevant for 3D superconducting cavities. A lot of this work was done by my colleague Chan U Lei but is not published elsewhere.

A photograph of an ellipsoidal cavity is shown in Fig. 5.1 a). This ellipsoid is chosen such that two principal axes have the same length, and is thus an oblate spheroid, with the symmetry axis being orthogonal to the seam plane. The mode structure of the resulting shape is quite rich, with 22 modes between 4 and 13 GHz (the first 20 are shown in Fig. 5.1 b)). There are several pairs of degenerate modes, but there is still enough variability to have modes with different participations. Since our cavity has no substrate and is made of one metal, there are only three loss channels: p_{cond} , p_{MA} , and y_{seam} .

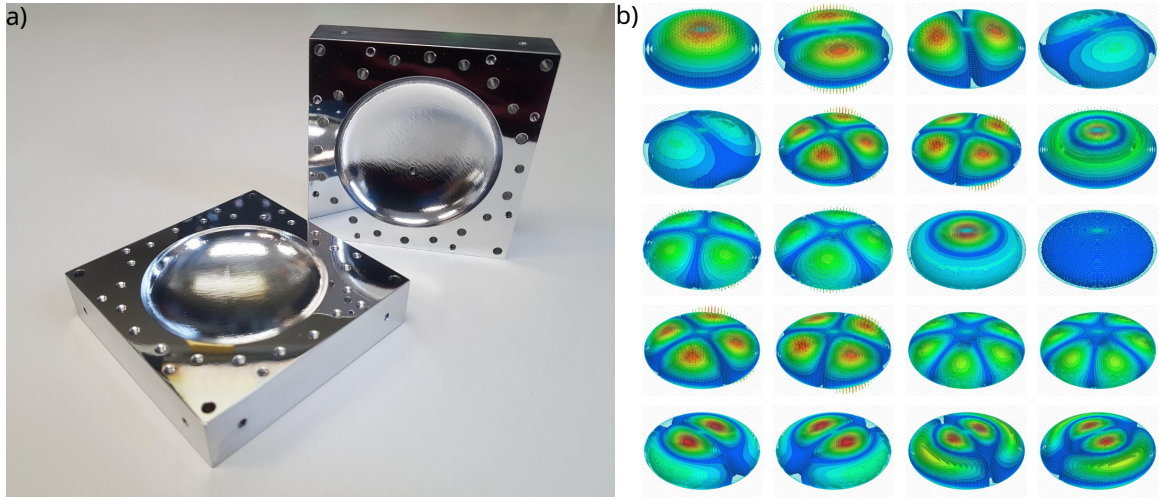


Figure 5.1: a) A photograph of a hand-polished 6061 aluminium ellipsoidal cavity. The cross-section in the cut plane is a circle with radius 28 mm, a cross-section perpendicular to this plane is an ellipse with semiminor axis 22.4 mm. A coupling hole is visible in one half of the cavity. b) Finite-element simulations of the first 20 modes of the cavity between 4 and 12.5 GHz. The modes at these frequencies are most similar to those of a cylindrical cavity.

Fig. 5.2 shows the three types of modes which we shall use to extract the different loss channels. a) is a general, seam-sensitive mode (compare to the TE101 for a

rectangular cavity); the first three modes in Fig. 5.1 b) are examples. b) is a mode which is insensitive to the seam, as there is no surface current flowing across it, the fourth, fifth, and eleventh mode are examples. c) is a mode which has no electric field at the surface at all, and thus has no seam loss or surface dielectric loss; compare the TE011 mode of a cylindrical cavity [Reagor et al., 2013]. The twelfth mode is an example (the twenty-first and twenty-second modes, not depicted, are also examples, and thus the field diagrams look very similar).

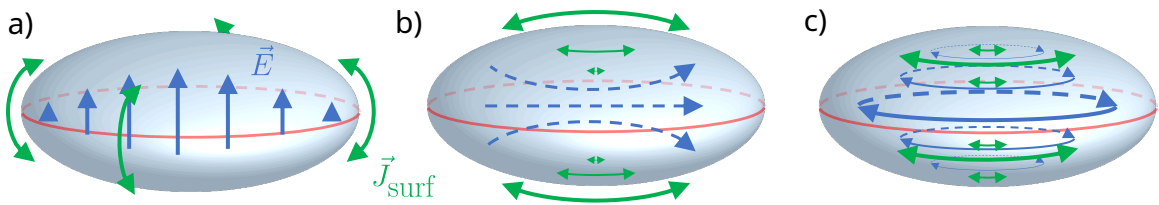


Figure 5.2: Diagrams of the three main types of modes we use in the ellipsoidal cavity. a) A seam-sensitive mode, with surface currents running across the seam. b) A seam-insensitive mode. c) A mode sensitive only to conductor loss, as there is no electric field at the surface.

Ignoring imperfections for the moment, using three such modes will result in a participation equation of the following form:

$$\begin{pmatrix} Q_a^{-1} \\ Q_b^{-1} \\ Q_c^{-1} \end{pmatrix} = \begin{pmatrix} y_{\text{seam},a} & p_{\text{MA},a} & p_{\text{cond},a} \\ 0 & p_{\text{MA},b} & p_{\text{cond},b} \\ 0 & 0 & p_{\text{cond},c} \end{pmatrix} \begin{pmatrix} g_{\text{seam}}^{-1} \\ q_{\text{MA}}^{-1} \\ q_{\text{cond}}^{-1} \end{pmatrix} \quad (5.2)$$

Note that we can also express the conductor loss via the geometric factor and surface resistivity. If the system were exactly as described above and completely noiseless, then we could solve directly for all of the q 's: \mathbf{P} is not just non-singular, but is even upper triangular! However, let us now consider the fact that there indeed is some uncertainty associated with every measurement.

If the Q 's are measured with some error, this error will propagate to our calculated q 's. Depending on the matrix \mathbf{P} and values for the q 's, this may result in uncertainties in a particular q that are larger than the value, meaning that we are effectively

insensitive to this loss channel (we cannot distinguish it from 0), even if our \mathbf{P} is invertible. We can see how this can happen by considering the situation for a strongly overcoupled resonator: even though we can numerically solve for Q_i , any noise on Q and Q_c will create overwhelming error on it. For this reason, it is easier to be sensitive to higher losses (lower q 's). For more details on the actual calculation using the covariance matrix, see [Read* & Chapman* et al., 2022]. The paper also introduces plots of sensitivity, the fractional uncertainty in a q_i for possible values of the other q 's given the expected participation matrix \mathbf{P} . If the fractional uncertainty approaches 1, we say that the given experiment is not sensitive to this loss channel in this regime. One can also see this from Monte Carlo [Woods et al., 2019]: if the extracted values for a parameter form a box extending all the way left on the log plot, the value of this parameter cannot be distinguished from zero, see Fig. 5.3.

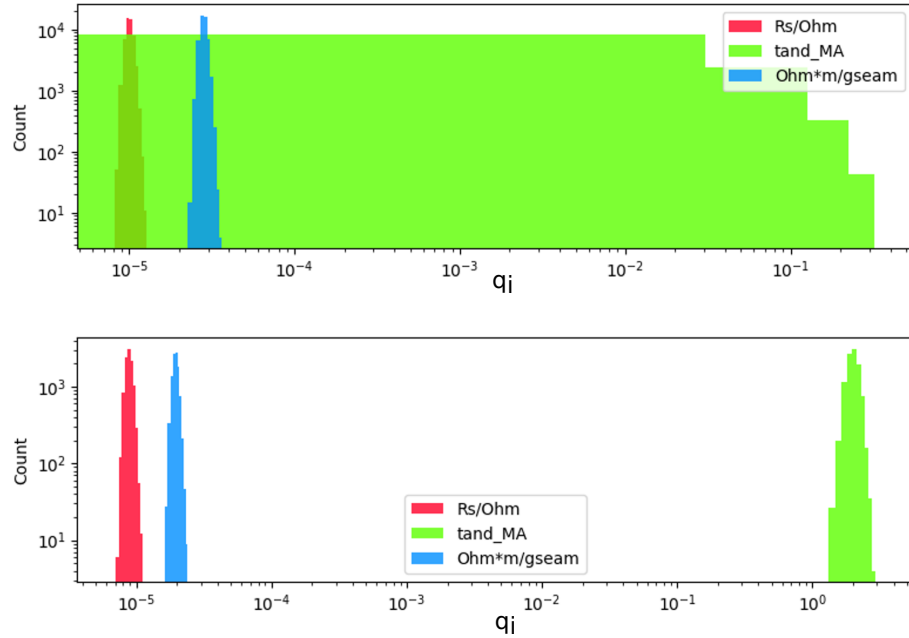


Figure 5.3: Losses extracted for the three loss channels in ellipsoidal cavities. The plotting is styled after the Monte Carlo method of [Woods et al., 2019], although note that since we are solving a linear system, we do not need to perform Monte Carlo, and can simply used least squares or invert the matrix. The top graph is for diamond-turned 6061 Al, with the measurement being insensitive to surface dielectric loss. The bottom is for hand-polished 6061 Al, in which case we can resolve q_{MA} (here expressed as $\tan \delta$).

As mentioned in Sec. 2.2.7, this part of the analysis depends heavily on what we assume the uncertainties in the Q 's to be. For the analysis of this experiment, we assume $\pm(5 - 10)\%$ error on Q , representing cooldown-to-cooldown or the lower end of device-to-device variation. Fig. 5.4 shows sensitivity plots for surface dielectric and seam loss for the ellipsoidal cavity. As we shall see once we calculate the values, we are in a parameter range where we are sensitive to seam loss, but insensitive to surface dielectric loss for hand-polished 6061 aluminium. Since we have a mode whose only loss channel is conductor loss, we are always sensitive to it.

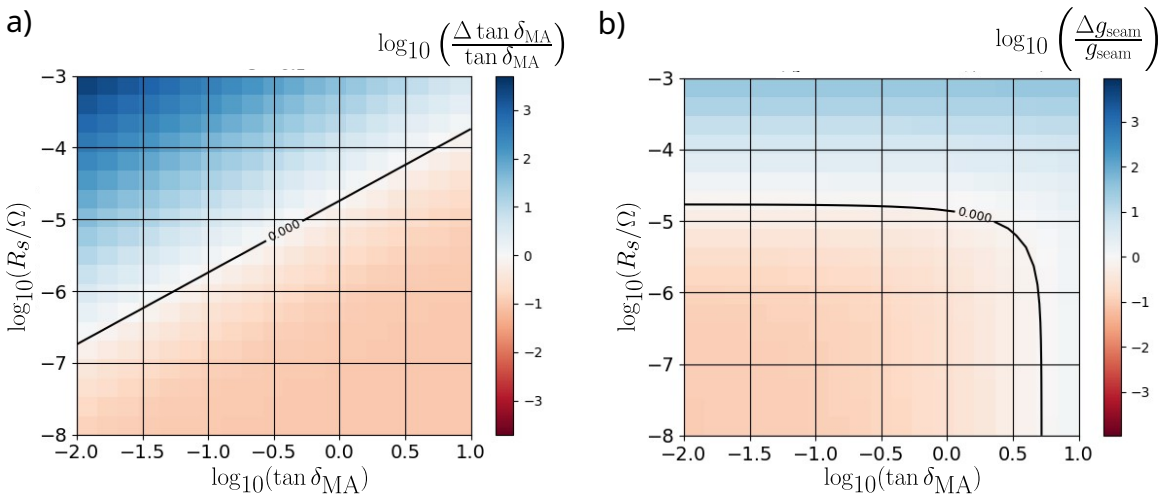


Figure 5.4: Two sensitivity plots for an ellipsoidal cavity assuming a 10% error on the measured Q 's. The line represents a fractional error of 1, red regions have a fractional error of less than 1, where we are sensitive to the loss channel, and blue regions have fractional error greater than 1, where we are not sensitive. a) shows sensitivity for surface dielectric loss (here expressed as $\tan \delta$ rather than q). b) shows sensitivity for seam loss, assuming a $g_{seam} = 6 \times 10^6 / (\Omega m)$. We do not present a sensitivity plot for conductor loss, as we have a mode that only has conductor loss and is thus always sensitive to it. We see that we are insensitive to surface dielectric loss for likely values.

The particular design of the ellipsoidal cavity permits a large number of material combinations and surface processing methods. Some of the ones we tested are depicted in Fig. 5.5. Since the cavities in both pieces are radially symmetric around the central axis, they could be diamond turned (essentially lathe with a diamond-tipped tool). This results in a smoother surface that can be achieved with hand polishing, and is

in fact mirror-like, see b). Since the cavity has a smooth surface and no high-aspect ratio or re-entrant parts, we can also coat the surface with other superconductors even with directional methods (e.g. evaporation), see a) and c)-f).

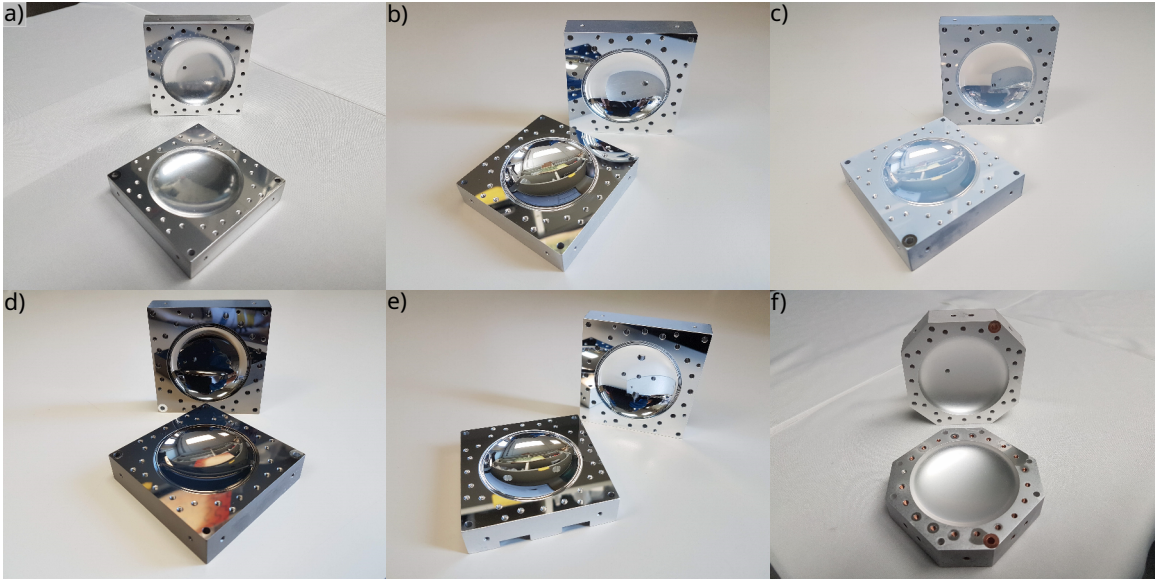


Figure 5.5: Photographs of ellipsoidal cavities with surfaces made of different materials or with different processes. a): hand-polished 6061 with $2\text{ }\mu\text{m}$ of indium evaporated on top. b): diamond-turned 6061 aluminium. c): diamond-turned 6061 with $1.6\text{ }\mu\text{m}$ Al sputtered on top. d): diamond-turned 6061 with 800 nm Nb sputtered on top. e): diamond-turned 6061 with $1\text{ }\mu\text{m}$ Al evaporated on top. f): hand-polished **OFHC** copper with $10\text{ }\mu\text{m}$ In evaporated on top. Note that most of the films had fairly poor adhesion and could be removed with adhesive tape.

Once we have measured at least one mode of each type for a given cavity, we can then solve the system for the losses q . However, there is a complication: as mentioned in Sec. 2.2.7, the results are not always consistent! In other words, for realistic assumptions about errors, choosing more than three modes often results in an inconsistent system. One way to deal with this is simply to assume larger errors. This can potentially be justified if we are trying to make conclusions about the material in general (and thus assume our errors to be representative of device-to-device variations). However, since we do in fact measure a single device, the errors on a Q value should really not be significantly larger than a percent (unless we are

overcoupled).

Another option is to simply pick three modes, one of each type, and solve that system. The other modes can then be used as a validation by “predicting” their Q ’s using the extracted q values and the \mathbf{P} matrix; see Fig. 5.6. a) shows an example of an obviously inconsistent system, while b) is not too far off. This indicates that, at least for device a), the participation model is insufficient to describe the losses. For more discussion on the implications of this, see Sec. 2.2.7.

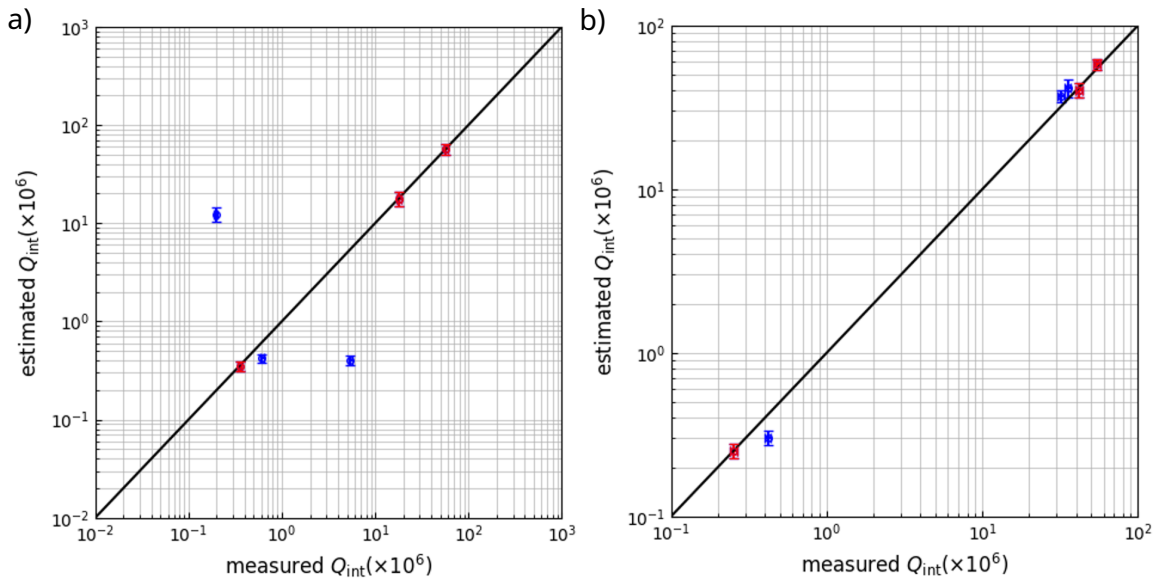


Figure 5.6: After extracting material properties from several modes, we can go back and “predict” the expected Q ’s for the other modes using the participation matrix. This figure depicts the estimated vs. measured Q for two devices: hand-polished 6061 Al (a) and diamond-turned 6061 Al (b). The three modes used to extract the properties are red, the other measured modes are in blue. Note that in a), two modes are predicted very poorly by the model, while in b), all the modes are fairly close.

Meanwhile, we continue with our three-mode analysis, choosing three modes that appear most orthogonal in participation. Table 5.1 presents the results of extracting the three loss channels from a number of different ellipsoidal cavities. I note that this data is presented more as a demonstration of what the method can achieve, and less of a statement that we have truly measured these values, since there are still unresolved questions regarding the data analysis. However, we can still observe some

| # | Material | $g_{\text{seam}} (\Omega^{-1}\text{m}^{-1})$ | q_{cond} | $R_s (\mu\Omega)$ | q_{MA} |
|----|----------------------------------|--|-------------------|-------------------|-----------------|
| 1 | 6061 Al | $1.4 \times 10^5 \pm 7 \times 10^3$ | 1200 | 3.6 ± 0.2 | > 2 |
| 2 | Hand-polished 6061 | $5.0 \times 10^4 \pm 3 \times 10^3$ | 480 | 8.9 ± 0.5 | 0.5 ± 0.05 |
| 3 | Diamond-turned 6061 | $3.6 \times 10^4 \pm 2 \times 10^3$ | 420 | 10 ± 0.5 | > 3.3 |
| 4 | 600 nm Al evap. on #2 | $1.3 \times 10^6 \pm 7 \times 10^4$ | 7500 | 0.56 ± 0.03 | 27 ± 7 |
| 5 | 600 nm Al evap. on #3 | $1.2 \times 10^7 \pm 9 \times 10^5$ | 1900 | 2.2 ± 0.1 | > 10 |
| 6 | 1.6 μm Al sput. on #5 | $> 3.3 \times 10^8$ | 6100 | 0.69 ± 0.09 | > 2 |
| 7 | 5N5 Al | $9.6 \times 10^4 \pm 5 \times 10^3$ | 1500 | 2.9 ± 0.2 | > 10 |
| 8 | #7 etched for 150 μm | $5.2 \times 10^4 \pm 3 \times 10^3$ | 9500 | 0.43 ± 0.02 | > 33 |
| 9 | 5 μm In evap. on #4 | 1×10^5 | 1925 | 2.2 | > 5.2 |
| 10 | 2 μm In evap. on #9 | 2×10^5 | 1386 | 3.0 | > 3.7 |
| 11 | 800 nm Nb sput. on #6 | 1×10^6 | 1540 | 2.7 | > 2.2 |
| 12 | #8 with de-Gaussing | 1.7×10^4 | 10010 | 0.42 | > 9.6 |
| 13 | 1 μm Al evap. on #12 | 1.1×10^6 | 2918 | 1.4 | > 5.8 |

Table 5.1: Results of measuring several ellipsoidal cavities. We use $\lambda = 50\text{nm}$ to calculate p_{cond} and $\omega = 2\pi \times 10.7\text{GHz}$ for R_s . There was a difference in calculation process between devices 1-8 and 9-13. Some notes about the particular devices: #4 and #5 were evaporated in four steps: $\pm 45^\circ$ tilts on the two orthogonal axes, 150 nm per evaporation, in order to better cover the sidewalls. #6 first was oxygen plasma ashed before Al sputtering. #9 was oxygen plasma ashed, and then 5:4 ArO₂ ion milled prior to evaporation, and then atmospheric plasma treated for indium bonding prior to assembly. #11 had the Al layer removed with Kapton tape, then ion milled for 10 min in Ar prior to Nb sputtering. #12 and #13 were measured in two nested magnetic shields, with the inner one being de-Gauessed, see App. C.

trends. First, we note that we can consistently achieve g_{seam} in the tens of thousands, and even in the millions in some cases. We also see that etching 5N5 aluminium improves its q_{cond} by several times. Thin-film Al deposited on 6061 is generally better than bare 6061 Al, while In is comparable, while evaporating a micron of Al onto 5N5 actually decreases the quality. Finally, we don't observe a difference with cooling in a lower magnetic field via de-Gaussing of the mumetal shield, see [Catelani et al., 2021].

I now list several other interesting observations which cannot be seen in the presented data. One is that the films generally had quite poor adhesion to the surface and could be removed with e.g. Kapton tape – in contrast to films on substrates like sapphire or silicon. A strange observation was that in temperature sweeps of an indium-coated cavity, a clear Al transition could be seen (Al has T_c of around 1.2 K,

In of around 3.4 K). The indium is thick enough that there should be no way for the aluminium to participate in the mode, which possibly indicates that some parts were not covered well (the corners of the cavity, or perhaps the coupling port?), although it is unclear how that would happen. This is still an unsolved question. Finally, I note that some of the devices had modes with Q of around or over 1 billion, such as the etched 5N5 and 600 nm of Al evaporated onto 6061. Although this is far better than the stub cavities and even better than the micromachined cavities, the result is achieved by diluting the fields even more in vacuum via a very large mode volume, meaning that the ellipsoidal cavity is likely not more useful as a quantum memory.

With ellipsoidal cavities, we have taken a step towards being able to separate the loss mechanisms present in superconducting resonators. However, this device design suffers from some limitations. As we have seen, for most of the realistic parameter space, it is not sensitive to surface dielectric loss. Additionally, it does not permit us to measure the quality of superconductors deposited on wafer substrates, which are ubiquitous in the field and thus of interest. For these reasons, new designs are currently being developed in the group, and I expect them to be published in the year or two after this thesis.

5.2 Materials Characterisation Using Traditional Methods

In the previous section, we explored ways to use superconducting microwave resonators to study the properties of the materials comprising them. This works because the resonators are some of the most sensitive devices to these losses. However, all of those measurements are phenomenological, and do not explain the causes of the loss. At best, it's possible to do trial-and-error to determine whether some material/process combination is better than another. If we wish to continue improving

the losses, it is therefore desirable to have ways to probe their microscopic causes. For example, see the following examples of contemporaneous works: [Place et al., 2020, Altoé*, Banerjee*, Berk*, Hajr* et al., 2022, Premkumar et al., 2020, Murthy et al., 2022]. In this section, I describe some recent work we have done on the subject, both with easier in-house measurements and with more complicated methods which were performed by our collaborators at [BNL](#), organised by Ignace Jarrige.

5.2.1 In-house Measurements

There is a number of measurements which we can perform in our facilities, without highly-specialised and complicated equipment (e.g. a synchrotron). I have already described in previous sections how we can use temperature sweeps to measure the kinetic inductance, T_c , and penetration depth for superconductors, as well as how we can use power/temperature sweeps to measure [TLS](#) critical photon numbers.

We also have access to an ellipsometer in our cleanroom. Ellipsometry measures the reflection of polarised light from a surface, which can be used to detect the thickness of a dielectric film on the surface. For example, we can use it to measure the thickness of the native oxide on an aluminium film. We can then compare the thicknesses for different processes (e.g. bulk vs. polished bulk vs. diamond-turned bulk vs. e-beam-evaporated thin-film, etc.), and use the real value instead of the assumed 3 nm. Since we do not learn the ϵ_r or $\tan \delta$ of the film, this is of limited use, unless we assume that these are the same and only the thickness changes in different cases; then we could optimise for thinnest oxide. For example, see Table 5.2. Ellipsometry requires a known model for the optical properties of the film, which is an additional assumption (since generally only certain common materials are characterised). Finally, the surface has to be sufficiently smooth to obtain a reflection.

Another tool at our disposal is the [SEM](#). Although generally this just gives us information about the structure of our devices, we can sometimes see effects which plau-

| # | Material | Thickness (nm) |
|---|--------------------------------------|----------------|
| 1 | Hand-polished 6061 Al | 14 |
| 2 | Diamond-turned 6061 Al | 3 |
| 3 | 600 nm Al evaporated on #2 | 3 |
| 4 | 1.5 μm Al sputtered on #3 | cannot fit |
| 5 | Polished high-purity Al | 9 |
| 6 | #5 etched for 2 minutes | 5 |
| 7 | #6 etched for 2 minutes | 3 |
| 8 | #7 etched for 5 minutes | 2.5 |
| 9 | #8 etched for 30 minutes | 1.3 |

Table 5.2: Ellipsometry of a number of Al surfaces. #4 provides an example of a failure mode of ellipsometry: sometimes, we cannot fit the reflection to the model (e.g. the surface is too rough). The numbers' absolute values would require further calibration to be trustworthy, since it is unclear that our native oxide should have the same properties as the one whose optical properties are assumed by the machine. However, it is probably fair to compare the thicknesses reported, e.g. etching high-purity Al does seem to (at least temporarily) reduce the thickness of the surface oxide.

sibly could affect quality. Aside from relatively-obvious large-scale failure modes, such as dosing/liftoff issues or cracks in sapphire caused by the e-beam writer (App. A.3), we can sometimes see glimpses of more subtle variations. For example, by carefully imaging our lifted-off e-beam Al (e.g. a transmon), we can see a differently-coloured region around the metal, see Fig. 5.7; compare this to the description of the “veil of death” in [Schuster, 2007] Sec. 5.2.4. This type of imaging serves to make us suspicious of certain interfaces, such as [SA](#) in the above example. It could be used with trial-and-error fabrication and some way to measure the individual loss channels in order to determine which image artefacts correspond to high or low quality, although to my knowledge, this has not been done.

Finally, I note that we have the capability to do basic elemental analysis using the [energy-dispersive x-ray spectroscopy \(EDX\)](#) in our [SEM](#). This works by detecting x-rays emitted by upper-level electrons transitioning to the empty lower-level states left over after their electrons are ejected by the e-beam. Different atoms have different characteristic wavelengths, allowing us to distinguish them. We can use this

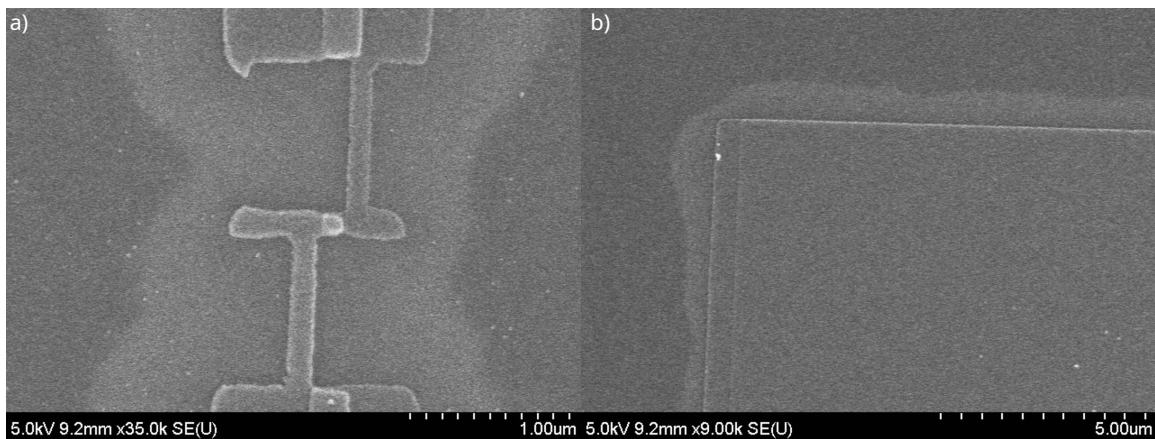


Figure 5.7: SEM of the junction (a) and corner of a pad (b) of a transmon. Note the differently-coloured shroud around the metal. Some possibilities include resist remnants, since this occurs around exposed regions, or solvent residues. Compare to the description of the “veil of death”.

information to determine which atoms are present (and in what ratios) within the area around our beam. However, the concentrations with which we are concerned can sometimes be too low to detect, and a lot of the time, we are interested not only in atomic composition but also in the chemical bonds between them. I am also not aware of any new results or explanations from this technique.

5.2.2 TEM

One of the more advanced techniques is [TEM](#). Although in principle, we have access to one in the university, the sample preparation and data analysis are both difficult and time-consuming, meaning that it is much more effective to work with professionals. In particular, the preparation of our samples for [TEM](#), measurement, and data analysis were carried out by Kim Kisslinger and Sooyeon Hwang at the Center for Functional Nanomaterials (CNF) at [BNL](#).

After we have finished processing the samples, they are cut with a [focussed ion beam \(FIB\)](#) for measurement with the [TEM](#). This involves coating the surface of the sample (with e.g. a platinum organometallic), then cutting out a piece several

microns by several microns by 50-100 nm with a [FIB](#) using e.g. gallium ions. The sample must be thin to allow the electrons to pass through it. The piece is finally attached to a copper “grid”. It is then put into the [TEM](#), which shoots electrons through the sample and then collects the transmitted (or scattered, in dark-field) ones. Aside from standard microscopy, the [TEM](#) also has a [high-angle annular dark-field \(HAADF\)](#) detector, and can perform [EDX](#). Combined, these give us the ability to obtain atomic-resolution images (the contrast from [HAADF](#) is also very strongly dependent on atomic number), as well as chemical composition maps of the sample.

In a preliminary study, we prepared several machined 5N5 aluminium “coupons”, half of which were just solvent cleaned, and half of which were etched around 160 μm in the same way as our cavities are. Of each process, two samples were measured: one taken at the surface, and one taken after 100 μm has been removed via lapping with diamond sand paper and water. We know from cavity experiments and multimode resonator measurements that etching improves the quality of the aluminium, but we do not know the cause. We suspect that machining the aluminium may introduce structural defects (cracks, strain, etc.) or implant contaminants from the tools to some depth beneath the surface (it generally seems that we need to etch around 100-150 μm before the quality improves). The ellipsometry measurements also hint that the surface oxide is thinner after etching. I shall use this as an example of the types of information that we can learn from the [TEM](#) study.

A note on interpreting TEM results.

When looking at a [TEM](#), we must always remember that what we are seeing is an average over the thickness of the sample, which is around 50-100 nm. If an interface of interest is not completely orthogonal to the plane of the image (as will almost certainly be the case), we will see it smearing out over an area. If there really is a truly flat interface, it may be possible to align the beam parallel to it fairly well. However, this is further confounded by the fact that if there are multiple interfaces, they are probably not parallel, and that most samples tend to be polycrystalline, so most of the time, there is not even a single “correct” direction. For these reasons, it may be difficult or impossible to learn both the thickness and chemical composition of an oxide, for example.

Let us first look at [TEM](#) and [EDX](#) of a piece of etched 5N5 aluminium coupon taken from the surface, see Fig. 5.8. This, and all of the following samples are prepared as cross-sections, meaning that the top of the piece in the visible image is the surface, and moving down takes us deeper into the coupon. The left image shows the whole piece (which is held by the copper grid). The dark parts are the same sample, just not thinned down. The lighter part above the sample is the platinum organometallic. We can see what looks like a few grain boundaries – the right image shows a zoomed-in [TEM](#) of a three-grain boundary. The grain boundary on the left is parallel to the beam and thus looks thin, the other two (which look stitched) are not in the plane of the beam, resulting in the wider appearance. To find the chemical composition of the sample, we use [EDX](#) on a section comprising most of the sample, the results are shown in the bottom chart. We see several expected elements, such as Al, Cu, Pt, Ga, and O. However, we also observe a small amount of Mo and Zr. Mo is on the 0.01% level, Zr is on the 0.5% level, both of which are too high for 5N5 aluminium. A potential source of Mo are the tools used in machining the sample: end mills can occasionally contain the element. As we shall see in the next figure, unetched 5N5 Al contains more Mo, potentially because it primarily gets implanted near the surface. There also appears to be less of the Mo in the samples taken 100 µm under the surface.

Fig. 5.9 depicts the same type of measurements but for an unetched surface. The

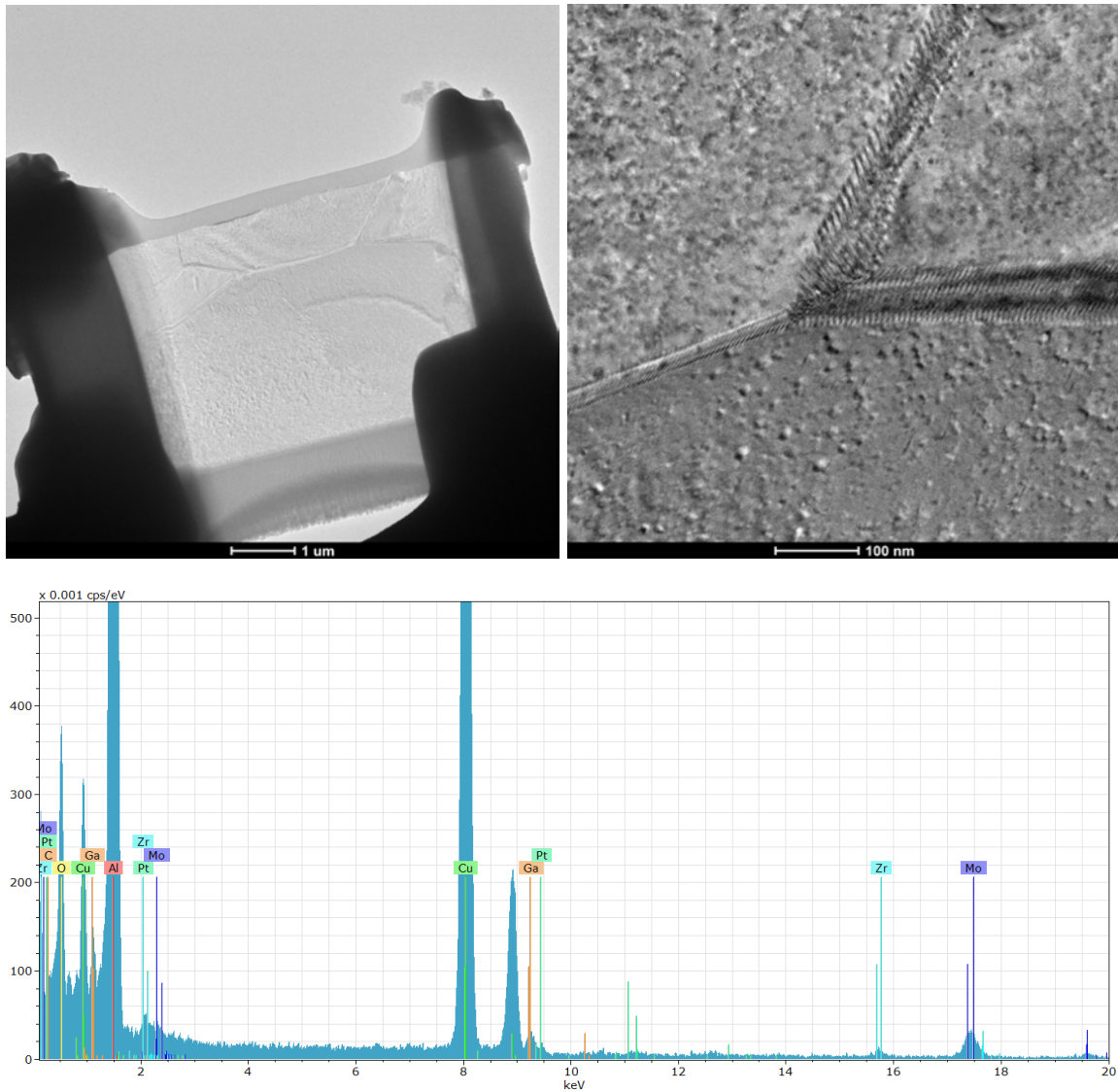


Figure 5.8: [TEM](#) and analysis of the surface of an etched 5N5 aluminium coupon piece. Top left: view of the whole sample. The dark part is the same sample, just not thinned down. The sample is a cross-section: the top edge is the surface, and moving down is going into the sample. What appears to be a few grains can be seen. Top right: zoomed-in view of a boundary between three grains. Bottom: [EDX](#) of most of the sample. We see the expected Al (sample), Cu (grid), Pt (sample coating), Ga (implanted by the [FIB](#)), and O (surface oxide). However, we also see Zr and Mo. Quantification of the [EDX](#) reports 1.85% O, 0.01% Mo, and 0.34% Zr by atomic number.

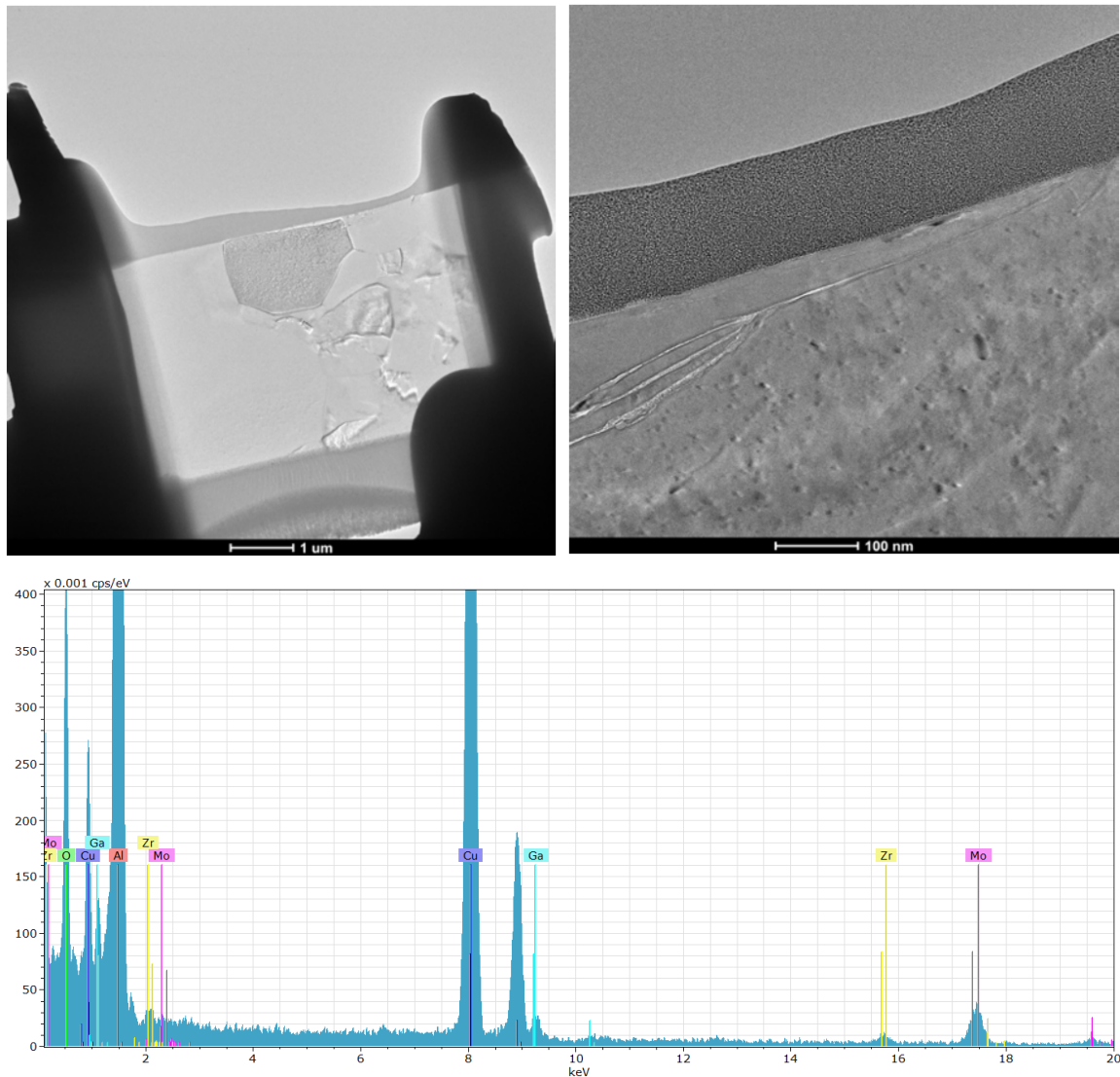


Figure 5.9: TEM and analysis of the surface of an unetched 5N5 aluminium coupon piece. Top left: view of the whole sample. The dark part is the same sample, just not thinned down. The sample is a cross-section: the top edge is the surface, and moving down is going into the sample. A large grain can be seen near the surface. Top right: zoomed-in view of a crack near the surface (the middle stripe is Pt, above is vacuum). Bottom: EDX of most of the sample. We see the expected Al (sample), Cu (grid), Pt (sample coating), Ga (implanted by the FIB), and O (surface oxide). However, we also see Zr and Mo. Quantification of the EDX reports 2.83% O, 0.02% Mo, and 0.41% Zr by atomic number.

[TEM](#) of the entire sample, top left, does not look significantly different. We note that there are some cracks near the surface, as seen in the top right zoomed-in image. As with the etched sample, we detect Mo and Zr aside from the expected elements. Quantification reports somewhat more of both.

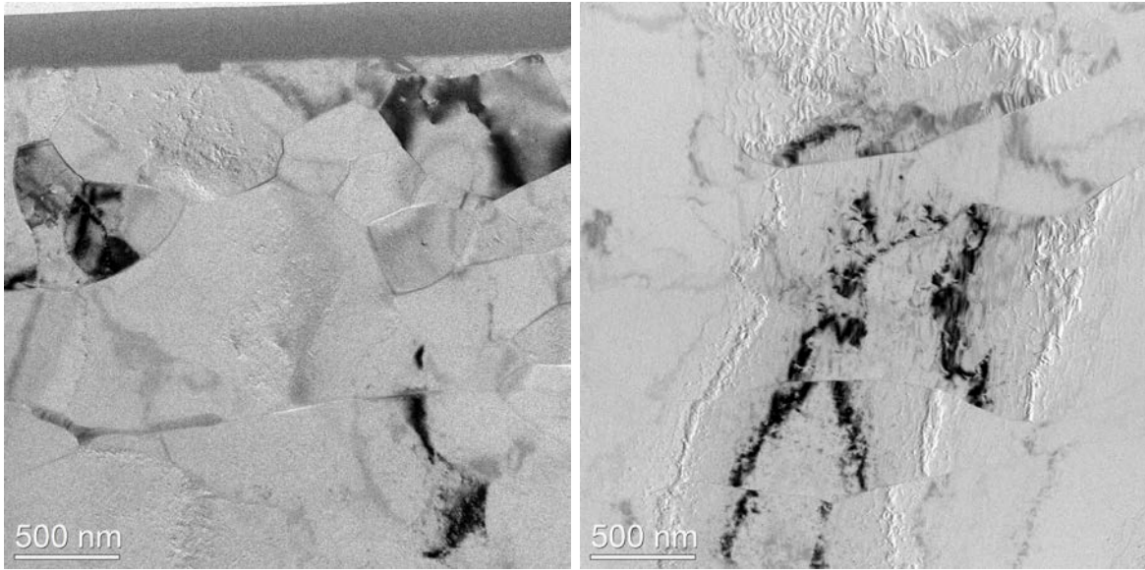


Figure 5.10: [TEM](#) of $100\text{ }\mu\text{m}$ underneath the surface of etched (left) and unetched (right) 5N5 aluminium. Note what appears to be a larger number of smaller grains than near the surface. The dark areas are defects or dislocations (note that they can change abruptly across a grain boundary). There is no obvious difference between the two images to me.

Fig. 5.10 depicts [TEM](#) images of pieces of the etched (left) and unetched (right) 5N5 aluminium coupons, except this time, collected below $100\text{ }\mu\text{m}$ from the surface. We see that in both cases, there appears to be more grain structure, with smaller grains. The darker areas are defects or dislocations. A common characteristic of these is that they can change discontinuously across grain boundaries, indicating that they are structural defects. I see no obvious difference between the two samples.

Fig. 5.11 shows a [HAADF](#) image (top left) and [EDX](#) map of an etched 5N5 aluminium sample taken below $100\text{ }\mu\text{m}$ under the surface at a location that appears to contain a copper inclusion. We see it in [HAADF](#) as a bright spot, since copper is much heavier than aluminium and the image is dark field. The [EDX](#) reveals less Al

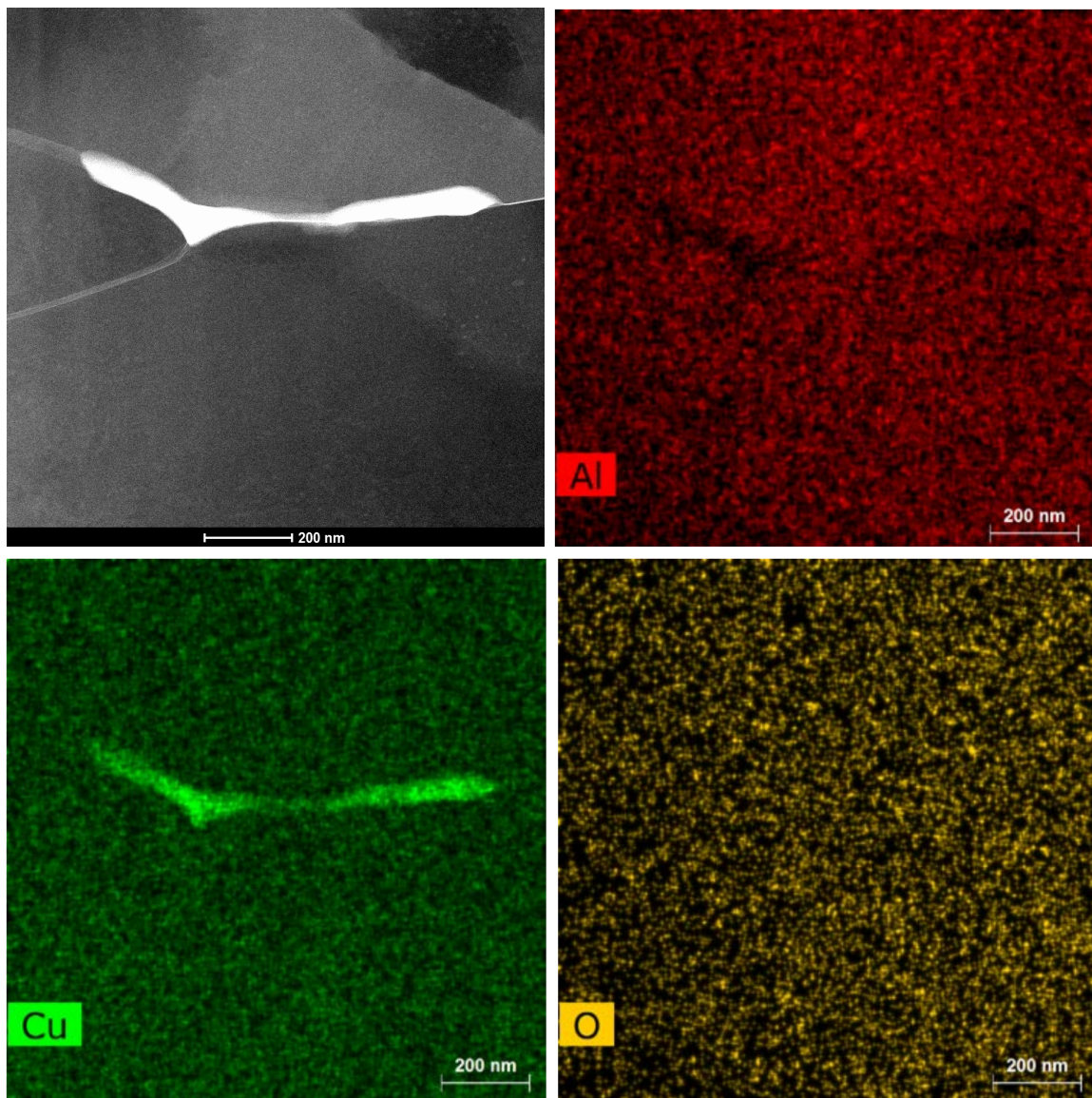


Figure 5.11: HAADF (top left) and an EDX map of a copper inclusion in a piece of etched 5N5 aluminium 100 µm beneath the surface. The higher-atomic number copper appears brighter than the aluminium in the dark-field image. Note that we see less aluminium and more copper in the bright region, with no difference in oxygen. The cause of this is unknown.

and more Cu in that location, while the O remains constant. It is unclear what would cause such an inclusion (if that is what this image actually indicates). This raises the question of what exactly “5N5” means – presumably, it is a statement of average concentration over a large volume, but perhaps does not necessarily preclude small sections of relatively-concentrated impurities within the Al. Could these contribute

to loss?

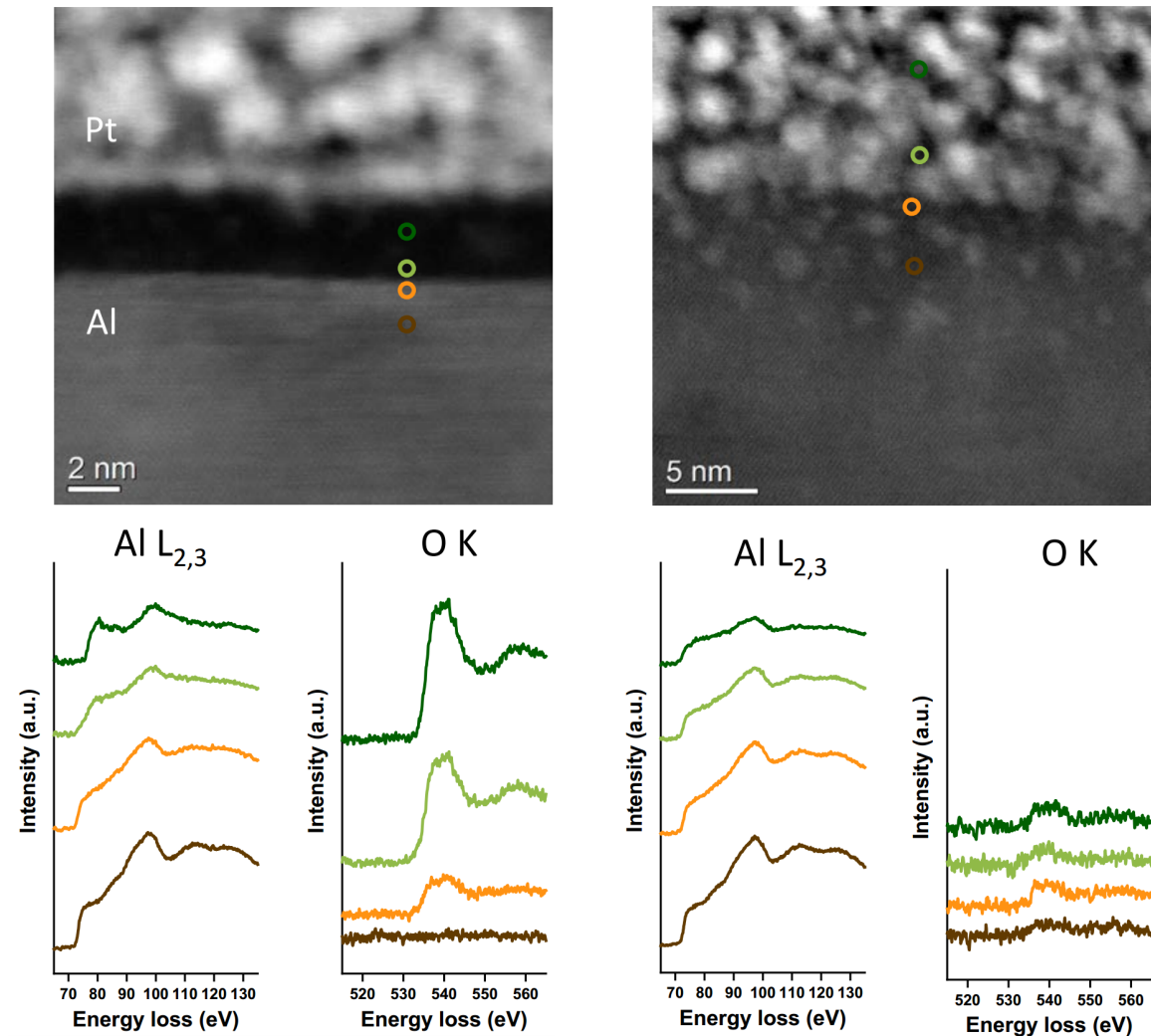


Figure 5.12: [TEM](#) (top) and [EELS](#) (bottom) of etched (left) and unetched (right) 5N5 aluminium. The [TEM](#) shows Al on the bottom, Pt on the top, and the oxide layer is in the middle. The etched sample appears to show a clear boundary, whereas the unetched one does not (in this case – this is not always true). To more precisely determine where the oxide layer is, we can perform [EELS](#) in the coloured circles. In the etched sample, the oxide starts near the orange and extends throughout the dark green (and likely further). In the unetched, the oxide goes through the orange to the dark green, where we start to see less Al.

So far, we have looked at [TEM](#) and [EDX](#) measurements of our samples and attempted to find some features of interest. Let us now instead examine something we already believe to be a loss mechanism, namely the surface dielectric. Fig. 5.12 shows

TEM (top) and **EELS** (bottom) of etched (left) and unetched (right) 5N5 aluminium coupon samples. In the etched sample, there appears to be a clear Al region, a clear Pt region, and what we can hypothesise to be a clear surface dielectric (here assumed to be an oxide for simplicity). To be sure, we can collect **EDX** data at several points along a line between these layers (represented by the coloured circles). We see that the brown point is entirely Al, the orange point has some oxide, and the green and dark green points have a lot of oxygen. Let us now compare the unetched sample. Here, the lines are not clear between the layers. **EDX** reveals that the oxide starts near the brown point, and the Al ends near the green point. However, as discussed in the note above, we cannot simply conclude that the unetched sample has a thicker oxide from this, since the orientation of the Al/oxide interface is by no means guaranteed to be parallel to the beam. This is especially true since there is not a well-defined axis to which to align the sample for our polycrystalline films. In fact, a tilt of the interface relative to the beam would be one explanation for the relatively smeared interfaces in the unetched image. Furthermore, the organometallic Pt compound which coats the sample contains oxygen, making it harder to distinguish where the native oxide ends. One way to compensate for the latter effect would be to coat the sample in a thin layer of gold before sending it over, preserving the native oxide layer.

Finally, I show another way we can use the information gained from this method in Fig. 5.13. Here, we see **TEM** (top) and **EELS** (bottom) of a boundary between two grains (left) and cracks near the surface of an unetched sample (right). From the **TEM**, we see stitching between the grains, indicating the grain boundary is likely not parallel to the beam; the cracks look different. **EELS** allows us to confirm the difference: we can see that there is no oxide in the grain boundary, and in fact, the chemical composition of that region is the same as inside the grains (at least in terms of Al and O). However, the cracks are heavily oxidised (orange, dark green points).

From the above, we have seen that the grain structure seems to change from

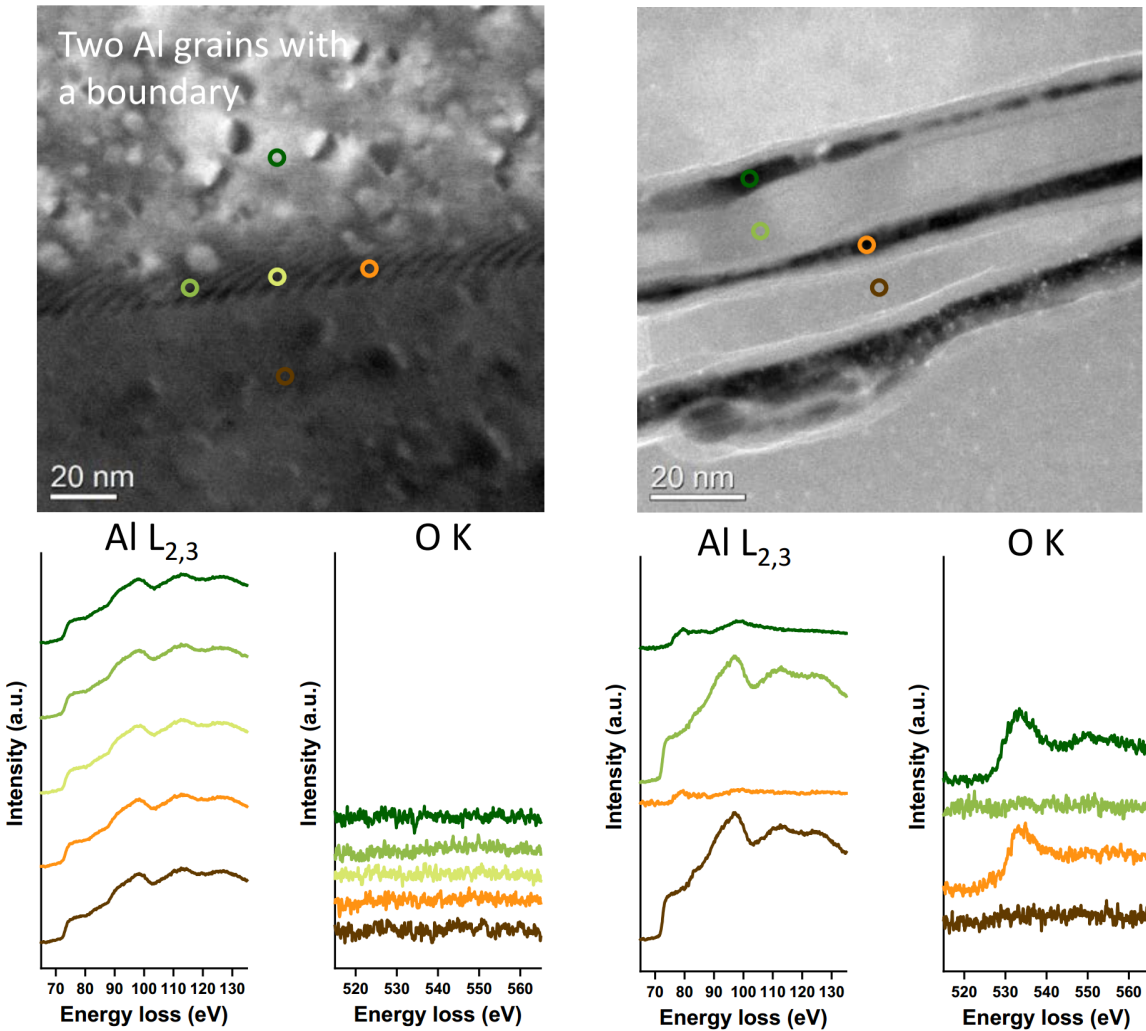


Figure 5.13: **TEM** (top) and **EELS** (bottom) of a grain boundary in etched 5N5 Al (left) and cracks near the surface of unetched 5N5 Al (right). Using the combination of **TEM** and **EELS**, we can probe the different kinds of boundaries. For the grain boundaries on the left, we see that there is only a re-alignment of the crystal direction, but no oxide is trapped in the interface. On the right, we can see cracks, which are filled with oxide (orange and dark green points).

near the surface to deeper into the sample, that there seems to be more Mo near the surface and when unetched (although it is unclear whether we can trust this, since the numbers extracted are below the precision of the instrument), that there seem to be copper inclusions in our Al, a suggestion that the oxide is thicker in unetched samples, and the existence of oxide-filled cracks near the surface of unetched machined samples. However, none of the above are definitive, they are shown more as illustrations of the

capabilities of a [TEM](#) as applied to our samples. To learn more we would need more samples and more careful analysis, which is hampered by the long preparation times for [TEM](#) samples but certainly is not impossible. One thing I have not shown is the ability to Fourier transform an atomic-resolution [TEM](#) to learn about the crystal structure, although this is really more applicable to more crystalline samples, such as our substrates or epitaxial films.

5.2.3 X-ray

Finally, I discuss measurements taken at the National Synchrotron Light Source II (NSLS-II) at [BNL](#). There were several types of measurement performed by different people.

XPS

I shall start with [x-ray photoelectron spectroscopy \(XPS\)](#) performed at NSLS-II. In [XPS](#), we shine x-rays onto the sample, and collect the ejected electrons. By subtracting the kinetic energy of the collected electrons from the energy of the x-ray photons, the binding energy of the electrons is obtained. We can then match peaks in the data to different atomic transitions, which generally have different energies. The images and data presented in this section are from Ira Waluyo. The data was taken with the In Situ and Operando Soft X-ray spectroscopy (IOS) beamline. The measurements were done on four 5N5 aluminium coupon samples, processed in different ways:

- **A:** Solvent cleaned (3 min sonicated in [NMP](#), acetone, isopropanol, followed by N_2 dry),
- **B:** Solvent cleaned followed by the standard aluminium etch,
- **B-DT:** Same as **B**, followed by diamond-turning,
- **C:** No processing after machining.

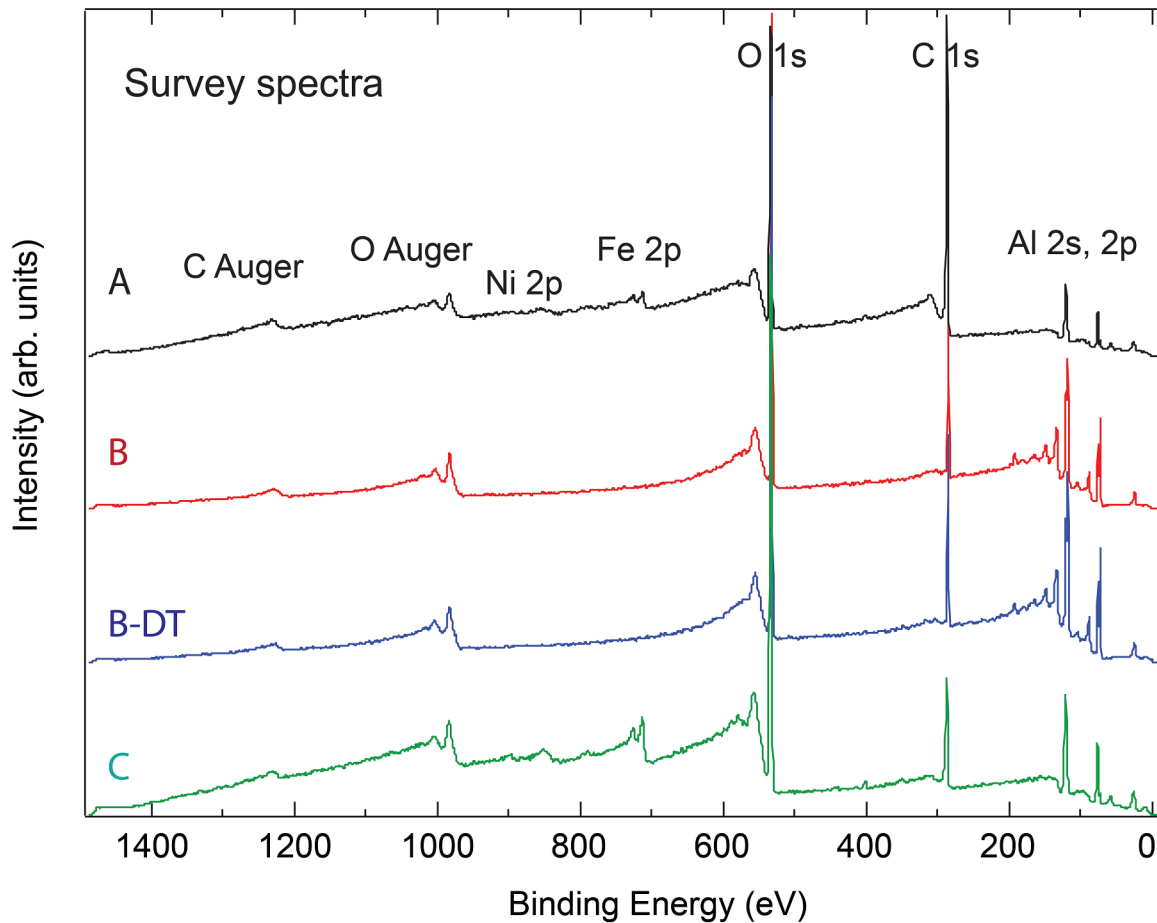


Figure 5.14: Survey XPS spectrum of the four 5N5 Al coupon samples, taken over a wide range of binding energies. This allows us to see regions of interest, which we can then measure in more detail. For example, here we see several features (labelled on the graph): two transitions for C and O (Auger and 1s), the Ni and Fe 2p transitions, and 2s and 2p transitions for Al. The four curves are translated vertically by different amounts for readability.

First, we take a survey spectrum over a broad range of binding energies, Fig. 5.14. From this survey, we can see peaks of potential interest to examine in more detail. Some of these have been labelled in the image. For example, the Fe 2p peaks appear larger in **A** and **C**. Auger refers to the energy of secondary electrons ejected in the Auger process: after a core electron is knocked out by the x-ray, an electron from a higher orbital falls to take its place. The resulting energy can kick out another electron from a higher orbital.

Let us now zoom in on some areas of interest. First, let us look at the peaks

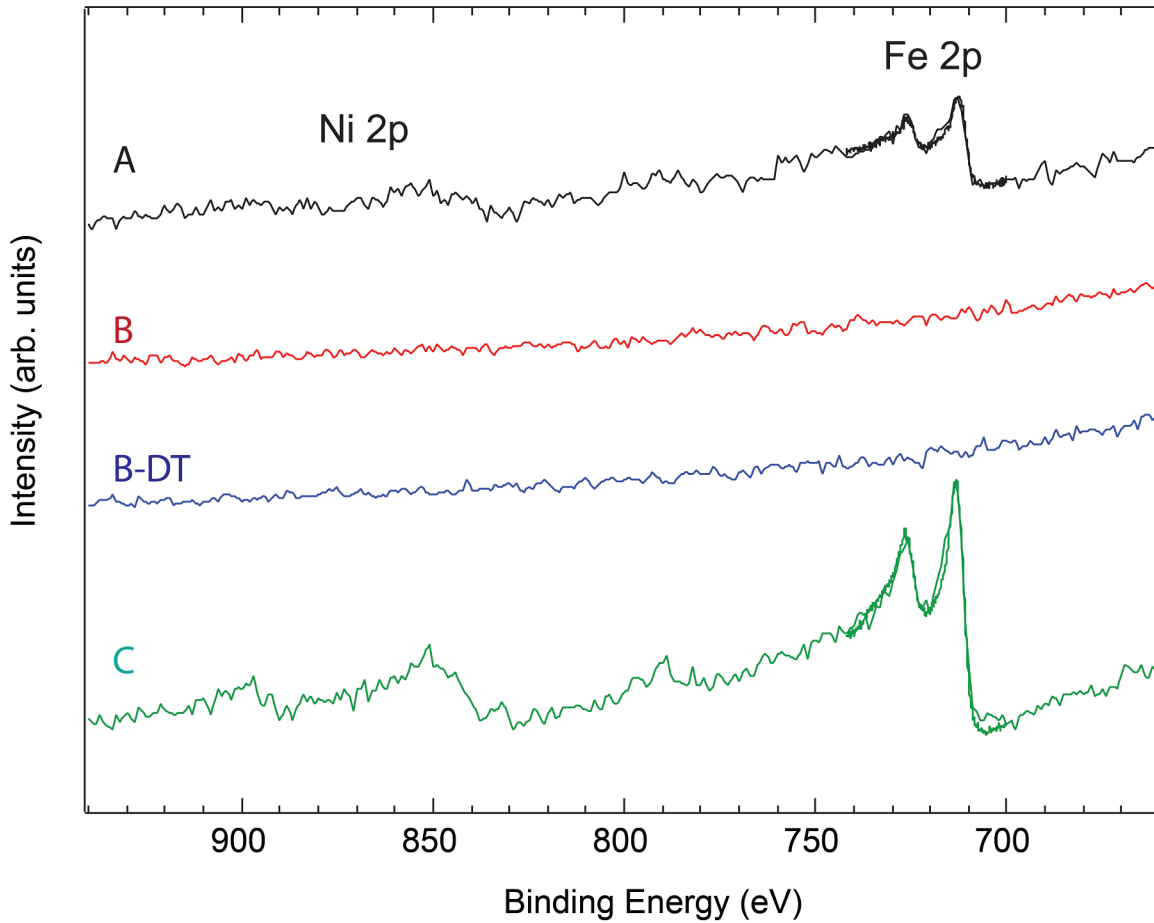


Figure 5.15: [XPS](#) of the 5N5 Al coupons focussed around the Ni 2p and Fe 2p transitions. We observe that iron is clearly present in **A** and **C**, and absent in the two **B** samples. Nickel can also be seen in **C**, and somewhat in **A**. This suggests that the etching process removes the nickel and iron from the surface of the aluminium. Since our sample is nominally 5N5 aluminium, it is likely that these contaminants are introduced during machining, possibly from the tools.

associated with Ni 2p and Fe 2p: Fig. 5.15. We clearly see that **A** and **C** have iron, while the two **B** spectra do not. Nickel is also present in **C** and probably **A**, and not in the **B**'s. This indicates that etching removes the nickel and iron impurities. Since our coupons are made of high-purity aluminium, we do not expect to see nickel or iron at such levels. It is likely that these are introduced in the machining process, and then removed by the etching.

By looking at the Al 2s and 2p (and P 2p) area of the spectrum, we can see what is likely another effect of the etching. Fig. 5.16 shows that the **B** spectra contain

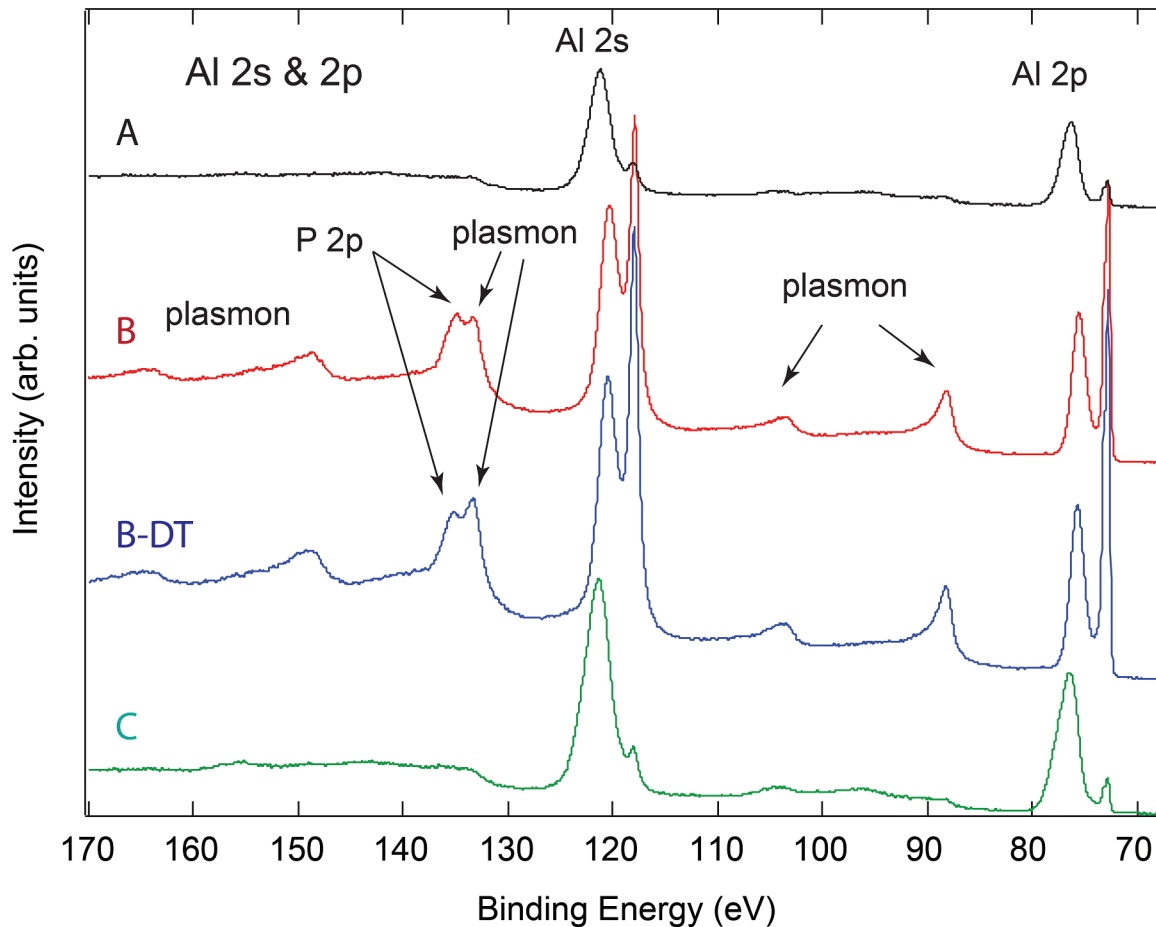


Figure 5.16: XPS of the 5N5 Al coupons focussed around the Al 2s and 2p peaks. In **A** and **C**, we see only the Al 2s and 2p peaks. However, in the two **B** spectra, we also see additional peaks corresponding to P 2p as well as associated plasmon peaks. This is likely due to the fact that the etchant we use, Transene Aluminum Etchant Type A, contains phosphoric acid.

a peak for P, which appears absent for **A** and **C**. I note that the etchant we use for our aluminium, Transene Aluminum Etchant A, contains phosphoric acid. It is likely that etching in this results in implantation of phosphorus. Furthermore, the amount of diamond turning we performed does not drastically affect the phosphorus peak, indicating that it penetrated deeper than the amount we removed. It could be worthwhile to diamond turn our sample deeper to see whether this changes. We also see plasmon peaks, which happen when the x-ray not only ejects an electron, but also excites a plasmon (a quantum of plasma oscillation – collective electron motion).

There are several other measurement areas not shown here. For example, the **B** samples has C 1s peaks that are around 2 eV lower in binding energy than for **A** and **C**, and **A**'s peak is much higher in intensity than the others; conversely, **A**'s O 1s peak is much lower in intensity than the others (and 1 eV higher in binding energy than the **B** ones, with **C** an additional 1 eV higher). Also, **C** seems to have a more pronounced Ca 2p peak than the rest of the samples. Finally, the valence band for the **B** samples has a clear drop near 0 energy, while **A** and **C** do not.

XRR

I shall now describe [x-ray reflectivity \(XRR\)](#) measurements performed at NSLS-II at [BNL](#). In [XRR](#), we shine x-rays at our sample at a very small, variable angle to the surface and collect the reflected signal. The intensity of the reflected signal as a function of angle depends on the properties of the surface of the sample. A model with a set number of layers is used to fit the reflection vs. angle data. The number of layers is an input parameter and is thus set to match what is expected to be found on the surface; several fits with different numbers of layers can be tested to see which is better. Once a number of layers is chosen, the fitting gives us information about the layers that best fits the data, including thickness, density, and roughness. The data and plots presented in this section are from Jean Jordan-Sweet at [BNL](#)/IBM and Christian Lavoie at IBM.

Several different samples were tested. The purpose of the first experiment was to determine whether our “cleaning” of the wafers changes the surface in any way. Three 50 mm, 100 μm -thick sapphire wafers were provided:

- **BP19:** a brand new wafer straight from the box,
- **BO19:** a wafer which was solvent cleaned (2 minutes in NMP, acetone, methanol, isopropanol, followed by an N_2 dry),

- **BM19:** a wafer which was solvent cleaned as above, coated in SC1827 photoresist at 2000 rpm for 90 s, baked for 5 min at 85 °C, and then stripped of resist via 2 minutes of acetone then methanol rinse repeated twice.

Since I prepared the samples but another person measured them, this experiment was able to be blinded: **BNL** were told what the three processes performed on the wafers were, but not which process matched to which label (the wafers were visually identical). This can help remove the effects of bias that a researcher may have about the expected results of the experiment.

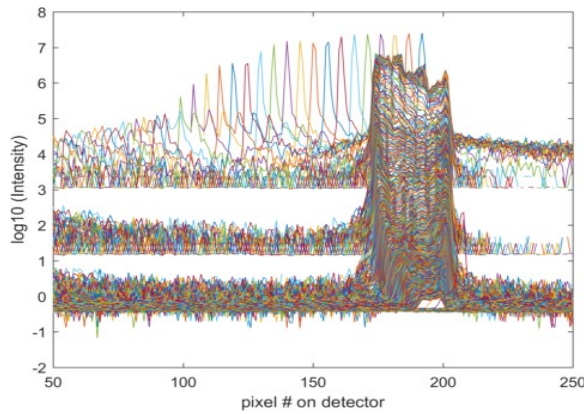


Figure 5.17: **XRR** of a thin sapphire wafer. Note the 41-pixel-wide beam width, which indicates a large deviation from flat – for thicker wafers from another group, this window is around 15 pixels wide. This makes fitting the data extremely difficult.

However, it turns out that the thin wafers are either too non-flat on their own, or bend too much in the vacuum chuck holding them to be fit well. (Anecdotally, I note that when making transmons from the 100 μm -thick wafers, I had the same problem in the e-beam writer). As a result, the reflection near the critical angle cannot be fit well, especially in the case of **BP19**. In fact, even correcting for basic curvature is not enough to explain the data.

Nevertheless, I shall show some sample fits, again, primarily to demonstrate the technique rather than make some conclusion about the processing. **BO19** is fit relatively better, Figs. 5.18 and 5.19 show the **XRR** fit to a one- and two-layer model,

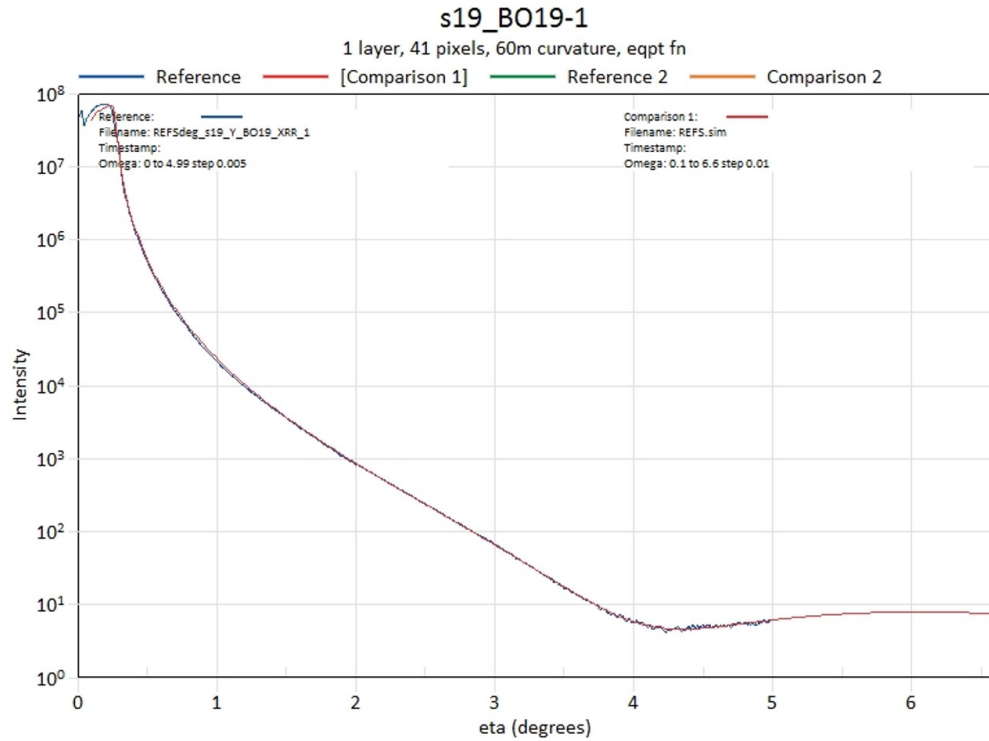


Figure 5.18: Sample [XRR](#) of a thin sapphire wafer which was solvent cleaned: **BO19**. This particular spectrum is fit to a single-layer model, which seems to do decently well, except near the critical angle. The layer has thickness of 5 Å, density of 64% of sapphire's (which is assumed to be 4.02 g/cm^3), and roughness of 0.6 Å. Under this layer is assumed to be infinite perfect sapphire. The goodness-of-fit is reported as 0.0198.

respectively. There does not appear to be a visible difference between the two fits. Furthermore, the second layer in the two-layer fit has a density of 97%, and is still only 20 Å thick, so the two fits are actually quite similar. Even in this data (which is the best of the three wafers), we still see some fit issues near the critical angle.

Table 5.3 shows the extracted fit parameters for all three wafers. There is no clear pattern which would indicate that the surface treatment makes a difference, even if we take the fit results at face value. We do see that across all three samples, there appears to be a layer of around 5 Å thick with a density of around 50-60% on the surface of our sapphire. This may be a real effect which could be investigated further.

We have also attempted to measure indium films on silicon using [XRR](#). The goal

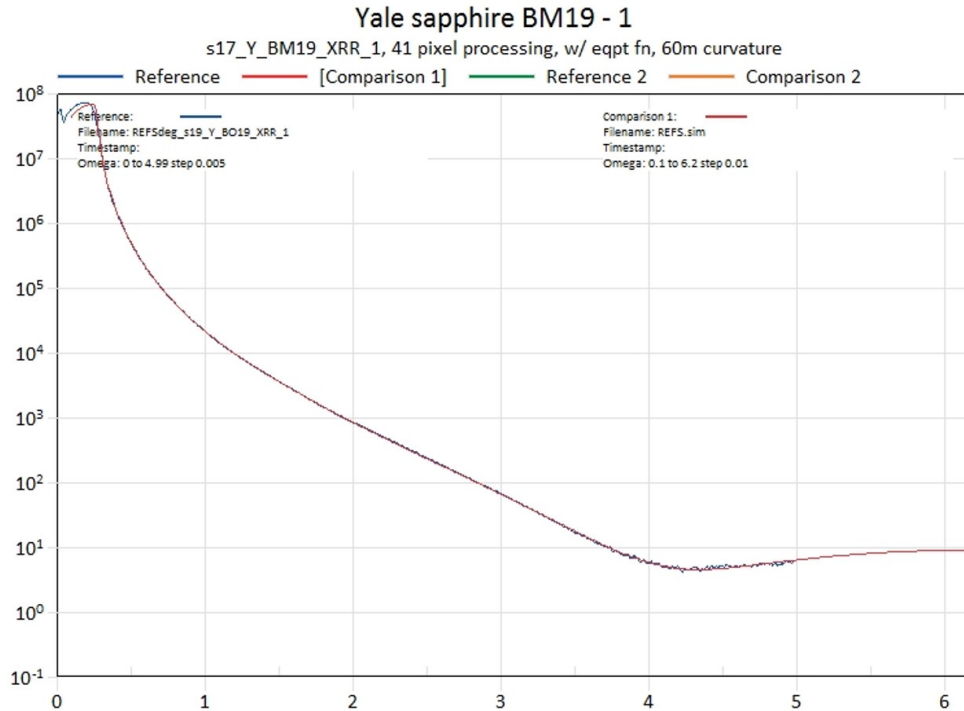


Figure 5.19: Sample XRR of a thin sapphire wafer which was solvent cleaned: **BO19**. This particular spectrum is fit to a two-layer model, which seems to do decently well and is not visually different from the one-layer fit. The top layer has thickness of 5 Å, density of 59% of sapphire's (which is assumed to be 4.02 g/cm^3), and roughness of 0.1 Å; the middle layer has thickness of 21 Å, density of 97%, and roughness of 0.1 Å. Under these layers is assumed to be infinite perfect sapphire. The goodness-of-fit is reported as 0.141. We note that the intermediate layer is not very different from regular sapphire, which helps explain why this is so similar to the one-layer model.

of the experiment was to determine whether ONTOS had any effects on the surface, so the two samples were a standard thermally-evaporated 1.2 μm -thick film on In on Si, and an identical one which was then treated with ONTOS. However, it turned out that the indium films were too rough to even get a reflection, so we were unable to acquire any data. We know from [SEM](#) and [atomic force microscopy \(AFM\)](#) that In films of this thickness form grains with height variation on the scale of hundreds of nm, which is too much of a difference for [XRR](#).

| Wafer | Layer | Thickness (Å) | Density (% ρ_{sapph}) | Roughness (Å) | GOF |
|-------------|-------|---------------|------------------------------------|---------------|-------|
| BP19 | 1 | 5.8 | 69 | 0.98 | 0.074 |
| BP19 | 1 | 5.7 | 57 | 0.78 | 0.064 |
| | 2 | 19 | 85 | 0.1 | |
| BO19 | 1 | 5.1 | 64 | 0.57 | 0.020 |
| BO19 | 1 | 5.0 | 59 | 0.1 | 0.14 |
| | 2 | 21 | 97 | 0.1 | |
| BM19 | 1 | 3.8 | 46 | 0.4 | 0.034 |
| BM19 | 1 | 4.6 | 51 | 0.68 | 0.022 |
| | 2 | 1.0 | 96 | 0.1 | |

Table 5.3: XRR fit results for the three sapphire wafers. Two-layer fits are in grey. Density is quoted in percent of sapphire density, which is assumed to be $\rho_{\text{sapph}} = 4.02 \text{ g/cm}^3$. As before, this table is meant to serve as an example of the type of analysis that can be performed, the fits themselves are not very trustworthy due to the bending of the wafers. There does not appear to be a clear pattern.

5.3 Outlook

In this chapter, we have discussed different ways to measure loss mechanisms in materials relevant for superconducting resonators and qubits. Multimode resonators have already allowed us to make some measurements of bulk aluminium, showing for example that etched high-purity aluminium has higher q_{cond} than in unetched high-purity or in 6061 Al. This knowledge allows us to predict the Q of new resonators designs. However, it does not tell us the causes for these losses.

We then used materials characterisation techniques to attempt to understand the microscopic causes. The most fruitful case turned out to be the comparison between etched and unetched 5N5 aluminium, although even there we did not have conclusive evidence for any particular source. Nevertheless, we were able to find clear differences: etching removed Ni and Fe contaminants (and introduced P as a tradeoff), and also changed the C and O environments as well as the valence band. The unetched material also appeared to have more oxide-filled cracks near the surface. A feature of this experiment that stood out was the fact that we had two processes to compare, in which one was known to achieve better results. Going forward, this

appears to be a promising way to conduct these studies, although to show causation rather than correlation, more needs to be done.

It is in general not trivial to combine direct microwave measurements of our devices with microscopic characterisation techniques. There are several difficulties: we are just starting to have ways to measure (as opposed to bound) all of our loss channels, the microscopic causes are frequently not known, requiring trial and error, the timescales for experiments at a shared facility, especially requiring beamlines, are much longer than for experiments in our lab. There is also the issue of knowledge: researchers in quantum computing are not acquainted with a lot of the materials characterisation techniques and do not know how to interpret the results, whereas researchers in materials science may not be familiar with the properties we're interested in. This is especially true since there are not yet known proxies for microwave loss measurements – there is not a way to predict how high of a q some loss channel will have without actually measuring it. A lot of obvious characteristics, such as how shiny or smooth a surface looks (or more sophisticated versions thereof) have not actually been shown to correlate with quality.

In the future, if this avenue of research is continued, much more learning will be necessary by both communities in order to start really understanding the causes of loss rather than performing somewhat arbitrary measurements in attempts to find correlations. Indeed, these questions are very difficult, and it may turn out to be the case that trial-and-error proves sufficient for the quantum computing community. However, I believe the work done in the past few years and the new collaborations launched can help us understand our materials much better, and hopefully improve our devices in the future.

CHAPTER 6

Conclusion and Outlook

In this thesis, I have given an overview of superconducting microwave resonators, discussed my work on two resonator types (micromachined cavities and suspended coaxial resonators), and described some preliminary studies on materials used to form the cavities. Since micromachined cavities are very sensitive to the seam at their joint, I developed and tested an ultra-high-quality microwave seam using indium bump bonding. The resulting cavities had a longer lifetime than the currently-used coaxial stub cavities. Suspended coaxial resonators allow for the centre conductors, which set the frequency of the resonator, to be switched out, and add a possible multiplexing dimension compared to the stub cavities. They also can match or slightly exceed the quality of the stub cavity even if made out of cheaper and easier-to-machine 6061 Al, rather than high-purity Al. I then presented recent work on the use multimode resonators to extract the properties of individual loss channels in the resonator. We were able to measure q_{cond} for bulk aluminium, although our devices were generally insufficiently sensitive to q_{MA} to get a measurement. Finally, I presented some exploratory studies of the our devices using traditional material

characterisation methods. We learned about some differences between etched and unetched high-purity aluminium.

Let me now briefly mention some things that did not work or did not work well. In terms of design, it is challenging to make larger structures with micromachined cavities, meaning structures with more elements than the cavity and a patchmon. For example, if you want to make two cavities coupled by a patchmon, one natural way is to stack the cavities one on top of the other, with the patchmon in the middle. However, any time you have more than two layers you want to bond, you have to be very careful to design all of the elements such that the resulting structure actually can be bonded. One may also consider coupling to the cavity via e.g. a [CPW](#) on one of the surfaces through a small aperture. However, coupling a micromachined cavity to any form of transmission line without incurring significant losses also proved difficult. I want to stress that these tasks are not impossible, but are not easy.

There were also several experimental difficulties. Suspended rod resonators using wire centrepins did not turn out to have high Q 's with any of the tested materials. Replacing the wire with machined rods did not help by as much as expected – I think it *is* possible to get high Q 's with such a design, but the amount of electromechanical engineering necessary likely outweighs any gains in design flexibility. I tried making transmons on 100 μm -thick sapphire in order to reduce the bulk dielectric participation. The fab on such a thin wafer proved to be difficult (for example, the wafer would bend in any vacuum chuck or in the e-beam sample holder), and the resulting transmon was not better than those made on regular-thickness sapphire. Similarly, I used 100 μm -thick sapphire for lasercut coaxial centrepins. These proved to be very fragile, and the only plausible mechanism for this being better than a thicker chip is the reduced amount of sidewall. I also note that the clamshell package design for the suspended stripline had too much vibration to be useful, likely due to the BeCu spring clip design, although these clips work well in other situations.

6.1 Future of Resonators

For a number of years, the predominant resonator used for bosonic quantum computing has been the machined 3-D cavity. As of the writing of this thesis, the stub cavity has mostly overtaken the rectangular cavity; the principle remains the same. Despite the long life and potential for scalability of the micromachined cavity, to my knowledge, none have been made since the publication of our paper. I believe this to be due to the fact that the investment in developing such a cavity is not currently worthwhile for any project: although a single micromachined cavity does have a longer lifetime than a stub cavity, this is generally not the main limiting factor in experiments. The true advantages of such a design manifest when one is making very large quantities of cavities. However, our branch of quantum computing is still operating with small single-digit numbers of devices, and there remain many interesting problems to solve and challenges to overcome in this regime. Therefore, I think it will be a number of years before something like the micromachined cavity becomes more commonplace for quantum information storage (although there may be more near-term applications in sensing). Additionally, such a design still has a fairly large footprint. There are ideas for how to use the knowledge gained in this research to make smaller on-chip resonators without sacrificing too much in Q , which in my opinion is promising as a more scalable bosonic architecture.

The suspended coaxial resonator is more straightforward to use as a near-term resonator, although it would probably take a form somewhat different than that presented here. It is relatively easy to make, and its essentially-identical mode structure makes it more of a drop-in replacement for the stub cavity. In fact, some lab members have already considered using such a system for their experiments. Desirable modifications would probably include simpler machining (avoiding wire EDM, for example) and a more robust clamping system.

I note that the field has been working with several-resonator devices for a long

time. There has been interest in increasing this scale for a number of years, and there are several potential paths forward. However, as mentioned above, there are still a large number of experiments on e.g. gates that can be performed with current devices. Given also the difficulty of scaling up, I think it will be some time before it becomes a main priority of academic groups. It is likely that this problem is being addressed by private companies, who have somewhat different priorities (as well as more engineers), although no information about this has been released to my knowledge. I am not sure whether the next generation of resonators will look more like the suspended coaxial resonators, resonators defined on a plane, flip-chip resonators, or perhaps an entirely new design. I think that the size of current devices is still too large (as is the size of a packaged chip with enough transmons to make a logical qubit) to make a computer that can run currently-known useful algorithms. Therefore, I think that size will become more important of a consideration as we scale up, and something like the on-chip design mentioned above is a likely candidate.

6.2 Future for Materials

Understanding losses in superconducting circuits has been of interest for many years. In fact, decades prior to superconducting quantum computing, incredibly high Q 's have been achieved in superconducting cavities, in part thanks to advanced surface treatment and joint welding methods developed as a result of loss studies. Although we still cannot separate all of the losses from different channels in sufficiently complicated devices, a lot of progress has been made toward achieving this goal. As we saw with some of the devices presented in this thesis, e.g. the suspended coaxial resonators, we can sometimes predict the quality of a new device from known material properties, and make corresponding design decisions. This is a remarkable achievement which enables a more purposeful way of building new devices.

Nevertheless, more work remains to be done on achieving better separation between the different surface loss channels, as well as on understanding the microscopic causes of loss. The knowledge of which particular surface is responsible for loss would guide efforts to increase coherence by allowing us to focus on the limiting surface(s). Without this, one may improve the quality of a non-limiting surface, but be unable to notice the change, and thus possibly conclude that no difference has been made. Understanding the microscopic causes of loss will enable targeting them directly, removing some of the trial-and-error associated with the current method, which relies on educated guesses.

I believe that multimode resonators are a good option for extracting the individual losses, and even learning about the homogeneity of the materials involved. They are no more difficult to make than standard devices, and the measurement tends to be even more straightforward. Of course, it also possible that sufficiently good materials or processes end up being discovered by trial and error, but multimode resonators can still help us understand exactly what is being improved. This can be useful in less-obvious ways: since the fundamental goal of the research is not to make a cavity with the highest Q , sometimes it may be worthwhile to sacrifice some loss for other advantages, such as size, ease of coupling, ease of production, etc. Knowing the properties of the different materials can help us design devices that are best suited for quantum computation.

Although there has long been interest in traditional materials characterisation, the presence of many active collaborations with material scientists is relatively recent in this field. Material scientists are not so many, and research is expensive (including time, especially anything involving beamlines or sometimes [TEM](#)), so the recent prominence of quantum computing combined with the additional funding offered as a result has probably helped. So far, there has been a relatively small number of works showing some detectable differences between different materials both in microwave

loss and in structure, but no clear causality has yet been established. Indeed, to my knowledge, no material improvements have yet been advised by traditional material characterisation methods. Of course, since this is new and traditional methods (especially ones involving beamlines) can take a very long time, it is possible that we will start seeing results in the next several years. This type of research will definitely be continued, considering the number of recently-formed and funded collaborations between universities and national labs, etc. In principle, it could be very helpful to know what is going on at the microscopic level in our devices. To achieve this, certainly a very large amount of work will have to be done, both in terms of making and testing devices, but also in terms of establishing a common language and knowledge base between the two communities, in order for this to happen. If it does, understanding the causes of loss would both be exciting from a fundamental science perspective, and open new avenues for making higher-coherence devices.

Appendices

APPENDIX A

Fabrication details

A.1 Basic processes

A.1.1 Cleaning or preparing the wafer

Basic solvent clean

The wafers arrive from the supplier in different types of packaging – some are in a multi-wafer box (this is true for the standard 2-inch and 4-inch sapphire wafers), some are in individual vacuum-sealed wafer holders (such as the 100 µm-thick sapphire wafers). For sapphire and silicon, the standard lab practice is to sonicate the wafer in solvents before fabrication, although to the author’s knowledge, there is no evidence that this removes any particular contaminants, or improves any metric of the resulting devices. The solvent rinse sometimes leaves spots visible under a light microscope, which can be removed with a careful [de-ionised \(DI\)](#) water rinse.

This standard process involves sonication for 2-5 min in NMP, acetone, and methanol, sometimes followed by a [DI](#) water rinse and finishing with a nitrogen blow-

| # | Description | Notes |
|-------|----------------------------------|--------------------------------------|
| 1 | Sonicate in NMP for 5 min | In quartz boat or face-up in beaker |
| 2 | Sonicate in acetone for 5 min | In quartz boat or a different beaker |
| 3 | Sonicate in methanol for 5 min | In quartz boat or a different beaker |
| (3.5) | Rinse with DI water | Optional, depends on resist used |
| 4 | Blow dry with nitrogen | Without letting solvent dry |

Table A.1: Standard process for cleaning wafers.

dry. The wafers are sonicated in Pyrex (likely borosilicate glass) beakers and typically held with stainless steel tweezers. **If using other tweezer materials, ensure their compatibility with the solvents, especially NMP!** Generally, the 4-inch wafers are simply placed into the beakers, while 2-inch wafers can be sonicated vertically in a quartz boat. The **DI** water rinse is sometimes avoided if the wafer is to be used for e-beam lithography, as the e-beam resist is very water-sensitive. It is important to note that the nitrogen dry works by blowing the remaining liquid off the wafer in drops, carrying away potential residues. Allowing it to simply dry will result in re-deposition of the residues on the surface of the wafer.

RCA clean clean for silicon

For silicon, a more advanced type of cleaning from the semiconductor industry called the **RCA clean** can be used. This term is used to describe several variants of a cleaning procedure. There are three main steps:

1. Organic clean: **DI** + ammonia water + hydrogen peroxide. Removes organic contaminants but grows a thin oxide layer.
2. Oxide removal: **BOE** etch. Optional step.
3. Ionic clean: **DI** + hydrochloric acid + hydrogen peroxide. This removes ionic contaminants.

A thorough **DI** rinse should be performed between steps. **PTFE** beakers can be used

| Step | Description | Notes |
|---------------|--|------------------|
| Organic clean | 10 min in 5:1:1 DI : NH ₄ OH : H ₂ O ₂ at 75 °C | Keep in DI after |
| Oxide removal | 30 seconds dip in 10:1 BOE | Step optional |
| Ionic clean | 10 min in 5:1:1 DI : HCl : H ₂ O ₂ at 75 °C | |

Table A.2: **RCA clean** cleaning process for silicon. The NH₄OH, HCl, and H₂O₂ are around 30% solutions. It is very important to clean the wafer well with **DI** water between steps, and a good idea to keep it in **DI** between steps to prevent re-contamination

(glass will be etched by the **BOE**, and materials like Pyrex (borosilicate) can cause ionic contamination).

Piranha clean to remove organics

Another cleaning procedure available to us is the piranha etch (“nh” in Portuguese is pronounced similarly to the Spanish ñ). This is a very aggressive method of removing any organic residues (although it will also etch some other materials). **Both mixing and using the piranha solution are quite dangerous, check with your cleanroom specialist before trying this!** Note also that this will react very strongly with any present organics, including solvents and photoresist, so make sure to remove most of these from your sample before using this etch.

The name “piranha” is used to refer to several related etch processes, namely some combination of hydrogen peroxide and either hydrochloric acid or ammonia solution (base piranha). In our case, we use the acid piranha. There are two opposite schools of thought regarding the order in which piranha must be mixed: some state the peroxide *must* be added to the acid, some state the acid *must* be added to the peroxide, again, check with your cleanroom specialist. The reaction is exothermic, so the solution heats up, and starts bubbling; going too quickly can result in visible gas/vapour release. I have added the peroxide to the acid, making sure to add only a small volume at a time, then waiting for the solution to calm down, and pouring in a different part of the beaker. I have also used a **PTFE** beaker (do not use other

| Step | Description | Notes |
|-------------|---|---------------------|
| Mix piranha | Pour 30% H ₂ O ₂ into concentrated H ₂ SO ₄ | See text for method |
| Etch | Etch sample in solution for desired time | |

Table A.3: Acid piranha etch/organic clean.

plastics!) and stainless steel tweezers (piranha will etch carbon fibre tweezers, leaving a residue everywhere, as well as various plastic-coated tweezers, even some labelled “PTFE”). I generally used a ratio of 2:1 concentrated H₂SO₄ to 30% H₂O₂, although higher ratios are acceptable as well.

A.1.2 Lithography

All of the photolithography in this work was performed using an EVG 620 mask aligner. The photomasks were chrome on sodalime, made by Photo Sciences, Inc.

Spinning photoresist

The first step in photolithography is to coat the sample with photoresist, which in our case was done using a spin coater (spinner). Before spinning resist, the wafer was generally baked at above 100 °C in order to remove any traces of water (especially if it had just been rinsed in DI following a cleaning step). This is more important for e-beam resist, as it’s more sensitive to water, but doesn’t hurt for photoresist. It is better to use a dedicated aluminium block on the hot plate surface, since the temperature tends to be more stable, and the hot plates tend to be dirty. After this, the wafer needs to be cooled to prevent baking the resist while it is being spun; this was done on a cold aluminium block.

This is sometimes followed by an HMDS prime (although this is meant for silicon, we sometimes also use it for sapphire). The priming is carried out via evaporation: the wafer is placed onto a glass slide (or two) in a petri dish. Then, HMDS is dripped onto the petri dish surface (not onto the sample!) with a dropper, and the petri dish

| Step | Description | Notes |
|-------------------|--|----------|
| Dehydration bake | Desired temperature >100 °C, time | Optional |
| Cool | On an aluminium block for a few minutes | Optional |
| HMDS prime | Evaporation, set number of drops, set time | Optional |
| Place in spinner | Using vacuum or vacuum-less chuck | |
| Coat with resist | Using dropper(s) or syringe with filter | |
| Spin | Two steps, set speed, acceleration, time | |
| Soft bake | Lower-temperature bake on hot plate | |

Table A.4: Spinning resist onto a wafer. The preparation steps are optional.

is covered for the desired amount of time.

Finally, we spin the resist onto the wafer. The wafer is held in the spinner using a vacuum chuck (except for the 100 μm -thick wafers, which were held with a vacuum-less chuck to prevent bending). Resist is collected in one or two droppers, depending on wafer size, and then squirted quickly to cover the area of the wafer, making sure to avoid bubbles or annuli (it is not as important to cover the outer edge of the wafer). If one is worried about contamination in the resist bottle, a syringe with a filter can be used, although I have found this is more likely to generate bubbles and did not seem to improve anything. The spinner then spins according to its program, which generally has two steps: a slower one with a lower acceleration to spread the resist over the wafer, and then a faster one to spin the resist to a desired thickness. It is then common to wipe the edge bead (thick ring of resist around the outer edge of the wafer) with a q-tip covered in acetone. Finally, the resists we use generally require a “soft bake” – that is, a relatively-low temperature bake after spinning.

Exposure

At this point, the wafer is ready for exposure through the photomask. The wafer is loaded into the mask aligner, followed by the mask (making sure the metal forming the features is on the side adjacent to the wafer!) The mask is aligned if necessary (see Fig. A.1 for alignment marks). Hard contact between the mask and wafer is

| Step | Description | Notes |
|--------------------|--------------------------------------|------------------|
| Exposure | Set dose, contact | |
| Post-exposure bake | Bake at set temperature for set time | Sometimes needed |

Table A.5: Exposure of the sample.

preferred, except for very thick resists which can actually stick to the mask. The exposure time is calculated by measuring the source intensity (power at the desired frequency per unit area), and obtaining the desired exposure dose from the resist manual or experimentation. Finally, some resists, such as many negative resists, require a post-exposure bake (reversal bake, in some cases).

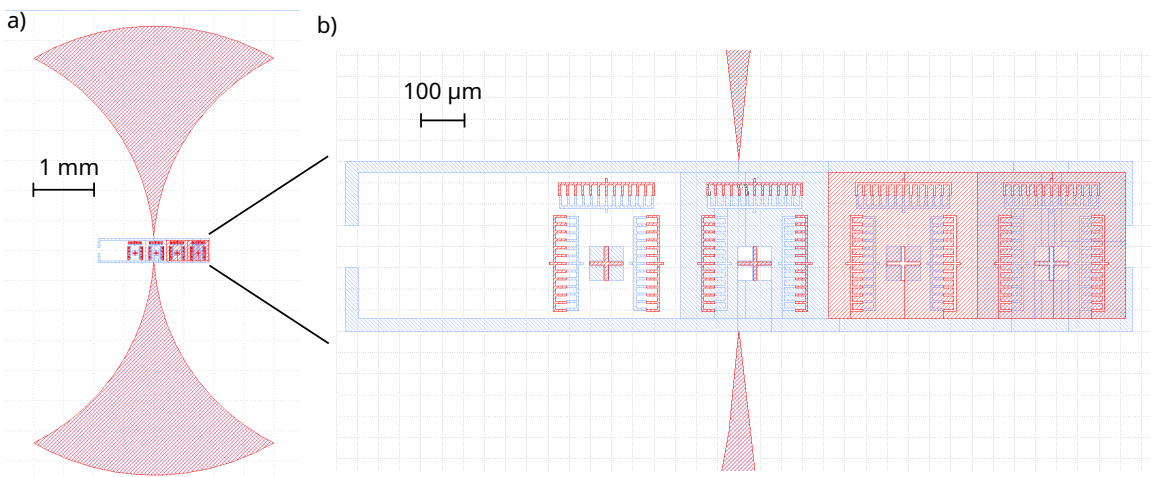


Figure A.1: An alignment mark from NASA. The two layers are in red and blue. a) View of the whole mark, including large features for finding the centre. b) Zoomed-in view of the centre, featuring vernier scales and alignment crosses for each possible polarity of the two resists. The vernier scales allow one to easily distinguish micron-scale misalignments in both directions using features that are hundreds of microns big.

Photoresist development

After exposure, the exposed features can sometimes be seen in a microscope already. The next step is development, in which a liquid developer is used to remove the developed resist (positive resist develops where it is exposed, negative resist develops where it is not exposed). Development is quite sensitive to the time, and also to the

| Step | Description | Notes |
|-------------------|--|----------|
| Development | Swirl in developer, e.g. MF-319, for a set time | |
| Rinse | Rinse in DI water thoroughly, removing all developer | |
| Examine | Optical microscope | |
| De-scum | Oxygen plasma ash | Optional |
| Measure thickness | Using a profilometer (mechanical or optical) | Optional |

Table A.6: Development and de-scumming of photoresist.

exact way the sample interacts with the developer. I generally put the sample in a beaker with developer, and swish it around in a circle at around 1-2 Hz. Sapphire can be difficult to see in developer, so I prepare the tweezers several seconds before it is time to take the sample out. After the sample is removed from developer, I immediately put it in [DI](#) water, generally in a pre-prepared beaker although a rinse can also work. It is a good idea to examine the sample after development to ensure that it is sufficiently developed. For a negative resist, undercut should be visible as a second line outside of the one forming the surface. An undercut will generally have smoothed-out features. It is also important to avoid overdeveloping – in a new process, it is a good idea to develop in small time chunks (e.g. 10-20 seconds at a time) and image the resist afterwards in order to find the correct development time.

After development, it can be a good idea to “de-scum” (remove some organic residues, e.g. photoresist residues left in developed areas) with an oxygen plasma “asher”. We use the AutoGlow 200 Plasma Cleaner. There are two plates with different exposure to the plasma: the top plate is directly exposed, and thus has a much higher etch rate, and is better suited for stripping.

Electron-beam resist development

E-beam resist is developed with a different developer than photoresist, namely with a mixture of 3:1 [IPA](#) and water maintained at 6 °C [Rooks et al., 2002]. A larger difference is the fact that the anticharging layer (gold, in my case) and any [poly\(styrene sulfonic acid\) \(PSSA\)](#), if used, needs to be removed first. Since the gold is on top of

| Step | Description | Notes |
|--------------------|---|--------------------------|
| Remove PSSA | Run under DI for a few seconds | Removes most gold |
| Remove gold | KI solution, around 20 s, DI rinse | |
| Development | Swirl in developer: IPA /water | Kept at 6 °C |

Table A.7: Development of e-beam resist. The **PSSA** removal step is only performed if **PSSA** was used (this is a non-standard part of the process).

the **PSSA**, one may think that it all comes off with it, but some gold can be seen on the edges of the patterns even when the **PSSA** is removed. The **PSSA** dissolves in water very quickly (order of a second), and gold comes off in a few seconds with KI solution.

A.1.3 Indium evaporation

At the beginning of this PhD, the indium used was electroplated using a Wafer Power Technology Beaker-on-a-Stick. The plating bath was indium sulphamate purchased from Indium Corporation. The last work to use the electroplater was [Brecht et al., 2017]. See [Brecht, 2017] for information on this.

In order to remove several difficulties associated with the electroplating process and increase the quality of the resulting film, a Lesker PVD-75 thermal evaporator was purchased exclusively for indium evaporation. All of the indium films after [Brecht et al., 2017] were evaporated here. The indium was purchased from Alfa Aesar in the form of 5 mm shot of 6N purity (metals basis). The crucibles for the PVD are made of alumina.

The wafer is loaded on the water-cooled substrate holder, which can rotate and is around 38 cm from the thermal source. The chamber is pumped to less than 10^{-6} Torr. The sample can then be ion milled with argon, with the possibility of adding oxygen. Generally, we use the argon ion milling, especially when we are evaporating on top of another metal, as this is thought to remove the surface oxide. Finally, we can evaporate the indium. We generally do this in two or three steps, depending on the

| Step | Description | Notes |
|-----------|--|-------------|
| Ion mill | Ar, and possibly O, for varying amount of time | See caption |
| Evaporate | 2 Å/sec, up to 500 nm | Slow rate |
| Evaporate | 20 Å/sec, up to 5 µm total | |
| Evaporate | 25 Å/sec if necessary | |

Table A.8: Thermal evaporation of indium. Argon ion mill parameters: flow: 14 sccm, discharge volts: 100, discharge amps: 3, cathode amps/volts: 19, emission amps: 3.

thickness. The first step is a slow evaporation at 2 Å/s for around 100 nm, followed by a faster evaporation at 20 Å/s. If we are going for over 5 µm, we continue at 25 Å/s (sometimes, we do 20 Å/s for 400 nm, then rest at 25 Å/s). The purpose of this is that it is believed that the original slow layer will have better adhesion to the wafer, but we then need to increase the speed to complete the evaporation in a reasonable amount of time (taking too long can result in the cryopump overheating). The two crystal monitors in the evaporator work for about 10 µm combined – if we wanted a thicker deposition, and were not limited by the heating up of the cryopump, we would need to turn off thickness monitoring for part of the evaporation and just keep a constant power. We also have to do this in the cases when one of the monitors fails. I note that overall, the evaporation process is not very stable, and it is generally recommended to monitor the evaporator during this process.

A.1.4 Electron-beam lithography

For electron beam lithography, the resist is prepared in the same way as for photolithography, except that a resist bilayer is used, and a gold anti-charging layer is sputtered on top of the resist. Due to the problems described in Sec. A.3, the thickness of the gold was varied, and a [PSSA](#) layer was sometimes spun on between the resist and gold. An alternate option, which did not work quite as well, was increasing the gold sputtering time from 60 s; several different times were tried up to 180 s.

| Step | Description | Notes |
|--------------|--|--|
| Dehydration | 5 min at 180 °C | Cool for 2 min |
| Spin EL13 | 1) 400 rpm, accel = 5, 10 s 2) 2000 rpm, accel = 10, 1:40 | Using syringe with 0.22 µm filter Non-vacuum chuck for thin wafer |
| Bake | 5 min at 180 °C | Cool for 2 min |
| Spin A4 | 1) 400 rpm, accel = 5, 10 s 2) 2000 rpm, accel = 10, 1:40 | Using syringe with 0.22 µm filter Non-vacuum chuck for thin wafer |
| Bake | 5 min at 180 °C | Cool for 2 min |
| Spin PSSA | 3000 rpm, 2 min; filter | Step optional |
| Bake | 1 min at 120 °C | To remove water |
| Sputter gold | 60–180 s | 60 s is standard |
| Expose | Raith EBPG | Did not exceed 100 nA |

Table A.9: Electron beam lithography.

A.1.5 Aluminium evaporation

Aluminium is evaporated in one of two Plassys e-beam evaporators. They both have the ability to tilt the stage relative to the evaporation direction, and one can also rotate the sample stage while this is happening, permitting the configuration depicted in Fig. 4.14. There is also the option to oxidise the sample, which can be used to make the oxide barrier for a Josephson junction or a capping layer for the outer aluminium. The parameters which can be varied are thus: thickness, angle, and rotation for each evaporation step, and pressure and time for each oxidation step. Prior to evaporation, an argon ion mill is usually performed in the evaporator.

A.1.6 Liftoff

The liftoff process we use depends on the type and thickness of resist. In this thesis, two main liftoff procedures were used: one for thick indium films, and one for thin aluminium films. We developed the thick indium liftoff for these projects in particular, whereas the aluminium liftoff has been standard in the lab.

| Step | Description | Notes |
|----------|--|--------------------------------|
| Liftoff | Using rig, 80-90 °C Ni555, 150-500 rpm | NMP also works |
| Liftoff | Change bath; can increase rotation speed | Optional, depends on status |
| Cleaning | Acetone, methanol, 1 or 2 times | Can add IPA |

Table A.10: Thick liftoff of AZnLOF2035 or 2070 using Technostrip Ni555 ([NMP](#) can be substituted). Note that sonicating indium can destroy the film, if desired, make sure to use a very weak sonicator.

Thick liftoff

This liftoff was used for films with thickness on the order of microns, primarily indium. The resists were AZnLOF2035 (thinner) and 2070 (thicker). We first tried to lift them off with hot [NMP](#), which worked, but not very well. I then switched to the recommended solvent Technistrip Ni555, at around 80-90 °C with a probe on the hot plate. We also made a custom liftoff rig, which comprised a [PTFE](#) ring with a slot for a 4-inch wafer and tapped holes for [PTFE](#) screws, on which the ring rests. There is also a mesh cut to the size of the beaker, which was placed on the same screws lower than the ring, leaving enough room underneath for a magnetic stir bar. We placed the wafer on the [PTFE](#) ring face-down in the solvent, with the mesh serving to protect the wafer from the stir bar. The liftoff would take many hours, sometimes I would leave it overnight, change the bath, then do another overnight liftoff. Sometimes, the film would partially peel off, and could be assisted by manual removal with tweezers or by squirting the solvent onto the wafer. It is important to avoid letting the wafer dry with unwanted metal on it, as it will no longer be possible to remove.

Thin liftoff

This is the standard liftoff process for aluminium. [NMP](#) at around 85 °C, acetone, and methanol are used. It typically takes only a few hours. It is sufficient to just place the wafer face-up in the beaker, although some squirting of [NMP](#) may occasionally be required to remove some leftover metal.

| Step | Description | Notes |
|-----------------|---------------------------------|--------------------------|
| Liftoff | Using 80-90 °C NMP | Works with wafer face-up |
| Sonicate in NMP | Around 2 mins | Better to use new bath |
| Cleaning | Acetone, methanol, 1 or 2 times | Can add IPA, sonication |

Table A.11: Thin liftoff of e-beam resist bilayers (or some thin photoresists).

A.1.7 Chip or wafer bonding

Prior to bonding, the chips are sometimes etched with HCl, or treated with the Ontos atmospheric plasma system from SET. With HCl, the chip is generally dipped into around 10% HCl in water for around a minute to remove the oxide directly before bonding. Ontos uses a proprietary process that uses a mixture of helium, nitrogen, and hydrogen. The advertised result is the replacement of indium oxide on the surface with nitride, which is supposed to be easier to break through in bonding. We did not verify these claims, but found no harm and possibly an improved consistency of bonding using this process; transmon room-temperature resistances were unaffected by the process. Immediately following this, the chips were bonded (“hybridised”) using the SET FC-150 wafer bonder. The two chips are held with custom-designed vacuum chucks, and a microscope with both an upward- and downward-facing objective is inserted between the two. First, their relative tilt is aligned using laser collimators. This requires a relatively large (a few square mm) reflective surface on the chips, such as a square of aluminium. The chips can also be aligned by collimating to the somewhat-reflective chucks, but this is less accurate. The two chips are then aligned (translationally) relative to each other.

Finally, they are bonded. The bonding arm has a force sensor, and follows a pre-defined force-vs.-time profile. We used profiles which increased the force (for the larger forces in 5-10 segments, between which it was held constant). The total run-time was thus generally several minutes. The forces increase profile was generally linear, although we did not experiment significantly with changing this. For the mi-

| Step | Description | Notes |
|------------------|-----------------------------------|----------|
| HCl etch | Around 1 min in 10% HCl in water | Optional |
| Plasma treatment | Ontos | Optional |
| Bond | Varying force, ramp, time | |
| 180° bond | Rotate bonded samples, bond again | Optional |

Table A.12: Chip bonding process. Both of the two pre-bonding treatments are optional, although it's probably a good idea to use at least one. The 180° bond is performed differently than a regular bond: since the two chips are already held together, nothing is placed onto the top chuck and we do not perform additional alignment, we simply press down with the same ramp. The purpose of this is to compensate for possible misalignments in angle.

cromachined cavity, we increased the force by around 20 kg over 30 s ramps, followed by around 10 s of a hold, with a 3 min hold at the end. To calculate the effective pressure, divide the maximum force by contact area.

The bonder also has the ability to heat up the top and bottom chucks individually. We did not use this feature much, as we were worried about growing additional oxide on the indium. However, we did try increasing the temperature to 60 °C and 100 °C during the final hold at maximum force for the micromachined cavity. The bonder can also “scrub” the two surfaces against each other; we experimented briefly with this, but only found it to destroy the bumps. Note that cleanliness is extremely important for the bonding process: since the height of the bumps is only a few microns, any speck of dust can mess up the bonding, therefore, the process should be performed in a cleanroom or at least tent.

A.2 Specific fabrication processes

In this section, I list the fabrication processes for specific devices mentioned in this thesis. Since for most designs, many devices were made, some with slightly different fabrication processes, I shall either give a representative process, or describe the variations. I will also use the basic fabrication processes as building blocks, refer

back to the relevant sections of Sec. A.1 for more details.

A.2.1 Interrupted stripline resonators

| Step | Description | Notes |
|--------------------|---|----------------------|
| Solvent clean | NMP, acetone, methanol | |
| Dehydration bake | 5 min at 150 °C | |
| HMDS prime | Evaporation, 15 drops, 10 min | |
| Spin AZnLOF2035 | 500 rpm, accel = 3, 10 s 3500 rpm, accel = 10, 2 min | Wipe edge bead |
| Bake | 3 min at 100 °C | |
| Expose | 80 mJ/cm ² @ 365 nm, sep. = 150 µm | Hard contact 1.5 bar |
| Bake | 1 min at 110 °C | |
| Develop | MF-319, 45 s | ~3 µm resist |
| Deposit indium | Ar ion mill 1-3 min, 1 µm evap. | Dual rates 2/20 Å/s |
| Liftoff | NMP at 85 °C | 2 baths |
| Dehydration bake | 5 min at 110 °C | Avoid melting In |
| HMDS prime | Evaporation, 15 drops, 10 min | |
| Spin AZnLOF2070 | 500 rpm, accel = 3, 10 s 800 rpm, accel = 17, 2 min | Wipe edge bead |
| Bake | 10 min at 100 °C | |
| Expose | 175 mJ/cm ² @ 365 nm | 150 µm, 1.5 bar |
| Bake | 1 min at 110 °C | |
| Develop | MF-319, 2:05 | ~12 µm resist |
| Deposit indium | Ar ion mill 3 min, 7 µm evap. | Three rates 2/20/25 |
| Liftoff | Technistrip Ni555 at 80 °C | 2-3 baths |
| Spin dicing resist | SC1827 3000 rpm, accel = 17, 1 min | For protection |
| Dice | | |
| Remove resist | With acetone, methanol | |
| Remove oxide | 1 min dip in 10% HCl or ONTOS | See caption |
| Bond | 120 s ramp to 1 kg, 90 s hold | ~170 MPa |

Table A.13: Fabrication process for the interrupted stripline resonator. The top and bottom chips were made on the same wafer and then diced apart. Some bonds were done with 150 g force, giving around 30 MPa pressure. The ONTOS recipe was 4 passes of 6:4:0.1:0 He:H/He:N₂:O₂ at 80 W. The H/He was 5% H in He. All gasses were ultra-high purity.

A.2.2 Micromachined cavity

| Step | Description | Notes |
|--------------------|---|---------------------|
| Solvent clean | NMP at 80 °C, methanol, DI | |
| RCA clean | At 80 °C | |
| Deposit nitride | 300 nm using PECVD | |
| Dehydration bake | 2 min at 120 °C | |
| HMDS prime | Evaporation, 15 drops, 10 min | |
| Spin S1813 | 3000 rpm, accel = 17, 1 min | Wipe edge bead |
| Bake | 1 min at 115 °C | |
| Expose | 50 mJ/cm ² @ 365 nm | |
| Develop | MF-319, 1 min | |
| Cover edge | Using S1813 | To prevent etch |
| Bake | 1 min at 120 °C | |
| Ash | Top plate, 300 mT, 175 W, 3 min | Oxygen de-scum |
| Nitride etch | CHF ₃ /O ₂ 50/5 sccm, 55 mTorr | 6:30, 120 W, 420 V |
| Remove resist | NMP 80 °C 10 min + sonicate | |
| Ash | Top plate, 300 mT, 175 W, 3 min | Oxygen de-scum |
| BOE etch | 10:1 for 20 sec, DI rinse | |
| Micromachine | 30% KOH etch 80 °C | 60 µm/hr |
| Rinse | Flowing DI for 30 min | |
| Ionic clean | H ₂ O:HCl:H ₂ O ₂ 5:1:1 80 °C 10 min | |
| Remove nitride | BOE 10:1 30 min | |
| Deposit indium | Ar ion mill 3 min, 10 µm evap. | |
| Spin dicing resist | SC1827 2500 rpm, accel = 17, 1 min | For protection |
| Bake | 85 °C, 5 min | |
| Dice | | |
| Remove resist | With NMP, acetone, IPA | |
| HMDS prime | Evaporation, 15 drops, 10 min | |
| Spin AZnLOF2070 | 500 rpm, accel = 3, 10 s | |
| | 2000 rpm, accel = 18, 2 min | |
| Bake | 7 min at 100 °C | |
| Expose | 175 mJ/cm ² @ 365 nm | |
| Bake | 1 min at 110 °C | |
| Develop | MF-319, 2 min | ~5 µm resist |
| Deposit indium | Ar ion mill 30 sec, 4 µm evap. | |
| Liftoff | NMP at 80-90 °C | 2-3 baths, sonicate |
| Spin dicing resist | SC1827 2500 rpm, accel = 17, 1 min | For protection |
| Bake | 8 min at 80 °C | Don't melt indium |
| Dice | | |
| Remove resist | NMP at 80 °C acetone, methanol | |
| Remove oxide | 1 min dip in 10% HCl or ONTOS | |
| Bond | 200 kg force (max available) | ~680 MPa, 180° |

Table A.14: Fabrication process for the micromachined cavity. See [Brecht, 2017] for details of the micromachining process. The bonding took around 7 minutes to increase the force to max, with a 3 min hold afterwards. The final hold was sometimes at 60 or 100 °C.

Note that the etches had depths through 1.5 mm, which took over 30 hrs and required a 2 mm-thick silicon wafer. The liftoff on the bumps was not always great, thicker resist might be a good idea, at maybe trying Technistrip Ni555. Gentle sonication was required in most cases to clear the bumps (this also removed unwanted indium whiskers). The top chip fabrication had no special features, see [Lei* & Krayzman* et al., 2020] for the overview.

A.2.3 Transmons

| Step | Description | Notes |
|--------------------|----------------------------------|------------------|
| Solvent clean | NMP, acetone, methanol, DI | |
| Dehydration bake | 5 min at 180 °C | 2 min cool |
| Spin MAA EL13 | 400 rpm, acl = 5, 10 s | |
| Bake | 2000 rpm, acl = 10, 1:40, filter | Non-vacuum chuck |
| Spin PMMA A4 | 5 min at 180 °C | 2 min cool |
| Bake | 400 rpm, acl = 5, 10 s | Non-vacuum chuck |
| Spin PSSA | 2000 rpm, acl = 10, 1:40, filter | |
| Bake | 5 min at 180 °C | 2 min cool |
| Sputter gold | 3000 rpm, 2 min, 0.22 µm filter | |
| Write | 1 min at 120 °C | |
| Remove PSSA | 90 s | |
| Remove gold | Custom pattern, see Fig. A.2 | |
| Develop | Rinse with DI | |
| Deposit aluminium | KI for about 20 s | DI rinse |
| Liftoff | 3:1 IPA/water at 6 °C, 2 min | Gentle swirl |
| Probe | Ar ion mill 30 s | See caption |
| Spin dicing resist | NMP at 80 °C, 2 hrs | Sonicate after |
| Dice | Room-temperature resistances | |
| Remove resist | SC1827 500 rpm 10 s | |
| | 1500 rpm 1.5 mins | |
| | With acetone, methanol | |

Table A.15: Transmon fabrication on 100 µm-thick sapphire wafers. The argon ion mill in the evaporator was 3.5:1 Ar:O₂, at 250 V and 5 mA. The aluminium evaporation was 21.3 nm at 20 °, 31.9 nm at -20 °, with 15 min of oxidation at 15 Torr in between. There was a capping layer of 5 min oxidation at 50 Torr at the end.

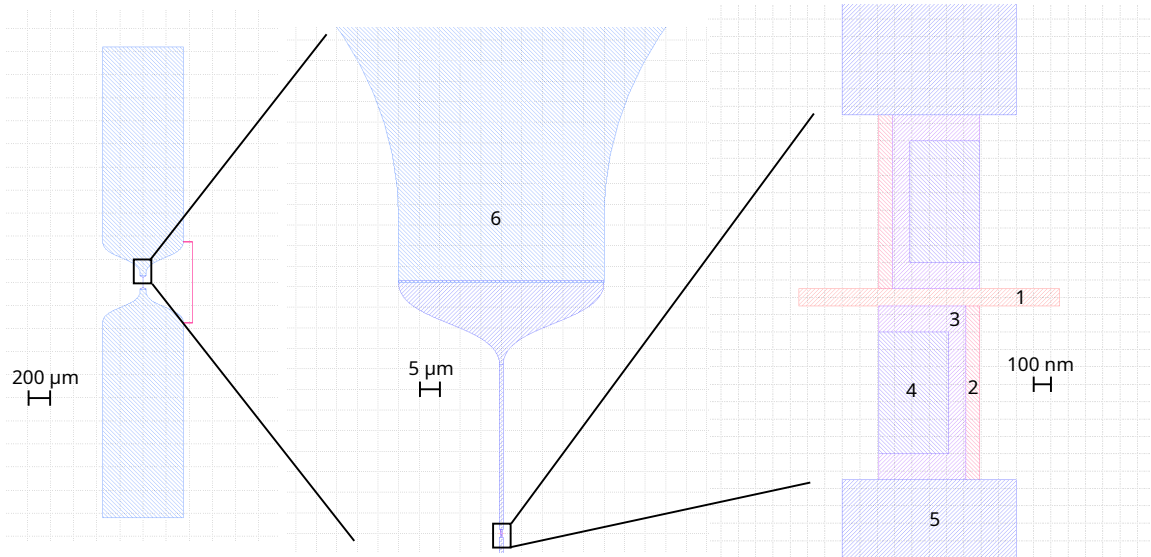


Figure A.2: E-beam pattern for writing the transmon. There are 7 layers in the pattern: 5 layers for fine features (1-5), one layer for the large features (6), and one layer for the shorting strap (in red). Resistance is varied by changing the length of layer 1.

A.3 Cracking Sapphire with the E-beam Writer

One issue encountered in e-beam lithography was the cracking of sapphire. This presented itself as micron-scale defects with characteristic hexagonal spiderweb crack structure. They can be seen even in an optical microscope, see Fig. A.3, and their full structure is revealed in SEM, see Fig. A.4. The cause is believed to be electric discharge, which cracks the sapphire; note that the symmetry (and direction) of the cracks corresponds to the crystal structure of the sapphire wafer.

I performed a number of experiments to rule out different causes. First, I note that this issue is unrelated to the metallisation, since it can be seen in the wafer before any aluminium is evaporated. I also note that if I look carefully, I can even see where these features will appear as small holes in the gold layer directly after writing. I have also shown that these are not caused by some inherent flaws in the sapphire, as they repeat consistently in the same relative spots on my write pattern: in the areas near the leads to the junction, as well as a few per pad. Since there is

| Section | Description | Relative dose |
|---------|----------------|---------------|
| 1 | Junction | 4.50 |
| 2 | Junction leads | 4.50 |
| 3 | Undercut | 1.00 |
| 4 | Undercut | 1.75 |
| 5 | Thin leads | 4.00 |
| 6 | Large features | 1.00 |
| Strap | Shorting strap | 1.00 |

Table A.16: The relative doses used for the transmon e-beam lithography. 1 corresponds to $370\text{-}380 \mu\text{C}/\text{cm}^2$. The fine features in sections 1-5 were written with 20 nA, the larger features – with up to 100 nA (sometimes with 20 or 50).

an overlap in exposure near the leads to the junction (necessary to prevent stitching errors due to my writing order), one may consider this a suspect; but I tested writes with smaller and even no overlap and continued to see the spots. I also tested lower currents, down to writing the entire wafer with 20 nA, to no effect. Finally, I note that I was also able to find a small number of these features on a colleague’s wafer.

One possible explanation is that these occur at the place where the beam is left at the end of writing a field, where the mechanical stage will have to move. The beam should be blanked here, but if the blanking is imperfect, we can accumulate charge at this location and eventually break through the dielectric resist (perhaps after cracking the gold first). Two things have been found to improve the situation: sputtering more gold (2-3 times as much as normal) decreases the number of these spots, spinning [PSSA](#) between the resist and gold almost entirely removed the problem. It is unclear what is the exact mechanism by which these help; it has been suggested that the thicker gold is more likely to stay intact than the thin layer, which can crack and then act as a lightning rod. Another possible solution (which I did not attempt) would be to change the order in which the field is written, so that the beam ends at a less important spot in it. If it is indeed an issue with the beam blunker, then fixing that may also help resolve this. Although I have no evidence that this affects the resulting transmon in any way (one could even conceivably come up with ways a

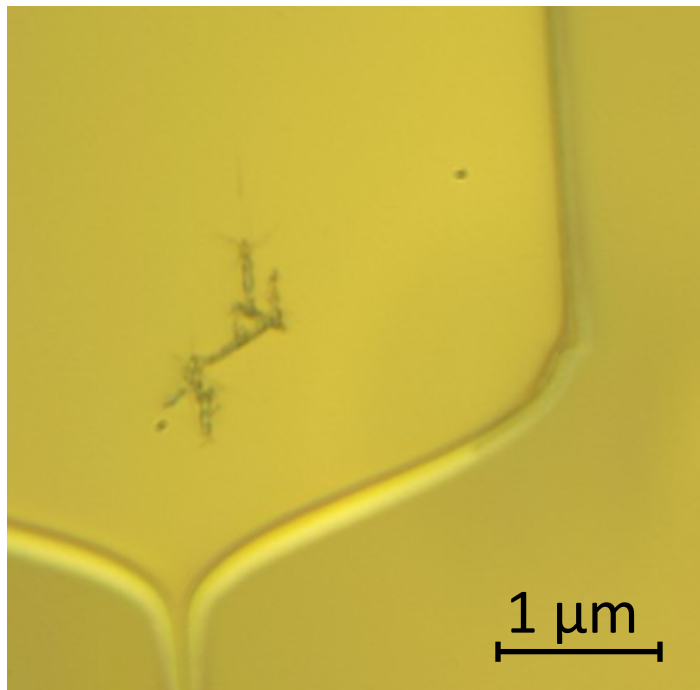


Figure A.3: A crack in the sapphire.

small hole in the pad could help by trapping a vortex), it is certainly better to not have such uncontrolled behaviour in the fabrication.

A.4 High-Purity Aluminium Etching

In order to achieve high quality for a device made of high-purity (e.g. 4N, 5N) aluminium, it must be etched [Reagor et al., 2013]. The current belief is that this either helps by removing mechanical damage caused by the machining, or by modifying the chemical composition of the surface (i.e. removing implantations from the tools and in return, adding some e.g. phosphorus from the acid). We use a process based on the above work; see also [Reagor, 2015]. First, the cavity is sonicated in solvents in order to remove machining oil, etc. Then, the tapped holes in the cavity are filled with PTFE screws, to protect the thread without adding contaminants from screws. The cavity is then placed in a PTFE holding rig inside a glass beaker, oriented in such a way as to let bubbles escape. A magnetic stir bar is placed under the cavity.

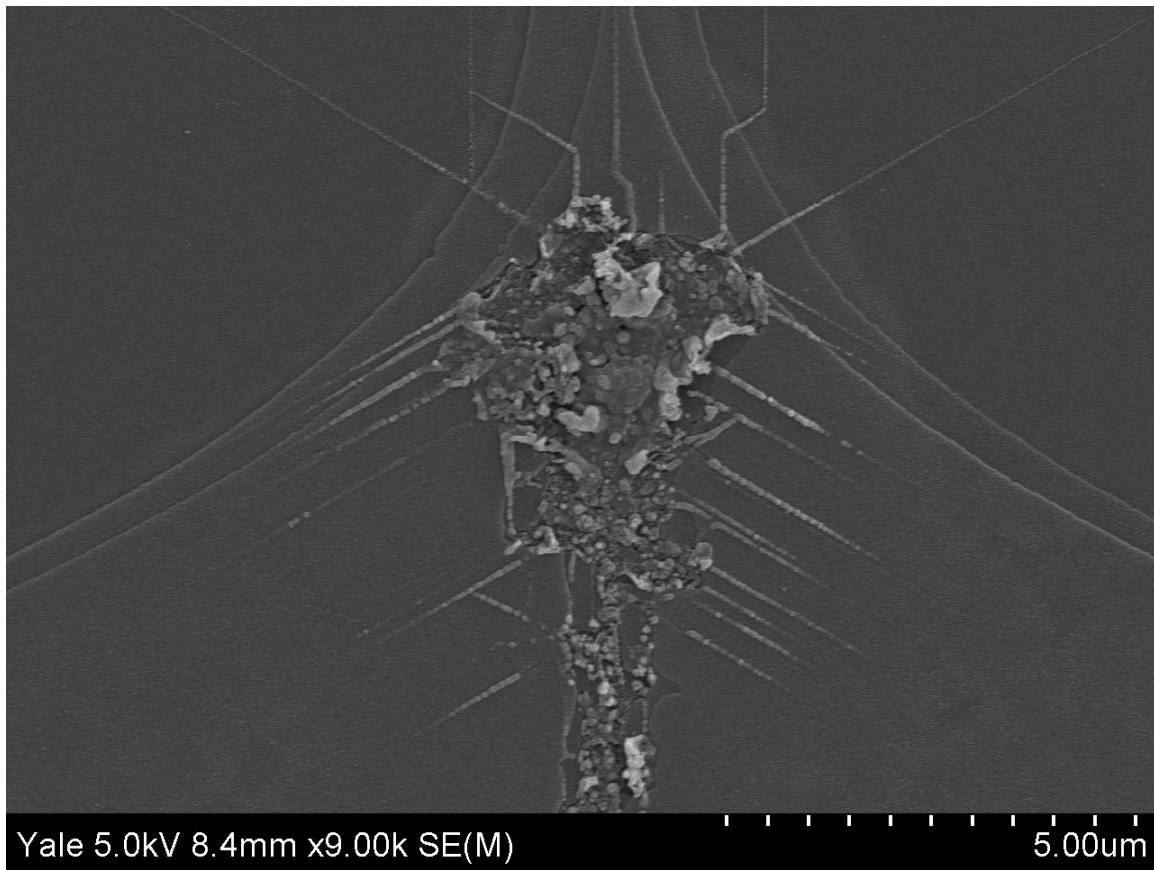


Figure A.4: A crack in the sapphire.

The cavity is then etched in Transene Aluminum etchant type A at 50 °C while the liquid is being stirred at around 600 rpm. When the bath becomes opaque, the cavity is transferred to another bath of etchant; in total, we normally etch in three or four baths. Each bath takes around 30 minutes, although at some point the clean-room switched hot plates, and the automatic temperature control started taking much longer. I switched to manual control at that point. After the last bath, the cavity is transferred to a beaker of DI water, rinsed for around a minute in the beaker, and then another minute outside the beaker.

APPENDIX B

Electromagnetic simulations

Electromagnetic simulations are carried out in Ansys HFSS, a finite-element solver. In this section, I shall briefly provide some tips to using it more effectively, in no particular order.

B.1 Meshing

HFSS uses adaptive meshing, which means that it tries to increase the mesh density in places that have large gradients. The user sets the initial mesh, and the rest is carried out automatically in multiple “passes”. The idea is to get to the point where making the mesh finer no longer affects the calculated values, at which point numerical error is likely small. Here are some suggestions for using this:

- The minimum frequency of the simulation should be close to the expected minimum frequency of interest. Changing this value can sometimes affect the results!
- Generally, going above 15 passes or so is too much, it is better to make the initial mesh finer. To avoid having too many elements, manually mesh the

more relevant parts more finely. It's possible to create separate objects in these regions and then set a finer initial mesh on them.

- At the same time, too few passes is also not good. It's generally a good idea to have at least a few (3 is a good number) converged passes in a row before concluding the simulation has actually converged – it's possible to accidentally get a few “converged” results in a row, only for the next one to change drastically!
- I generally use mixed-order basis functions.
- Meshing a curved surface is very tricky and prone to errors, see Fig. B.1 for an example. Curvilinear meshing is possible, and offers settings for explicit surface approximation; check the manual for this. I generally find it easier to just manually use polyhedra, e.g. a cylinder with a many-sided (16 or more) polygon as base instead of a circular cylinder. Note that this systematically over/underestimates e.g. the volumes of solids, although the error drops in number of sides.
- For thin membranes, avoid meshing them one element-deep. If they are so thin that you don't expect the fields to change in them, then just model them as surfaces.
- Be careful of frustrated lattices, which can *almost* tile the surface perfectly, but have a defect somewhere. A small perturbation to this can cause the defect to move and change the result numerically.
- Make sure you're converging on the actual parameters of interest. If they are more complicated than the frequency and Q , create calculator expressions for them, and converge on those using the expression cache.
- Choose appropriate standards for your convergence criteria: there is no point requiring numerical error to be lower than other error types. For example, if you

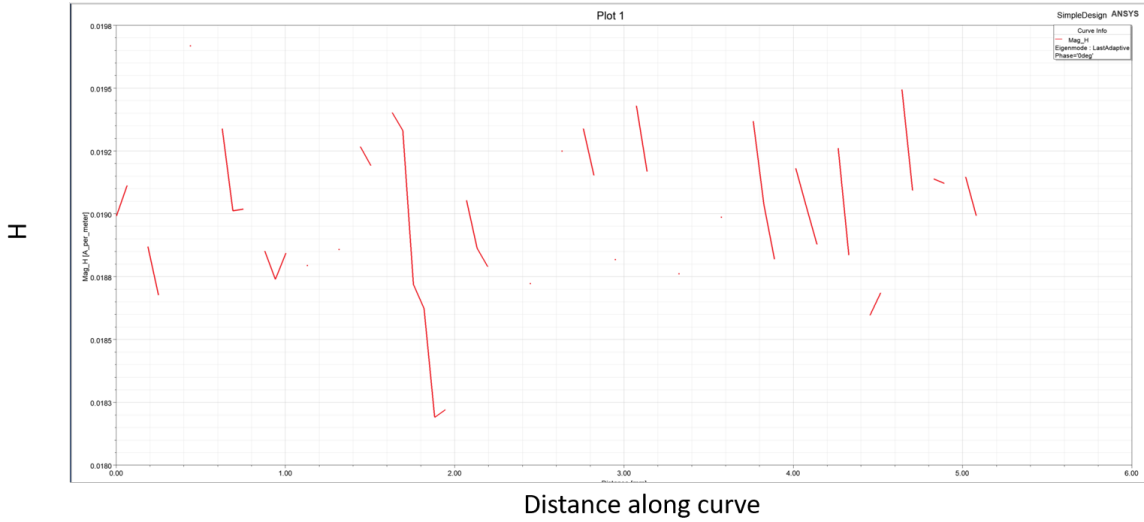


Figure B.1: Issues with using a curved mesh. I am plotting magnetic field around a cylinder, note the large number of holes: this is caused by the circle along which I take the values to not overlap with the surface of the cylinder. This sometimes gives errors about points not being located in any mesh elements.

can only know the length of your resonator to 25 μm due to machining precision and the full length is 25 mm, there is no point predicting the frequency to better than 0.1%. In such a case, your simulation need not be more precise than your calipers. For coupling Q , even a factor of 2 is frequently good enough.

B.2 Couplings, participations

To simulate coupling Q , make everything in the simulation lossless, and assign a lumped RLC boundary of 50Ω to the coupling port. The Q returned by an eigenmode simulation is now your coupling Q ! Make sure to use classic meshing instead of TAU, as this does better in the low-field regions in which our coupling ports are generally placed. Also it is generally a good idea to manually mesh the port and maybe coupling pin finely, as adaptive meshing likely still will not be enough. Finally, for very weak couplings ($Q_c \gg 10^6$) where the coupling pin is in a sub-cutoff waveguide, it is generally better to simulate a few points with lower coupling (three points with a

slightly longer pin) and then fit to an exponential. This tends to work better than trying to resolve very weak couplings in direct simulation.

To calculate participations in thin surfaces (thin in relation to length scales over which the field changes, such that we can assume the field is constant throughout the surface thickness), simulate the surface layer as a 2D sheet. For a concrete example, simulating p_{MA} directly would require meshing on the order of nanometres, which is possible, but makes for either a very complicated meshing structure or an unwieldy number of elements in the mesh (and likely both). If it is really necessary to have such a large range of scales in the simulation, it is better to simulate a 2D slice. As mentioned in Sec. 2.2.4, collapsing a layer with $\epsilon_r \neq 1$ means that we need to manually keep track of the boundary conditions for the electric field. I also note that it's a good idea to explicitly calculate the total energy in the mode via $E = \frac{1}{2} \int |\vec{E} \cdot \vec{D}| dV = \frac{1}{2} \int |\vec{B} \cdot \vec{H}| dV$. Although we set this parameter in the simulation (generally to 1 J), calculating it explicitly allows us to check for errors, both numerical errors and the situation in which the the total energy of the mode gets changed (this tends to happen when running external interfaces for HFSS, e.g. pyHFSS for pyEPR, etc.)

B.3 Fields calculator

First, it's helpful to spend a few minutes reading about reverse Polish notation if one is not familiar with it, as this is what the fields calculator uses. A few tips:

- `Mat1...` gives access to position-dependent material properties (e.g. permittivity).
- It is important to check what data type the commands expect, as this is not always clear. The different parameters are: real/complex, scalar/vector, global/particular geometry. The combinations of these yield `Scl`, `Csc`, `Vec`,

`Cvc`, `Lin`, `Srf`, `Vol`, `SclLin`, `VecLin`, `SclSrf`, `VecSrf` (scalar, complex scalar, vector, complex vector, line, surface, volume, scalar on a line, vector on a line, scalar on a surface, vector on a surface). Sometimes, it is smart enough to do conversion, e.g. you can add a `Scl` and a `Csc`.

- It is also important to keep track of where a field is defined. For example, in calculating seam loss, you may want to take the tangent of J_{surf} and \hat{l} along a particular line (so you can find their dot product). However, this doesn't work, since J_{surf} is only defined in respect to a surface! J_{vol} works fine with tangent.

In general, the manual for the fields calculator is somewhat opaque.

B.4 Potpourri

- If you already have a solution and want to add a non-model object (e.g. a curve along which to plot a field) without losing the solution: go ahead and add the object. This will invalidate the solution. Set the object to non-model and copy it. Now, *undo* its addition, thereby re-validating the solution. You may now safely paste the non-model object without invalidating the solution.
- HPC and parallel processing can help speed up simulations with a large number of variations.
- Phase is confusingly specified in both degrees and radians, depending on context. When degrees are used, `deg` is specified. For example, electric field is max at 0, magnetic field is max at 90 `deg`.
- If your system has at least one plane of symmetry, it's possible to use symmetric boundary conditions to cut down on problem size. You can then use `Perfect E` or `Perfect H` along the split to choose the symmetry of the calculated mode.

APPENDIX C

De-Gaussing Magnetic Shielding

If we wish to reduce the magnetic field the samples experience beyond what is offered by a single μ -metal can, we need to use de-Gaussing. The reason is that the material from which they are made saturates in a fairly low magnetic field, lower than that of Earth's ambient. In order to bring it down, we can de-Gauss the shield inside of another shield. The residual magnetic field of a functioning shield was measured to be 1 to a few mG (at room temperature), which is significantly lower than the Earth's field. While the de-Gauussed shield is kept inside another shield, it will remain unsaturated and not strongly magnetised, allowing us to achieve a lower field of a few tenths to around a mG (again, at room temperature), bringing the field down by a factor of several. If we then take the shield back out, we can measure its residual field increase again, as expected.

The setup for de-Gaussing is shown in Fig. C.1. The process is quite straightforward: we simply drive an AC magnetic field through the can, slowly ramping down the strength. This is achieved by wrapping enamelled wire around the can to create an inductor, then driving a current through it using a variac connected to the wall

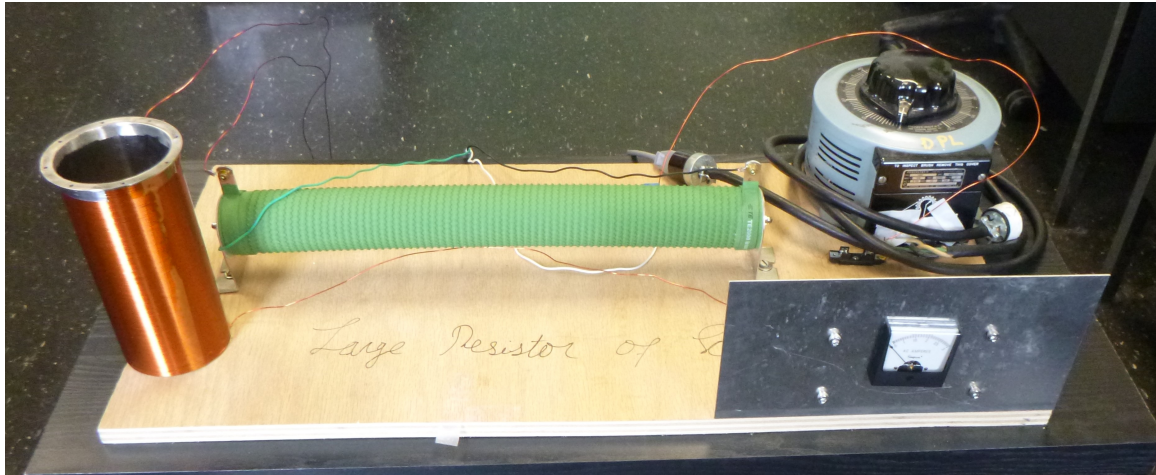


Figure C.1: The setup used for de-Gaussing the magnetic shielding cans. It is not fully hooked up and the fuse is not installed in the image. A variac is used to control the voltage from the wall outlet, which is connected to a coil around the can in series with a Large Resistor of ScienceTM, a current meter, and a fuse. The can needs to be inside another can (not pictured) to avoid immediate re-magnetisation. **NOTE: the way this is wired in the picture is not electrically safe. Do not leave exposed wires or connections! The resistor may also get hot after prolonged use.**

outlet. A 1 kOmega, high-power Large Resistor of ScienceTM absorbs most of the power, while an AC ammeter provides a reading of the current and a fuse protects against shorts. The variac is slowly (over tens of seconds) turned down from maximum to zero, de-Gaussing the can. Note that the can needs to be inside of another μ -metal shield, otherwise it will immediately saturate from the Earth's magnetic field again.

The reason for trying to reduce the magnetic field is the worry that conductor loss could be limited by resistivity from vortices, which result from trapping magnetic flux in the superconductor. See [Bardeen and Stephen, 1965] for an accessible treatment of vortices, and [Catelani et al., 2021] for our case in particular. We have not seen any evidence that reducing the ambient magnetic field via de-Gaussing our cans affects conductor Q in our devices.

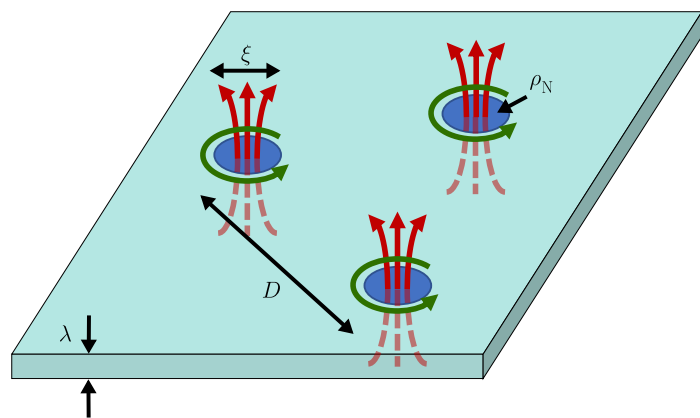


Figure C.2: A diagram of flux vortices penetrating a superconducting surface. ξ is the coherence length in the superconductor, which corresponds to the radius of the core of the vortex, D is the distance between vortices, ρ_N is the normal metal resistivity, and λ the penetration depth of the metal, which is how far around the vortex core the current flows.

APPENDIX D

Mattis-Bardeen Fitting Code

The code which was used to fit the temperature response of resonators using Mattis-Bardeen theory in [Lei* & Krayzman* et al., 2020, Read* & Chapman* et al., 2022] and throughout the rest of this thesis can be found at <https://github.com/levkrayzman/MattisBardeenFit>. I note that this code has been continuously developed for several years, so there is no single version used to generate all plots. The version pushed in the first commit is the most recent version as of the writing of this thesis.

The repository contains several files:

- `MattisBardeenFit.py`: The main code. As of this writing, this contains the fitting code, the sigma table generating code, as well as the main code. It would likely be a good idea to split this into multiple files (e.g. the fitting code as a package) – it is possibly, but not probable that I will end up doing this in the future.
- `Sigma1Table.dat` and `Sigma2Table.dat`: The tables of the complex conduction

tivities for a weakly-coupling superconductor. Note that these are general and thus can be pre-computed (as long as appropriate substitutions are made). The code that generates these is in the main code, and can be modified if more meshing is needed.

- `fitresults_temp.csv`: A sample csv file containing temperature sweep results for an aluminium suspended coaxial resonator. The data itself is nothing special, and is simply included to demonstrate proper input file formatting.

The basic structure of the code is the following: first, we define some constants for the materials involved. Then, we use them as inputs to the equation for gap as a function of temperature. We compute this using a combination of analytic approximations and an interpolation table using the exact expression. We then need the complex conductivites, which we have already pre-computed as a table which can be read in. If additional precision is desired, the code used to generate the tables is included and can be run with different parameters. Finally, we fit the data to the Mattis-Bardeen model and generate plots and fit results.

I shall refrain from explaining the details of how the code works; I hope that the comments in the file itself are helpful here. As with any scientist-written code, expect unfinished parts, suboptimal structuring and inefficient algorithms. Although I have tested some parts (the sigma tables generation, in particular), there of course may still be bugs in the code. If you discover an error, feel free to let me know, although I do not guarantee that I will fix it; I have no particular plans to maintain the package. Some interesting extensions would include ability to fit multiple metals in the same sweep (assuming sufficiently different T_c), inclusion of commonly-used approximation as fit options for comparison, and inclusion of the [TLS](#) model, allowing to fit a resonator over a range of temperatures in which it exhibits both [TLS](#) losses and thermal quasiparticle losses.

APPENDIX E

Useful Tables

E.1 Material Properties

In this section, I list some properties of materials relevant to this work. These present a combination of book values, values measured during the course of this thesis, as well as some additional values measured by my labmates.

| Material | Source | T_c (K) | λ_0 (nm) | ξ_0 (nm) | $\frac{2\Delta_0}{k_b T_c}$ | θ_D |
|------------------|---------------|-----------|------------------|--------------|-----------------------------|------------|
| Al | Textbook | 1.2 | 16 | 1600 | 3.3 | 420 |
| In | | 3.4 | 21 | 440 | 3.6 | 109 |
| Nb | | 9.3 | 39 | 38 | 3.8 | 276 |
| Ta | | 4.5 | — | — | 3.6 | 258 |
| 6061 Al | FWGMR | 0.9-1.1 | 300-700 | — | — | — |
| DT 6061 Al | | 1.0 | 160 | — | — | — |
| 5N5 Al | | 1.2 | 130-180 | — | — | — |
| Etched 5N5 Al | | 1.2 | 50-110 | — | — | — |
| Etched DT 5N5 Al | | 1.1 | 50 | — | — | — |
| 6061 Al | Suspended rod | 1.2 | 200-260 | — | — | — |
| 4N Ta | | 4.7 | 80-190 | — | — | — |
| 4N Nb | | >7 | — | — | — | — |
| Evaporated In | DC test | 2.8-3.3 | — | — | — | — |

Table E.1: Table of basic properties of some superconductors. This table was compiled partially using data from Chan U Lei and Suhas Ganjam (see future publication). The first section contains textbook values which are taken from the back cover of [Van Duzer and Turner, 1981]. The next section contains values measured using a Forky Whispering-Gallery Mode Resonator (FWGMR), which are multimode resonators. Values are obtained using temperature sweeps are fits, which are not very precise. DT 6061 Al refers to 6061 Al that has been diamond turned (same for 5N5). The next section represents measurements from suspended rods, with the outer conductor of Al, and the inner conductor as described. Again, temperature sweeps are used. Finally, the In is measured using a DC measurement of a long thin strip, measured in a Physical Property Measurement System (PPMS).

E.2 Participations

In this section, I collect the participations from Sec. 2.2 in one place for easy reference.

| Loss channel | Participation/numerator | q/denominator |
|--------------------|---|--|
| Bulk dielectric | $p = \frac{\int_{V_d} \vec{E} \cdot \vec{D} dV}{\int_V \vec{E} \cdot \vec{D} dV} = \frac{\epsilon \int_{V_d} \vec{E} ^2 dV}{\int_V \epsilon(\vec{x}) \vec{E} ^2 dV}$ | $q_{\text{diel,bulk}}$ |
| Surface dielectric | $p = \frac{t \int_{S_d} \vec{E}_{\text{sim}} ^2 dS}{\epsilon_r \int_V \epsilon_r(\vec{x}) \vec{E} ^2 dV}$ | $q_{\text{diel,surf}}$ |
| Conductor | $p = \frac{\lambda \int_{\text{surf}} H ^2 dA}{\int_V H ^2 dV}$ | q_{cond} |
| Seam | $y_{\text{seam}} = \frac{\int_{\text{seam}} \vec{J}_s \times \hat{l} ^2 dl}{\omega \int \vec{H} \cdot \vec{B} dV} = \frac{\int_{\text{seam}} \vec{H}_{\parallel} ^2 dl}{\int \vec{H} \cdot \vec{B} dV}$ | g_{seam} |
| Surface dielectric | $G_E = \frac{\int_{S_d} \vec{E} ^2 dS}{\int_V \epsilon(\vec{x}) \vec{E} ^2 dV}$ | $\Lambda = \frac{1}{1/(\epsilon t \tan \delta)}$ |
| Conductor | $G_M = \omega \mu \frac{\int_V H^2 dV}{\int_S H^2 dS}$ | R_s |

Table E.2: Table of common forms of participations. See the referenced sections for more general forms and a list of assumptions. Some alternate forms are presented in the bottom portion of the table. For clarity, I have labelled the geometric factors for surface dielectric and conductor as the electric geometric factor G_E and magnetic geometric factor G_M , respectively.

Bibliography

- [Abrikosov et al., 1959] Abrikosov, A A, Gor'kov, L P, and Khalatnikov, M. A Superconductor in a High Frequency Field. *Soviet Physics JETP*, 35:182 (1959). (Cited on page 41).
- [Albert et al., 2018] Albert, Victor V., Noh, Kyungjoo, Duivenvoorden, Kasper, Young, Dylan J., Brierley, R. T., Reinhold, Philip, Vuillot, Christophe, Li, Linshu, Shen, Chao, Girvin, S. M., Terhal, Barbara M., and Jiang, Liang. **Performance and structure of single-mode bosonic codes.** *Physical Review A*, 97(3):032346 (2018). (Cited on page 11).
- [Allen et al., 1971] Allen, M. A., Farkas, Z. D., Hogg, H. A., Hoyt, E. W., and Wilson, P. B. **Superconducting Niobium Cavity Measurements at SLAC.** *IEEE Transactions on Nuclear Science*, 18(3):168–172 (1971). (Cited on page 64).
- [Altoé*, Banerjee*, Berk*, Haja* et al., 2022] Altoé, M. Virginia P., Banerjee, Archan, Berk, Cassidy, Haja, Ahmed, Schwartzberg, Adam, Song, Chengyu, Alghadeer, Mohammed, Aloni, Shaul, Elowson, Michael J., Kreikebaum, John Mark, Wong, Ed K., Griffin, Sinéad M., Rao, Saleem, Weber-Bargioni, Alexander, Minor, Andrew M., Santiago, David I., Cabrini, Stefano, Siddiqi, Irfan, and Ogletree, D. Frank. **Localization and Mitigation of Loss in Niobium Superconducting Circuits.** *PRX Quantum*, 3(2):020312 (2022). (Cited on pages 13, 31, and 137).
- [Arrangoiz-Arriola et al., 2019] Arrangoiz-Arriola, Patricio, Wollack, E. Alex, Wang, Zhaoyou, Pechal, Marek, Jiang, Wentao, McKenna, Timothy P., Witmer, Jeremy D., Van Laer, Raphaël, and Safavi-Naeini, Amir H. **Resolving the energy levels of a nanomechanical oscillator.** *Nature*, 571(7766):537–540 (2019). (Cited on page 11).
- [Arute et al., 2019] Arute, Frank, Arya, Kunal, Babbush, Ryan, Bacon, Dave, Bardin, Joseph C., Barends, Rami, Biswas, Rupak, Boixo, Sergio, Brandao, Fernando G. S. L., Buell, David A., Burkett, Brian, Chen, Yu, Chen, Zijun, Chiaro, Ben, Collins, Roberto, Courtney, William, Dunsworth, Andrew, Farhi, Edward, Foxen, Brooks, Fowler, Austin, Gidney, Craig, Giustina, Marissa, Graff, Rob, Guerin, Keith, Habegger, Steve, Harrigan, Matthew P., Hartmann, Michael J., Ho, Alan, Hoffmann, Markus, Huang, Trent, Humble, Travis S., Isakov, Sergei V.,

- Jeffrey, Evan, Jiang, Zhang, Kafri, Dvir, Kechedzhi, Kostyantyn, Kelly, Julian, Klimov, Paul V., Knysh, Sergey, Korotkov, Alexander, Kostritsa, Fedor, Landhuis, David, Lindmark, Mike, Lucero, Erik, Lyakh, Dmitry, Mandrà, Salvatore, McClean, Jarrod R., McEwen, Matthew, Megrant, Anthony, Mi, Xiao, Michelsen, Kristel, Mohseni, Masoud, Mutus, Josh, Naaman, Ofer, Neeley, Matthew, Neill, Charles, Niu, Murphy Yuezen, Ostby, Eric, Petukhov, Andre, Platt, John C., Quintana, Chris, Rieffel, Eleanor G., Roushan, Pedram, Rubin, Nicholas C., Sank, Daniel, Satzinger, Kevin J., Smelyanskiy, Vadim, Sung, Kevin J., Trevithick, Matthew D., Vainsencher, Amit, Villalonga, Benjamin, White, Theodore, Yao, Z. Jamie, Yeh, Ping, Zalcman, Adam, Neven, Hartmut, and Martinis, John M. **Quantum supremacy using a programmable superconducting processor.** *Nature*, 574(7779):505–510 (2019). (Cited on pages 1 and 3).
- [Axline et al., 2016] Axline, C., Reagor, M., Heeres, R., Reinhold, P., Wang, C., Shain, K., Pfaff, W., Chu, Y., Frunzio, L., and Schoelkopf, R. J. **An architecture for integrating planar and 3D cQED devices.** *Applied Physics Letters*, 109(4):042601 (2016). (Cited on pages 5, 68, and 106).
- [Axline, 2018] Axline, Christopher James. *Building Blocks for Modular Circuit QED Quantum Computing.* PhD thesis, Yale University (2018). (Cited on pages 29 and 104).
- [Bardeen et al., 1957] Bardeen, J., Cooper, L. N., and Schrieffer, J. R. **Theory of Superconductivity.** *Physical Review*, 108(5):1175–1204 (1957). (Cited on page 44).
- [Bardeen and Stephen, 1965] Bardeen, John and Stephen, M. J. **Theory of the Motion of Vortices in Superconductors.** *Physical Review*, 140(4A):A1197–A1207 (1965). (Cited on page 193).
- [Bishop, 2010] Bishop, Lev Samuel. *Circuit Quantum Electrodynamics.* PhD thesis, Yale University (2010). (Cited on page 6).
- [Blais et al., 2021] Blais, Alexandre, Grimsmo, Arne L., Girvin, S. M., and Wallraff, Andreas. **Circuit quantum electrodynamics.** *Reviews of Modern Physics*, 93(2):025005 (2021). (Cited on page 6).
- [Blais et al., 2004] Blais, Alexandre, Huang, Ren-Shou, Wallraff, Andreas, Girvin, S. M., and Schoelkopf, R. J. **Cavity quantum electrodynamics for superconducting electrical circuits: An architecture for quantum computation.** *Physical Review A*, 69(6):062320 (2004). (Cited on page 6).
- [Bouchiat et al., 1998] Bouchiat, V., Vion, D., Joyez, P., Esteve, D., and Devoret, M. H. **Quantum Coherence with a Single Cooper Pair.** *Physica Scripta*, T76(1):165 (1998). (Cited on page 4).
- [Braunstein and van Loock, 2005] Braunstein, Samuel L and van Loock, Peter. Quantum information with continuous variables. *Quantum information with continuous variables*, 77(2):65 (2005). (Cited on page 3).

- [Brecht, 2017] Brecht, Teresa. *Micromachined Quantum Circuits*. PhD thesis, Yale University (2017). (Cited on pages 31, 35, 41, 61, 66, 87, 173, and 181).
- [Brecht et al., 2017] Brecht, T., Chu, Y., Axline, C., Pfaff, W., Blumoff, J. Z., Chou, K., Krayzman, L., Frunzio, L., and Schoelkopf, R. J. **Micromachined Integrated Quantum Circuit Containing a Superconducting Qubit**. *Physical Review Applied*, 7(4):044018 (2017). (Cited on pages 17, 75, and 173).
- [Brecht et al., 2016] Brecht, Teresa, Pfaff, Wolfgang, Wang, Chen, Chu, Yiwen, Frunzio, Luigi, Devoret, Michel H., and Schoelkopf, Robert J. **Multilayer microwave integrated quantum circuits for scalable quantum computing**. *npj Quantum Information*, 2:16002 (2016). (Cited on page 61).
- [Brecht et al., 2015] Brecht, T., Reagor, M., Chu, Y., Pfaff, W., Wang, C., Frunzio, L., Devoret, M. H., and Schoelkopf, R. J. **Demonstration of superconducting micromachined cavities**. *Applied Physics Letters*, 107(19):192603 (2015). (Cited on pages 5, 35, 71, 72, 76, and 87).
- [Brooks et al., 2013] Brooks, Peter, Kitaev, Alexei, and Preskill, John. **Protected gates for superconducting qubits**. *Physical Review A*, 87(5):052306 (2013). (Cited on page 2).
- [Burkhart et al., 2021] Burkhart, Luke D., Teoh, James D., Zhang, Yaxing, Axline, Christopher J., Frunzio, Luigi, Devoret, M.H., Jiang, Liang, Girvin, S.M., and Schoelkopf, R.J. **Error-Detected State Transfer and Entanglement in a Superconducting Quantum Network**. *PRX Quantum*, 2(3):030321 (2021). (Cited on pages 95 and 98).
- [Calusine et al., 2018] Calusine, G., Melville, A., Woods, W., Das, R., Stull, C., Bolkhovsky, V., Braje, D., Hover, D., Kim, D. K., Miloshi, X., Rosenberg, D., Sevi, A., Yoder, J. L., Dauler, E., and Oliver, W. D. **Analysis and mitigation of interface losses in trenched superconducting coplanar waveguide resonators**. *Applied Physics Letters*, 112(6):062601 (2018). (Cited on pages 31, 83, and 127).
- [Campagne-Ibarcq*, Eickbusch*, Touzard*, et al., 2020] Campagne-Ibarcq, P., Eickbusch, A., Touzard, S., Zalys-Geller, E., Frattini, N. E., Sivak, V. V., Reinhold, P., Puri, S., Shankar, S., Schoelkopf, R. J., Frunzio, L., Mirrahimi, M., and Devoret, M. H. **Quantum error correction of a qubit encoded in grid states of an oscillator**. *Nature*, 584(7821):368–372 (2020). (Cited on pages 3 and 11).
- [Catelani et al., 2021] Catelani, G., Li, K., Axline, C. J., Brecht, T., Frunzio, L., Schoelkopf, R. J., and Glazman, L. I. Ac losses in field-cooled type I superconducting cavities. *arXiv:2110.02866 [cond-mat]* (2021). (Cited on pages 32, 135, and 193).
- [Chen et al., 2022] Chen, Qi-Ming, Partanen, Matti, Fesquet, Florian, Honasoge, Kedar E., Kronowetter, Fabian, Nojiri, Yuki, Renger, Michael, Fedorov, Kirill G., Marx, Achim, Deppe, Frank, and Gross, Rudolf (2022). The scattering coefficients

of superconducting microwave resonators: II. System-bath approach. (Cited on page 51).

[Chen et al., 2021] Chen, Zijun, Satzinger, Kevin J., Atalaya, Juan, Korotkov, Alexander N., Dunsworth, Andrew, Sank, Daniel, Quintana, Chris, McEwen, Matt, Barends, Rami, Klimov, Paul V., Hong, Sabrina, Jones, Cody, Petukhov, Andre, Kafri, Dvir, Demura, Sean, Burkett, Brian, Gidney, Craig, Fowler, Austin G., Paler, Alexandru, Puterman, Harald, Aleiner, Igor, Arute, Frank, Arya, Kunal, Babbush, Ryan, Bardin, Joseph C., Bengtsson, Andreas, Bourassa, Alexandre, Broughton, Michael, Buckley, Bob B., Buell, David A., Bushnell, Nicholas, Chiaro, Benjamin, Collins, Roberto, Courtney, William, Derk, Alan R., Eppens, Daniel, Erickson, Catherine, Farhi, Edward, Foxen, Brooks, Giustina, Marissa, Greene, Ami, Gross, Jonathan A., Harrigan, Matthew P., Harrington, Sean D., Hilton, Jeremy, Ho, Alan, Huang, Trent, Huggins, William J., Ioffe, L. B., Isakov, Sergei V., Jeffrey, Evan, Jiang, Zhang, Kechedzhi, Kostyantyn, Kim, Seon, Kitaev, Alexei, Kostritsa, Fedor, Landhuis, David, Laptev, Pavel, Lucero, Erik, Martin, Orion, McClean, Jarrod R., McCourt, Trevor, Mi, Xiao, Miao, Kevin C., Mohseni, Masoud, Montazeri, Shirin, Mruczkiewicz, Wojciech, Mutus, Josh, Naaman, Ofer, Neely, Matthew, Neill, Charles, Newman, Michael, Niu, Murphy Yuezhen, O'Brien, Thomas E., Opremcak, Alex, Ostby, Eric, Pató, Bálint, Redd, Nicholas, Roushan, Pedram, Rubin, Nicholas C., Shvarts, Vladimir, Strain, Doug, Szalay, Marco, Trevithick, Matthew D., Villalonga, Benjamin, White, Theodore, Yao, Z. Jamie, Yeh, Ping, Yoo, Juhwan, Zalcman, Adam, Neven, Hartmut, Boixo, Sergio, Smelyanskiy, Vadim, Chen, Yu, Megrant, Anthony, and Kelly, Julian. **Exponential suppression of bit or phase errors with cyclic error correction.** *Nature*, 595(7867):383–387 (2021). (Cited on page 11).

[Chou et al., 2018] Chou, Kevin S., Blumoff, Jacob Z., Wang, Christopher S., Reinhold, Philip C., Axline, Christopher J., Gao, Yvonne Y., Frunzio, L., Devoret, M. H., Jiang, Liang, and Schoelkopf, R. J. **Deterministic teleportation of a quantum gate between two logical qubits.** *Nature*, 561(7723):368–373 (2018). (Cited on page 7).

[Chow et al., 2021] Chow, Jerry M, Dial, Oliver, and Gambetta, Jay M. (2021). IBM Quantum breaks the 100-qubit processor barrier. (Cited on page 3).

[Chu et al., 2017] Chu, Yiwen, Kharel, Prashanta, Renninger, William H., Burkhart, Luke D., Frunzio, Luigi, Rakich, Peter T., and Schoelkopf, Robert J. **Quantum acoustics with superconducting qubits.** *Science*, 358(6360):199–202 (2017). (Cited on page 11).

[Clarke et al., 1988] Clarke, John, Cleland, Andrew N., Devoret, Michel H., Esteve, Daniel, and Martinis, John M. **Quantum Mechanics of a Macroscopic Variable: The Phase Difference of a Josephson Junction.** *Science*, 239(4843):992–997 (1988). (Cited on page 4).

- [Collin, 2001] Collin, Robert E. *Foundations for Microwave Engineering*. John Wiley & Sons (2001). (Cited on pages 14, 25, and 50).
- [Datta et al., 2005] Datta, Madhav, Ōsaka, Tetsuya, and Schultze, J. W., editors. *Microelectronic Packaging*. Number v. 3 in New Trends in Electrochemical Technology. CRC Press, Boca Raton, FL (2005). (Cited on page 65).
- [de Leon, 2021] de Leon, Nathalie P. Discovering new platforms for high coherence qubits using direct materials characterization. In *Bulletin of the American Physical Society*, volume Volume 66, Number 1. American Physical Society (2021). (Cited on pages 30 and 40).
- [de Neeve et al., 2022] de Neeve, Brennan, Nguyen, Thanh-Long, Behrle, Tanja, and Home, Jonathan P. **Error correction of a logical grid state qubit by dissipative pumping**. *Nature Physics*, 18(3):296–300 (2022). (Cited on page 11).
- [DeNigris et al., 2018] DeNigris, N. S., Chervenak, J. A., Bandler, S. R., Chang, M. P., Costen, N. P., Eckart, M. E., Ha, J. Y., Kilbourne, C. A., and Smith, S. J. **Fabrication of Flexible Superconducting Wiring with High Current-Carrying Capacity Indium Interconnects**. *Journal of Low Temperature Physics*, 193(5):687–694 (2018). (Cited on page 65).
- [Devoret et al., 1985] Devoret, Michel H., Martinis, John M., and Clarke, John. **Measurements of Macroscopic Quantum Tunneling out of the Zero-Voltage State of a Current-Biased Josephson Junction**. *Physical Review Letters*, 55(18):1908–1911 (1985). (Cited on page 2).
- [Devoret et al., 1984] Devoret, Michel H., Martinis, John M., Esteve, Daniel, and Clarke, John. **Resonant Activation from the Zero-Voltage State of a Current-Biased Josephson Junction**. *Physical Review Letters*, 53(13):1260–1263 (1984). (Cited on page 2).
- [Dunsworth et al., 2017] Dunsworth, A., Megrant, A., Quintana, C., Chen, Zijun, Barends, R., Burkett, B., Foxen, B., Chen, Yu, Chiaro, B., Fowler, A., Graff, R., Jeffrey, E., Kelly, J., Lucero, E., Mutus, J. Y., Neeley, M., Neill, C., Roushan, P., Sank, D., Vainsencher, A., Wenner, J., White, T. C., and Martinis, John M. **Characterization and reduction of capacitive loss induced by sub-micron Josephson junction fabrication in superconducting qubits**. *Applied Physics Letters*, 111(2):022601 (2017). (Cited on page 83).
- [Eickbusch et al., 2022] Eickbusch, Alec, Sivak, Volodymyr, Ding, Andy Z., Elder, Salvatore S., Jha, Shantanu R., Venkatraman, Jayameenakshi, Royer, Baptiste, Girvin, S. M., Schoelkopf, Robert J., and Devoret, Michel H. (2022). Fast Universal Control of an Oscillator with Weak Dispersive Coupling to a Qubit. (Cited on page 15).

- [Flühmann et al., 2019] Flühmann, C., Nguyen, T. L., Marinelli, M., Negnevitsky, V., Mehta, K., and Home, J. P. **Encoding a qubit in a trapped-ion mechanical oscillator.** *Nature*, 566(7745):513–517 (2019). (Cited on page 11).
- [Foxen et al., 2017] Foxen, B., Mutus, J. Y., Lucero, E., Graff, R., Megrant, A., Chen, Yu, Quintana, C., Burkett, B., Kelly, J., Jeffrey, E., Yang, Yan, Yu, Anthony, Arya, K., Barends, R., Chen, Zijun, Chiaro, B., Dunsworth, A., Fowler, A., Gidney, C., Giustina, M., Huang, T., Klimov, P., Neeley, M., Neill, C., Roushan, P., Sank, D., Vainsencher, A., Wenner, J., White, T. C., and Martinis, John M. **Qubit compatible superconducting interconnects.** *Quantum Science and Technology*, 3(1):014005 (2017). (Cited on pages 65 and 75).
- [Frattini et al., 2018] Frattini, N. E., Sivak, V. V., Lingenfelter, A., Shankar, S., and Devoret, M. H. **Optimizing the Nonlinearity and Dissipation of a SNAIL Parametric Amplifier for Dynamic Range.** *Physical Review Applied*, 10(5):054020 (2018). (Cited on page 116).
- [Gao, 2008] Gao, Jiansong. *The Physics of Superconducting Microwave Resonators.* PhD thesis, California Institute of Technology (2008). (Cited on pages 32, 33, and 41).
- [Gao et al., 2008a] Gao, Jiansong, Daal, Miguel, Vayonakis, Anastasios, Kumar, Shwetank, Zmuidzinas, Jonas, Sadoulet, Bernard, Mazin, Benjamin A., Day, Peter K., and Leduc, Henry G. **Experimental evidence for a surface distribution of two-level systems in superconducting lithographed microwave resonators.** *Applied Physics Letters*, 92(15):152505 (2008a). (Cited on pages 29, 41, 44, 46, 47, and 51).
- [Gao et al., 2008b] Gao, J., Zmuidzinas, J., Vayonakis, A., Day, P., Mazin, B., and Leduc, H. **Equivalence of the Effects on the Complex Conductivity of Superconductor due to Temperature Change and External Pair Breaking.** *Journal of Low Temperature Physics*, 151(1-2):557–563 (2008b). (Cited on page 43).
- [Geerlings et al., 2013] Geerlings, K., Leghtas, Z., Pop, I. M., Shankar, S., Frunzio, L., Schoelkopf, R. J., Mirrahimi, M., and Devoret, M. H. **Demonstrating a Driven Reset Protocol for a Superconducting Qubit.** *Physical Review Letters*, 110(12):120501 (2013). (Cited on page 121).
- [Geerlings et al., 2012] Geerlings, K., Shankar, S., Edwards, E., Frunzio, L., Schoelkopf, R. J., and Devoret, M. H. **Improving the quality factor of microwave compact resonators by optimizing their geometrical parameters.** *Applied Physics Letters*, 100(19):192601 (2012). (Cited on page 16).
- [Girvin, 2011] Girvin, S. M. (2011). Superconducting Qubits and Circuits: Artificial Atoms Coupled to Microwave Photons. Lectures delivered at École d’Été Les Houches. (Cited on page 115).

- [Gittleman and Rosenblum, 1964] Gittleman, J.I. and Rosenblum, B. **Microwave properties of superconductors.** *Proceedings of the IEEE*, 52(10):1138–1147 (1964). (Cited on page 41).
- [Glover and Tinkham, 1957] Glover, R. E. and Tinkham, M. **Conductivity of Superconducting Films for Photon Energies between 0.3 and 4 0 k T c.** *Physical Review*, 108(2):243–256 (1957). (Cited on page 41).
- [Göppel et al., 2008] Göppel, M., Fragner, A., Baur, M., Bianchetti, R., Filipp, S., Fink, J. M., Leek, P. J., Puebla, G., Steffen, L., and Wallraff, A. **Coplanar waveguide resonators for circuit quantum electrodynamics.** *Journal of Applied Physics*, 104(11):113904 (2008). (Cited on page 16).
- [Green, 1965] Green, H.E. **The Numerical Solution of Some Important Transmission-Line Problems.** *IEEE Transactions on Microwave Theory and Techniques*, 13(5):676–692 (1965). (Cited on page 70).
- [Grigoras et al., 2022] Grigoras, K., Yurtagül, N., Kaikkonen, J.-P., Mannila, E. T., Eskelinen, P., Lozano, D. P., Li, H.-X., Rommel, M., Shiri, D., Tiencken, N., Simbierowicz, S., Ronzani, A., Hätilen, J., Datta, D., Vesterinen, V., Grönberg, L., Biznárová, J., Roudsari, A., Fadavi, Kosen, S., Osman, A., Hassel, J., Bylander, J., and Govenius, J. Qubit-compatible substrates with superconducting through-silicon vias. *arXiv:2201.10425 [cond-mat, physics:quant-ph]* (2022). (Cited on page 87).
- [Gyenis et al., 2021] Gyenis, András, Mundada, Pranav S., Di Paolo, Agustin, Hazard, Thomas M., You, Xinyuan, Schuster, David I., Koch, Jens, Blais, Alexandre, and Houck, Andrew A. **Experimental realization of a protected superconducting circuit derived from the 0–π qubit.** *PRX Quantum*, 2(1):010339 (2021). (Cited on pages 2 and 13).
- [Heeres et al., 2015] Heeres, Reinier W., Vlastakis, Brian, Holland, Eric, Krastanov, Stefan, Albert, Victor V., Frunzio, Luigi, Jiang, Liang, and Schoelkopf, Robert J. **Cavity State Manipulation Using Photon-Number Selective Phase Gates.** *Physical Review Letters*, 115(13) (2015). (Cited on pages xiv and 118).
- [Heidler et al., 2021] Heidler, Paul, Schneider, Christian M. F., Kustura, Katja, Gonzalez-Ballesteros, Carlos, Romero-Isart, Oriol, and Kirchmair, Gerhard. **Non-Markovian Effects of Two-Level Systems in a Niobium Coaxial Resonator with a Single-Photon Lifetime of 10 milliseconds.** *Physical Review Applied*, 16(3):034024 (2021). (Cited on page 60).
- [Houzet et al., 2019] Houzet, M., Serniak, K., Catelani, G., Devoret, M. H., and Glazman, L. I. **Photon-Assisted Charge-Parity Jumps in a Superconducting Qubit.** *Physical Review Letters*, 123(10):107704 (2019). (Cited on page 42).

- [Isagawa, 1978] Isagawa, S. Fabrication of a superconducting niobium cavity by the diffusion-bonding method. *Journal of Applied Physics*, 49(2):881–885 (1978). (Cited on page 64).
- [Joshi et al., 2021] Joshi, Atharv, Noh, Kyungjoo, and Gao, Yvonne Y. Quantum information processing with bosonic qubits in circuit QED. *Quantum Science and Technology*, 6(3):033001 (2021). (Cited on page 11).
- [Khalil et al., 2012] Khalil, M. S., Stoutimore, M. J. A., Wellstood, F. C., and Osborn, K. D. An analysis method for asymmetric resonator transmission applied to superconducting devices. *Journal of Applied Physics*, 111(5):054510 (2012). (Cited on page 51).
- [Kim et al., 2011] Kim, Z., Suri, B., Zaretsky, V., Novikov, S., Osborn, K. D., Mizel, A., Wellstood, F. C., and Palmer, B. S. Decoupling a Cooper-Pair Box to Enhance the Lifetime to 0.2 ms. *Physical Review Letters*, 106(12):120501 (2011). (Cited on page 4).
- [Kitaev, 2006] Kitaev, Alexei. Protected qubit based on a superconducting current mirror. *arXiv:cond-mat/0609441* (2006). (Cited on page 2).
- [Knill et al., 2001] Knill, E., Laflamme, R., and Milburn, G. J. A scheme for efficient quantum computation with linear optics. *Nature*, 409(6816):46–52 (2001). (Cited on page 12).
- [Koch et al., 2007] Koch, Jens, Yu, Terri M., Gambetta, Jay, Houck, A. A., Schuster, D. I., Majer, J., Blais, Alexandre, Devoret, M. H., Girvin, S. M., and Schoelkopf, R. J. Charge-insensitive qubit design derived from the Cooper pair box. *Physical Review A*, 76(4):042319 (2007). (Cited on page 4).
- [Krastanov et al., 2015] Krastanov, Stefan, Albert, Victor V., Shen, Chao, Zou, Chang-Ling, Heeres, Reinier W., Vlastakis, Brian, Schoelkopf, Robert J., and Jiang, Liang. Universal control of an oscillator with dispersive coupling to a qubit. *Physical Review A*, 92(4):040303 (2015). (Cited on page xiv).
- [Krinner et al., 2022] Krinner, Sebastian, Lacroix, Nathan, Remm, Ants, Di Paolo, Agustin, Genois, Elie, Leroux, Catherine, Hellings, Christoph, Lazar, Stefania, Swiadek, Francois, Herrmann, Johannes, Norris, Graham J., Andersen, Christian Kraglund, Müller, Markus, Blais, Alexandre, Eichler, Christopher, and Wallraff, Andreas. Realizing repeated quantum error correction in a distance-three surface code. *Nature*, 605(7911):669–674 (2022). (Cited on page 11).
- [Krupka et al., 2006] Krupka, J., Breeze, J., Centeno, A., Alford, N., Claussen, T., and Jensen, L. Measurements of Permittivity, Dielectric Loss Tangent, and Resistivity of Float-Zone Silicon at Microwave Frequencies. *IEEE Transactions on Microwave Theory and Techniques*, 54(11):3995–4001 (2006). (Cited on page 25).

- [Lei* & Krayzman* et al., 2020] Lei, Chan U, **Krayzman, Lev**, Ganjam, Suhas, Frunzio, Luigi, and Schoelkopf, Robert J. **High coherence superconducting microwave cavities with indium bump bonding**. *Applied Physics Letters*, 116(15):154002 (2020). (Cited on pages 5, 13, 30, 61, 182, and 195).
- [Mallek et al., 2021] Mallek, Justin L., Yost, Donna-Ruth W., Rosenberg, Danna, Yoder, Jonilyn L., Calusine, Gregory, Cook, Matt, Das, Rabindra, Day, Alexandra, Golden, Evan, Kim, David K., Knecht, Jeffery, Niedzielski, Bethany M., Schwartz, Mollie, Sevi, Arjan, Stull, Corey, Woods, Wayne, Kerman, Andrew J., and Oliver, William D. Fabrication of superconducting through-silicon vias. *arXiv:2103.08536 [cond-mat, physics:physics, physics:quant-ph]* (2021). (Cited on page 87).
- [Manucharyan et al., 2009] Manucharyan, Vladimir E., Koch, Jens, Glazman, Leonid I., and Devoret, Michel H. **Fluxonium: Single Cooper-Pair Circuit Free of Charge Offsets**. *Science*, 326(5949):113–116 (2009). (Cited on page 2).
- [Mariantoni et al., 2011] Mariantoni, Matteo, Wang, H., Yamamoto, T., Neeley, M., Bialczak, Radoslaw C., Chen, Y., Lenander, M., Lucero, Erik, O'Connell, A. D., Sank, D., Weides, M., Wenner, J., Yin, Y., Zhao, J., Korotkov, A. N., Cleland, A. N., and Martinis, John M. **Implementing the Quantum von Neumann Architecture with Superconducting Circuits**. *Science*, 334(6052):61–65 (2011). (Cited on page 5).
- [Martinis et al., 2005] Martinis, John M., Cooper, K. B., McDermott, R., Steffen, Matthias, Ansmann, Markus, Osborn, K. D., Cicak, K., Oh, Seongshik, Pappas, D. P., Simmonds, R. W., and Yu, Clare C. **Decoherence in Josephson Qubits from Dielectric Loss**. *Physical Review Letters*, 95(21) (2005). (Cited on page 29).
- [Martinis et al., 1985] Martinis, John M., Devoret, Michel H., and Clarke, John. **Energy-Level Quantization in the Zero-Voltage State of a Current-Biased Josephson Junction**. *Physical Review Letters*, 55(15):1543–1546 (1985). (Cited on page 2).
- [Mattis and Bardeen, 1958] Mattis, D. C. and Bardeen, J. **Theory of the Anomalous Skin Effect in Normal and Superconducting Metals**. *Physical Review*, 111(2):412–417 (1958). (Cited on pages 41 and 42).
- [McRae et al., 2017] McRae, C R H, Béjanin, J H, and Pagel, Z. Thermocompression bonding technology for multilayer superconducting quantum circuits. *Appl. Phys. Lett.*, page 6 (2017). (Cited on page 65).
- [McRae et al., 2020a] McRae, C. R. H., McFadden, A., Zhao, R., Wang, H., Long, J. L., Zhao, T., Park, S., Bal, M., Palmstrøm, C. J., and Pappas, D. P. Dielectric loss in epitaxial Al/GaAs/Al trilayers for superconducting circuits. *arXiv:2009.10101 [physics, physics:quant-ph]* (2020a). (Cited on page 84).
- [McRae et al., 2020b] McRae, C. R. H., Wang, H., Gao, J., Vissers, M. R., Brecht, T., Dunsworth, A., Pappas, D. P., and Mutus, J. **Materials loss measurements**

- using superconducting microwave resonators. *Review of Scientific Instruments*, 91(9):091101 (2020b). (Cited on pages 29 and 125).
- [Minev et al., 2016] Minev, Z. K., Serniak, K., Pop, I. M., Leghtas, Z., Sliwa, K., Hatridge, M., Frunzio, L., Schoelkopf, R. J., and Devoret, M. H. **Planar Multilayer Circuit Quantum Electrodynamics**. *Physical Review Applied*, 5(4) (2016). (Cited on pages 17 and 87).
- [Müller et al., 2019] Müller, Clemens, Cole, Jared H, and Lisenfeld, Jürgen. **Towards understanding two-level-systems in amorphous solids: Insights from quantum circuits**. *Reports on Progress in Physics*, 82(12):124501 (2019). (Cited on page 29).
- [Murthy et al., 2022] Murthy, A. A., Lee, J., Kopas, C., Reagor, M. J., McFadden, A. P., Pappas, D. P., Checchin, M., Grassellino, A., and Romanenko, A. **TOF-SIMS analysis of decoherence sources in superconducting qubits**. *Applied Physics Letters*, 120(4):044002 (2022). (Cited on pages 31 and 137).
- [Nakamura et al., 1999] Nakamura, Y., Pashkin, Yu A., and Tsai, J. S. **Coherent control of macroscopic quantum states in a single-Cooper-pair box**. *Nature*, 398(6730):786–788 (1999). (Cited on pages 2 and 4).
- [Nam, 1967] Nam, Sang Boo. **Theory of Electromagnetic Properties of Strong-Coupling and Impure Superconductors. II**. *Physical Review*, 156(2):487–493 (1967). (Cited on page 41).
- [Nguyen et al., 2019] Nguyen, Long B., Lin, Yen-Hsiang, Somoroff, Aaron, Mencia, Raymond, Grabon, Nicholas, and Manucharyan, Vladimir E. **High-Coherence Fluxonium Qubit**. *Physical Review X*, 9(4):041041 (2019). (Cited on page 13).
- [Nielsen and Chuang, 2000] Nielsen, Michael A. and Chuang, Isaac L. *Quantum Computation and Quantum Information*. Cambridge University Press (2000). (Cited on page 5).
- [O'Brien et al., 2017] O'Brien, William, Vahidpour, Mehrnoosh, Whyland, Jon Tyler, Angeles, Joel, Marshall, Jayss, Scarabelli, Diego, Crossman, Genya, Yadav, Kamal, Mohan, Yuvraj, Bui, Catvu, Rawat, Vijay, Renzas, Russ, Vodrahalli, Nagesh, Bestwick, Andrew, and Rigetti, Chad. **Superconducting Caps for Quantum Integrated Circuits**. *arXiv:1708.02219 [physics, physics:quant-ph]* (2017). (Cited on page 65).
- [Ofek* & Petrenko* et al., 2016] Ofek, Nissim, Petrenko, Andrei, Heeres, Reinier, Reinhold, Philip, Leghtas, Zaki, Vlastakis, Brian, Liu, Yehan, Frunzio, Luigi, Girvin, S. M., Jiang, L., Mirrahimi, Mazyar, Devoret, M. H., and Schoelkopf, R. J. **Extending the lifetime of a quantum bit with error correction in superconducting circuits**. *Nature*, 536(7617):441–445 (2016). (Cited on pages 3 and 11).
- [Paik et al., 2011] Paik, Hanhee, Schuster, D. I., Bishop, Lev S., Kirchmair, G., Ceteani, G., Sears, A. P., Johnson, B. R., Reagor, M. J., Frunzio, L., Glazman, L. I.,

- Girvin, S. M., Devoret, M. H., and Schoelkopf, R. J. **Observation of High Coherence in Josephson Junction Qubits Measured in a Three-Dimensional Circuit QED Architecture.** *Physical Review Letters*, 107(24):240501 (2011). (Cited on page 5).
- [Pappas et al., 2011] Pappas, David P., Vissers, Michael R., Wisbey, David S., Kline, Jeffrey S., and Gao, Jiansong. **Two Level System Loss in Superconducting Microwave Resonators.** *IEEE Transactions on Applied Superconductivity*, 21(3):871–874 (2011). (Cited on pages 83 and 84).
- [Petersan and Anlage, 1998] Petersan, Paul J. and Anlage, Steven M. **Measurement of resonant frequency and quality factor of microwave resonators: Comparison of methods.** *Journal of Applied Physics*, 84(6):3392–3402 (1998). (Cited on page 51).
- [Phillips, 1987] Phillips, W A. **Two-level states in glasses.** *Reports on Progress in Physics*, 50(12):1657–1708 (1987). (Cited on page 29).
- [Pippard, 1953] Pippard, Alfred Brian. An experimental and theoretical study of the relation between magnetic field and current in a superconductor. *Proceedings of the Royal Society of London. Series A. Mathematical and Physical Sciences*, 216(1127):547–568 (1953). (Cited on page 41).
- [Place et al., 2020] Place, Alex P. M., Rodgers, Lila V. H., Mundada, Pranav, Smitham, Basil M., Fitzpatrick, Mattias, Leng, Zhaoqi, Premkumar, Anjali, Bryon, Jacob, Sussman, Sara, Cheng, Guangming, Madhavan, Trisha, Babla, Harshvardhan K., Jaeck, Berthold, Gyenis, Andras, Yao, Nan, Cava, Robert J., de Leon, Nathalie P., and Houck, Andrew A. New material platform for superconducting transmon qubits with coherence times exceeding 0.3 milliseconds. *arXiv:2003.00024 [cond-mat, physics:physics, physics:quant-ph]* (2020). (Cited on pages 13 and 137).
- [Pop et al., 2014] Pop, Ioan M., Geerlings, Kurtis, Catelani, Gianluigi, Schoelkopf, Robert J., Glazman, Leonid I., and Devoret, Michel H. **Coherent suppression of electromagnetic dissipation due to superconducting quasiparticles.** *Nature*, 508(7496):369–372 (2014). (Cited on page 4).
- [Pöpel, 1989] Pöpel, R. (1989). Electromagnetic Properties of Superconductors. In Kose, Volkmar, editor, *Superconducting Quantum Electronics*, pages 44–78. Springer Berlin Heidelberg, Berlin, Heidelberg. (Cited on page 41).
- [Pozar, 2011] Pozar, David M. *Microwave Engineering, 4th Edition.* Wiley (2011). (Cited on pages 33, 34, and 50).
- [Premkumar et al., 2021] Premkumar, Anjali, Weiland, Conan, Hwang, Sooyeon, Jäck, Berthold, Place, Alexander P. M., Waluyo, Iradwikanari, Hunt, Adrian, Bisogni, Valentina, Pelliciari, Jonathan, Barbour, Andi, Miller, Mike S., Russo, Paola, Camino, Fernando, Kisslinger, Kim, Tong, Xiao, Hybertsen, Mark S., Houck, Andrew A., and Jarrige, Ignace. **Microscopic relaxation channels in materials for superconducting qubits.** *Communications Materials*, 2(1):72 (2021). (Cited on page 31).

- [Premkumar et al., 2020] Premkumar, Anjali, Weiland, Conan, Hwang, Sooyeon, Jaeck, Berthold, Place, Alexander P. M., Waluyo, Iradwikanari, Hunt, Adrian, Bisogni, Valentina, Pelliciari, Jonathan, Barbour, Andi, Miller, Mike S., Russo, Paola, Camino, Fernando, Kisslinger, Kim, Tong, Xiao, Hybertsen, Mark S., Houck, Andrew A., and Jarrige, Ignace. Microscopic Relaxation Channels in Materials for Superconducting Qubits. *arXiv:2004.02908 [cond-mat, physics:physics, physics:quant-ph]* (2020). (Cited on page 137).
- [Probst et al., 2015] Probst, S., Song, F. B., Bushev, P. A., Ustinov, A. V., and Weides, M. Efficient and robust analysis of complex scattering data under noise in microwave resonators. *Review of Scientific Instruments*, 86(2):024706 (2015). (Cited on pages 51 and 55).
- [Purcell, 1946] Purcell, Edward. Spontaneous Emission Probabilities at Radio Frequencies. *Physical Review*, 69(11-12):674–674 (1946). (Cited on page 21).
- [Quintana et al., 2014] Quintana, C. M., Megrant, A., Chen, Z., Dunsworth, A., Chiaro, B., Barends, R., Campbell, B., Chen, Yu, Hoi, I.-C., Jeffrey, E., Kelly, J., Mutus, J. Y., O’Malley, P. J. J., Neill, C., Roushan, P., Sank, D., Vainsencher, A., Wenner, J., White, T. C., Cleland, A. N., and Martinis, John M. Characterization and reduction of microfabrication-induced decoherence in superconducting quantum circuits. *Applied Physics Letters*, 105(6):062601 (2014). (Cited on page 83).
- [Read* & Chapman* et al., 2022] Read, Alexander P., Chapman, Benjamin J., Lei, Chan U., Curtis, Jacob C., Ganjam, Suhas, Krayzman, Lev, Frunzio, Luigi, and Schoelkopf, Robert J. (2022). Precision measurement of the microwave dielectric loss of sapphire in the quantum regime with parts-per-billion sensitivity. (Cited on pages 91, 107, 127, 128, 131, and 195).
- [Reagor, 2015] Reagor, Matthew. *Superconducting Cavities for Circuit Quantum Electrodynamics*. PhD thesis, Yale University (2015). (Cited on pages 35, 41, and 185).
- [Reagor et al., 2013] Reagor, Matthew, Paik, Hanhee, Catelani, Gianluigi, Sun, Luyan, Axline, Christopher, Holland, Eric, Pop, Ioan M., Masluk, Nicholas A., Brecht, Teresa, Frunzio, Luigi, Devoret, Michel H., Glazman, Leonid, and Schoelkopf, Robert J. Reaching 10 ms single photon lifetimes for superconducting aluminum cavities. *Applied Physics Letters*, 102(19):192604 (2013). (Cited on pages 22, 127, 130, and 185).
- [Reagor et al., 2016] Reagor, Matthew, Pfaff, Wolfgang, Axline, Christopher, Heeres, Reinier W., Ofek, Nissim, Sliwa, Katrina, Holland, Eric, Wang, Chen, Blumoff, Jacob, Chou, Kevin, Hatridge, Michael J., Frunzio, Luigi, Devoret, Michel H., Jiang, Liang, and Schoelkopf, Robert J. Quantum memory with millisecond coherence in circuit QED. *Physical Review B*, 94(1):014506 (2016). (Cited on pages 5, 13, 23, 113, and 115).

- [Reed et al., 1973] Reed, R.P., Schramm, R.E., and Clark, A.F. **Mechanical, thermal, and electrical properties of selected polymers.** *Cryogenics*, 13(2):67–82 (1973). (Cited on page 105).
- [Reinhold, 2019] Reinhold, Philip. *Controlling Error-Correctable Bosonic Qubits.* PhD thesis, Yale University (2019). (Cited on page 116).
- [Romanenko et al., 2020] Romanenko, A, Pilipenko, R, Zorzetti, S, Frolov, D, Awida, M, Belomestnykh, S, Posen, S, and Grassellino, A. Three-Dimensional Superconducting Resonators at $T < 20$ mK with Photon Lifetimes up to $\tau = 2$ s. *Physical Review Applied*, 13(3) (2020). (Cited on pages 4, 16, 64, and 82).
- [Rooks et al., 2002] Rooks, M. J., Kratschmer, E., Viswanathan, R., Katine, J., Fontana, R. E., and MacDonald, S. A. **Low stress development of poly(methylmethacrylate) for high aspect ratio structures.** *Journal of Vacuum Science & Technology B: Microelectronics and Nanometer Structures*, 20(6):2937 (2002). (Cited on page 172).
- [Rosenberg et al., 2017] Rosenberg, D., Kim, D., Das, R., Yost, D., Gustavsson, S., Hover, D., Krantz, P., Melville, A., Racz, L., Samach, G. O., Weber, S. J., Yan, F., Yoder, J. L., Kerman, A. J., and Oliver, W. D. **3D integrated superconducting qubits.** *npj Quantum Information*, 3(1) (2017). (Cited on page 65).
- [Sandberg et al., 2013] Sandberg, Martin, Vissers, Michael R., Ohki, Thomas A., Gao, Jiansong, Aumentado, José, Weides, Martin, and Pappas, David P. **Radiation-suppressed superconducting quantum bit in a planar geometry.** *Applied Physics Letters*, 102(7):072601 (2013). (Cited on page 16).
- [Schreier et al., 2008] Schreier, J. A., Houck, A. A., Koch, Jens, Schuster, D. I., Johnson, B. R., Chow, J. M., Gambetta, J. M., Majer, J., Frunzio, L., Devoret, M. H., Girvin, S. M., and Schoelkopf, R. J. **Suppressing charge noise decoherence in superconducting charge qubits.** *Physical Review B*, 77(18):180502 (2008). (Cited on page 4).
- [Schuster, 2007] Schuster, David. *Circuit Quantum Electrodynamics.* PhD thesis, Yale University (2007). (Cited on pages 6 and 138).
- [Shnirman et al., 1997] Shnirman, Alexander, Schön, Gerd, and Hermon, Ziv. **Quantum Manipulations of Small Josephson Junctions.** *Physical Review Letters*, 79(12):2371–2374 (1997). (Cited on page 4).
- [Teufel et al., 2011] Teufel, J. D., Donner, T., Li, Dale, Harlow, J. W., Allman, M. S., Cicak, K., Sirois, A. J., Whittaker, J. D., Lehnert, K. W., and Simmonds, R. W. **Sideband cooling of micromechanical motion to the quantum ground state.** *Nature*, 475(7356):359–363 (2011). (Cited on page 12).
- [Tinkham, 2015] Tinkham, Michael. *Introduction to Superconductivity.* Dover Books on Physics. Dover Publ, Mineola, NY, 2 ed edition (2015). (Cited on pages 43 and 45).

- [Turneaure, 1972] Turneaure, J. P. The Status of Superconductivity for RF Applications. In *Applied Superconductivity Conference*, volume Pub. No. 72CH0682-5-TABSC, pages 621–630, Annapolis, Maryland. IEEE (1972). (Cited on page 4).
- [Turneaure et al., 1991] Turneaure, J. P., Halbritter, J., and Schwettman, H. A. **The surface impedance of superconductors and normal conductors: The Mattis-Bardeen theory.** *Journal of Superconductivity*, 4(5):341–355 (1991). (Cited on page 41).
- [Turneaure and Weissman, 1968] Turneaure, J. P. and Weissman, Ira. **Microwave Surface Resistance of Superconducting Niobium.** *Journal of Applied Physics*, 39(9):4417–4427 (1968). (Cited on pages 4 and 128).
- [Van Duzer and Turner, 1981] Van Duzer, Theodore and Turner, C. W. *Principles of Superconductive Devices and Circuits.* Elsevier, New York (1981). (Cited on pages 33, 44, 45, and 198).
- [Wade and Banister, 1975] Wade, K. and Banister, A. J. *The Chemistry of Aluminium, Gallium, Indium and Thallium.* Number Ch. 12 in Comprehensive Inorganic Chemistry. Pergamon Press, Oxford, reprinted, with corr edition (1975). (Cited on page 75).
- [Wallraff et al., 2004] Wallraff, A., Schuster, D. I., Blais, A., Frunzio, L., Huang, R.-S., Majer, J., Kumar, S., Girvin, S. M., and Schoelkopf, R. J. **Strong coupling of a single photon to a superconducting qubit using circuit quantum electrodynamics.** *Nature*, 431(7005):162–167 (2004). (Cited on page 6).
- [Walsh and Tomaselli, 1990] Walsh, P. J. and Tomaselli, V. P. **Theory of microwave surface impedance in superconductors and normal metals.** *American Journal of Physics*, 58(7):644–650 (1990). (Cited on page 41).
- [Wang et al., 2015] Wang, C., Axline, C., Gao, Y. Y., Brecht, T., Chu, Y., Frunzio, L., Devoret, M. H., and Schoelkopf, R. J. **Surface participation and dielectric loss in superconducting qubits.** *Applied Physics Letters*, 107(16):162601 (2015). (Cited on pages 26, 29, and 128).
- [Wang et al., 2022] Wang, Chenlu, Li, Xuegang, Xu, Huikai, Li, Zhiyuan, Wang, Junhua, Yang, Zhen, Mi, Zhenyu, Liang, Xuehui, Su, Tang, Yang, Chuhong, Wang, Guangyue, Wang, Wenyan, Li, Yongchao, Chen, Mo, Li, Chengyao, Linghu, Ke-huan, Han, Jiaxiu, Zhang, Yingshan, Feng, Yulong, Song, Yu, Ma, Teng, Zhang, Jingning, Wang, Ruixia, Zhao, Peng, Liu, Weiyang, Xue, Guangming, Jin, Yirong, and Yu, Haifeng. **Towards practical quantum computers: Transmon qubit with a lifetime approaching 0.5 milliseconds.** *npj Quantum Information*, 8(1):3 (2022). (Cited on page 13).
- [Wenner et al., 2011] Wenner, J., Barends, R., Bialczak, R. C., Chen, Yu, Kelly, J., Lucero, Erik, Mariantoni, Matteo, Megrant, A., O’Malley, P. J. J., Sank, D., Vainsencher, A., Wang, H., White, T. C., Yin, Y., Zhao, J., Cleland, A. N., and

- Martinis, John M. [Surface loss simulations of superconducting coplanar waveguide resonators](#). *Applied Physics Letters*, 99(11):113513 (2011). (Cited on page 27).
- [Woods et al., 2019] Woods, W., Calusine, G., Melville, A., Sevi, A., Golden, E., Kim, D.K., Rosenberg, D., Yoder, J.L., and Oliver, W.D. [Determining Interface Dielectric Losses in Superconducting Coplanar-Waveguide Resonators](#). *Physical Review Applied*, 12(1):014012 (2019). (Cited on pages 128 and 131).
- [Zhou et al., 2022] Zhou, Chao, Lu, Pinlei, Praquin, Matthieu, Chien, Tzu-Chiao, Kaufman, Ryan, Cao, Xi, Xia, Mingkang, Mong, Roger, Pfaff, Wolfgang, Pekker, David, and Hatridge, Michael (2022). A modular quantum computer based on a quantum state router. (Cited on page 7).
- [Zmuidzinas, 2012] Zmuidzinas, Jonas. [Superconducting Microresonators: Physics and Applications](#). *Annual Review of Condensed Matter Physics*, 3(1):169–214 (2012). (Cited on pages 33, 41, and 46).

ProQuest Number: 29397311

INFORMATION TO ALL USERS

The quality and completeness of this reproduction is dependent on the quality
and completeness of the copy made available to ProQuest.



Distributed by ProQuest LLC (2023).

Copyright of the Dissertation is held by the Author unless otherwise noted.

This work may be used in accordance with the terms of the Creative Commons license
or other rights statement, as indicated in the copyright statement or in the metadata
associated with this work. Unless otherwise specified in the copyright statement
or the metadata, all rights are reserved by the copyright holder.

This work is protected against unauthorized copying under Title 17,
United States Code and other applicable copyright laws.

Microform Edition where available © ProQuest LLC. No reproduction or digitization
of the Microform Edition is authorized without permission of ProQuest LLC.

ProQuest LLC
789 East Eisenhower Parkway
P.O. Box 1346
Ann Arbor, MI 48106 - 1346 USA